First measurement of the fragmentation fraction ratio f_s/f_d with tree level hadronic decays at 7 TeV pp collisions

Cover: Justine Kaplun (under the supervision of Cristian Bacchi) and Ivo Kaplun

Printed by Ipskamp Drukkers.

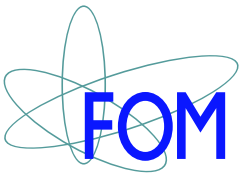

This work is part of the research programme of the 'Stichting voor Fundamenteel Onderzoek der Materie (FOM)', which is financially supported by the 'Nederlandse Organisatie voor Wetenschappelijk Onderzoek (NWO)'

VRIJE UNIVERSITEIT

First measurement of the fragmentation fraction ratio f_s/f_d with tree level hadronic decays at 7 TeV pp collisions

ACADEMISCH PROEFSCHRIFT

ter verkrijging van de graad Doctor aan
de Vrije Universiteit Amsterdam,
op gezag van de rector magnificus
prof.dr. L.M. Bouter,
in het openbaar te verdedigen
ten overstaan van de promotiecommissie
van de faculteit der Exacte Wetenschappen
op woensdag 19 september 2012 om 13.45 uur
in de aula van de universiteit,
De Boelelaan 1105

door

Barbara Storaci

geboren te Milaan, Italië

promotor:	prof. dr. M.H.M. Merk
copromotor:	dr. N. Tuning

Alle gioie della mia vita:
Sam, JuJu e Camille
e a chi è già nel nostro cuore
ma non ancora qui con
il suo sorriso.

Contents

Introduction

Truth is ever to be found in simplicity, and not in the multiplicity and confusion of things.
Isaac Newton

The Standard Model (SM) of particle physics is a theory describing the strong and electroweak interactions between elementary particles. This theory was confirmed by a wealth of experimental results over the last decades. Despite its success, the SM is not considered to be the conclusive theory of elementary particles, since it contains a large number of free parameters and fails to explain fundamental issues like the dominance of matter over antimatter in the universe and the presence of dark matter. The possibility of physics beyond the SM (also referred as New Physics (NP)) is clearly open.

There are two possible ways to search for new physics: direct searches, as e.g. in the ATLAS and CMS experiments, looking for the production of new on-shell particles, and indirect searches, as e.g. those performed in the LHCb experiment, where new virtual particles are exchanged at the quantum level. The advantage of this second technique is that, thanks to the virtual nature of the new particles, it is possible to see their effects at lower beam collision energy than that needed to produce them directly.

Rare B-meson decays occurring via flavour-changing neutral currents are good candidates to search for NP-effects, since in the SM they are forbidden at tree level and large enhancements of their branching ratios may result from the exchange of new particles. One of the most promising decay channels for the indirect search of new physics is the neutral B-meson decaying in two muons. This decay is extremely rare, but its branching fraction is theoretically well predicted in the SM and NP-contributions can significantly enhance it.

At hadron colliders, branching ratios of B-decays are determined through comparison to B^0 decays with precisely known branching fractions, measured at the B factories. However, this requires the knowledge of the parameter f_s/f_d, that represents the probability ratio that a b-quark hadronizes with a d or a s-quark. This parameter was already measured by the experiments at LEP and Tevatron colliders but its value can a priori not be extrapolated to the LHC environment since it can in principle depend on the center-of-mass energy as well as on transverse momentum and on pseudo-rapidity of the produced B-meson. A direct de-

termination of the f_s/f_d ratio in LHCb can be achieved through the combined measurement of the hadronic decays $B^0 \to D^- K^+$, $B_s^0 \to D_s^- \pi^+$ and $B^0 \to D^- \pi^+$. These are very favourable from an experimental point of view for LHCb, robust with respect to NP contributions and theoretically well understood. The precision of the f_s/f_d measurement affects the NP discovery potential for the $B_s^0 \to \mu^+\mu^-$ decay. For large data samples and small experimental systematic uncertainty, the uncertainty in f_s/f_d becomes the key element for a discovery of new physics, determining the limiting value of the branching fraction for which one can claim evidence of new physics.

In the family of $B_{(s)}^0 \to D_{(s)}^- h^+$ decays, the tree-level Cabibbo-suppressed decay mode $B_s^0 \to D_s^\pm K^\mp$ offers an alternative method of testing the SM. In fact, the properties of weak interactions with quarks are expressed through relations that can be represented in a triangle in the complex plane, the Cabibbo-Kobayashi-Maskawa (CKM) Unitarity Triangle. The properties of this triangle, the side lengths, total area and angles, can be evaluated experimentally by studying particular B-decays. The least precise measured parameter of the unitary triangle is the angle γ. The high abundance of $b\overline{b}$ pairs, together with an excellent proper time resolution, an excellent particle identification and trigger capability to select hadronic final states, allows the LHCb experiment to determine this parameter through a decay–time dependent analysis using the $B_s^0 \to D_s^\pm K^\mp$ decay.

This manuscript is organised as follows. First, in chapter 1, a theoretical introduction on the importance of measuring f_s/f_d at a hadron collider is provided. The theoretical background (based on factorisation) leading to a measurement of this parameter through hadronic decays of the type $B_{(s)}^0 \to D_{(s)}^- h^+$, and the related formulæ used for the numerical evaluation from data, are presented. In chapter 2, an overview of the LHCb detector and its performance is given. The LHC experiments have to cope with a high interaction rate of 40 MHz. Fast FE-electronics is required and the quality of the data must continuously be monitored to guarantee good performance for track reconstruction, as presented in chapter 3. Another crucial experimental aspect is the ageing rate of the Outer Tracker (OT) gas detector. The OT modules were designed to withstand a large irradiation dose during the planned ten years of operation. However, the modules have shown a rapid gain loss under mild irradiation in the laboratory. Chapter 4 is devoted to describe the ageing phenomenon as well as studies of potential solutions proposed to overcome the problem. The quality of the OT performance affects the track reconstruction efficiency, a key ingredient for any physical analysis. In chapter 5 a new method is presented to determine the track reconstruction efficiency from the data itself. The method is applied to real data as well as to the simulation to evaluate their agreement.

Finally two analyses based on $B_{(s)}^0 \to D_{(s)}^- h^+$ hadronic decays are presented. The relative abundance, obtained analysing 35 pb^{-1}, of the three tree decay modes $B^0 \to D^- K^+$, $B^0 \to D^- \pi^+$ and $B_s^0 \to D_s^- \pi^+$ are presented in chapter 6. From these, the relative branching ratio of $B^0 \to D^- K^+$ with respect to $B^0 \to D^- \pi^+$ is determined, resulting in the current world-best measurement, and two new measurements of the fragmentation fraction f_s/f_d. The importance of the f_s/f_d measurement are put in perspective in chapter 7 where their impact on the $B_s^0 \to \mu^+\mu^-$ measurement is discussed. The paper describing the $B_s^0 \to D_s^\pm K^\mp$ and $B_s^0 \to D_s^- \pi^+$ branching fractions measurement performed at LHCb with 0.37 fb^{-1} in included

as chapter 8. These measurements result in two branching fraction evaluations with a total uncertainty significantly smaller than the previous world average measurements. The decay $B_s^0 \to D_s^- \pi^+$ presented here is the most precise B_s^0 decay mode presently measured. The $B_s^0 \to D_s^\pm K^\mp$ branching fraction can be considered as the first ingredient towards the time dependent measurement of the angle γ that will be performed when more data will be available.

First Chapter

Hadronic tree decays of $B^0_{(s)}$–mesons

All models are wrong. Some are useful.
George E. P. Box

1.1 Introduction

Before LHCb started taking data, only few decay channels of the B^0_s meson had been observed at the Tevatron and at the KEKB-facility [1]. The large $b\overline{b}$ cross section at the LHC allows to explore a large number of B^0_s–decays, including those with small branching fractions. Several rare decays can be used for precise tests of the Standard Model (SM) and the measurement of the branching fraction of the rare decay $B^0_s \to \mu^\pm\mu^\mp$ is a prime example where improved knowledge of f_s/f_d is needed to reach a high sensitivity in the search for physics beyond the Standard Model. This is discussed in chapter 7 of this thesis.

At B factories electrons and positrons collide at 10.58 GeV, the mass of the $\Upsilon(4S)$ resonance, producing a high rate of events that decay almost instantaneously into a pair of B–mesons. The $\Upsilon(4S)$ resonance provides a clean source of B–mesons as it decays for 48.4%(51.6%) of the cases into a B^0–$\overline{B^0}$ (B^+B^-) pair [2]. In this environment absolute branching fractions of many B^0 decays can be measured. On the other hand B^0_s–mesons are too massive to be produced at the $\Upsilon(4S)$–energy. At hadron colliders, pp or $p\overline{p}$ beams collide and several types of b–mesons can be produced. Since in this environment the number of $B^0_{(s)}$–mesons initially produced is not known precisely, relative branching fraction measurement are performed.

The ratio of probabilities of a b quark to fragment into a B^0 or into a B^0_s–meson, known as f_s/f_d, enters in the evaluation of the branching ratio (BR) of any B^0_s mode relative to a well known B^0 decay mode. This parameter was measured at LEP and Tevatron through semi–leptonic decays [3]. However the fragmentation fractions ratio is in principle dependent on the centre-of-mass energy, as well as on transverse momentum and pseudo–rapidity of the B–meson, and an extrapolation at LHCb of this parameter is therefore not reliable. It was proposed in [4, 5] to measure the fragmentation fraction at LHCb with hadronic decays.

This parameter can be measured also through semi–leptonic decays [6], but in the case of hadronic decay channels the full final state is reconstructed. The two measurements are complementary and can be combined to obtain the world best measurement of f_s/f_d parameter.

Since the measurement of the fragmentation fraction ratio f_s/f_d with tree level hadronic decays is the main research topic of this thesis, first the concept of factorisation will be discussed, which is a crucial ingredient in the theoretical calculation of branching fractions and which can be tested experimentally. Subsequently, the evaluation of f_s/f_d with hadronic decays of the type $B^0_{(s)} \to D_{(s)}h$ is presented.

1.2 Decay topologies

Both b and c quarks are considered heavy quarks, and the *"heavy–light"* decays of the type $B^0_{(s)} \to D_{(s)}h$ are characterised by the transition $b \to c$ with the production of two mesons: a *heavy* one that can be a $D^{\pm}$ or $D_s^{\pm}$ meson and a *light* one, h. The study in this thesis is limited to those decays where the light meson is a pseudo–scalar, where h is either a charged pion or a charged kaon.

Three topologies are allowed for tree level decays:

- **Colour–favoured tree amplitude** (T): decays associated to a transition $\overline{b} \to \overline{c}u\overline{q}$ (q = d or s) in which the $\overline{q}u$ system from the W forms a pseudo–scalar meson, while the $\overline{c}$ combines with the spectator quark to form the other meson.
- **Colour–suppressed amplitude** (C): decays associated to the transition $\overline{b} \to \overline{c}u\overline{q}$ ($q = d$ or s) in which the $\overline{q}u$ quarks from the W hadronize to the two mesons.
- **Exchange amplitude** (E): decays in which the $\overline{b}$ quark and the initial q quark in the decaying B meson exchange a W and become a $\overline{c}u$ pair. A $q\overline{q}$ pair from the vacuum completes the hadronization.

Fig. 1.1 shows the diagrams for these three topologies.

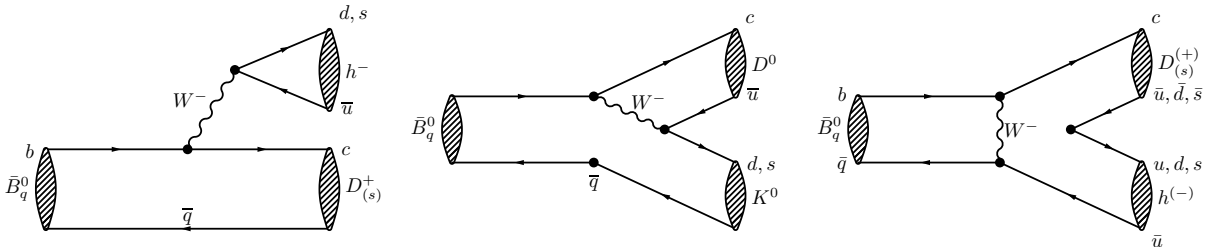

(a) T (b) C (c) E

Figure 1.1: The colour–allowed tree (T), colour–suppressed (C) and exchange (E) topologies contributing to heavy–light decays ($q \in \{u, d, s\}$)

1.3 Factorisation

The theoretical description of non–leptonic weak decays of B–mesons concerns a low–energy effective Hamiltonian containing local four–quark operators. Consequently, in the calculation of the transition amplitude, there are non–perturbative hadronic matrix elements of these operators. In literature, the matrix element of a four–fermion operator is approximated by the product of two currents, i.e. the exchange of gluons between the final states $D_{(s)}$ and h is neglected. This concept is referred to as "factorisation"[1] and is exploited in the heavy–quark limit for a variety of B–decays in [7, 8]. Assuming factorisation, the transition $B^0_{(s)} \to D^+_{(s)} h^-$ for the colour–allowed tree diagram can be written as [9]:

$$< D^+_{(s)} h^- | H_W | \overline{B}^0_{(s)} >= \frac{G_F}{\sqrt{2}} V_{cb} V^*_{uq} a_1 < D^+_{(s)} | (\overline{c}b)_L | \overline{B}^0_s >< h^- | (\overline{q}u)_L | 0 > \tag{1.1}$$

where the quantity a_1 describes the deviation from naive factorisation and it is found to be a quasi–universal quantity $|a_1| \simeq 1.05$ [7] in "QCD factorisation" for colour–allowed tree decays with very small process–dependent non–factorisable corrections. The first matrix element, $< D^+_{(s)} | (\overline{c}b)_L | \overline{B}^0_s >$, is the form factor, also indicated in literature as $F(B \to D)$, while the second corresponds to the decay constant of the hadron f_π or f_K.

Factorisation test

Other tree level decays are semi–leptonic decays, such as $B^0_{(s)} \to D_{(s)} l\nu$. Semi–leptonic decay rates can be compared to the branching fraction of colour–favoured tree decays to test factorisation as originally proposed in [10], because these semi–leptonic decays do not suffer from strong interactions between the final state particles. The semi–leptonic decay rate is measured as a function of the four–momentum transfer to the lepton pair, q^2, and can be parametrised with the formalism proposed by Caprini, Lellouch, and Neubert [11]. From the ratio of the differential rates of semi–leptonic decays evaluated at a specific $q^2 = m^2_h$, to account for the dependence of the form factor on q^2, and the branching fraction of a hadronic tree decay, a test of factorisation can be performed. For example, in the case of the $\overline{B^0} \to D^+ K^-$ mode, the value of $|a_1|$ can be evaluated as follows [7]:

$$R_K = \frac{BR(\overline{B^0} \to D^+ K^-)}{d\Gamma(\overline{B^0} \to D^+ l^- \overline{\nu_l})/dq^2|_{q^2=m^2_K}} = 6\pi^2 \tau_{B^0} |V_{us}|^2 f_K^2 |a_1(DK)|^2 \tag{1.2}$$

where τ_{B^0} is the B^0 lifetime, q^2 the four–momentum transfer to the lepton pair, $|V_{us}|$ the corresponding element of the Cabibbo–Kobayashi–Maskawa matrix, and f_K the decay constant of the K meson. The results of the factorisation tests for the decays $B^0 \to D^{(*)-} K^+$ are given

[1] Notice that there are several definitions of "factorisation" as, for example, the possibility to separate long distance contributions from a short distance part (that is calculable with perturbative QCD). In this thesis, the term "factorisation" is used to refer to the approximation that the matrix element of a four fermion operator is written as the product of two current, i.e. no gluons are exchanged between the two fermions in the final state.

Table 1.1: Determination of the factor $|a_1|$ extracted from the comparison of the hadronic branching ratios and the semi–leptonic decay rate. The uncertainty is estimated by adding the uncertainties of the hadronic branching ratio and the semi–leptonic rate in quadrature. The correlations between the form–factor parameters for the semi–leptonic decay rate are take into account [5].

Topology	Decay	BR	$\|a_1\|$	
		($\times 10^4$)	*BABAR*	Belle
T	$\overline{B^0} \to D^+ K^-$	2.0 ± 0.6	0.89 ± 0.13	0.88 ± 0.16
T	$\overline{B^0} \to D^{*+} K^-$	2.14 ± 0.16	0.96 ± 0.05	0.99 ± 0.05

in Tab. 1.1. At present, the statistical uncertainty of the $B^0 \to D^- K^+$ mode is too large to allow for a precise test of factorisation. This will become achievable with 1.1 fb^{-1} already acquired in 2011 with the LHCb experiment.

1.4 f_s/f_d fragmentation fraction

In order to compare the branching fractions of B_s^0–decays to a known B^0–decay the relative fraction of produced B_s^0–mesons over B^0–mesons needs to be known. In other words, the fragmentation fraction of b–quarks to hadronize as a B_s^0 and B^0–mesons f_s/f_d needs to be determined.

The argument can also be reversed and specific B^0 and B_s^0 decays, of which the ratio of branching fractions is theoretically well understood, can be used to measure f_s/f_d. Suitable decays to measure fragmentation fractions at LHCb have to be such that:

- the ratio of their branching ratios must be easy to measure at LHCb (i.e. charged particles in the final state);
- the decays must be robust with respect to the impact of New Physics (NP) contributions (i.e. only tree level decays, no penguin diagram contributions);
- the ratio of their branching ratios must be theoretically well understood within the Standard Model (SM) (i.e. pure colour–favoured tree diagram processes).

The decays fulfilling all these requirements are $B_s^0 \to D_s^- \pi^+$ and $B^0 \to D^- K^+$. These decay channels are pure colour–allowed tree–diagram topologies (T) and factorisation is shown to work well in these transitions [7].

The branching ratio of the decays can be written as [4]:

$$BR(\overline{B_q^0} \to D_q^+ h^-) = \frac{G_F^2 (m_{B_q}^2 - m_{D_q}^2)^2 |\overrightarrow{q}| \tau_{B_q}}{16\pi m_{B_q}^2} |V_q^* V_{cb}|^2 [f_h F_0(B \to D)]^2 |a_1(D_q h)|^2 \qquad (1.3)$$

Table 1.2: Parameters used in the numerical analysis.

m_{B^0}	5279.17 MeV/c^2	$m_{B_s^0}$	5366.3 MeV/c^2
m_{D^+}	1869.60 MeV/c^2	$m_{D_s^+}$	1968.47 MeV/c^2
m_{K^+}	497.61 MeV/c^2	m_{π^+}	139.57 MeV/c^2
f_π	130.41 MeV/c^2	f_K	156.1 MeV/c^2
$\|V_{ud}\|$	0.97425	$\|V_{us}\|$	0.2252

with $h = K$ and π for $q = d$ and s, respectively. Here, G_F is Fermi's constant, m denotes meson masses, $\overrightarrow{q}$ is the momentum of the final–state D_q and h mesons in the rest frame of the $\overline{B_q^0}$ meson, τ_{B_q} is the lifetime of the $\overline{B_q^0}$ meson, $V_q^* V_{cb}$ with $V_q = V_{ud}$ and V_{us} for $q = d$ and s respectively, contains the relevant elements of the Cabibbo–Kobayashi–Maskawa (CKM) matrix, f_h is the h–meson decay constant, and F_0 is the form factor. The numerical value of the quantities used in the calculations are summarised in Tab. 1.2. The quantity $a_1(D_q h)$ describes the deviation from naive factorisation, as discussed in the previous section.

Using Eq. 1.3, the ratio of the branching ratios for $B_s^0 \to D_s^- \pi^+$ and $B^0 \to D^- K^+$ results in:

$$\frac{BR(B_s^0 \to D_s^- \pi^+)}{BR(B^0 \to D^- K^+)} = \frac{\Phi_s}{\Phi} \frac{\tau_{B_s}}{\tau_B} \left| \frac{V_{ud}}{V_{us}} \right|^2 \left(\frac{f_\pi}{f_K} \right)^2 \left[\frac{F(B_s^0 \to D_s)}{F(B^0 \to D)} \right]^2 \left| \frac{a_1(D_s\pi)}{a_1(DK)} \right|^2 \tag{1.4}$$

where $\Phi_{(s)}$ is the phase–space:

$$\Phi_{(s)} = \frac{\left(m_{B_{(s)}}^2 - m_{D_{(s)}}^2 \right)^2}{32\, m_{B_{(s)}}^3} \sqrt{\left(m_{B_{(s)}}^2 - m_{D_{(s)}}^2 - m_h^2 \right)^2 - 4\, m_{D_{(s)}}^2\, m_h^2} \tag{1.5}$$

The ratio of the corresponding number of signal events observed in the experiment is then given by:

$$\frac{N_{D_s\pi}}{N_{DK}} = \frac{f_s}{f_d} \frac{\epsilon_{D_s\pi}}{\epsilon_{DK}} \frac{BR(B_s^0 \to D_s^- \pi^+)}{BR(B^0 \to D^- K^+)} \tag{1.6}$$

where the ϵ are the detector efficiencies. Using Eq. 1.3 the expression for f_s/f_d is obtained [4]:

$$\frac{f_s}{f_d} = 0.0743 \frac{\tau_{B_d}}{\tau_{B_s}} \left[\frac{1}{\mathcal{N}_a \mathcal{N}_F} \frac{\epsilon_{DK}}{\epsilon_{D_s\pi}} \frac{N_{D_s\pi}}{N_{DK}} \right] \tag{1.7}$$

with

$$\mathcal{N}_a \equiv \left| \frac{a_1(D_s\pi)}{a_1(DK)} \right|^2, \mathcal{N}_f \equiv \left[\frac{F(B_s^0 \to D_s)}{F(B^0 \to D)} \right]^2. \tag{1.8}$$

The factors $\mathcal{N}_a$ and $\mathcal{N}_f$ contain the theoretical uncertainties in the f_s/f_d determination due to U–spin–breaking effects.

Ratios of hadronic decays can be studied using three symmetries: the isospin symmetry involving the exchange of u and d quark (when spectator), U–spin symmetry with the

exchange of the d and s quarks and the SU(3) symmetry with the exchange s, u, d. The uncertainty on the QCD prediction for ratios of hadronic quantities is reduced by using the fact that the strong interaction is flavor blind and the symmetry can be broken only because of differences in the quark masses. The related correction is called the SU(3)–breaking effect.

The first factor can be written as:

$$\mathcal{N}_a \approx 1 + Re(a_1^{NF}(D_s\pi) - a_1^{NF}(D_dK)) \tag{1.9}$$

where a_1^{NF} describes the non–universal, i.e. process–dependent, non–factorisable contributions to the decays. These contributions cannot be calculated reliably. However they are suppressed by at least one power of Λ_{QCD}/m_b, and they are numerically expected at the few percent level[7]. The deviation of Eq. 1.9 from a value of 1 is not only suppressed by Λ_{QCD}/m_b, but also by the fact that it is a U–spin breaking difference. Any decay topology contributing to $B^0 \to D^-K^+$ has a counterpart in $B_s^0 \to D_s^-\pi^+$ which is related to the B^0 case through the interchange of all down and strange quarks. Consequently, taking all these considerations into account, $1-\mathcal{N}_a$ is conservatively expected to be at most a few percent, calculated to be $\mathcal{N}_a = 1.00 \pm 0.02$ [4].

The main uncertainty in Eq. 1.7 is the ratio of form factors, $\mathcal{N}_F$, where U–spin breaking corrections arise from d and s spectator–quark effects. Unfortunately, $F(B_s \to D_s)$ form factors have so far received only small theoretical attention and the calculation, using QCD–sum–rule techniques gives $\mathcal{N}_F = 1.24 \pm 0.08$, [9]. Recently a new calculation became available [12], $\mathcal{N}_F = 1.094 \pm 0.088 \pm 0.030$. In this lattice–QCD calculation, the dominant error, currently, is the statistical uncertainty and it might be possible to reduce it.

An alternative method for the determination of f_s/f_d at LHCb, $B^0 \to D^-\pi^+$ together with $B_s^0 \to D_s^-\pi^+$, was proposed [5] to compensate for large statistical uncertainty of the decay $B^0 \to D^-K^+$ with the first data of LHCb. In fact, the impact of the exchange topology on the $B^0 \to D^-\pi^+$ is expected to be small, while this channel has a branching ratio ~ 15 times larger than $B^0 \to D^-K^+$ as it is not Cabibbo–suppressed. The expression for the extraction of f_s/f_d from the ratio of $B^0 \to D^-\pi^+$ and $B_s^0 \to D_s^-\pi^+$ is:

$$\frac{f_s}{f_d} = 0.982\,\frac{\tau_{B_d}}{\tau_{B_s}}\left[\frac{1}{\widetilde{\mathcal{N}_a}\mathcal{N}_F\mathcal{N}_E}\,\frac{\epsilon_{D\pi}}{\epsilon_{D_s\pi}}\,\frac{N_{D_s\pi}}{N_{D\pi}}\right] \tag{1.10}$$

where the numerical factor takes phase–space effects into account,

$$\widetilde{\mathcal{N}_a} \equiv \left|\frac{a_1(D_s\pi)}{a_1(D\pi)}\right|^2, \mathcal{N}_F \equiv \left[\frac{F_0^{(s)}(m_\pi^2)}{F_0^{(d)}(m_\pi^2)}\right]^2 \tag{1.11}$$

describe SU(3)–breaking effects, and

$$\mathcal{N}_E \equiv \left|\frac{T}{T+E}\right|^2 \tag{1.12}$$

takes into account the effect of the additional exchange diagram in the $B^0 \to D^-\pi^+$ decay. The extra term due to the exchange topology was calculated to be: $\mathcal{N}_E = 0.966 \pm 0.056 \pm 0.05$

[5]. The determination of the ratios of event yields of the decays $B^0 \to D^- K^+$, $B_s^0 \to D_s^- \pi^+$ and $B^0 \to D^- \pi^+$ are discussed in chapter 6 and the resulting values for the ratio of fragmentation fractions will be presented.

The application of this measurement for the extraction of the best upper limit for the measurement of the branching fraction of the $B_s^0 \to \mu^\pm \mu^\mp$ decay are presented in chapter 7. This decay plays a key–role in the indirect search of new physics since its branching fraction is well predicted in the Standard Model and new physics contribution can enhance it considerably.

Second Chapter

The LHCb experiment

It is always better to be optimistic and be wrong than to be pessimistic and being right.
Anonymous

In this chapter the LHCb experiment is introduced. In Sec. 2.1 an introduction of the accelerator and its conditions during the 2010 and 2011 data taking periods are described and in Sec. 2.2 the main components of LHCb detector are presented. The attention is then focused in Sec. 2.3 on a description of the Outer Tracker subdetector for which detailed studies regarding readout quality and radiation resistance are presented in this thesis in chapter 3 and chapters 4, respectively.

2.1 The Large Hadron Collider and the 2010 run period

The Large Hadron Collider [13], LHC, is the world's most powerful particle accelerator. This machine is placed at CERN, 100 m underground, and is capable of accelerating both protons and heavy ions (Pb-Pb).

The LHC machine is designed to achieve collisions with a centre–of–mass energy of $\sqrt{s}$ = 14 TeV at a maximum luminosity of $10^{34}\,\mathrm{cm}^{-2}\mathrm{s}^{-1}$ with proton beams. During the 2010 and 2011 data taking periods the machine operated at a centre-of-mass energy of $\sqrt{s}$ = 7 TeV. LHCb collected the data corresponding to an integrated luminosity around 37 pb^{-1} in 2010 and 1.1 fb^{-1} in 2011 resulting in a total amount of 10^{11} $b\bar{b}$ particle pairs produced in the detector acceptance. The trend of the integrated luminosity is shown in Fig. 2.1.

Along the LHC tunnel four main experiments are placed. LHCb [14] is the experiment dedicated to the study of CP violation and rare decays of b–hadrons to search indirectly for new particles, while other two experiments, ATLAS [15] and CMS [16] are general purpose experiments with a broad physics program, including direct searches for new particles. ALICE [17] is a dedicated heavy ion experiment that studies the behaviour of nuclear matter at high energies, and in particular the properties of the quark–gluon plasma.

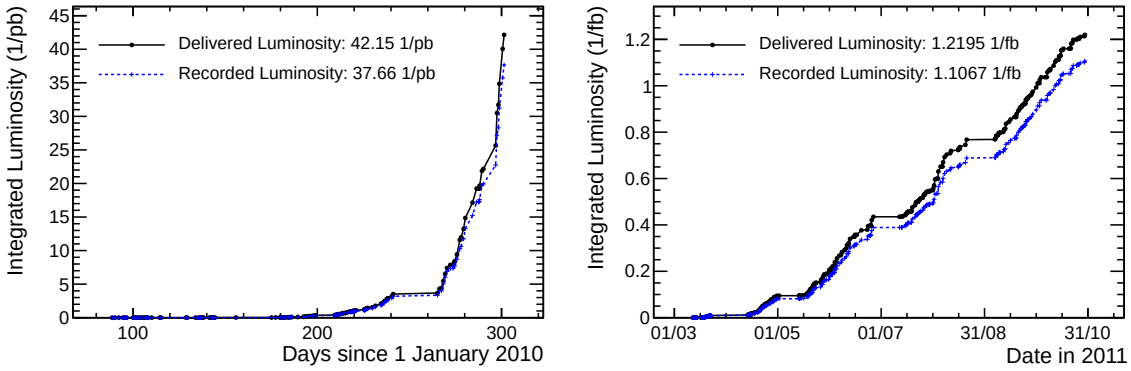

(a) (b)

Figure 2.1: Integrated luminosity for the 2010 (a) and 2011 (b) data taking periods. The difference between the curves corresponds to the LHCb data taking efficiency, which on average corresponds to ~ 90%

2.2 The LHCb experiment

The LHCb experiment is dedicated to study heavy flavour physics at the LHC. Its primary goal is to look for indirect evidence of new physics in CP violation and rare decays of beauty and charm hadrons. In the pp collisions at the LHC b–quarks will be produced in $b\overline{b}$ pairs. The simulation with PYTHIA[18] of b and $\overline{b}$ quarks production in pp collisions shows that the formation of the b–hadrons is concentrated at small (forward direction) or large (backward direction) angles along the beam, as shown in Fig. 2.2. On that basis LHCb has been designed as a single–arm forward spectrometer, see Fig. 2.3, with the experimental polar coverage around the direction of one of the proton beams ranging from 10 to 300 mrad in the x–z plane and from 10 to 250 mrad in the y–z plane.

In addition to b–hadrons the forward acceptance contains a high density of particles produced in the underlying event, as well as particles produced in pile–up interactions occurring simultaneously to $b\overline{b}$ events. Selection and reconstruction of rare B–decays in an environment with high background rates imply the following experimental requirements for the detector:

- **Mass Resolution**: The momenta of charged particles are measured as they traverse a magnet dipole with a bending power of 4 Tm. A high precision in the mass reconstruction results in narrow mass peaks and allows to suppress the combinatorial background due to random combinations of tracks. The mass peak obtained with 2011 data for the decays $B_s^0 \to D_s^{\pm} K^{\mp}$ is shown in Fig. 2.4 as an example of the excellent mass resolution and particle identification capabilities in LHCb.

  The mass determination requires an excellent momentum measurement of the charge particles. The typical momentum reconstruction of $\delta p/p$ between 0.3 and 0.5 % results in expected mass resolution of 24 MeV/c^2 for 2–body B–decays [19].

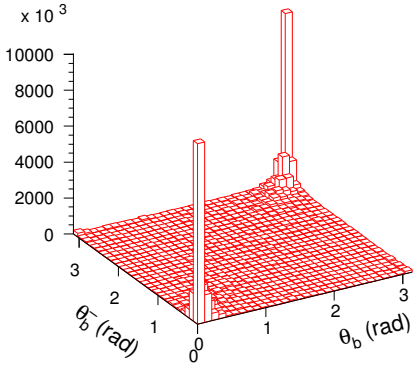

Figure 2.2: Polar angle distribution of b– and $\overline{b}$–hadrons produced in pp interaction as calculated by the PYTHIA event generator.

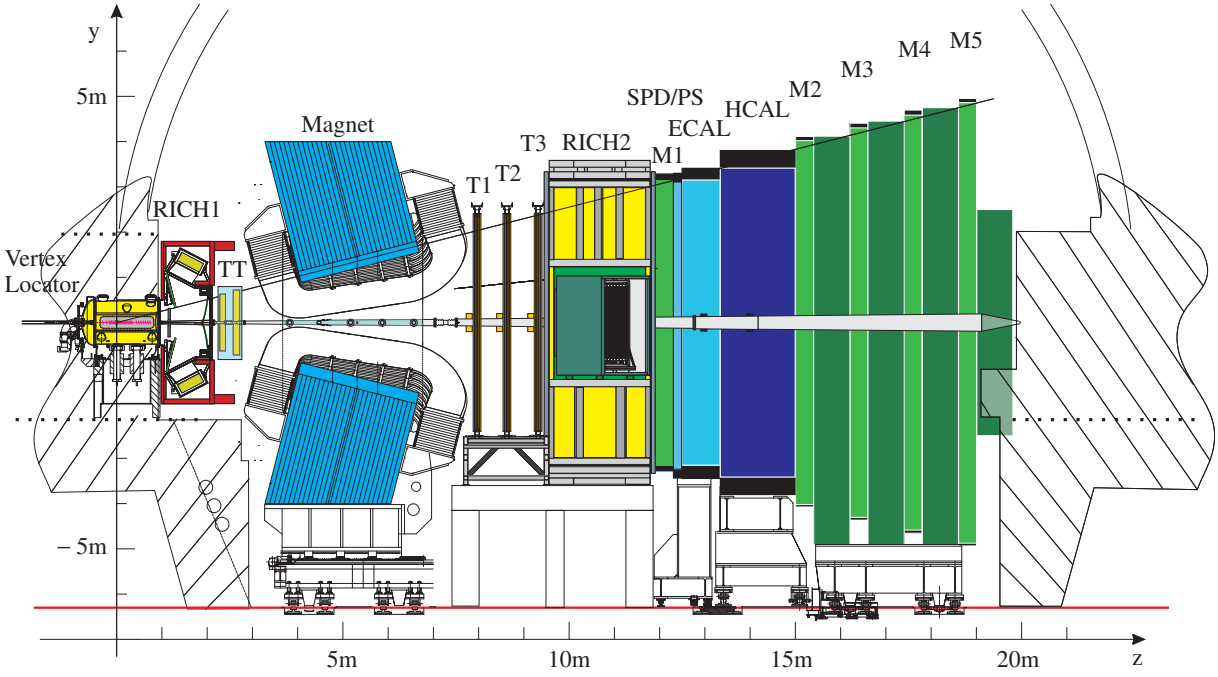

Figure 2.3: Side view of the LHCb detector (non-bending plane, y–z).

- **Vertexing and decay time resolution**: A good track impact parameter resolution leads to high separation power of displaced vertices with respect to the primary collision vertex. The typical impact parameter resolution in LHCb can be represented as $\sigma(IP) = 13.2\ \mu m + 24.7 \mu m / p_T$ [20]. In addition the B–decay time resolution should be suffi-

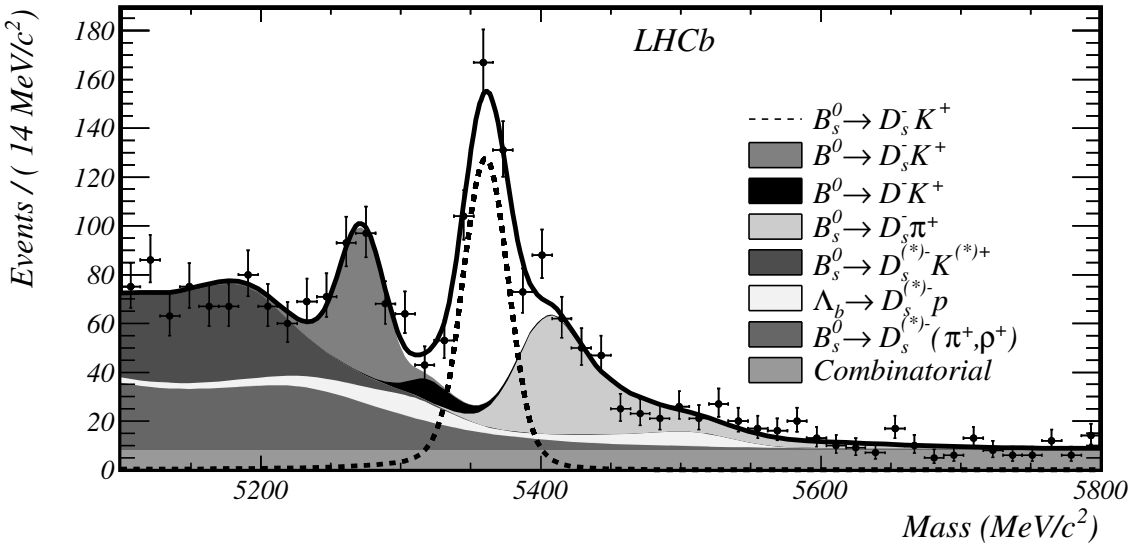

Figure 2.4: Invariant mass distribution for the $B_s^0 \to D_s^{\pm} K^{\mp}$ decay channel with 336 pb^{-1} of 2011 data. The excellent mass resolution and particle identification capability at LHCb allowed the discrimination of the $B_s^0 \to D_s^{\pm} K^{\mp}$ peak from the partially reconstructed backgrounds.

cient to resolve the fast B_s^0 oscillations and measure time dependent CP asymmetries. An example of measured asymmetry for B_s^0 candidates in bins of the decay time t modulo $2\pi/\Delta m_s$ is shown in Fig. 2.5

- **Particle Identification for hadrons and leptons**:
  - Hadron identification ($\pi/K/p$ separation) is used in the reconstruction of many hadronic B–decay channels, like $B_{(s)}^0 \to D_{(s)}^- \pi^+$ and $B_{(s)}^0 \to D_{(s)}^- K^+$, see Fig. 2.4. In addition, kaon identification is used in flavour tagging methods. The kaon identification efficiency is typically around $95.46 \pm 0.25\%$ with a pion mis–identification probability of about $7.06 \pm 0.06\%$ [21];
  - Lepton identification is used to select (semi–)leptonic decay channels, and is for example used to identify electrons and muons for flavour tagging.
- **Triggering**: the trigger serves to firstly supplies minimum bias events and provide an enriched B–event sample and secondly to selectively reconstruct individual B–decay final states. For this a fast online track reconstruction algorithm is executed at an early stage of the trigger.

An example of an LHCb event display is shown in Fig. 2.6 for an event identified as a $B_s^0 \to \mu^{\pm}\mu^{\mp}$candidate.

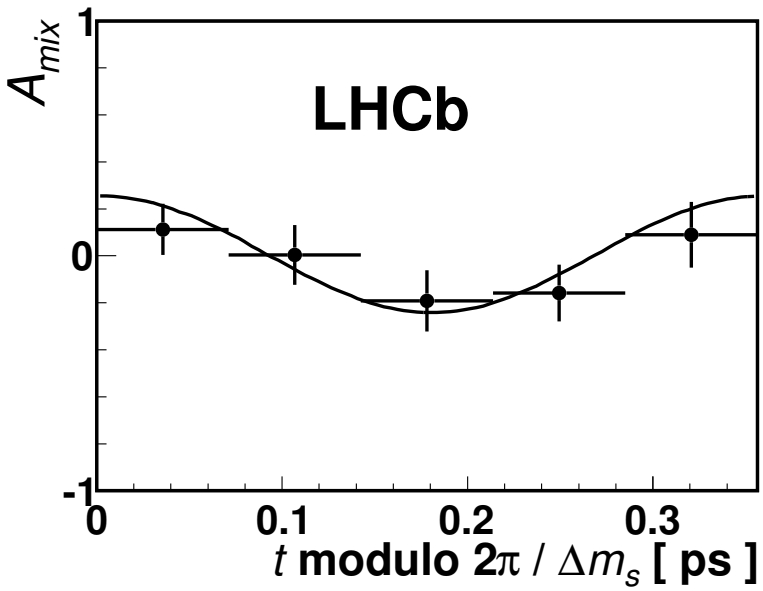

Figure 2.5: Measured asymmetry for B_s^0 candidates in bins of the decay time t modulo $2\pi/\Delta m_s$ [22]. The projection of the likelihood fit is superimposed.

2.3 Tracking system

To ensure selection and reconstruction of B–decays, a detector with high tracking capabilities is required. A high efficiency to select high multiplicity decays, like $B^0 \rightarrow D^-(K^-\pi^+\pi^+)\pi^+$, a high resolution to suppress backgrounds, and a high vertex resolution to resolve fast B_s^0 oscillations (4 times per B_s^0 lifetime)[1] are needed.

The LHCb tracking system consists of silicon strip detectors and straw-tube drift chambers. More details on the tracking sub-detector are given in the next subsections.

Vertex Locator

To reconstruct the position of the primary and secondary vertices the Vertex Locator (VELO), a silicon strip detector, is used. The VELO is composed of 23 stations consisting of two measurement layers each. One of the measurement layers provides the radial coordinate (r) and the other the azimuthal coordinate (ϕ). The sensors are placed at a radial distance of 8 mm from the beam, which is smaller than the aperture required by the LHC during beam injection. For this reason the detector consists of two equal halves that are retracted in between physics runs up to a distance of 30 mm. The VELO allows to reconstruct primary vertices with a resolution between 10 to 40 μm in the x direction and between 50 and 250 μm in the z direction, using between 40 and 5 tracks, respectively, as shown in Fig. 2.7.

[1] The period of B_s^0 oscillation is about $t = \frac{2\pi}{\Delta m} = 0.35$ ps, which results in 4 oscillations within the B_s^0 lifetime of 1.4 ps

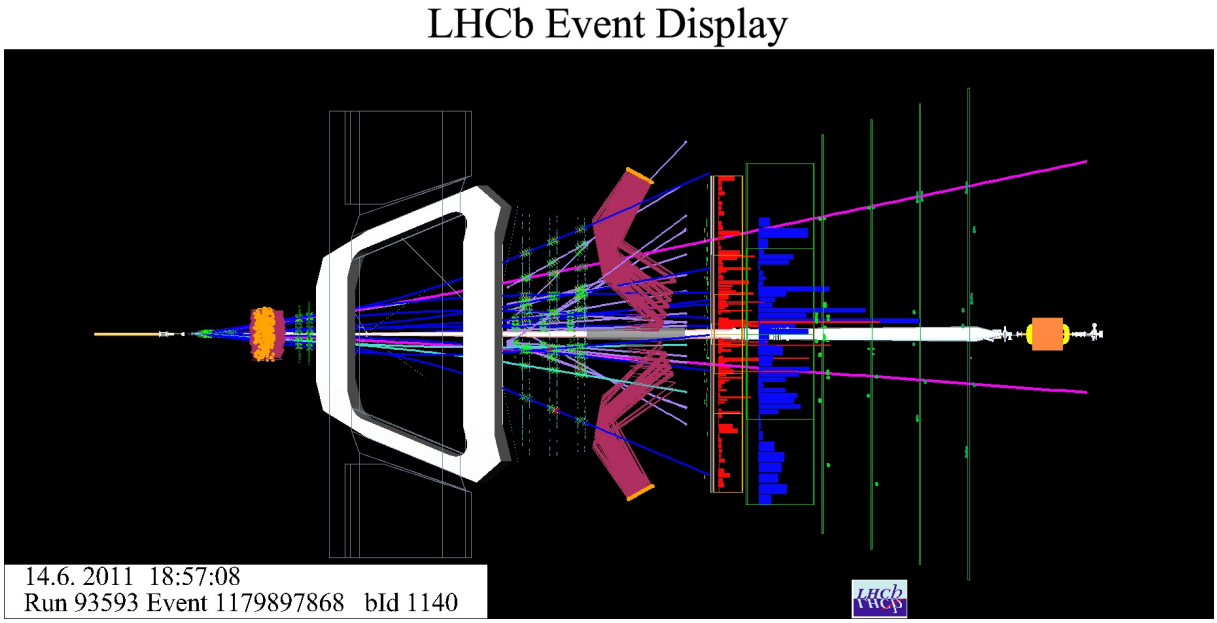

(a)

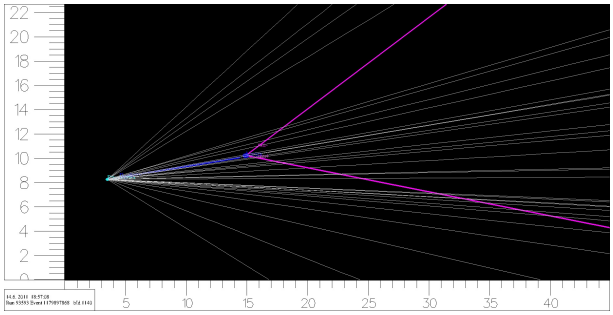

(b)

Figure 2.6: Example of an LHCb event display for an event identified as a $B_s^0 \to \mu^\pm\mu^\mp$ candidate (a). Zoom on the primary–secondary vertex region inside the VELO. The two magenta tracks are muon candidates (b).

The Tracker Turicensis

The Tracker Turicensis (TT) is a silicon strip detector placed between the VELO and the magnet. The TT provides precise measurements of the charged particle trajectories at the entrance of the B-field and as such contributes to their momentum measurement. Moreover, the TT allows to reconstruct long-lived neutral particles, like the K_s^0, that decay outside the acceptance of the VELO. It is composed of two stations containing two measurement layers each. The four layers have strips oriented with a stereo angle $0°, -5°, 5°, 0°$. During 2010 run 99.6% of the TT detector channels were functional [23] and provided clusters with a measurement resolution 62 μm.

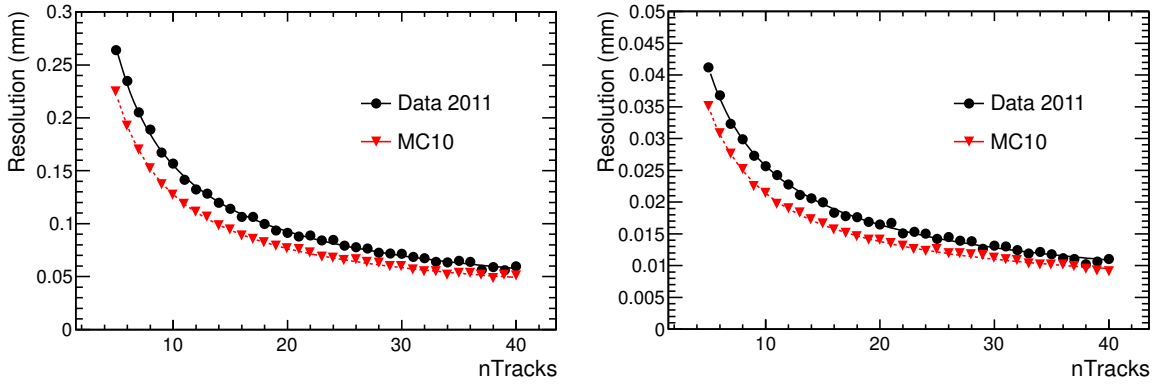

(a) (b)

Figure 2.7: Primary vertex position resolution in real data for the x horizontal coordinate, perpendicular to the beam (a), and the z coordinate parallel to the beam (b).

The Inner Tracker

The Inner Tracker system (IT) is placed in the high rapidity region around the beam pipe downstream the magnet. To be able to cope with the high particle flux, around the beam line, a silicon strip detector technology was chosen. All three IT stations consist of four individual detector boxes, and each of them containing four detection layers of silicon strips with the same stereo orientation as the TT detector. During 2010 98.6% of the IT channels were functional [23] providing measurements with a resolution of 58 μm, while the occupancy was approximately 2.3%.

The Outer Tracker

The Outer Tracker (OT) is a gaseous detector based on straw tube technology, with the anode-wire under positive high voltage (1550 V) and the cathode-straw connected to ground. The counting gas mixture consists of Ar(70%), CO_2 (28.5%), and O_2 (1.5%).

A schematic illustration of the working principle of a straw-tube detector is shown in Fig. 2.8 (a). A charged particle crossing the straw ionises the counting gas producing electron-ion pairs. The electric field between the anode and the cathode separates the electrons and ions. While the heavy ions slowly drift toward the cathode, the electrons quickly gain kinetic energy, and, when they reach the ionisation potential of the counting gas, free more electrons generating an avalanche. The arrival of the electrons at the anode-wire and of ions at the cathode–wall both induce a detectable electrical signal. The drift speed is approximately 70μm/s. The time of the occurrence of the fast electron pulse with respect to the LHC clock is a measure of the drift time.

The OT consists of three stations (T1-T3) surrounding the IT. Similarly to the IT, each station consist of four layers, the outside layers are oriented vertically while the two central layers are tilted by $\pm 5^\circ$. Each module contains two staggered layers of 64 straws, called

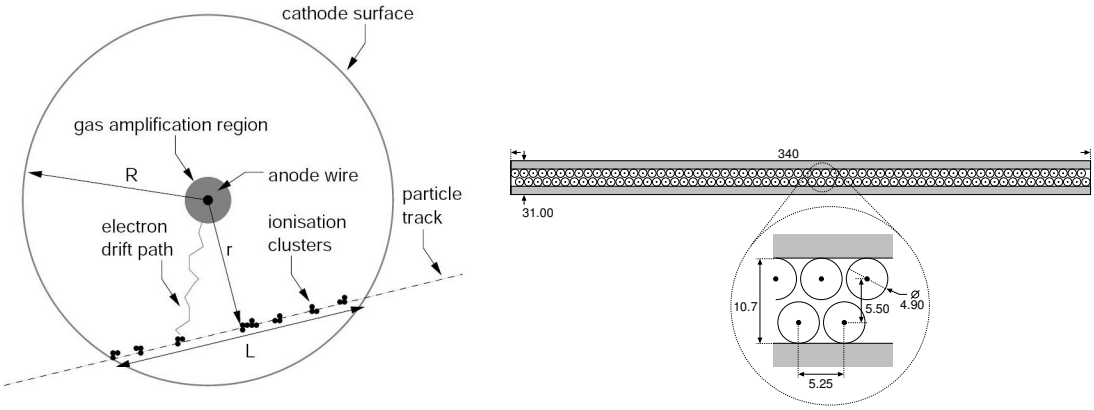

(a) (b)

Figure 2.8: Schematic illustration of the detection principle of a straw-tube (a). Cross section of an OT module (b).

mono-layers, see Fig. 2.8 (b).

The modules are mounted on a frame structure (C-frame). One station contains four C-frames, two on either side of the beam pipe. Seven long modules per layer in one C-frame, called F-modules, cover the full vertical detector acceptance with a total length of 4.9 m. The inner region of the OT, above and below the IT detector boxes, consists of shorter modules, called S-modules. S1-modules, with a length of 2.4 m, are located at the side of the beam pipe adjacent to the last F-module, and S2 and S3-modules, with a length of 2.3 m, are located above and below the beam pipe. For a schematic representation of this modules structure see Fig. 3.4 in chapter 3.

More details about the electronic readout and monitoring system are given in chapter 3, while detailed studies of the ageing rate of the detector modules are presented in chapter 4.

Track reconstruction efficiency

The track reconstruction strategy is based on two steps: first, the track finding pattern recognition algorithm to determine which groups of hits (track) belong to individual particles, followed by the track fitting algorithm to determine the optimal trajectory parameters.

The track reconstruction algorithms are described in [24] and are shortly summarised in chapter 5. Several methods to evaluate the tracking efficiency from data were developed. One method, the "tag-and-probe" method, using decays of $K_s^0 \to \pi^{\pm}\pi^{\mp}$, selects events where the "tag pion" is completely reconstructed by the tracking system, while the other, "probe pion", is reconstructed using only a track segment in the VELO matched with a cluster in the calorimeter. The tracking efficiency is evaluated by matching the "probe track" with a segment in the T-stations. An agreement of the efficiency between data and Monte Carlo simulation within 3-4% is found [23]. An alternative method to determine the tracking efficiency without using a specific decay channel is presented in chapter 5 of this thesis.

2.4 Particle Identification

Particle identification (PID) is a fundamental requirement for LHCb and is provided by Ring Imaging Cherenkov detectors (RICH1 and RICH2), electromagnetic and hadronic calorimeters (ECAL and HCAL), and muon chambers.

Hadron identification, in particular the ability to distinguish between pions and kaons, is of crucial importance for the analyses of many B-decays, especially where the final state of interest is purely hadronic. Also, kaons and leptons are crucial to determine the initial flavour of the B meson, known as flavour tagging. The LHCb RICH system provides pion–kaon separation, covering a momentum range between 2 GeV/c up to 100 GeV/c, see Sec. 2.4. The calorimeters provide identification of electrons, photons, and hadrons in addition to the measurement of their energy and position, see Sec. 2.4. The muon system provides identification of muons to a high level of purity, see Sec. 2.4, essential for many CP-sensitive measurements that have J/ψ mesons in the final states, or rare decays such as $B_s^0 \to \mu^\pm\mu^\mp$ or $B^0 \to K^{*0}\mu^\pm\mu^\mp$. In addition to their usage in the offline reconstruction, the energy information from the ECAL and HCAL, and the momentum information from the muon detector are used in the lowest level of the trigger system, see Sec. 2.5.

Ring Imaging Cherenkov Detectors

The capability to distinguish between pions and kaons is essential for the extraction of the relative yields of decays like $B^0 \to D^-\pi^+$, $B^0 \to D^-K^+$, $B_s^0 \to D_s^-\pi^+$ and $B_s^0 \to D_s^\pm K^\mp$ with different combinations of pions and kaons in the final state. To distinguish the final states in LHCb, particle identification in the momentum range between 2 GeV/c up to 100 GeV/c is needed. The most suitable technique to cover the required momentum range is the use of RICH detectors with various radiators.

RICH detectors exploit the Cherenkov effect, the emission of radiation due to the passage of a charged particle in a dielectric medium at a speed larger than the phase velocity of the light in that medium. The particle type is derived from its mass, which can be obtained combining a measurement of the velocity of the particle with its momentum estimate. The Cherenkov radiation is emitted in a cone with respect to the particle trajectory, and the particle velocity can be extracted from the emission angle θ_c of the Cherenkov radiation through:

$$cos(\theta_c) = \frac{1}{n\beta} \tag{2.1}$$

where $\beta = v/c$, and n is the refractive index of the dielectric medium.

Due to the strong correlation between momentum and polar angle of the decay products in B–decays in LHCb, see Fig. 2.9 (a), two RICH detectors have been constructed, one upstream (RICH1) and one downstream (RICH2) of the magnet.

The RICH1 detector, located between the VELO and the TT, identifies low momentum particles over a polar angle acceptance from 25 mrad to 300(250) mrad in the horizontal(vertical) plane. A suitable radiator for tracks below 10 GeV/c in RICH1 is solid silica aerogel, see Fig. 2.9 (b), while the intermediate region of the spectrum, i.e. 10-60 GeV/c, is well

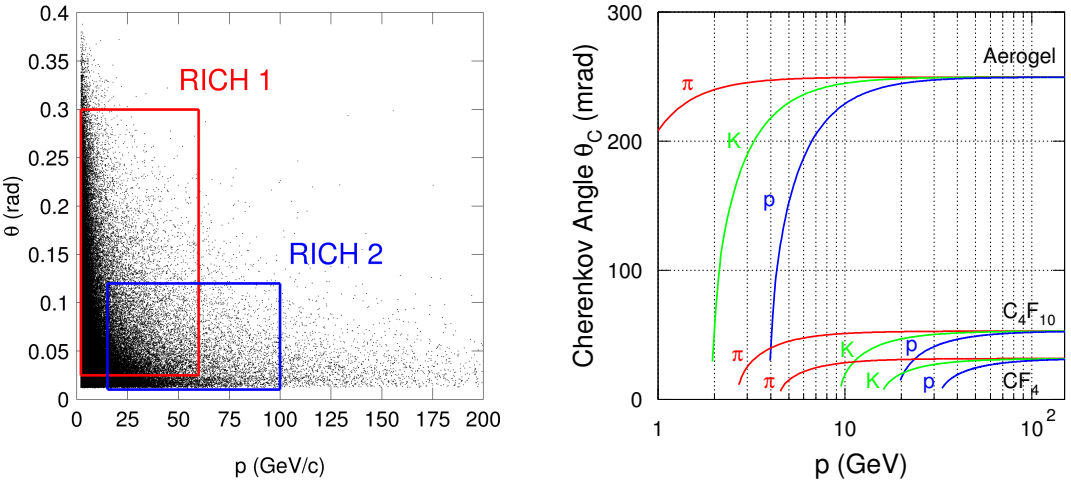

(a) (b)

Figure 2.9: (a): A scatter plot of polar angle θ versus the momentum for all the tracks in simulated $B_s^0 \to D_s^- \pi^+$ events. (b): The Cherenkov angle θ_c plotted for each of the three radiators used in LHCb as a function of the charged particle momentum.

matched by gaseous C_4F_{10}. RICH2 is located just after the T stations and covers the region from 15 mrad to 120(100) mrad in the horizontal(vertical) plane, populated mostly by high momentum particles. To detect these high momentum tracks gaseous CF_4 is used as radiator. The distribution of the Cherenkov angle θ_c as a function of momentum for all tracks in simulated events is shown in Fig. 2.9 (a). The distribution of Cherenkov angle θ_c as a function of momentum for various particle types is shown in Fig. 2.9 (b) for the three radiators, showing the momentum range in which each radiator can be used to distinguish the various particle types.

The arrangement of optics is similar in both sub-detectors: spherical focusing mirrors project the Cherenkov photons into a series of flat mirrors which then reflect them into a series of photon detectors arrays, located outside the detector acceptance. The photon detector used is the Hybrid Photon Detector (HPD) [25, 26].

To distinguish between the $\pi/K/p$ hypotheses a likelihood is built. The pattern of hits observed in the RICH detectors is compared with the pattern expected under a given particle hypothesis, and the likelihood is determined from this comparison. The difference between the logarithm of the likelihood (DLL) for the different hypotheses is used to distinguish the particles:

$$\mathrm{DLL}(K-\pi) = \ln(L(K)) - \ln(L(\pi)) \tag{2.2}$$

$$\mathrm{DLL}(p-\pi) = \ln(L(p)) - \ln(L(\pi)) \tag{2.3}$$

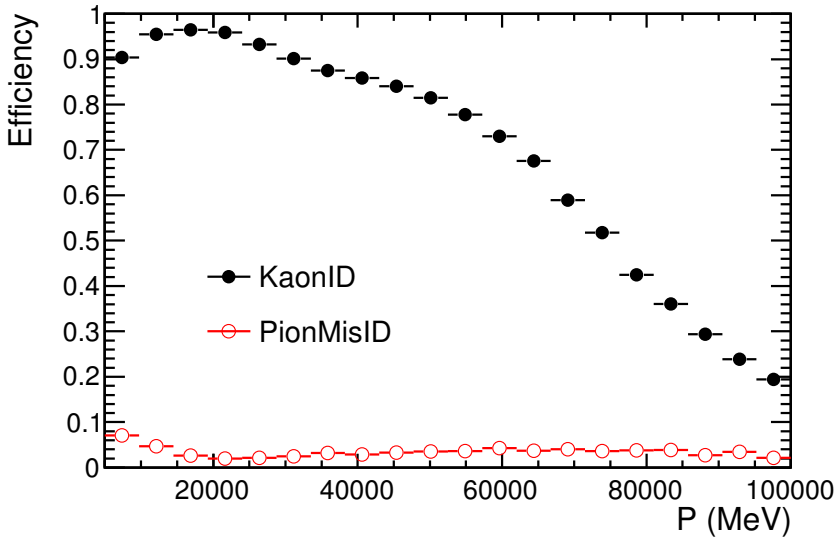

Figure 2.10: Probability, as a function of momentum, to correctly identify a kaon (full black circles) and to wrongly identify a pion as a kaon (open red circles), for a PID cut of $DLL(K-\pi)>5$ [29].

$$\mathrm{DLL}(K-p) = \ln(L(K)) - \ln(L(p)) \tag{2.4}$$

The particle identification performance depends on the likelihood cut chosen in the analysis. The PID performance of both the RICH detectors is monitored by studying specially-obtained calibration samples [27, 28]. These are particle decays that are chosen such that the type of particle associated to a track can be determined purely from the decay kinematics, without the use of PID information. In particular, to measure the $K-\pi$ separation power of the RICH detectors, the decay $D^{*\pm} \to D^0(K\pi)\pi^\pm$ is used. Here the tightly constrained D^*–D mass difference, in combination with the D^0 mass window, is effective in reducing the background rate while maintaining high signal efficiency. The measured efficiency and misidentification rate for kaons is shown in Fig. 2.10 as a function of momentum for $DLL(K-\pi)>5$, a standard requirement used in the analysis.

The calorimeters

Calorimeters provide the identification of electrons, photons and hadrons and measure their energy. Since the calorimeter information is used both offline as well as in the first trigger step, these systems must provide a fast signal, within 4 μs latency, see Sec. 2.5.

The calorimeter system [30] of LHCb is placed downstream RICH2 and consists of an electromagnetic (ECAL) and an hadronic (HCAL) calorimeter. Two additional detectors, a scintillator pad detector (SPD) and a preshower (PS) are placed just in front of the ECAL. As the particle rate varies over the calorimeter surface a variable lateral segmentation is

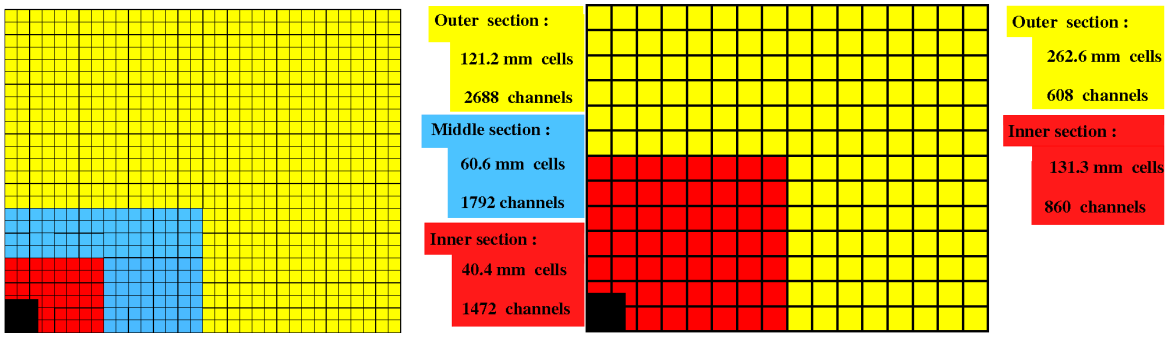

(a) (b)

Figure 2.11: Lateral segmentation of the Scintillator Pad Detector, PreShower and electromagnetic calorimeter cells (a) and of the hadronic calorimeter (b); one quarter of the detector front face is shown.

adopted. For the SPD, PS and ECAL a segmentation of three zones with different cell–sizes was chosen, defining the so called inner (40.4 mm cells), middle (60.6 mm cells), and outer regions (121.2 mm cells), see Fig. 2.11 (a), while two regions are defined for the HCAL, see Fig. 2.11 (b).

Both electromagnetic and hadronic calorimeters consist of alternate layers of absorber material (lead for ECAL and iron for HCAL) and scintillator material. In the absorber material the incoming particles produce a cascade of secondary particles. The ionisation induced by this cascade excites the atoms of the scintillating material. These atoms emit scintillation light as they return to their ground state. This light is transmitted to a photomultiplier tube via wavelength-shifting fibers. The energy of the incident particle is directly proportional to the amount of collected scintillation light.

The ECAL measures the energy of incident electrons and photons that interact with the lead via electromagnetic processes with a resolution of [30]:

$$\frac{\sigma(E)}{E} = \frac{10\%}{\sqrt{E}} \oplus 1.5\% \tag{2.5}$$

where the first term (E in GeV) is a statistical term describing possible fluctuations in the shower creation process, and the second term has a systematic origin.[2]

In contrast, the HCAL measures the energy of incident hadrons that interact with iron via nuclear processes with an energy resolution of [30]:

$$\frac{\sigma(E)}{E} = \frac{80\%}{\sqrt{E}} \oplus 10\% \tag{2.6}$$

[2]The $\oplus$ symbol represents the addition in quadrature.

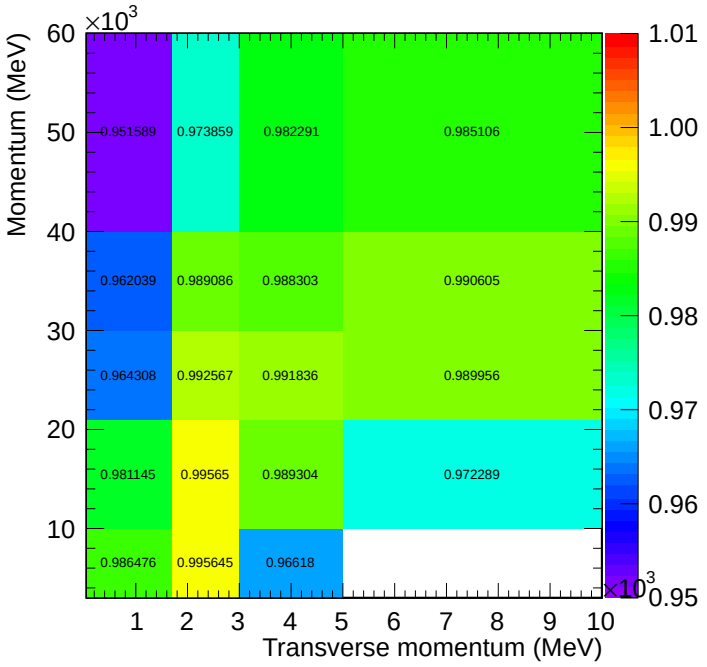

Figure 2.12: MuonID efficiency as measured in data (1.02fb^{-1}) using $J/\psi \to \mu^{\pm}\mu^{\mp}$ coming from a B–meson, in bins of momentum and transverse momemtum [31].

Muon detectors

The LHCb muon system guarantees muon–particle identification (muonID). At the same time it provides a good estimate of the transverse momentum, p_T, for triggering purposes. The detector is composed of five stations, labelled M1-M5, positioned around the beam axis. Stations M2 to M5 are multi-wire proportional chambers (MWPCs). They are located downstream of the calorimeter, with 80 cm thick iron plates interspersed between each station to absorb hadrons.

The station M1 is not used for particle identification purposes; it is placed in front of the calorimeter to ensure accurate reconstruction of the muon trajectory, minimising the effect of multiple scattering in the calorimeters. Due to the high particle flux expected around the inner region of this upstream station, a technology with extended longevity and higher granularity is used, namely triple-GEM (Gas Electron Multiplier) detectors.

The muon PID efficiency is monitored using $J/\psi \to \mu^{\pm}\mu^{\mp}$ inclusive decays with the "tag-and-probe method". $1.02\ \text{fb}^{-1}$ of data allows to produce a 2D–map as a function of momentum and transverse momentum, as shown in Fig. 2.12.

2.5 Trigger system

The task of the trigger system is to select interesting events from the pp interactions reducing the event rate to a manageable data size for storage. The LHCb trigger is divided in three stages: one hardware level, (L0), and two software (high) levels, (HLT1 and HLT2). The L0 trigger reduces the LHC interaction rate down to 1 MHz at a fixed latency of 4 μs using information from the calorimeters and the muon stations, by requiring the presence of at least one high E_T hadron ($\sim$ 3.6 GeV), electron or photon ($\sim$ 2.5 GeV), or a high p_T muon ($\sim$ 1.48 GeV). Awaiting a positive L0 decision the data is stored on–detector in a 168 event deep pipeline buffer. Upon a positive L0 signal, the full detector data is read out into the HLT data acquisition system. The HLT utilises a computing farm to process events in parallel and reduces the rate to 3 kHz, at which events are written to storage. The HLT is split into two stages. In the first stage, HLT1 [32], the L0 trigger decision is confirmed by associating track segments in the VELO or T-stations to the L0 calorimeter clusters or muon segments. An event selection based on track momentum, transverse momentum, χ^2 and impact parameter χ^2 is performed to reduce the 1 MHz output of L0 to 50 kHz. The second stage (HLT2) processes events at a rate that allows to perform a full reconstruction that is similar to what is done offline[33, 34]. There are many HLT2 lines dedicated to trigger on various types of events. As an example, the so called HLT2 topological lines are designed to trigger efficiently on B–decays with at least two charged daughters [33]. The reconstructed objects that caused the trigger to fire are stored in the event–data and they are used later on offline to trace, for each event, the correspondent trigger line for which the event was considered signal. Using the stored information it is possible to classify the triggered events in the following categories:

- **Triggered on signal (TOS)**: events in which particles originated from the decay of interest (signal particles) are responsible for a positive trigger decision.
- **Triggered independent of signal (TIS)**: events in which particles not originate from the decay of interest (non-signal particles) caused a trigger.
- **Trigger on both (TOB)**: events in which both child particles from the candidate signal decay and random tracks from the rest of the event are combined to form the trigger candidate.

Note that TOS and TIS categories are not exclusive and they can be used to determine the trigger efficiency.

Third Chapter

Front-End electronics monitoring

La scienza e' il capitano e la pratica sono i soldati.
Leonardo da Vinci

3.1 FE overview

The LHC experiments have to cope with a high interaction rate of 40 MHz, and therefore fast Front-End (FE) electronics are required. In this chapter the monitoring procedures on the data quality of the Outer Tracker (OT) electronics is described.

The OT FE electronics is hosted in modular units (FE-boxes) installed at both ends of each detector module. A FE-box, see Fig. 3.1, contains all the electronics required to read out the hit signals from the straw tubes to determine their timing with respect to the LHC clock and to transmit them to the data acquisition system, if a positive L0 decision is received. The external part of this unit consists of an aluminium frame built to fit to the straw module and providing grounding and shielding. The service boards hosted in the FE-box are: 4 high-voltage boards providing high voltage to the anodes, 8 boards hosting the amplifier chips to amplify and discriminate the analog signals, 4 boards hosting the TDC chips to digitise the analog signals, and 1 board to serialise data for optical transmission to the data acquisition system (the TELL1 boards). A brief description of these boards is given in the next sections.

The quality of the data, i.e. detector noise levels, the signal time linearity, and the number of dead channels, are periodically monitored to guarantee good performance for track reconstruction. A description of the monitoring facilities provided by the electronics combined with the software developed to check the detector status are presented in this chapter.

High Voltage board

The HV board provides the interface between the FE-electronics and the anode wires. The essential function of the board is to host 32 capacitors of 330 pF to decouple the positive

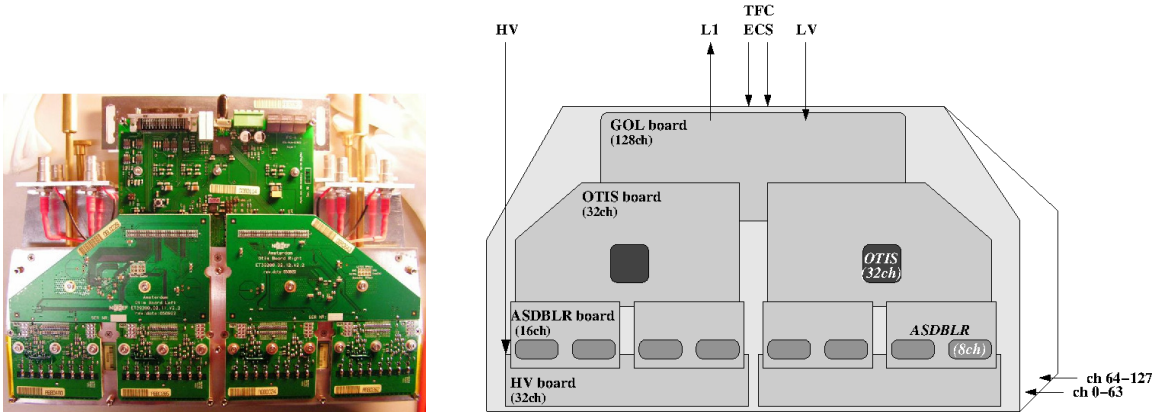

(a) (b)

Figure 3.1: Picture of a FE-box without its cover. Some of the boards are visible: from top to bottom: a GOL/AUX Board, two OTIS boards and four ASDBLR boards. The HV boards are not visible as they are beneath the ASDBLR boards on the other side of the aluminium chassis (a). Schematic drawing of a FE-box (b).

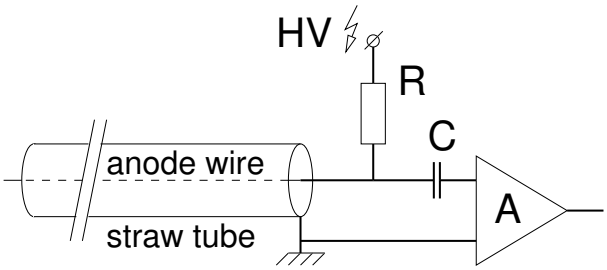

Figure 3.2: Schematic drawing of the straw tube connections. The high voltage (HV) is connected through a series resistance R to the anode wire; the straw tube wall acting as the cathode, is grounded. The preamplifier A is isolated from the HV by the insulation capacitor C.

high voltage to the anode wires from the small hit charges of about 100 fC[1] to the ASDBLR preamplifiers, as show in Fig. 3.2. Each FE -box hosts 4 HV boards.

ASDBLR board

The hit signals from the anode wires are amplified, shaped and discriminated by 8-channel ASDBLR (Amplifier Shaper Discriminator with BaseLine Restoration) chips [35, 36] originally developed for the ATLAS Transition Radiation Tracker by the university of Pennsylvania. Its key design objective is a high rate capability while maintaining a low noise level. The ASD-

[1] 30 primary electrons amplified by a gain of $2 \cdot 10^4$ yields result in total a signal of about 100 fC: $30\ e^- \times 2 \cdot 10^4 \times 1.6 \cdot 10^{-19}$ C ≈ 100 fC

BLR chips have been produced with a technology that guarantees low crosstalk[2] (0.2%), low noise (≤1 fC) and a radiation hardness withstanding 3.5×10^{14} n/cm^2 [37]. The ASDBLR chip selection [38], prior to mounting in the FE -box, guarantees a good uniformity of the discriminators such that a common threshold can be used for the entire OT readout system without any loss of efficiency or increased noise levels, see Sec. 3.2. Two ASDBLR chips are assembled on one ASDBLR board, and one FE -box contains 8 ASDBLR Boards.

OTIS board

The timing of the ASDBLR output signals is managed by a custom Time to Digital Converter (TDC): the OTIS (Outer tracker Time Information System). It is guaranteed to be radiation hard exceeding 1 Mrad irradiation. With its 32-channel inputs, the OTIS Board is able to read signals from 4 ASDBLR chips, covering half a monolayer of an OT module and providing the ASDBLR chips with the operating threshold voltages. The OTIS TDC operates synchronous to the 40 MHz bunch crossing clock and provides intermediate data storage in a 4 μs L0 pipeline. The architecture of the OTIS TDC core is shown in Fig. 3.3 to help the reader in following the data flow.

At the inputs, level comparators receive the hit signals from the ASDBLR chips. A programmable channel mask register blocks hot or noisy channels from entering the data stream. The actual time measurement is performed by means of a Delay Locked Loop (DLL), providing fine time steps of 150 ps within a 25 ns clock cycle. The state of the DLL is copied to the corresponding Hit Register (HR), translated to a 6 bit time word by the Decoders (D), and written to the pipeline buffer. The pipeline is 160 cells deep and covers the L0 trigger latency of 4 μs. The bunch counter (BX) value is written into the buffer as well, to check the buffer synchronisation. Upon a L0 trigger, the corresponding hits and the BX value are copied to the derandomiser buffer. This buffer, accommodating for instantaneous variations of the L0 rate, is 48 cells deep to store up to 16 consecutive L0 triggers while allowing a maximum of 3 BX to be searched upon a single trigger signal. The event data is stored in a readout buffer before being transferred off the chip through the 8-bits wide readout interface in 36 clock cycles. An additional feature, also shown in Fig.3.3, of the OTIS are 4 independent DACs, to provide threshold levels to the ASDBLR chips. The OTIS settings and DAC levels are programmable through an I^2C interface.

GOL board

The data transport is performed by the Gigabit Optical Link (GOL)[39], operating at 1.6 Gbits/s rate and mounted on the GOL /AUX Board. The GOL accepts 32 bit wide words at 40 MHz rate. The data of 4 OTIS chips are transported by a single chip; therefore only one GOL Board is mounted inside a FE -box. The GOL Board provides also the bias to the OTIS and ASDBLR by means of radiation-hard voltage regulators and distributes the slow (ECS) and fast control (TFC) signals to the FE -box. Optical fibers, driven by a VCSEL laser, bring the data

[2]The crosstalk is defined as the presence of a signal in more than one channel while a test pulse is injected in only one channel.

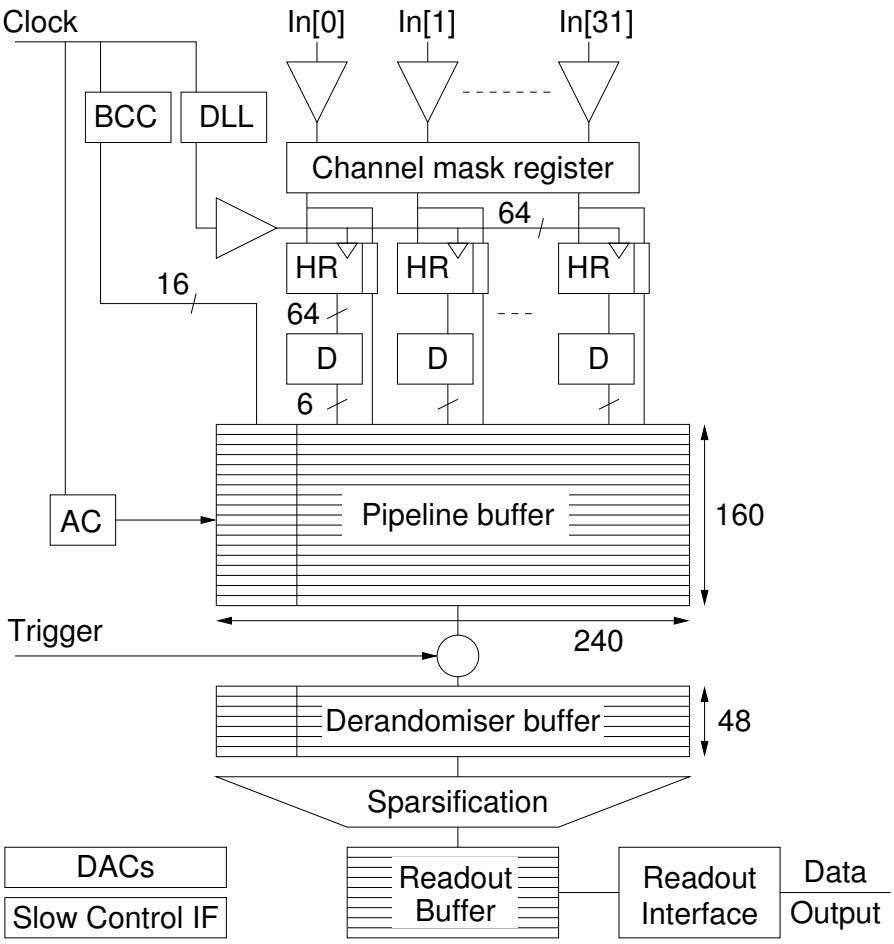

Figure 3.3: Architecture of the OTIS TDC.

to the counting house at an output rate of 1.6 Gbits/s into the TELL1 buffer board, which performs a zero suppression operation and ships data to the HLT computer farm.

3.2 FE monitoring

During commissioning and operating phases of the LHCb detector, the stability and the quality of the OT FE -electronics performance are monitored. For calibration tasks, a test-pulse facility has been provided. If a "calib" trigger is sent by the Readout Supervisor (ODIN), the FE -electronics generates test-pulses injected via the ASDBLR test input.Test-pulse combinations can be generated, affecting even or odd or, alternatively, all channels.

Four types of test runs are provided:

- **Noise Threshold Scan**: a sequence of random triggers at increasing ASDBLR threshold settings.

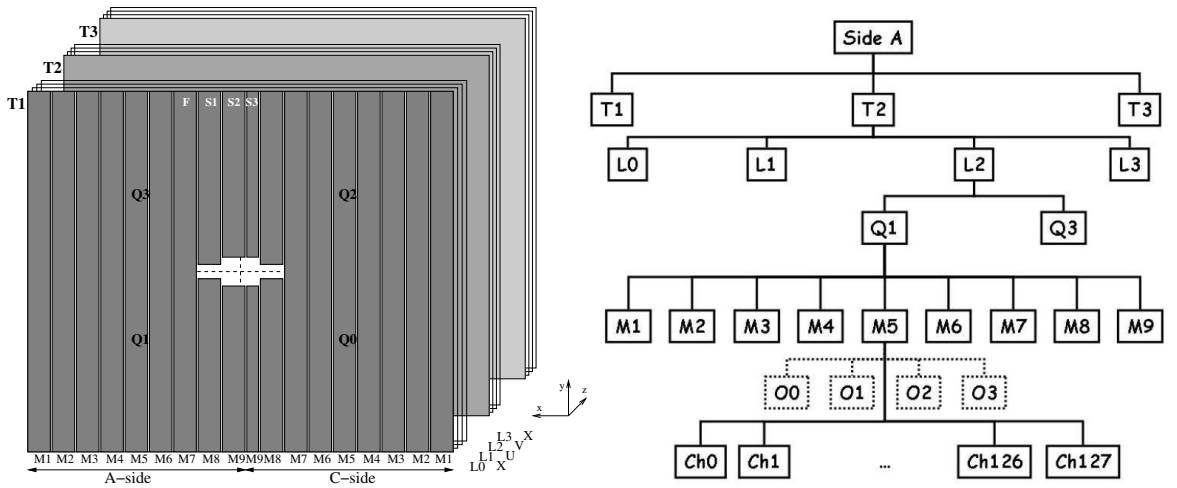

(a) (b)

Figure 3.4: Schematic view of the OT module layout. Shown are the three stations T1, T2, T3 each containing detector modules in four measurement planes (a). OT detector hierarchy structure in the software. Notice that "O0, O1, ..." stands for OTIS0, OTIS1. These components are represented with a dashed line since their separation is important only at the software level where plots can be produced also at the level of these sub-components (b).

- **Threshold Scan**: a sequence of triggers with test-pulses at increasing threshold settings.
- **Test Pulse**: a sequence of triggers with test-pulse at a fixed threshold.
- **Delay Scan**: a sequence of triggers (at fixed threshold) at increasing test-pulse delay settings.

A set of parameters characterises each test and they are used to evaluate the detector status. The details are presented below.

Online-Offline calibration software

A dedicated software package, BOSKABOUTER, is developed to provide an overview of the detector status, uncovering possible problems or faulty behaviour detected in the monitoring runs. The program displays the results of each of the calibration/monitoring runs in the form of summary plots for individual detector parts. The detector modules are geographically organised according to the scheme defined in Ref. [40] and shown in Fig. 3.4 (a). In the software, this corresponds to a logic hierarchy as shown in Fig. 3.4 (b). A channel is identified by its entire path in this hierarchy[3].

[3] E.g. the 1st channel of the 1st FE-box of the 1st layer of the 1st station on the A side by *"T1.L0.Q1.M1.OTIS0.CH0"* (notice that odd quarters are on the A side, while even quarters are on the C side).

The core of the software is a set of recursive functions that allows to access the hierarchy structure at each level, giving the possibility to easily run each kind of analysis at each detector level. The abundance of detector elements, e.g. 53760 straw channels, requires a well-structured organisation of summary plots. Two output formats are chosen: ROOT and PDF. In the case of the ROOT file format [41] the hierarchical structure of the detector is reproduced in the stored folder structure. In the case of the PDF files several plots per page are shown. For each specific analysis an acceptance range is set for the relevant parameters. A detector element is defined as "problematic" if at least one parameter is outside the acceptance range. Problematic elements of the OT detector are collected in summary tables or can be detected by inspecting the summary plots. Dedicated analyses can be run over only these elements to further investigate any problems.

Noise scan

The noise scan analysis aims at identifying channels that have an "abnormal" level of noise that may be due to dark pulses from the detector, bad FE -electronics shielding, etc. To do that a set of diagnostic tools are provided:

- **Hitmap Analysis**: the hitmap histogram summarises the hit frequency of all channels. It produces 2D histograms (for example one per active FE-box) plotting channel numbers on the X-axis, threshold values on the Y-axis and the hit–occupancy[4] on the Z-axis, see Fig. 3.5 (a, b).

- **Occupancy Analysis**: the occupancy histograms are 1D slices of the hitmap histogram at given threshold values, see Fig. 3.5 (c, d).

- **Noisy Channels Analysis**: the noise histograms are 1D occupancy histograms at the half-station and half-detector level (side A or side C), and a 2D histogram having threshold values on the X-axis, occupancy values on the Y-axis, and the number of channels with a given occupancy at a given threshold on the Z-axis, see Fig. 3.6 (a). Also a 1D histogram of the mean occupancy (averaged over all active channels in a half-detector) as a function of threshold is provided, see Fig. 3.6 (b).

Threshold scan

The threshold scan analysis aims at monitoring the gain of the FE -Electronics preamplifier, in order to locate dead channels, gain deteriorating effects, etc.

The ASDBLR chip selection, prior to their mounting in the FE -Box, guarantees a good uniformity of the discriminators such that a common threshold can be used for the entire readout without loss of efficiency or increased noise levels. To describe the hit–efficiency

[4] The occupancy is the ratio between the number of events in which a signal was registered over the number of triggers.

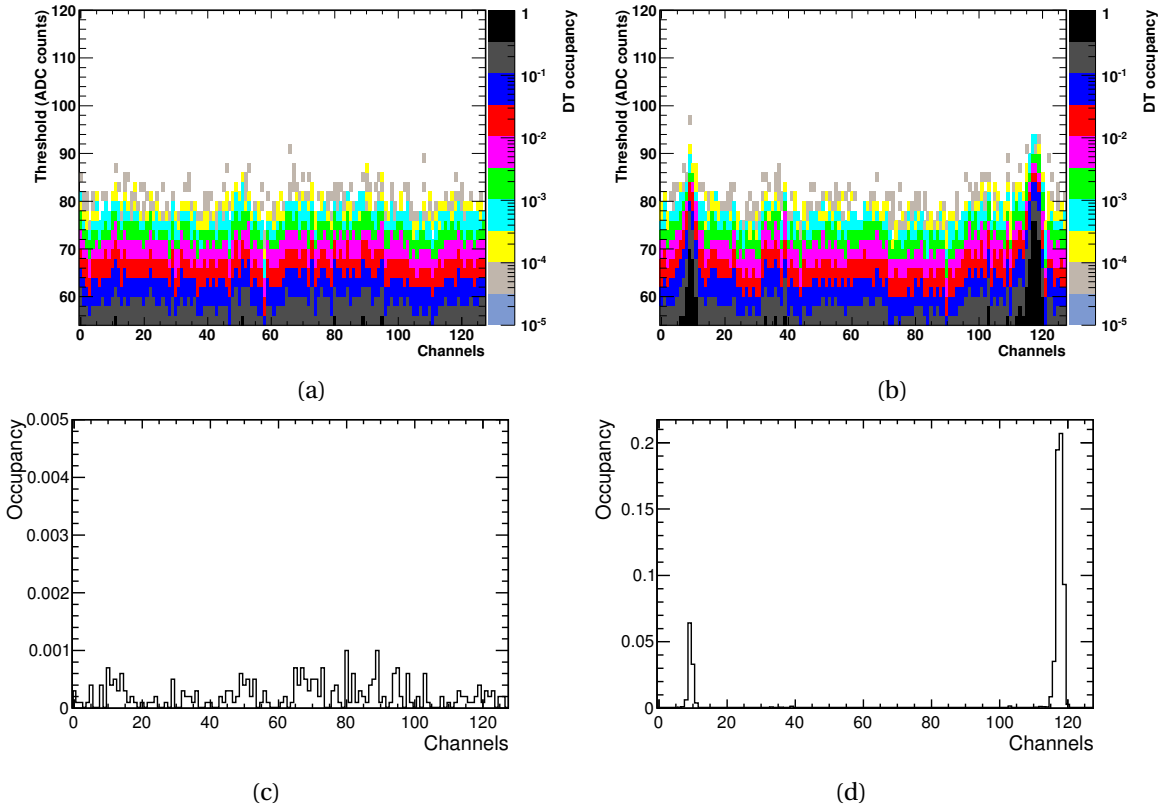

Figure 3.5: Example of histograms used to detect noisy channels (1 ADC count ≈ 10 mV) in the case of a FE-box with all good channels (a) 2D-hitmap histogram, (c) 1D-histogram, and in case of a FE-box with two groups of noisy channels (around channels 10 and 120) (b) 2D-hitmap histogram, (d) 1D-histogram. The 1D-histograms are produced at a threshold of ~ 790 mV.

versus threshold an error function is used, assuming Gaussian noise. The stability of the half-efficiency point for all the channels is studied and the relative variation between channels is expected to be less than ±60 mV [38].

The uniformity of this response is monitored and again a set of diagnostic tools is provided.

- **Hitmap Analysis and Occupancy Analysis**: the Hitmap and Occupancy analyses of a threshold scan are analogous to those performed for the noise scan, described above.
- **Error Function Analysis**: the error function analysis uses hitmap histograms as input and performs an error function fit [42] to each vertical slice of the hitmap histograms. Such slices contain the occupancy profiles of all active channels as a function of the ASDBLR threshold. The values of the parameters (mean and sigma) and of the χ^2 obtained from the fit are then stored in the output histograms. An example of the error

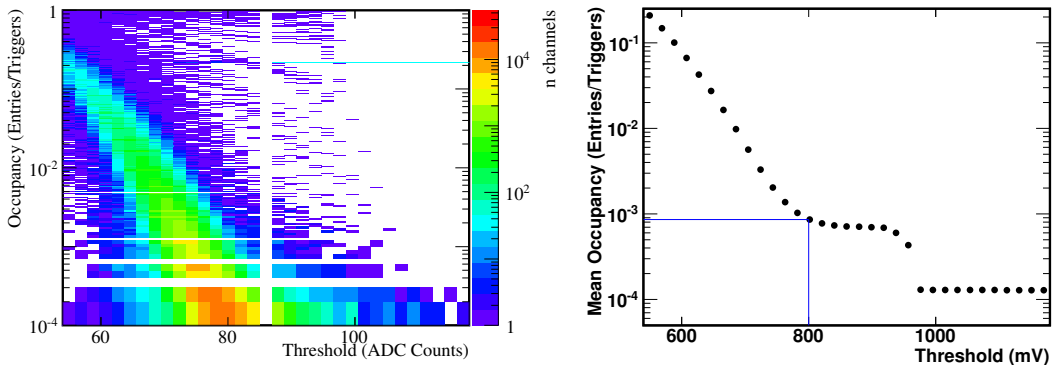

(a) (b)

Figure 3.6: (a): an example of output from the noisy–channels analysis. 2D-histogram of the noise level in the entire Outer Tracker. Notice that the statistics is not enough to have all the bins on the y axis filled, while, the threshold at 860 mV was not recorded. (1 ADC count ≈ 10 mV). (b): 1D-histogram of the mean occupancy as a function of threshold with a noise level for the entire detector smaller of 8×10^{-4} at the working threshold.

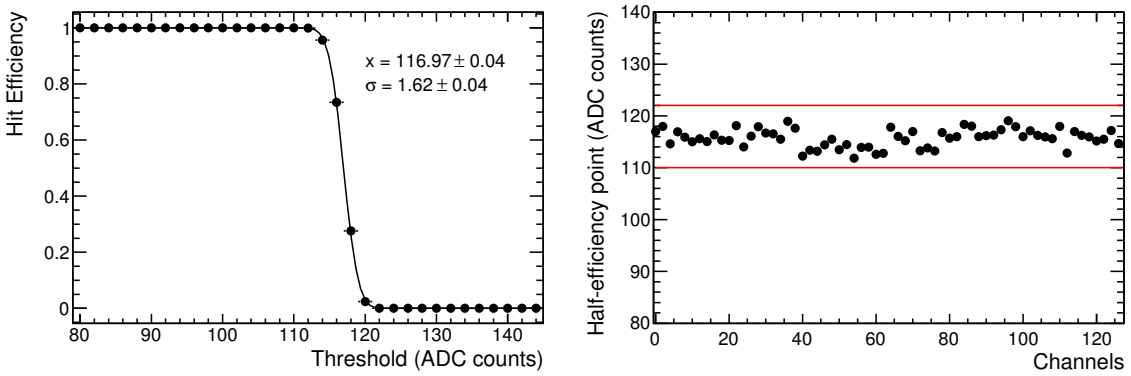

(a) (b)

Figure 3.7: (a): an example of hit-efficiency as function of threshold for a fixed input charge. x and σ are the mean and the width of the Gaussian. From this curve the half–efficiency point is determined. (b): stability of the half-efficiency point for channels in one FE-box. The horizontal lines indicate the predefined acceptance window (1 ADC count ≈ 10 mV).

function fit and of the stability of the half-efficiency point in a FE-box are shown in Figs. 3.7 (a) and 3.7 (b) respectively.

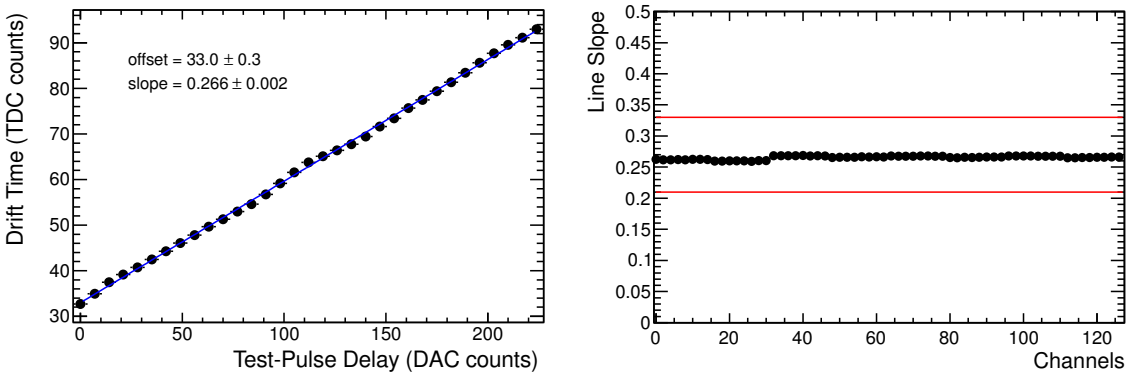

(a) (b)

Figure 3.8: (a): an example of a linear fit of the drift time measured and the injected delay. The slope corresponds to 1 if both axis are converted to ns. (1 DAC count ≈ 0.1 ns, while 1 TDC count ≈ 0.39 s). (b): stability of the slope from the linear fit the timing measurement for all the channels in a FE-box.

Delay scan

The delay scan analysis aims at detecting defects in the timing of the OT channel responses (offsets, non-linearities etc.). In this run a test pulse with a known delay is injected into the electronics. The following analyses are performed:

- **Delay–map Analysis (Active Channels Only)**: the output of the delay–map analysis are 2D histograms (one per active FE–box) having channel numbers on the X–axis, delay values on the Y–axis, and the mean drift time of the channels with an active test–pulse on the Z–axis.
- **Timing Distributions**: the output of the analysis of the timing distributions are drift–time distributions or the mean drift–time values for a given value of the test-pulse delay.
- **Linear Fit to Timing**: this analysis monitors the time response of the OT channels. Therefore, linear functions are fitted to the mean drift–time as a function of the test–pulse delay and the distributions of the resulting parameters are produced for all active channels in one FE–box. A linear fit of a single channel is shown in Fig. 3.8 (a). As an example, the linear–fit slope distribution for channels in a FE–box is shown in Fig. 3.8 (b). Clearly, all channels are within the acceptance window.

3.3 Outer Tracker status

The analyses described above were continuously used during 2009-2011 data–taking period to detect and replace noisy or broken components. An example of a plot used to localise

components to be replaced is shown in Fig. 3.5. Typical problems affecting the detector can be summarised as follows:

- **HV**: higher currents at nominal working voltage due to straw deformation, impurities on the wire, or the presence of a broken wire.
- **dead channels**: non responsive channels. These components are mostly detected with noise and threshold scans.
- **noisy channels**: channels that have an abnormal level of noise. These components are detected with noise scans.
- **synchronisation**: problems in the distribution of the fast control signals (i.e. clock, trigger, reset, etc). This leads often to missing triggers or wrong BX number in data. In most of the cases these problems are detected through error messages from the TELL1, but in some cases also with the delay scan.
- **DLL**: loss of synchronisation of the OTIS delayed-locked-loop (see Sec. 3.1). This occurs either due to chip malfunctions or to problems in the clock distribution to the chip. It is signaled as error in the OTIS DLL registers.
- $\boldsymbol{I^2C}$: errors in communication between the FE-boards and the experimental control system. It is signaled by the problems in uploading the chip settings.
- **VCSEL**: mechanical failure of one of the components of the laser system used to send data from the GOL board, see Sec. 3.1. It is detected as the absence of signals from an entire FE-box and as a total absence of light in the receiving diode.

The replaced FE -boxes in 2009-2011 with their related problems are summarised in Tab. 3.1. During all this data–taking period the number of working channel was constantly higher than 98%.

Table 3.1: Summary of replaced FE-box and repaired HV channels in the Outer Tracker between beginning 2009 and summer of 2011.

Problems	Exchanged FE-Box		
	2009	2010	2011
dead channels	2 (0.46%)	5 (1.16%)	1 (0.23%)
DLL	2 (0.46%)	2 (0.46%)	–
synchronisation	5 (1.16%)	2 (0.46%)	–
VCSEL	1 (0.23%)	4 (0.93%)	1 (0.23%)
I^2C	2 (0.46%)	1 (0.23%)	–
noisy channels	1 (0.23%)	11 (2.55%)	–
	Repaired HV channels		
	2009	2010	2011
HV	2 (0.12%)	2 (0.12%)	2 (0.12%)

Fourth Chapter

Ageing studies: monitoring and curing procedures

The only way to overcome a problem is to cope with it.
Piergiorgio Giudici

4.1 Introduction

Tests have shown that the OT–modules suffer from significant decrease of the gas gain under moderate irradiation [43, 44]. The first evidence of ageing in its current form was found in 2005. Since then a large number of ageing tests have been performed to determine the cause of the ageing and to find a solution to the problem.

This chapter is devoted to describe the ageing phenomenon as well as studies of potential solutions proposed to overcome the problem. Special emphasis is placed on the cure of possible gain loss by means of invoking large currents, referred to as high voltage training.

Ageing in gas detectors

Gaseous detectors that operate in a high-radiation environment can have their performance compromised by ageing effects[1]. Gain loss, worsening of the energy resolution, discharges, sparking or mechanical damages, such as wire etching, are examples of ageing phenomena that can degrade the performance of a gas detector over time. From a microscopic point of view, ageing effects are characterised by the creation of a variety of molecular substances (oxides, polymers and others) that can be accumulated as deposits on the electrode surfaces [45, 46, 47].

The OT–modules were designed to withstand a large irradiation dose during the planned ten years of operation [48]. The radiation hardness tests performed on prototype modules

[1] In this text we consider as ageing only effects due to radiation, while we ignore any possible mechanical failure.

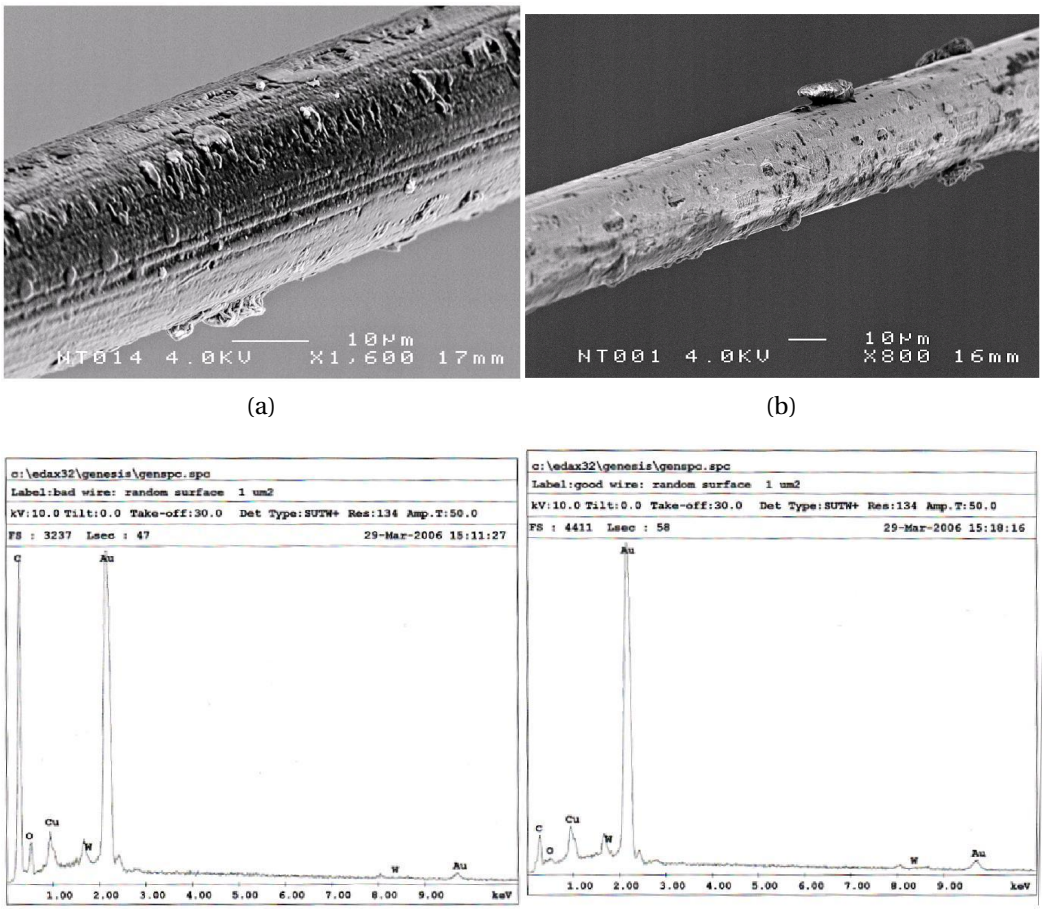

(a) (b)

(c) (d)

Figure 4.1: (a): a Scanning Electron Microscope (SEM) picture of an irradiated OT wire sample, (b): SEM picture of a not irradiated OT wire sample, (c): Energy Dispersion X–ray (EDX) spectra for an irradiated OT wire. A clear carbon peak is observed. (d): EDX spectra for an not irradiated OT wire sample. Note still the presence of a small carbon peak.

indicated that this would be feasible with the chosen design. However, more recent tests on final modules have shown a rapid gain loss of modules under mild irradiation corresponding to a few nA/cm for a period of 20 hours. Under the influence of irradiation, a small insulating layer of a hydrocarbon-containing substance is deposited on the anode wire (Fig. 4.1), thereby reducing the signal response of the detector.

The ageing pattern observed in the modules shows several unusual characteristics rarely reported in literature by other drift chamber detector studies:

- **Gas flow dependence**: most of the gain loss occurs upstream of the source, producing an asymmetric pattern (“half–moon” shape), see Fig. 4.2;
- **Intensity dependence**: the gain loss is not largest directly below the source, where the intensity is highest.

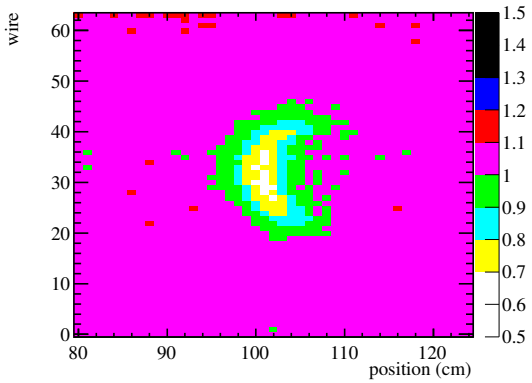

Figure 4.2: Ratio plot showing the typical "half–moon" shape of the gain loss region. The color scale represents the relative detector gain.

These characteristics can be explained by assuming that, at sufficiently high intensity, radicals are produced that prevent the formation of insulating carbon deposits. The area of the gain loss and the relation between gain loss and source intensity depend on the balance between the malicious molecules that deposit on the wire and beneficial radicals that prevent this. If the beneficial radicals live long enough, they can also prevent ageing downstream of their point of creation, explaining the upstream-downstream asymmetry[2]. The detection of ozone at the output of an irradiated module makes ozone a good candidate for the beneficial radical. This empirical model is supported by the observation that the addition of O_2 to the counting gas seems to prevent ageing, see Sec. 4.4.

4.2 Ageing monitoring system

Laboratory setup

Irradiation tests were carried out on a small selection of detector modules using a 2 mCi[3] ^{90}Sr source. The high voltage on the anode wires was set at 1600 V and the gas flow (with a mixture of 70/30 Ar/CO_2) was 20 l/hr, corresponding to approximately one volume exchange per hour. The irradiation source was kept at 20 mm distance from the module by an aluminum collimator of 6 mm diameter opening. Ionization due to electrons from the source that scatter into the gas volume could be detected above one per cent of the maximal intensity over an area of 60×60 mm^2.

Before and after irradiation the response of each wire in the module was checked with a 20 mCi ^{90}Sr source. The full module width was irradiated in steps of 1 cm along its length and the corresponding current per wire was measured and recorded. The ratio of currents

[2] Notice that this model is in agreement with the evidence that with no gas flow, the symmetry in the ageing profile is restored.

[3] $1\text{Ci} = 3.7 \cdot 10^{10}$ Bq

as measured before and after the irradiation results in a two dimensional map of the gain changes to visualise the results. The setup is depicted in Figs. 4.3.

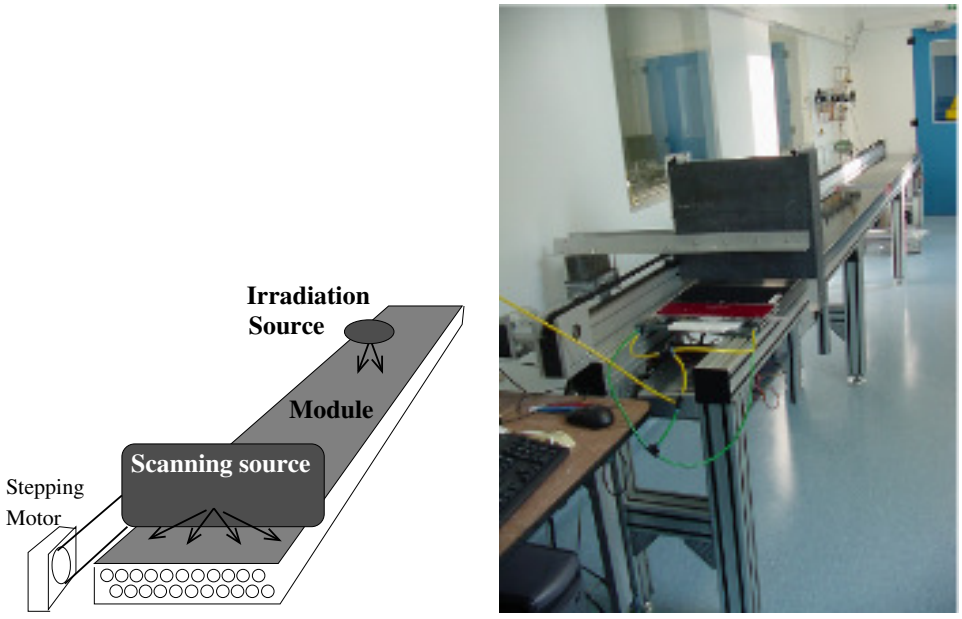

(a) (b)

Figure 4.3: (a): schematic view of the irradiation and scanning setup, (b): photograph of the irradiation setup in laboratory.

Experimental setup in situ

Given the fast decrease of detector response under irradiation observed in the laboratory, special care of monitoring the detector response in situ is needed. For this, a scanning setup was designed.

A special frame with stepping motor has been installed on one side of the beam–pipe allowing to scan nine modules mounted in the first C–frame. The scanning frame has occasionally been moved between stations T1 and T2 to test a larger number of modules. The radiation resistance of the detector modules is monitored at various stages of the commissioning and operation of the detector. For that, the detector was irradiated with a 2 mCi ^{90}Sr source.

Before and after irradiation the detector response was measured with a scan using two ^{90}Sr sources with each an activity of 2 mCi, see Fig. 4.4.

The two sources were collimated with a slit of 1×34 cm^2, similar to the laboratory setup. The sources are moved with a step motor along the scanning frame with steps of 1 cm and the current is measured with a current-meter identical to the one used during laboratory tests.

The readout system and the analysis software are identical to those used in the laboratory, and the mechanical parameters were tuned to achieve a similar accuracy for the labo-

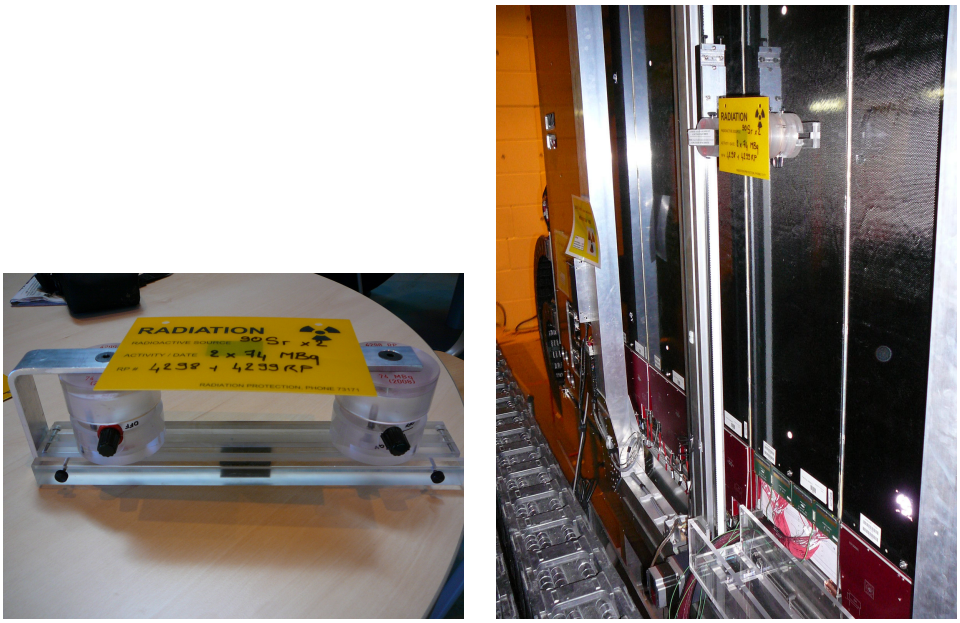

(a) (b)

Figure 4.4: The source holder with two ^{90}Sr sources (a). Scanning system in situ. The front–end electronics is replaced by a dedicated current–meter (b).

ratory and in situ results. As the system is intended to periodically monitor the modules a set of robustness checks are carried out to guarantee the reproducibility of the measurements.

Analysis

The gain loss can be quantified by comparing the current behaviour after and before an irradiation. To account for gain variations due to changes in atmospheric pressure, the ratio of the currents is normalised using the average value obtained outside a region where the source was present. The area around the source position is selected to study the effect of the irradiation in detail.

Two quantities are used to estimate the ageing effect: the average of the two measurements of the current in one straw for a given position with maximum gain loss in the source region, and the integrated deviation from 1 of all the measurements inside the source region and divided by the number of measurements considered. If there are no gain changes in the irradiated area these two quantities must be 1 and 0, respectively. It should be noted that the "maximum gain loss" evaluation is biased as long as there is no gain loss, since the two lowest fluctuations are taken.

Two 2D–maps are produced to show the behaviour of the module:

- **single scan map:** it is the result of the module scan. The x–axis is the length of the module, the y–axis is the wire number and the color scale, z–axis, is the current read out normalised with the source profile. An example of a single scan map is shown in

Fig. 4.11 (a,b). In these maps the ageing is evident as a structure with an half–moon shape. Notice that only relative differences in color are relevant, while the color scale itself varies from scan to scan due to atmospheric conditions. In these maps the wire locators are evident as two vertical white lines.

- **ratio map:** it is the ratio of two single scans before and after an irradiation. The color scale in this case show the relative gain of the module and it is not affected by the atmospheric conditions. Only the damages produced in the irradiation campaign between the two single scans considered will be visible. An example of this map is given in Fig. 4.2.

4.3 The culprit

It is important to know the culprit of the ageing phenomenon, in order to better understand the microscopic mechanism, and to avoid the use of similar substances in future gas detectors.

The main candidate for the culprit of the ageing in the OT modules was the glue or one of its components. A systematic outgassing study of ten glue candidates is reported in literature [49, 50, 51]. These analyses showed that the glue used, Araldite AY103, has good electrical and mechanical properties and has not shown any outgassing during the tests. However, the manufacturer in 2003 switched from AY103 to AY103-1, which contains the same hardener and resin, but a different plastifier: di-isopropyl-naphthalene instead of dibutyl phthalate.

To identify the origin of the insulating deposits a set of dedicated modules were produced. First, an openable test module (module 501) was constructed based on an aluminium frame on which 32 straws are mounted. The openable chamber is equipped with only one layer of straws. The clamps holding the straws in place have room for 64 straws, in the same arrangement as in a F-module, but placing only 32 straws provided more place to safely remove straws or wires and allowed the addition of extra straws made with different materials at a later stage. The module is sealed with a kapton foil transparent to radiation. A large O-ring guarantees gas tightness and avoids the use of glue in the construction. The module size, 45×242 cm^2, is similar to an S–module and the active area of the straws is about 225 cm in length. Individual straws were injected with various types of glue [52, 44], which lead to the first indication that the plastifier in AY103-1 causes gain loss.

Tests performed on the openable chamber provided compelling evidence that the ageing is related to the plastifier in the glue used to seal the modules. Their results can be summarised as follows:

- No sign of gain loss was observed in the openable chamber with no glue present after 480 hours of irradiation with a locally induced current density of maximal 75 nA/cm on the wire, corresponding to an induced collected charge of approximately 0.13 C/cm.
- Significant gain loss was observed in the openable chamber in 20 hours after the injection of glue used in the construction of the OT module (the epoxy Araldite AY-103-1) with identical ageing characteristics as the ones seen in the standard OT modules.

- The openable chamber no longer suffers from gain loss after the glue had been removed. This indicates that the pollutants that cause the ageing are constantly being emitted by the glue. Once the emission stops, further irradiation causes no gain loss.

Secondly, two F-modules were produced with different types of glue: Tra–Bond 2115 and Araldite AY105-1. The latter glue is similar to Araldite AY103-1 with the only difference that it does not contain any plastifier. A detailed description of the studies carried out on this module can be found elsewhere [43] while a description of the main results obtained with the Tra–Bond module are presented in the next section. Test on both modules gave consistent results.

Tra–Bond module

The Tra–Bond 2115 glue is provided in bags of 7 g containing the appropriate quantities of hardener and resin, as prepared by the producer. The straws and the feed-through board were glued to the panel using 18 bags, mixed with 8 g of silica. For two spacers 4 bags with 2 g silica were used, and finally, the sidewalls were glued to the module with 36 bags and 16 g of silica. The module was gas-tight to approximately $3 \cdot 10^{-6}$ l/s at 7 mbar overpressure, which is similar to the most gas–tight modules constructed during mass production.

The current behaviour was measured using the scanning system presented in Sec. 4.2. Only one side of the module was read out, limiting the study to half a monolayer, i.e. a surface of $245 \times 34 \text{cm}^2$. Two irradiation campaigns were carried out on the module. One with the 2 mCi irradiation source during 506 hours irradiating a small circular area with a diameter of about 6 cm, and the second using the 20 mCi scanning source during 539 hours irradiating the full width of the module over a length of about 4 cm. Figs. 4.5 and 4.6 show time evolution of the gain loss for the two studies.

The results obtained from these two studies, are both qualitatively and quantitatively different from the irradiation results using AY103-1 and can be summarised as follows:

- Presence of a maximum gain loss smaller than 5% in both cases after an integrated dose of approximately 0.1 C/cm/wire.
- The gain loss is not localised under the source, but it is spread in a region downstream from the source.
- The area of gain loss is increasing with time while the maximum damage is approximately constant over time as is shown in Figs. 4.7 and 4.8.
- In the case of the 20 mCi scanning source a small area with gain loss can be observed upstream the source in the first 200 hours of irradiation. For larger irradiation times the gain loss is fully shifted to the region downstream the source.

In conclusion the modules sealed with the Tra–Bond 2115 glue are more radiation resistant than the modules sealed with AY103-1 glue.

Summary of ageing tests with different sealing glues

The conclusion of these studies is that the significant gain loss after few hours of irradiation of OT modules sealed with Araldite AY103-1 is due to the plastifier di-isopropyl-naphthalene present in the glue. For both modules that were constructed with glues not containing this plastifier, the Tra–Bond 2115 and the Araldite AY105-1 glues, a limited gain loss smaller than 5% is observed after an integrated dose of around 0.1 C/cm/wire. Moreover, even if the area of the gain loss is increasing with time, the maximum damage is constant over time for modules sealed with Tra–Bond 2115 glue. Subsequent tests [53] have shown that after 1000 hours of irradiation, resulting in a maximal accumulated charge of 0.25 C/cm at the point of highest intensity[4], a gain loss of $(5\pm2)\%$ was observed. Such a gain loss correspond to a negligible reduction on the tracking efficiency and therefore the Tra–Bond 2115 and AY105-1 glues are good candidates for constructing new modules for the upgrade of the LHCb experiment in case the straw tube technology will be chosen.

[4] An integrated dose of 0.25 C/cm corresponds to 1 year of 10^7 s LHC running/year (at an incident rate of 250 kHz per cm wire length) at a nominal luminosity of $2 \times 10^{32}\text{cm}^{-2}\text{s}^{-1}$, or equivalently a data volume corresponding to 2 fb^{-1}.

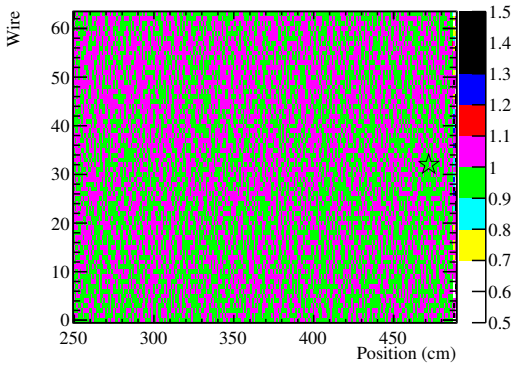

(a) Irrad. time 20 h

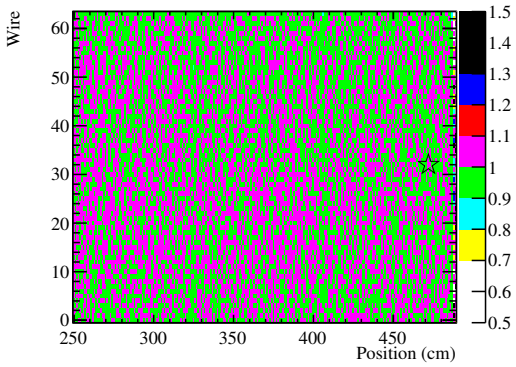

(b) Irrad. time 164 h

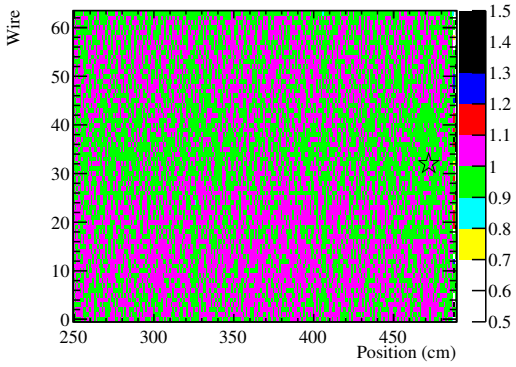

(c) Irrad. time 260 h

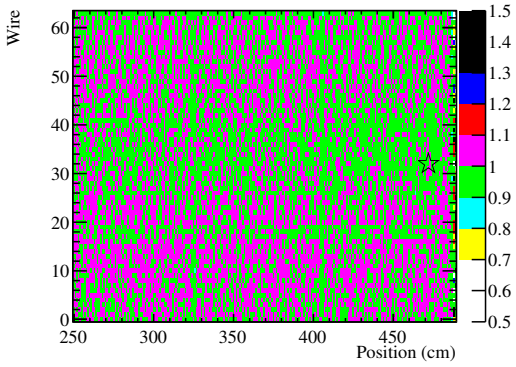

(d) Irrad. time 315 h

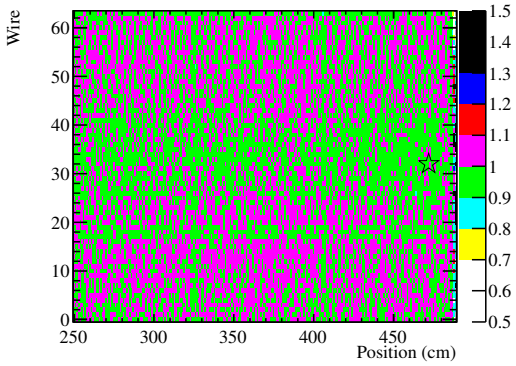

(e) Irrad. time 414 h

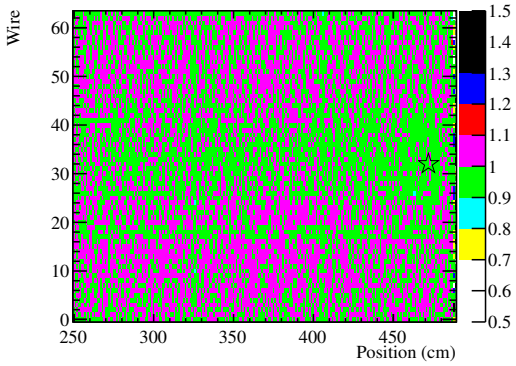

(f) Irrad. time 506 h

Figure 4.5: Time evolution of the source region due to the irradiation with a collimated source of 2mCi. The location of the source was at 472 cm (star), above wires 29–34. The gas flowed from right to left. The colour code represents the relative detector gain.

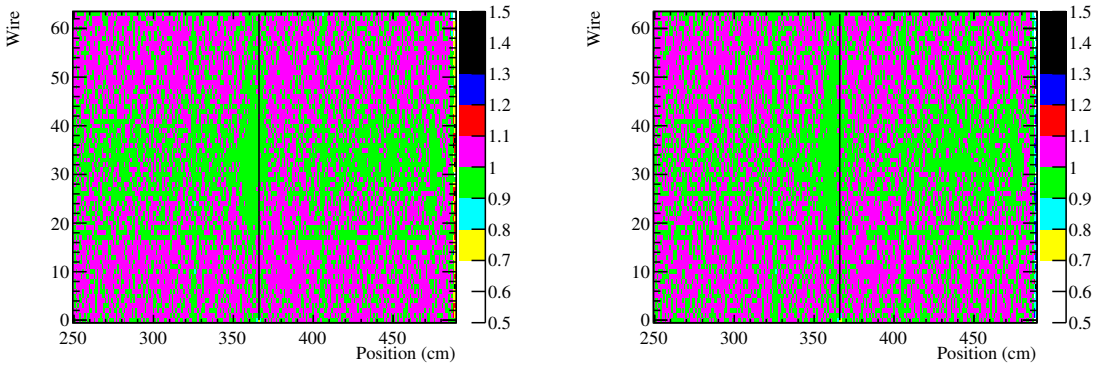

(a) Irrad. time 149 h

(b) Irrad. time 193 h

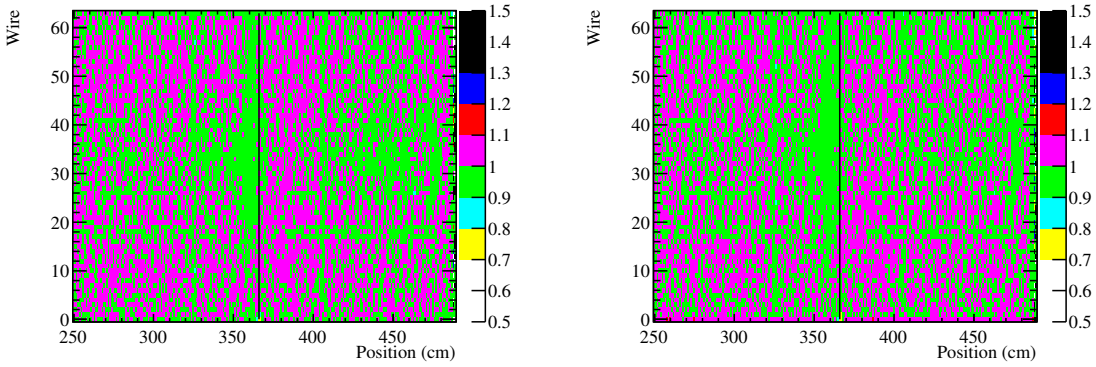

(c) Irrad. time 237 h

(d) Irrad. time 332 h

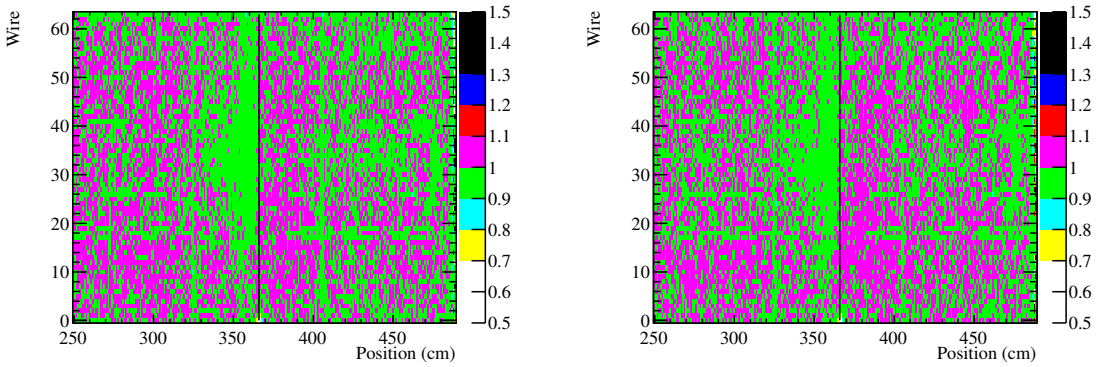

(e) Irrad. time 495 h

(f) Irrad. time 539 h

Figure 4.6: Time evolution of the source region due to the irradiation with a collimated source of 20mCi. The location of the source was at 366 cm (line), irradiating the full width of the module. The gas flowed from right to left. The colour code represents the relative detector gain.

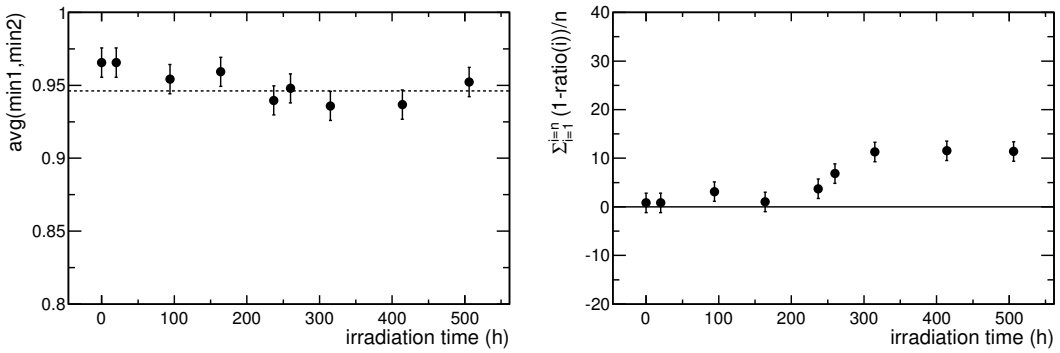

(a) (b)

Figure 4.7: Evolution of the parameters used to quantify the gain loss in the module constructed with Tra–Bond glue during the 506 h of the irradiation with the 2 mCi source; (a) the evolution of the maximum gain loss is shown, and (b) the evolution of the integrated gain loss is shown. For the definition of these quantities, see Sec. 4.2. The reference line for no–ageing in (a) is shown with a dashed line and it is obtained with several independent measurements in different regions of the detector in case of no irradiation. In (b) the reference line of no–ageing is, by definition, at 0 and it is shown with a solid line.

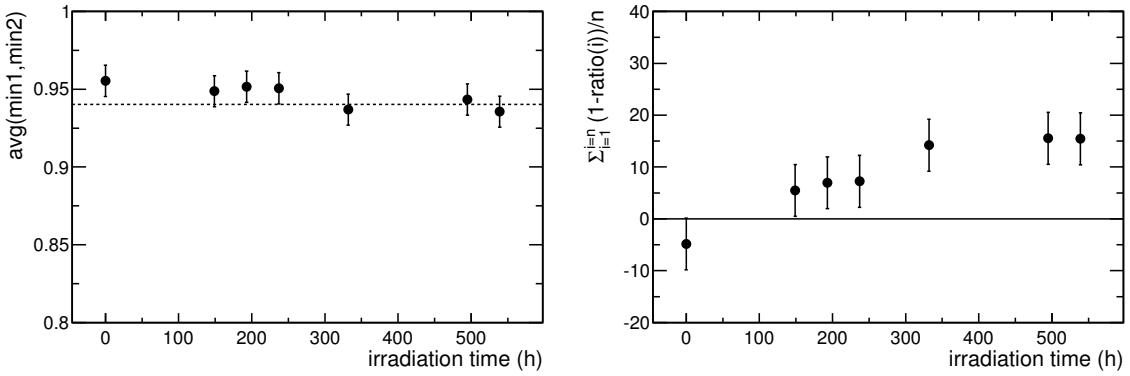

(a) (b)

Figure 4.8: Evolution of the parameters used to quantified the gain loss during the 539h in the module constructed with Tra–Bond glue of the irradiation with the 20 mCi scanning source; (a) the evolution of the maximum gain loss is shown, and (b) the evolution of the integrated gain loss is shown. For the definition of these quantities, see Sec. 4.2. The reference line for no ageing in (a) is shown with a dashed line and it is obtained with several independent measurements in different regions of the detector in case of no irradiation. In (b) the reference line of no–ageing is, by definition, at 0 and it is shown with a solid line.

4.4 Prevention techniques

Outgassing

Flushing time

Given the fact that the plastifier in Araldite AY103-1 glue caused the gain loss in the OT detector, long term flushing is expected to transport away the vapours originating from outgassing of the glue. Indeed, Fig. 4.9 shows the maximum gain loss caused by an irradiation of 20 hours as a function of flushing time. The ageing rate for successive irradiations decreases significantly. All the OT modules have been flushed continuously since the completion of installation in the LHCb experiment in Spring 2007. Although, flushing the modules is beneficial, the ageing rate is not negligible even after a few years of flushing and therefore other solutions must be considered.

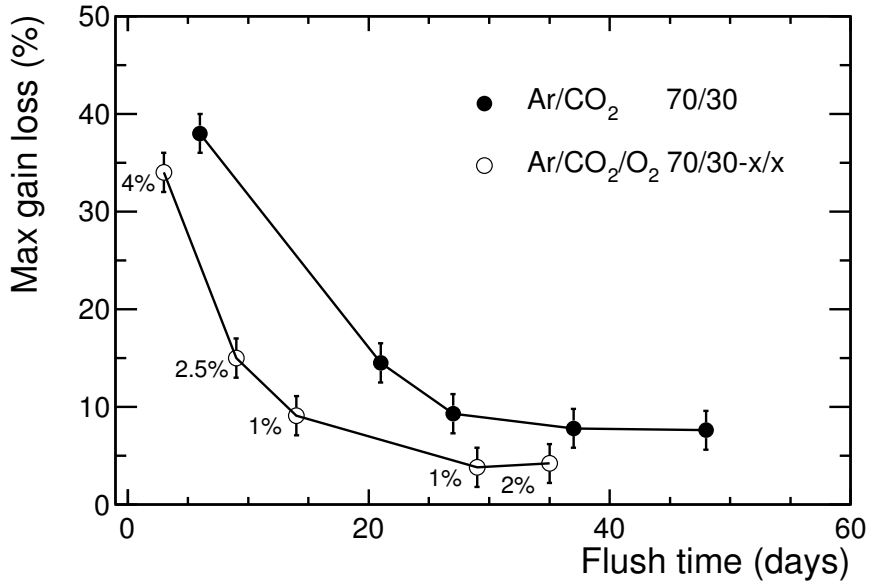

Figure 4.9: The maximum gain loss decreases for successive irradiation of about 20 hours each, as a function of flushing time. Also, the ageing rate is smaller when a few percent of oxygen is added to the gas mixture, varying between 1% and 4%, corresponding to a gas mixture $Ar/CO_2/O_2$ $70/30-x/x$. The improvement does not strongly depend on the exact amount of oxygen.

Heating

Outgassing processes generally occur faster at higher temperatures, therefore heating a module before irradiation might help to prevent ageing effects.

Heating tests performed at the Physikalisches Institut in Heidelberg showed promising results [54]. Modules that suffered from ageing effects after 20 hours of irradiation became radiation resistant after a heating treatment. The heating setup was duplicated at Nikhef.

Heating tests were performed by wrapping the module in electric blankets. Thin aluminium plates were placed on top of the modules, to improve the heat conduction between the electric blankets and the module. The temperature was kept at 45°C. The module and blankets were wrapped in bubble wrap to insulate the module. The treated modules were heated for a period of around two weeks each, while flushing the module with CO_2 at 5-10 l/h. The heating test performed at Nikhef, Heidelberg and in situ at CERN showed contradictory results, see Tab. 4.1.

The heating treatment has repeatedly shown promising results in preventing further ageing of OT modules. However, some heating tests resulted in minimal or no improvement, and some heated modules even became more susceptible to ageing after the treatment. In particular, the heatings performed at Heidelberg usually yield better results than the tests carried out at Nikhef or at CERN, but no clear explanation of this effect can be provided.

Oxygen

Oxygen has been used in other gas detectors, inspired by its beneficial effect on irradiation damage [55, 56]. Tests on the OT show that the ageing rate for a gas mixture with O_2 is re-

Table 4.1: Summary of heating results.

	Prod. Site	Mod. No.	Before	After	Results
Heating at Nikhef	Heidelberg	192	Good	Very Good	↗
	Nikhef	30	Poor	Poor	→
	Warsaw	99	Very Bad	Poor	↗
	Warsaw	121	Poor	Very Bad	↘
	Warsaw	44	Poor	Very Bad	↘
Heating at CERN	Heidelberg	191	Unknown	Good	?
	Warsaw	63-23	Unknown	Poor	?
	Nikhef	58	Poor	Poor	→
Heating at Heidelberg	Heidelberg	170	Poor	Excellent	↗
	Heidelberg	157	Good	Very Good	↗
	Heidelberg	44	Very Good	Very Good	→
	Heidelberg	179	Good	Excellent	↗
	Nikhef	123	Bad	Good	↗
	Nikhef	5	Poor	Good	↗
	Nikhef	58	Very Good	Very Good	→
	Warsaw	96	Bad	Poor	↗
	Warsaw	46	Very Bad	Bad	↗

duced by approximately a factor of two, see Fig. 4.9 [57, 58]. The amount of oxygen has been varied between 1% and 4%, but the improvement does not strongly depend on the exact amount of oxygen.

Due to the small diameter of the OT straw tubes, the number of electrons captured by the oxygen is limited and the average signal height at the anode wire is only reduced by 11% (29%) when 2.5%(4.5%) O_2 is added to the gas mixture while the drift speed is not affected, as is shown by simulation [43]. The comparison of a mixture with 2% O_2 with a gas with with 0% O_2 shows that the detection efficiency close to the straw boundary slightly reduces.

A sensitive ozone (O_3) meter has been placed at the gas outlet during irradiation tests of test modules in Heidelberg [59]. The ozone concentration increases with increased high voltage, indicating that ozone is formed in the avalanche region [57]. The production of ozone under the source is presumably the reason that no gain loss is observed downstream of the source. This is consistent with the observation that the ageing rate is larger for increasing gas flow, when the produced ozone is transported away more efficiently.

The concentration of O_3 has also been determined for various oxygen concentrations. For increasing oxygen concentrations, larger amounts of ozone were measured. However, above 1% of oxygen, the ozone concentration does not increase, supporting the observation that no difference in the ageing rate is expected between 1% and 4% O_2. The final gas mixture of the OT contains 1.5% of O_2.

4.5 Recovery with High Voltage training

As presented in previous sections, several prevention techniques are devised obtaining, in most of the cases, a reduction of the gain loss rate, but none of them is able to reduce the ageing rate to a negligible level. In addition to these preventive measures, studies are performed to define a treatment to remove the insulating deposits on the anode wire. The chosen procedure consists in the application of large high voltage values. These HV values bring the OT drift-tubes in the discharge regime and produce high dark currents, and is henceforth referred to as high voltage training [52]. The HV–training procedure has proven to recover previous gain losses, and, to some extent, even to temporarily prevent future irradiation damages [60]. Analogous observations have been reported in the literature [61, 62]. Various parameters have been varied to optimise the gain recovery. HV–training campaigns at various values of the high voltage, and for extended periods of time have been tried, as well as the addition of oxygen and humidity to the gas mixture. In all tests the only relevant parameter for curing an aged spot appears to be the value of the current.

In the nominal HV–training procedure the high currents are induced by increasing the externally applied HV. As described in Sec. 4.4, the OT detector nominally operates with a gas mixture of $Ar/CO_2/O_2$ ratio of 70/28.5/1.5 at an high voltage of 1550 V, corresponding to a gain of approximately 5×10^4 [63]. Typically, the gain doubles for every 70 V of increase of the high voltage. The proportional regime in a Ar/CO_2 70/30 gas mixture ranges approximately from 1540 V to 1800 V [64]. Above 1800 V, the dark current rises sharply from approximately 10 nA per straw at 1850 V to typically 10μA per straw at 1900 V (the actual value of the current

strongly depends on the wire quality and the processing time at that HV value).

The typical behaviour of a module observed during the HV–training campaigns can be summarised as follows:

- An initial strong increase in current with increasing HV (between 1840 V to 1870 V) reaching typically 200 μA, see Fig. 4.10 b).
- A subsequent drop of the current from 200 μA to 10 μA in approximately 19 hours, see Fig. 4.10 c).
- Consecutive HV–training attempts need higher HV values to achieve similar starting values for the currents[5]. Again, the currents typically drop after 19 hours to a few nA.

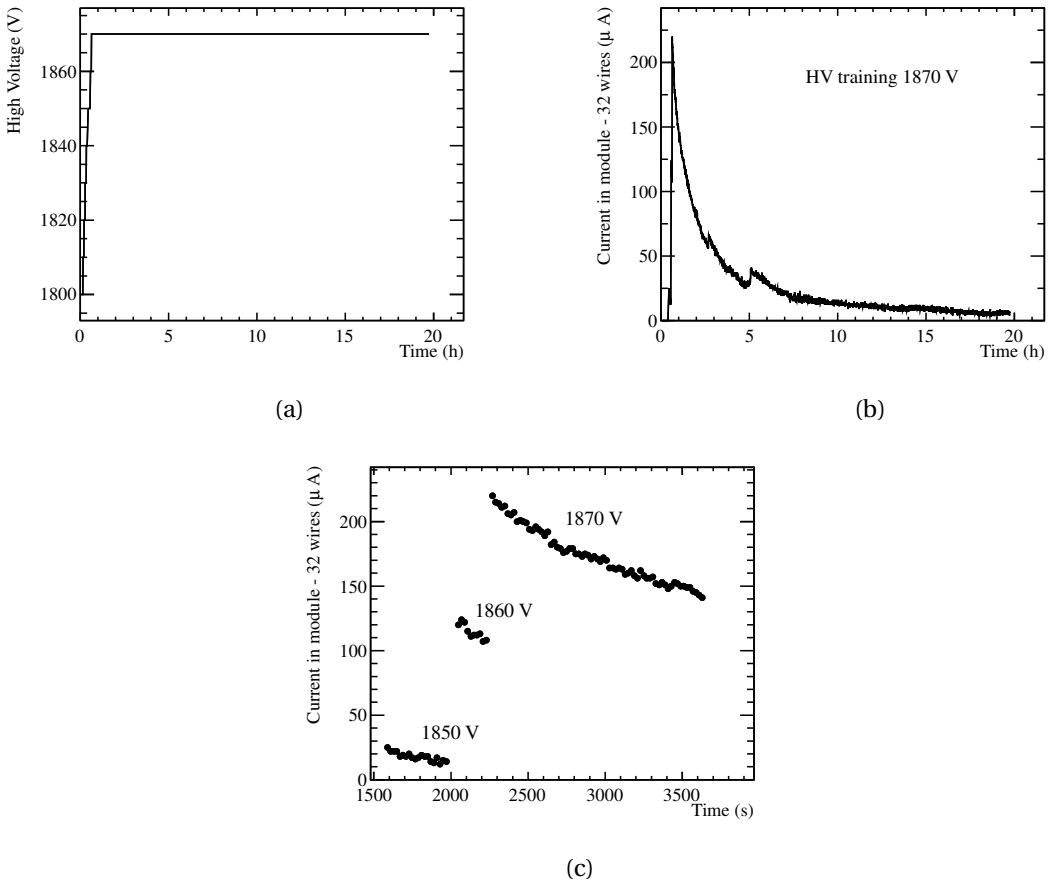

Figure 4.10: Current as a function of HV and time. a) The HV versus time, b) the current behaviour in time, c) zoom in the first time bins where HV is raised.

An alternative way to obtain high currents is to increase the gain by changing the amount of argon in the Ar/CO_2 gas mixture from 70/30 to 90/10, while keeping the high voltage at the

[5]The maximum HV value tested was 2040 V.

nominal value of 1550 V. This technique was tested [65, 43] obtaining similar healing results as increasing the HV. Increasing the HV is technically less involved than changing the gas mixture, so a HV–training technique is preferred as a possible in–situ solution. It has to be noticed, that not all the damages could be repaired using the HV–training technique, presumably because the local occurrence of high currents are not necessarily located at the desired wire position. Alternatively, high currents can be directly induced on the affected wire section placing a source on the damage ("HV–training with a source") [66]. This technique can in principle overcome the limitation of the normal HV–training.

The HV–training procedure was tested in situ and a procedure for a large scale HV–training has been prepared in case of need, see next section. In addition, extensive studies were performed in the laboratory to reproduce the current intensities expected from the LHC beam[43]. From these studies a strong dependence of the ageing rate on the irradiation profile is observed. It is difficult to predict the ageing rate from the LHC beam, given the delicate balance between malicious glue vapours and beneficial ozone radicals.

Recovery

The HV–training procedure were extensively tested on four modules in the laboratory and in one in–situ in the LHCb pit [60]. The main results are explained in this section and summarised in Tab. 4.2.

The HV training procedure was applied in situ on a module with the nominal gas mixture of 70/28.5/1.5 $Ar/C0_2/O_2$ for 16 hours at 1950 V[6]. Figure 4.11 illustrates the detector response before and after HV–training and the recovery effect obtained. The top half (channels 1-32) of the module is trained while the bottom half is left as reference. The first plot, Fig. 4.11 a), shows the presence of a damage around 105 cm. From the second plot, Fig. 4.11 b), it is clear that part of the gain is recovered. From the ratio of these two scans the gain increase in the top half is evident, Fig. 4.11 c).

A study of the evolution of the healing with time is performed on module M030 by performing several intermediate scans as shown in Fig. 4.12. In these plots several damaged areas, the white regions, were produced with irradiation campaigns in different positions of the module and also with different gas–flow directions. To study the HV–training behaviour, again the bottom half of the module is used as reference, and on top half the HV training procedure is applied. Most of the damages are cured in the first 22 hours.

A large scale HV–training procedure for the entire detector has been prepared. A short HV–training of one hour is foreseen, starting at a current about 1600 μA for 256 straws, after which the currents decrease fast. After that, a second HV–training of about 15 hours is started at a higher high voltage, with a current above 1600 μA for 256 straws. Safety measures are implemented such that the high voltage is lowered if the current would unexpectedly increase.

[6]Large dark current appear around 1850 V, then quickly drop. After 30 minutes at 1850 V and 1870 V, the HV was set to 1900 for 1.5 hour, then the HV training was done at 1950 V for 13.5 hours.

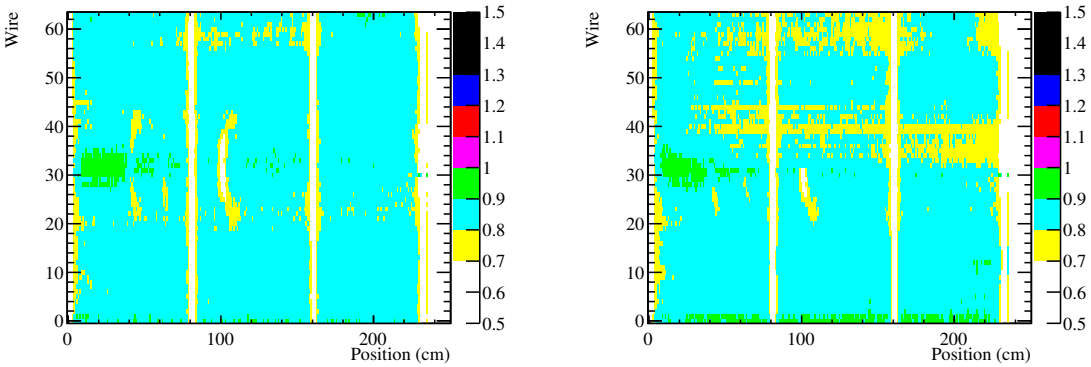

(a) Single scan before HV–training

(b) Single scan after HV–training

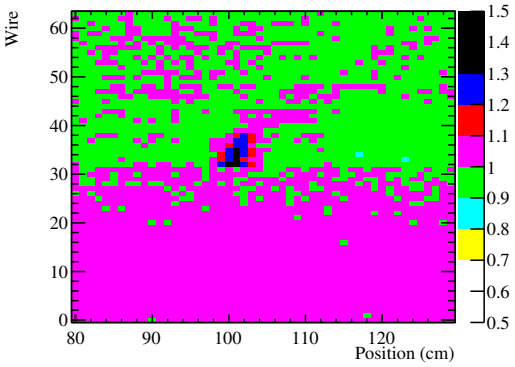

(c) Ratio of the two scans

Figure 4.11: Results of an HV–training section applied to the upper half (wires 33-64) of the module (S1-122-125 on position T2L0Q1M8). (a) and (b): single scan maps before and after the HV training campaign. The color scale is in arbitrary units since no correction for the atmospheric conditions is applied. The "half–moon" shape of the typical gain loss is evident in (a). Note that the white regions around 80 and 160 cm in (a) and (b) are the wire–locators. (c): a recovery of the gain around position 105 cm. Note that the green/purple split between the two halves of the detector is not relevant and it is due to a temporary[7] behaviour seen in most cases after the HV training. No clear explanation of this effect can be provided.

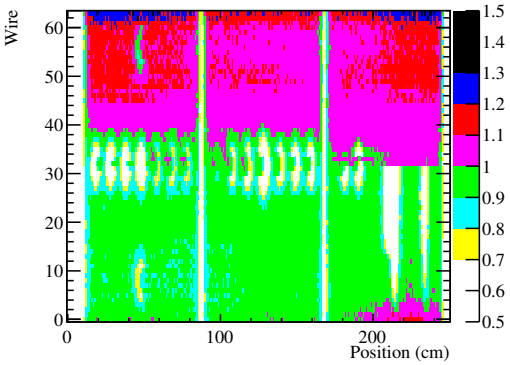

(a) Before HV

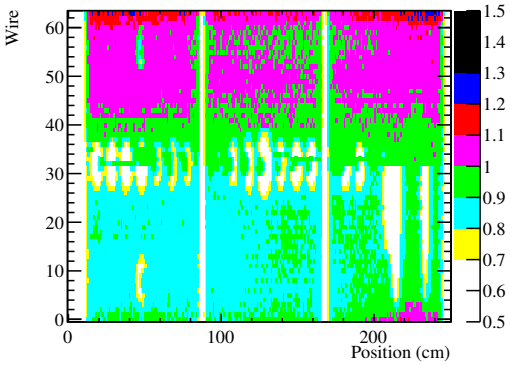

(b) After 3 hours

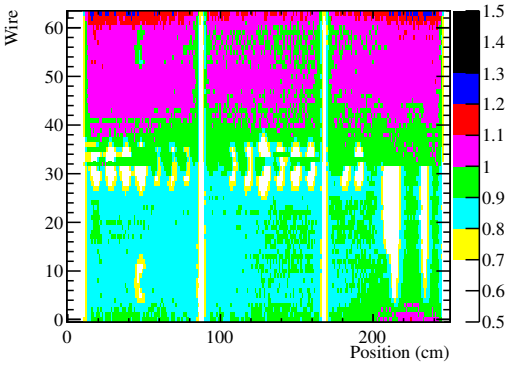

(c) After 5 hours

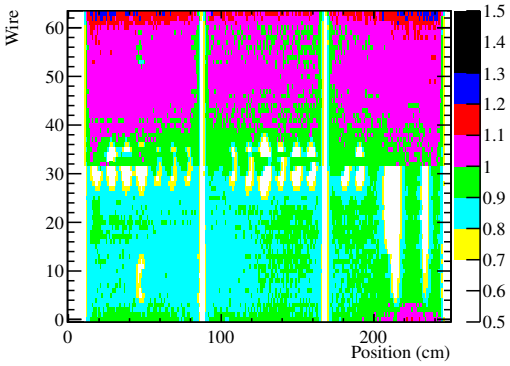

(d) After 7 hours

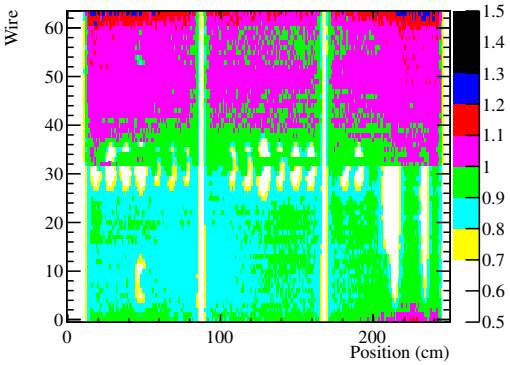

(e) After 8 hours

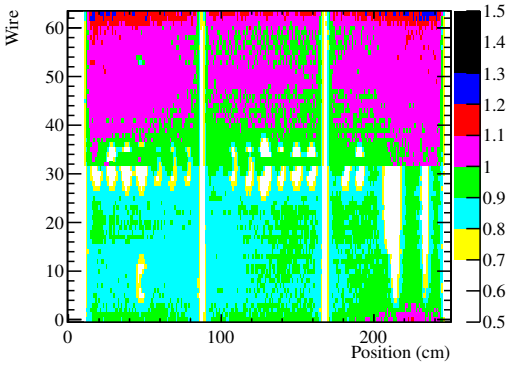

(f) After 9 hours

Figure 4.12: The time evolution of the curing process from the HV–training of the upper half (wires 33-64) of the “B” monolayer of module M030. From top to bottom, the gradual curing is illustrated by scans taken every few hours. In these single scan maps the color scale is in arbitrary units since no correction for the atmospheric conditions is applied. (Cont.)

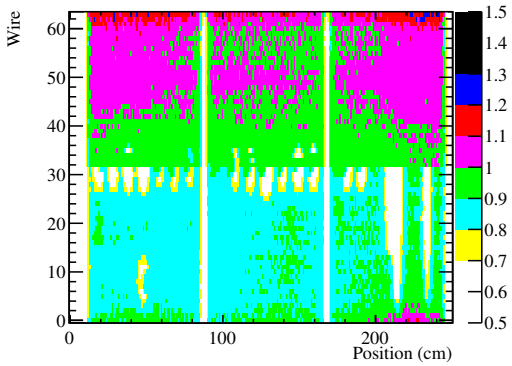

(g) After 22 hours

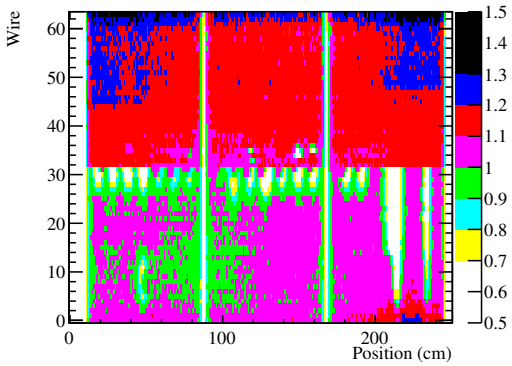

(h) After 23 hours

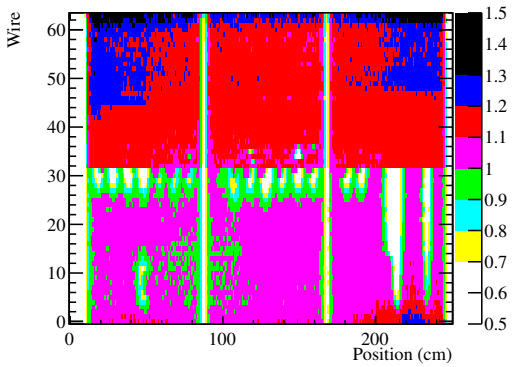

(i) After 25 hours

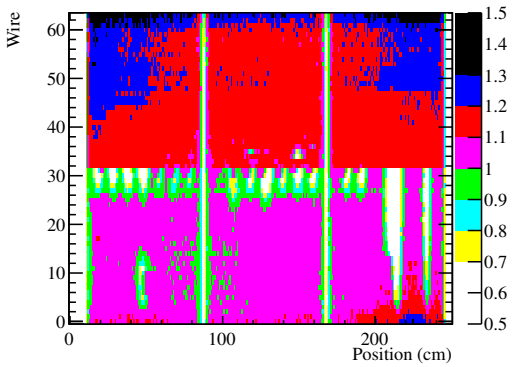

(j) After 26 hours

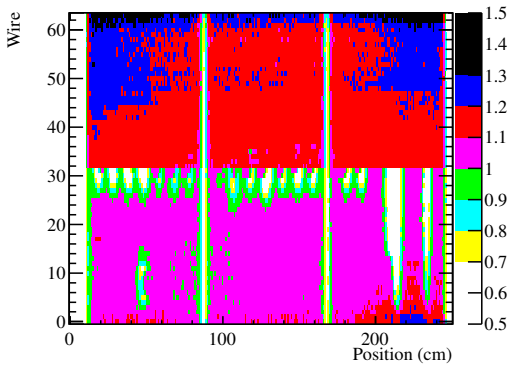

(k) After 27 hours

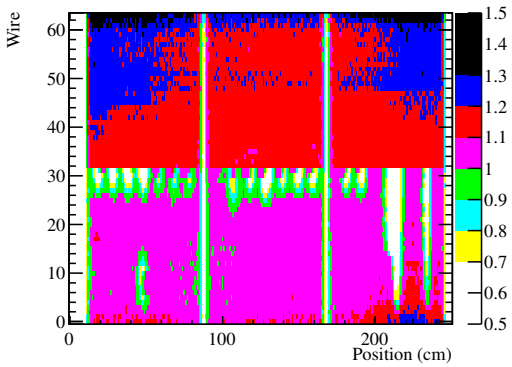

(l) After 28 hours

Figure 4.12: (Cont.) The time evolution of the curing process from the HV–training of the upper half (wires 33-64) of the "B" monolayer of module M030. From top to bottom, the gradual curing is illustrated by scans taken every few hours. In these single scan maps the color scale is in arbitrary units since no correction for the atmospheric conditions is applied.

Mod	Date	HV (V)	I (μA)	HV time (hrs)	Ch	Flush time (days)	Effect on irr. spots Cure	Prevention	Comment
3A	17/8/06	1870	200 $\searrow$ 7	20	1-32	32	half spot	<20 hrs	
3A	19/8/06	1910	250 $\searrow$ 90	26	1-32	34	whole spot	~206 hrs	
3A	7/9/06	1910	400 $\searrow$ 80	20	1-32	53	spot after 340hrs	~235 hrs	
3A	24/9/06	1910	400 $\searrow$ 80	20	1-32	53	spot after 350hrs	<96 hrs	
30B	31/8/06	1870	180 $\searrow$ 80	10	1-32	2	half spot	-	
30B	31/8/06	1930	730 $\searrow$ 445	15	1-32	2	whole spot	<20 hrs	
30B	5/9/06	1930-50	800 $\searrow$ 475	16+16	1-32	7	only big spot	<85 hrs	
30B	18/9/06	1910	520 $\searrow$ 320	14	1-32	20	only (same) big spot	>20 hrs	
30B	3/4/08	1910-55	970 $\searrow$ 420	23+14+8	1-32	29	also all small spots	-	
S1L121A	20/6/07	1890	250 $\searrow$ 130	20	1-32	6	only half of 1 spot	same wires	
S1L121B	27/8/07	1890	< 1	20	1-32	10	no	no	1.25% O_2
S3U99A	27/ 9/07	1970	200 $\searrow$ 9	18	1-16	23	half	>20 hrs	2.5% O_2
S3U99A	25/10/07	2040	200 $\searrow$ 70 $\nearrow$ 150	18	1-16	51	all	-	1.0% O_2
2A	18/4/08	1905	600 $\nearrow$	1	33-64	8	some	-	
2A	18/4/08	1910-20	600 $\nearrow$	4	33-64	8	no	-	
2A	8/5/08	1920-30	800 $\nearrow$	5	1-64	28	no	-	
2A	16/5/08	1945	580 $\searrow$ 430	64	1-32	36	no	>21 hrs	
2A	26/6/08	1930	740 $\searrow$ 600	15	1-32	77	no	-	5 ppm H_2O
2A	9/7/08	1930	300 $\nearrow$	7	1-32	12	no	-	40,000ppm H_2O
2A	24/7/08	1910	330 $\rightarrow$ 330	16	1-32	27	no	-	4,000 ppm H_2O

Table 4.2: The results of various HV–training procedures.

Wire inspection

With large dark currents up to 20μA per wire, the HV–training procedure is rather aggressive compared to normal OT detector operation. Potentially, unknown chemical or physical reactions might occur on the wire surface or in the gas mixture, that in turn may damage the wire surface or lead to the formation of deposits. To assess these risks, aggressive HV–trainings were performed on four wires inside an openable test-module from which wire samples can easily be extracted. Subsequently, the wire samples were inspected under a scanning electron microscope (SEM) and analysed with energy dispersion X-ray spectroscopy (EDX).

Four wires were first irradiated and suffered from a gain loss of about 10%. Subsequently, these wires were trained in two sessions of one night each, at 1870 V and 1880 V, respectively with currents around 50 μA per wire. This is a factor of five times higher than what was shown to be sufficient to cure a wire from radiation damage. After the HV–training, scans confirmed that the HV–training cured the previously induced gain loss. After the inspection, the conclusion of this study is that the HV–training procedure with currents up to around 50 μA per wire for a period of 35 hours induced no mechanical damage to the gold plating of the anode wire and produced no extra depositions on the wire surface [60].

Prevention

Another characteristic of the HV–training is the evidence of a certain immunity against gain loss by further irradiation, called the "prevention effect", occurring in most of the cases after an HV–training session. An example of obtained results is shown in Fig. 4.13 in terms of gain loss as a function of irradiation time. The figure illustrates both the gain recoveries obtained in three consecutive HV–trainings, as well as the preventive effect of the HV–trainings, shown by the fact that no gain loss is observed in the trained detector half for the first 200 hours of irradiation following the HV–training. The detailed mechanism behind the immunity period subsequent to the HV–training is currently not understood. Possibly the HV–training "cleans" the anode surface temporarily hampering the deposition of the insulating layer.[8]

4.6 OT Performance after LHC operation

Reference measurements

The nine modules located in C-frame T2-Q13-XU were scanned in 2009 to obtain a reference measurement before the modules were subjected to irradiation from the LHC beam. In addition, four modules in C-frame T2-Q13-XU and three in C-frame T1-Q13-XU have been irradiated to evaluate the ageing rate in situ and quantify the effects of heating and of the addition of oxygen in the gas mixture. A summary of the irradiation results is shown in Tab. 4.3.

[8] It is also been speculated that the HV–training smooths the gold surface of the anode wire, thereby reducing the catalytic effect of gold of the process $CO_2 + O \rightarrow O_2$. As a result, a larger concentration of atomic oxygen can then reduce the deposits of the isopropyl-naphthalene on the wire.

Table 4.3: Ageing results for modules in C-frame T2-Q13-XU and T1-Q13-XU. The maximal damage in brackets in case of a second irradiation is the total damage after the two irradiations.
Notice that the second irradiation of module 57-18 (42 hours) was at a different position on the module than the 14 hours irradiation.
*: Although the irradiation of module F-90 in January 2010 after addition of oxygen had a maximal gain loss of 6%, no clear irradiation spot could be seen. The same holds for the irradiation of module S122-125 in July 2010 and the irradiation of module F-194 in July 2010.

C-frame	Module	Type	Irr. Time (hrs.)	Max Damage	Comment
T2-Q13-XU	90	F (NI)	14 (+14)	7% (9%)	before heating
	90	F (NI)	66	9%	before heating
	90	F (NI)	18	8%	after heating
	90	F (NI)	16	7%	after heating
	90	F (NI)	17	6%*	after addition of O_2
T2-Q13-XU	122-125	S1 (WS)	17(+70)	16% (38%)	before heating
	122-125	S1 (WS)	15	16%	after heating
	122-125	S1 (WS)	19	13%	after heating
	122-125	S1 (WS)	17	7%	after addition of O_2
	122-125	S1 (WS)	14	10%*	after addition of O_2
T2-Q13-XU	194	F (HD)	21	8%	before heating
	194	F (HD)	18	7%	after heating
	194	F (HD)	13	5%*	after addition of O_2
T2-Q13-XU	204	F (HD)	18	9%	before heating
T1-Q13-XU	17	F (NI)	14	12%	after heating
T1-Q13-XU	57-18	S1 (WS)	14	6%	after heating
	57-18	S1 (WS)	42	6%	after heating
T1-Q13-XU	188	F (HD)	21	7%	after heating

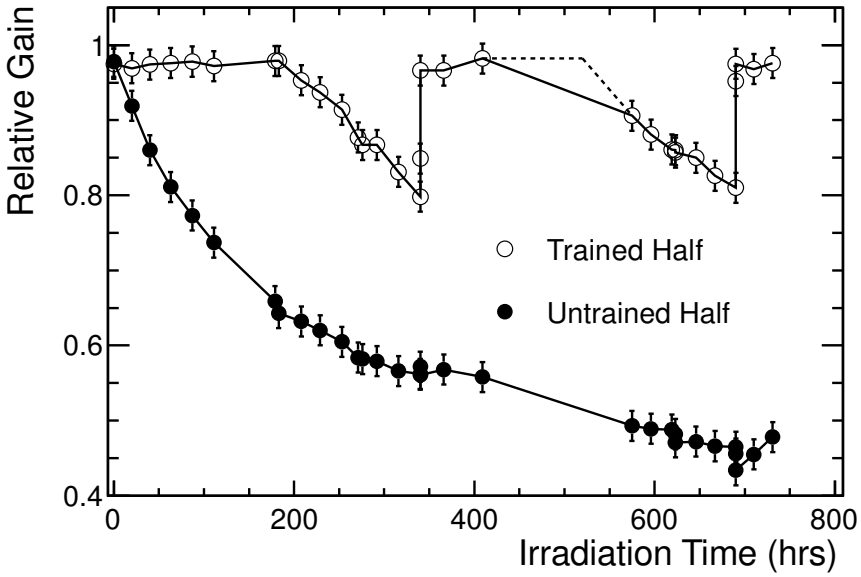

Figure 4.13: The relative gain is deteriorating as a function of irradiation time. However, the HV trained half of the module recovers the gain. Furthermore, the three HV–training procedure (at 0, 300, and 700 hours, respectively) all show a temporary prevention of further gain loss.

The irradiation results before and after heating in situ of C-frame T2-Q13-XU show that shortly after heating in situ no significant improvement in ageing rate was seen.

The addition of 1.5% oxygen to the drift gas mixture shows a clear improvement on the ageing rate. On module F-90 it is difficult to distinguish the irradiation area with gain loss after the same irradiation time, whereas before a damage about 7% was observed. For the same irradiation a factor 2 less gain loss for module S1-122-125 is observed. These results are consistent with the irradiation tests performed in the laboratory.

2011 measurements

During 2010 and 2011 run periods, possible ageing in the OT was monitored with two methods:

- Threshold scan using tracks, with dedicated runs during LHC operation
- Scan with radioactive ^{90}Sr source of all modules of C-frame T2Q13XU during technical stops.

The detector hit–efficiency is determined as a function of the threshold setting in the electronics while taking data. The threshold value at which the efficiency reach 50% is correlated to detector gain. Using this correlation, the variation in time of the 50% threshold value

is a measure of the variation in gain [67]. The stability of this parameter for the entire detector was monitored every 200 pb^{-1} until the total integrated delivered luminosity of around $\sim 1.3\ fb^{-1}$ was collected. No sign of gain loss is observed so far [67].

During technical stops, radioactive ^{90}Sr scans with the monitoring setup in situ were performed on all modules of C-frame T2Q13XU. In none of the nine modules a gain loss is observed. An example of two ^{90}Sr scans, before and after LHC operation, are shown in Fig. 4.14 a) and Fig. 4.14 b) respectively. The normalised ratio of the detector response is given in Fig. 4.14 c) and no gain variation along the entire detector length is observed.

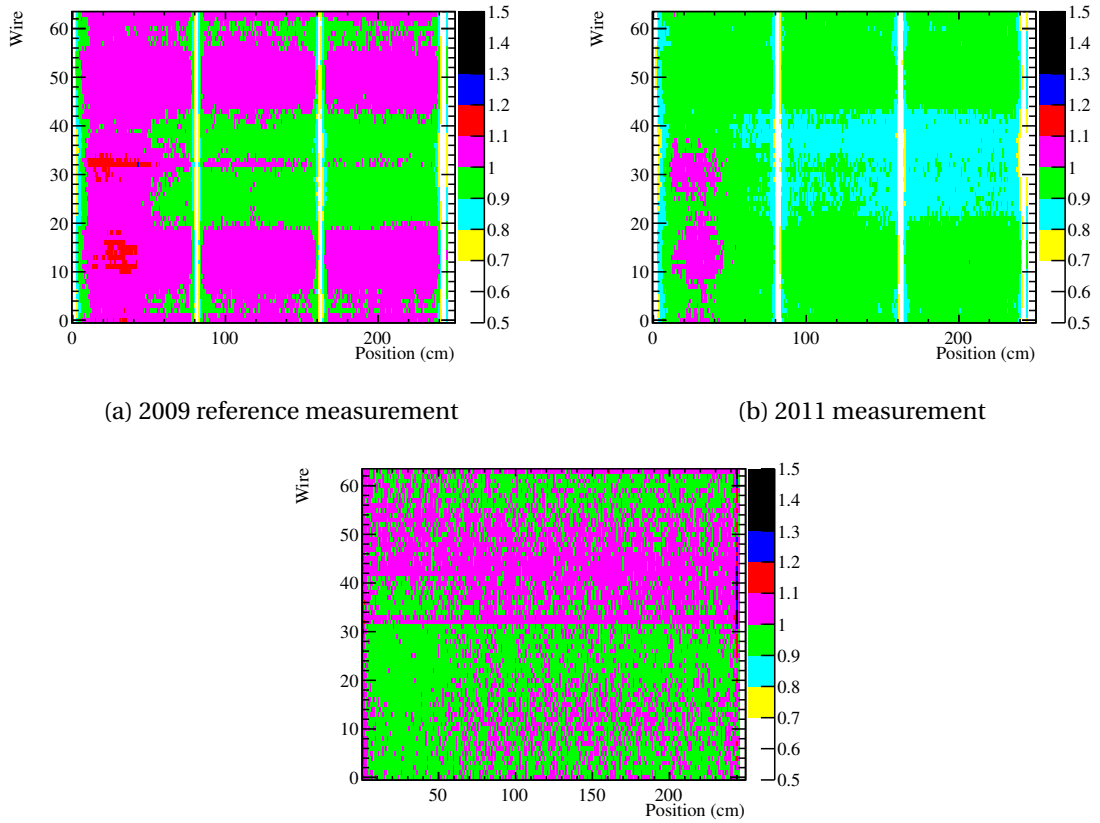

(a) 2009 reference measurement

(b) 2011 measurement

(c) Ratio of 2009 and 2011 measurements

Figure 4.14: Results of the scan of the module in position T2Q1L0M6 in 2009 (a) and 2011 (b) and their ratio (c). The color scale in the two single scan maps is in arbitrary units since no correction for the atmospheric condition is applied, while in the ratio of the two scans represents the relative gain. No gain variation along the detector is observed.

In addition, the area with lower gain as provoked by an irradiation campaign before LHC operation (see also Fig. 4.11), has removed completely, as shown in Fig. 4.15. This is probably due to the fact that beneficial radicals were produced during the running period and they removed previous deposits on the wire with a similar mechanism of the HV–training with the

source. No confirmation of this effect can be provided since it was not possible to damage a module in situ with an irradiation campaign.

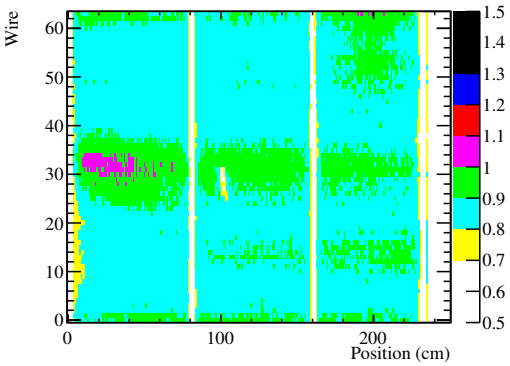

(a) Single scan in January 2011

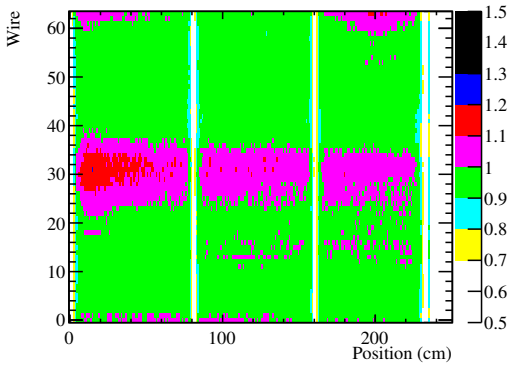

(b) Single scan in June 2011

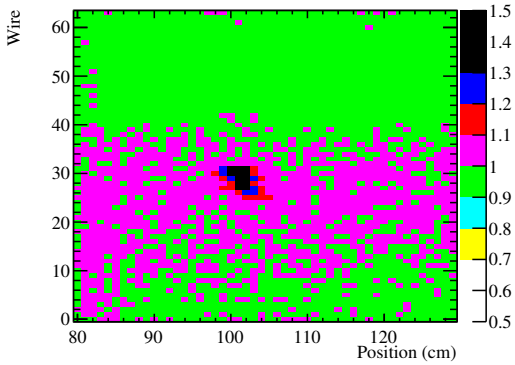

(c) Ratio of the two scans

Figure 4.15: Results of the scan of module in position T2Q1L0M8 in January 2011 (a) and in June 2011 (b). From the ratio of the two single scans (c) a gain recovery placed around 105 cm is observed. This is probably due to the fact that beneficial radicals were produced during the running period and they removed previous deposits on the wire with a similar mechanism of the HV–training with the source. The color scale in the two single scan maps is in arbitrary units since no correction for the atmospheric condition is applied, while in the ratio of the two scans represents the relative gain. No gain variation along the detector is observed.

Fifth Chapter

Tracking efficiency

As regards obstacles, the shortest distance between two points can be a curve.
Bertolt Brecht

5.1 Introduction

In LHCb several methods have been developed to determine the track finding efficiency for charged particles. The techniques based on the "tag-and-probe" method, as mentioned in Sec. 2.3, uses specific decay channels like the $K_s^0 \to \pi^\pm\pi^\mp$. The main advantage of this technique is that the selection of a specific decay channel guarantees a good ratio signal to background, but the result can be biased by the selection used. An alternative technique, that can be easily performed per type of track is described in this chapter.

The goal of the analysis described here is to compare the tracking efficiency extracted from data and from simulation (MC) for tracks that traverse all tracking stations, i.e. tracks that pass through the Velo and reach the calorimeters. As described in the next section, several algorithms have been developed to reconstruct tracks in LHCb, and the method is meant to evaluate the agreement for each tracking algorithm separately and it is limited only by the acceptance of the calorimeter. Relying on the Velo, this method cannot be used to evaluate the efficiency of this sub-detector.

Before the description of the data–driven method used to evaluate the tracking efficiency for all the tracking algorithms, an introduction on the track types and on the techniques used to reconstruct tracks in LHCb is given in the next sections.

Reconstruction strategy and track types

A track represents the path of a charged particle through the detector. The track reconstruction strategy is based on two steps: first, the track finding pattern recognition to determine which groups of hits (track) belong to individual particles, then the track fitting to determine

Table 5.1: Tracking Algorithms available in LHCb. The X indicates whether hits of a particular subdetector are included on the track.

Name	Velo	TT	T	Algorithm
Velo	X			combining hits in the Velo
Upstream	X	X		combining Velo tracks and TT hits
T Segment			X	combining hits of IT and/or OT
Downstream		X	X	combining T–tracks and TT hits
Match	X	(X)	X	match T-station tracks to Velo tracks, and add TT hits
Forward	X	(X)	X	extending Velo tracks to the T-station, and add TT hits
Long	X	(X)	X	combination of the best candidates from Match and Forward

the optimal trajectory parameters. The efficiency studied here corresponds to combined track finding and track fitting algorithms; however the fitting algorithm has an efficiency close to 100%, see below.

A particle's path through the LHCb spectrometer is reconstructed from the hits created in the tracking sub-detectors. These are the Vertex Locator (Velo), Tracker Turicensis (TT), Inner Tracker (IT) and Outer Tracker (OT), see Sec. 2.3. The tracks reconstructed are classified according to the sub-detectors used in the track reconstruction, and according to the particular reconstruction algorithm that is used as summarised in Tab. 5.1. A short description of each algorithm is given in the next section. Detailed descriptions can be found in [24].

Pattern recognition

The track reconstruction starts with the search for track "seeds", the initial track candidates. The Velo and T–stations register sufficient hits of a traversing charged particle to be used as a starting point for the track search. Moreover, the magnetic field in these regions is low and an initial search for a straight line candidate is possible. In the case of a Velo–seed a straight segment is obtained using the Velo R and ϕ cluster coordinates. A Velo–seed provides an initial track state without momentum information. Alternatively, a T–seed is obtained using IT and OT x and stereo hits. In this case a parabolic parametrisation follows the initial straight line assumption to account for the low, but not negligible, magnetic field. An initial momentum estimation is made either from the measurement of the curvature, or by assuming that the track originates from the nominal interaction point.

Proceeding from these seeds, the following algorithms are performed to find a track of a specific type. Usually, these algorithms are executed in sequence, generally using only the seeds and the hits that have not been used in previously executed algorithms. Notice that running the algorithms in sequence gives artificially low results for algorithms that are executed later in the sequence. Since the goal of the analysis presented in this chapter is to calibrate the MC and not to determine an absolute efficiency of algorithms in the sequence,

all tracking algorithms are instead run independently on all detector hits.

- **Long Search**: starting from a Velo–seed an attempt is made to form a track with hits in the T–stations. Long tracks are created from a Velo seed to which first T–system information and later TT hits are added. Two algorithms are developed. The "forward pattern recognition" creates Long tracks first combining Velo–seeds with individual T–detector hits. A combination of a Velo–seed and a single T–station hit provides an estimate of the momentum of the track candidate and its trajectory. Around this trajectory a search for hits in other stations, including the TT station, is performed. The "match pattern recognition" creates Long tracks by combining Velo-seeds with T–seeds. It considers T–seeds with a minimum momentum estimate of 2 GeV/c, obtained from the parabolic curvature during the seeding. The Velo and T–seeds are extrapolated to match and the pair is considered a track candidate with a matching χ^2 criterion. For a Velo–seed that is paired with multiple T–seeds, the combination with the smallest χ^2 is selected. A TT hit is added when its distance to the track candidate is smaller than 3 mm[68]. One TT hit is allowed per layer, and at least three layers need to contribute to the track candidate for the TT part to be valid.

  In the standard LHCb reconstruction sequence, all Velo and T–seeds used by these algorithms are discarded before searching for other track types. However, as mentioned earlier, this is not done for the efficiency calculation presented below.

- **Upstream Search**: an "upstream track" is a track passing only through the Velo and the TT detectors. They are typically low momentum as well as high angle tracks leaving the detector volume before the magnet. They are found by extrapolating the Velo–seed to the TT stations, using an individual cluster to calculate the momentum and the other clusters to confirm the track. The method is similar to the forward track finding presented before.

- **Downstream Search**: a "downstream track" is created from a T–seed and TT hits. They typically represent a long living particle decaying outside the Velo. A similar procedure of the one used for the upstream search is performed but the initial momentum estimate is obtained assuming that the T–track originates from the nominal vertex position.

- **Velo and T–Track Search**: remaining Velo and T seeds that have not been associated are also stored as tracks, either with no (Velo track) or a poor (T tracks) momentum estimate.

Track fitting

After the tracks are found their trajectories are fitted with a Kalman filter fit. The effects of the multiple scattering and a correction for dE/dx energy loss are accounted for in the fit. The track is represented by a sequence of states where each state parametrises the path of

the particle at a specific z coordinate in the detector[1]. A state is composed by a state vector and a covariance matrix. The state vector contains the track parameters and is defined as $(x, y, t_x, t_y, q/p)$, where x and y are the Cartesian coordinates, $t_x = dx/dz$ and $t_y = dy/dz$ are the track slopes, q is the charge of the particle, p its momentum. The covariance matrix quantifies the uncertainty in each of the track parameters and their covariance. After a number of iterations the estimated state parameters are optimal in the sense that the Kalman filter has minimised the estimated parameter error covariances. The quality of the reconstructed tracks is monitored by the χ^2 of the fit and the failure rate is about 0.1%. This is negligible compared to the pattern recognition efficiency.

Datasets

The study was carried out on data taken in 2009 and early 2010 and a comparison to the corresponding MC samples was done. The method was validated using MC–truth information, see Sec. 5.4.

During the 2009 run, relatively low energy beams collided in LHCb at the LHC injection energy, corresponding to a centre-of-mass energy of 0.9 TeV. Both the beam sizes and the crossing angle were larger than those designed for high-energy collisions. As a consequence, the 2009 data were recorded with the two Velo halves positioned 15 mm away from their nominal data-taking position, resulting in a reduced polar and azimuthal coverage. The luminosity of the analysed sample is found to be $6.8 \pm 1.0\ \mu\text{b}^{-1}$[69]. The momentum and transverse momentum distribution for Long tracks for 2009 and 2010 data are shown in Figs. 5.1. A fair agreement between data and MC simulation is observed.

In 2010 all sub-detectors were fully operational in nominal conditions. The data used in this study correspond to an integrated luminosity around 3 nb^{-1} at a centre-of-mass energy of 7 TeV.

5.2 The efficiency validation method

The efficiency analysis is carried out purely at the level of tracks: no event selection or particle identification criterion is applied and the results are therefore valid before any physics analysis.

The structure of the LHCb spectrometer was shown in Fig. 2.3 in chapter 2. This study is based on track candidates that consist of a Velo track associated to a calorimeter cluster. All particles that produce hits in the Vertex Locator and a cluster in the Electromagnetic Calorimeter must be represented by tracks in the tracking system. A combination of a Velo track and a matching ECAL cluster is called a track candidate for the efficiency analysis. The track finding efficiency is defined as the ratio of track candidates that are actually reconstructed in LHCb as tracks with hits in the tracking stations, over all track candidates formed in this analysis. An LHCb track can be recognised by different algorithms, as mentioned in

[1]Notice that the geometry of LHCb is such that the traversing particle results in hits at either continually increasing or continually decreasing z.

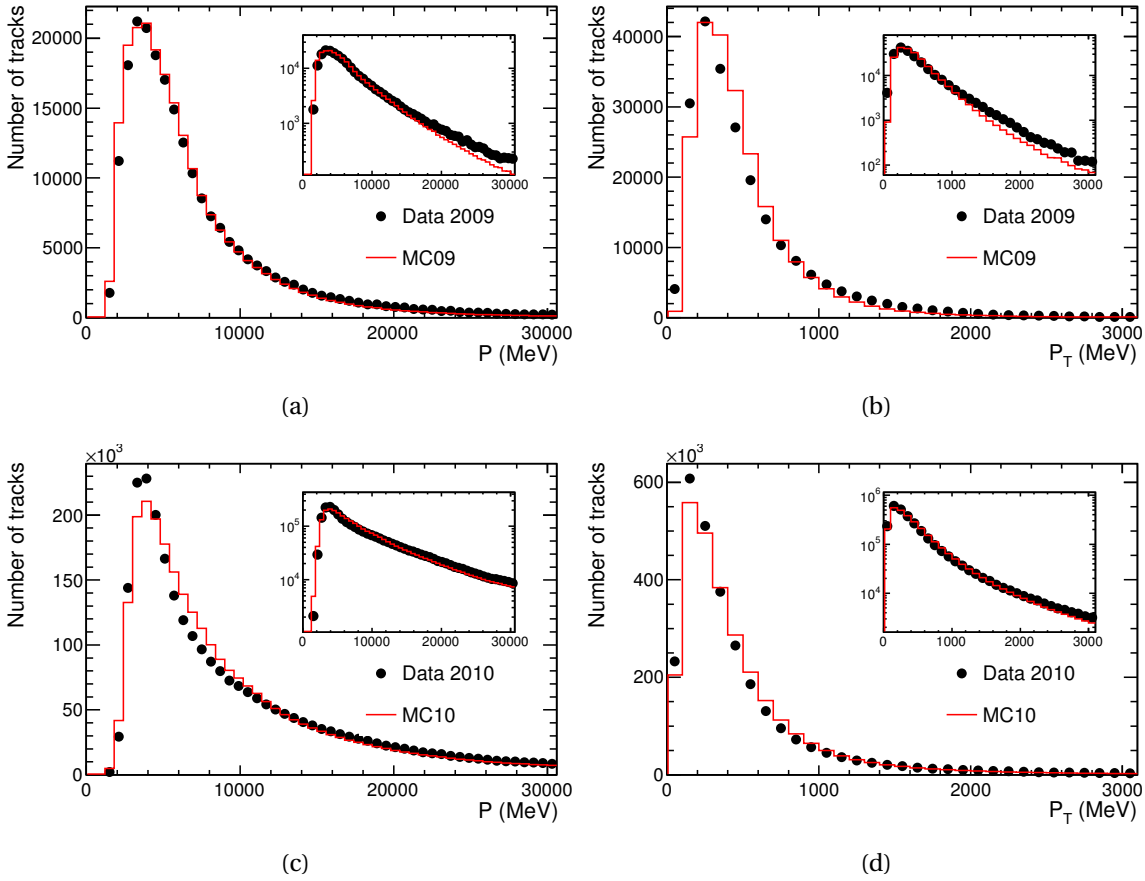

Figure 5.1: Momentum spectrum for Long track candidate in data and simulation (MC) samples for 2009 (a) and 2010 (c). Transverse momentum spectrum for Long track candidate in data and MC samples for 2009 (b) and 2010 (d). The inserts show the same plots on logarithmic scale.

the introduction. For all algorithms the specific tracking efficiency is estimated for both data and a simulated data sample, and the results are compared.

The track candidates are formed independently from the T–station hits by matching Velo segments, obtained fitting hits in the Velo with a straight line, to calorimeter clusters. Each Velo segment is combined with each calorimeter cluster. An iterative procedure is adopted to assign a momentum value to this segment in such a way that it can be extrapolated to the calorimeter cluster with a distance on x smaller than 1 mm. The centre of the electromagnetic calorimeter is used to identify the z position of the cluster.

To distinguish fake Velo-Calo combinations from true track candidates, the distribution of the differences in y of the cluster and the extrapolated Velo-Calo trajectory is studied. Since the bending power of the LHCb magnet has almost no horizontal component tracks are expected to be straight lines in the y–z projection. All the good candidates, i.e. the combination of a Velo segment with a corresponding calorimeter cluster, will therefore be dis-

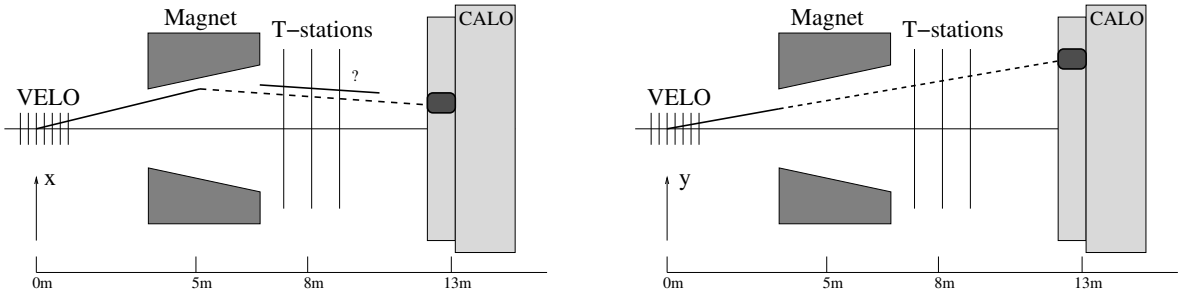

Figure 5.2: Sketch of the Velo-Calo method for the tracking efficiency extraction in the $x-z$ plane (a) and in the $y-z$ plane (b).

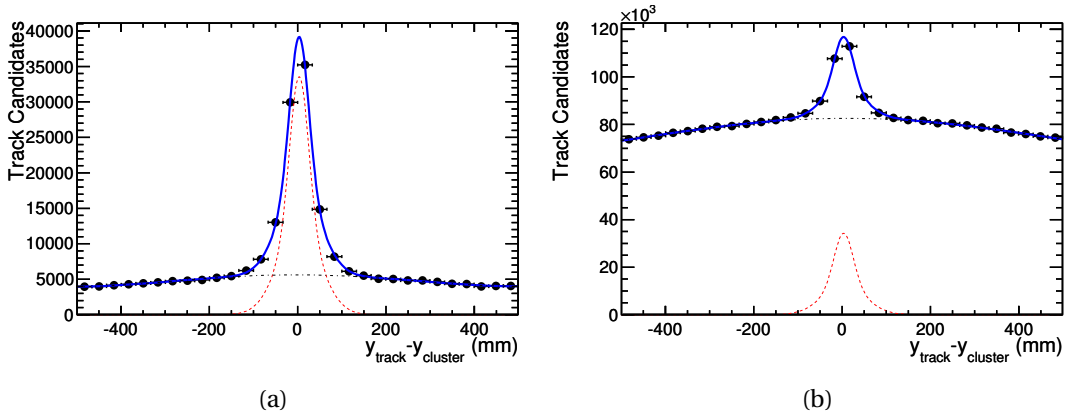

Figure 5.3: Distance in the y-axis between the calorimeter cluster and the trajectory (Δy distribution) at the calorimeter for "found" tracks (a) and "all" tracks (b). The signal component, fitted with a double Gaussian, is drawn in red-dashed line, while the background component, fitted with a a 4^{th} degree polynomial, is drawn in black-dashed-dot line.

tributed around zero, while the fake candidates will be distributed on the entire spectrum. The method is shown in Fig. 5.2.

A fit to the peak in the Δy distribution gives the total number of correct track candidates. Subsequently, the number of track candidates that are reconstructed in the tracking stations need to be estimated. The definition of these "found" tracks is described in the next section.

An example of fitted Δy distributions for "found" and "all" tracks are shown in Fig. 5.3. The signal shape is fitted with a double Gaussian while the background of fake track candidates is described with a 4^{th} degree polynomial. The signal shape in the "found" distribution is used in the fit to the "all" distribution. More details on the validity of this assumption are given in Sec. 5.4.

5.3 Track finding efficiency at the T–System

To evaluate the efficiencies of tracking algorithms a class of “found” tracks needs to be defined. This is based on Velo-Calo track candidates that successfully match with reconstructed tracks. This general definition applies to all tracking algorithms, except the “Velo tracking algorithm”, as already mentioned. An additional class of "found tracks" is defined that applies only to the “Long tracking algorithm”. The efficiencies obtained with the two classes of “found tracks” are compared for the “Long tracking algorithm” and discussed at the end of this section.

- **Class I**: a Velo-Calo track candidate is defined as “found” if its horizontal position x and slope t_x at the T–Station region are compatible, within a defined window, with the corresponding parameters of the reconstructed track. The “found” candidate is then associated to the corresponding track type. In figure and text these candidates will be referred to with the name of the algorithm associated, see Tab. 5.1.

- **Class II**: a Velo-Calo track candidate is considered as “found” if the Velo segment is actually part of the reconstructed track for the Long tracking algorithm. Note that this definition does not include the acceptance window required for “class I” track candidate. On the other hand it can be applied only to long tracks.

For “class I” found track candidates the window for $\Delta x = x - x_{rec}$ and $\Delta t_x = t_x - t_{xrec}$ is obtained from the Δx and Δt_x distributions, see Fig. 5.5.

In Fig. 5.4 (a) the correlation between the values of Δx and Δt_x is shown. Both positive and negative correlations can be observed. The negative correlation is due to ghost tracks at the inner region of the calorimeter, as will be discussed later. The positive correlation is caused by the fact that if the calorimeter cluster is reconstructed at a shifted position, both Δx and Δt_x will be too large (or too small). The observed correlation between Δx and Δt_x depends on the distance between the z-position of the point of comparison (in the T-stations) and the calorimeter plane. If both Δx and Δt_x are used to find the track, optimally a combination of Δx and Δt_x is used that accounts for this correlation. In particular, this correlation can be removed applying a linear correction $\Delta x' = \Delta x - \Delta z \cdot \Delta t_x$ where Δz is 3370 mm, corresponding to the focal plane of the magnet[2].

In Figs. 5.4 (a) and 5.4 (b) the distributions before and after this correction are shown. For the inner, middle and outer regions of the calorimeter the same value of Δz could be used to describe the positive correlation, independent of the tracking algorithm and both for data and MC events. An example of the distribution for the track parameters before and after the correction is shown in Fig. 5.5. It is interesting to notice the presence of a second correlation, with opposite direction with respect to the previous one. It mainly occurs for the inner region of the calorimeter. The candidates leading to these points are ghost tracks from the combination of a Velo track with a T-track originating from two different particles. This type of tracks has an incorrect Velo track association but the T–Station part corresponds

[2]Note that the calorimeter cluster is at a z = 8570 mm while the magnet center is located $z \sim 5200$ mm, leading to a correction of 3370 mm.

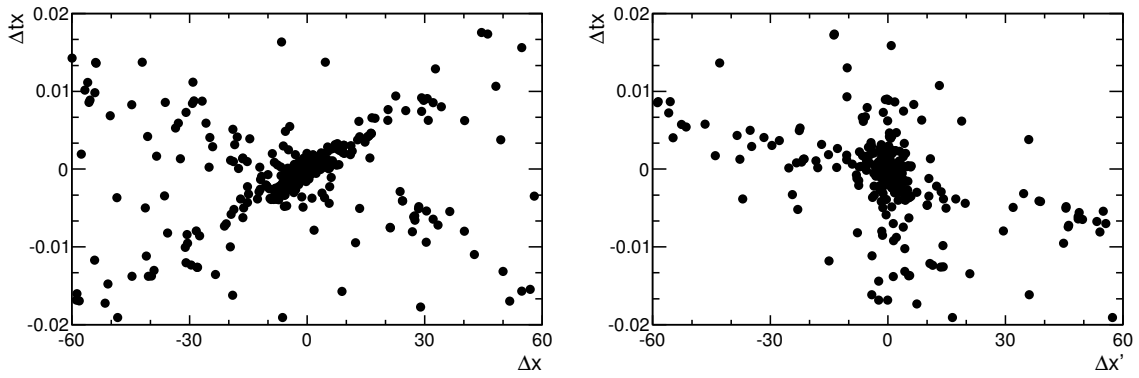

(a) (b)

Figure 5.4: (a): Δx vs Δt_x distribution at the T–System. A limited data sample was used for this plot. (b): $\Delta x'$ vs Δt_x distribution, obtained with a linear correction $\Delta x' = \Delta x - 3370\Delta t_x$.

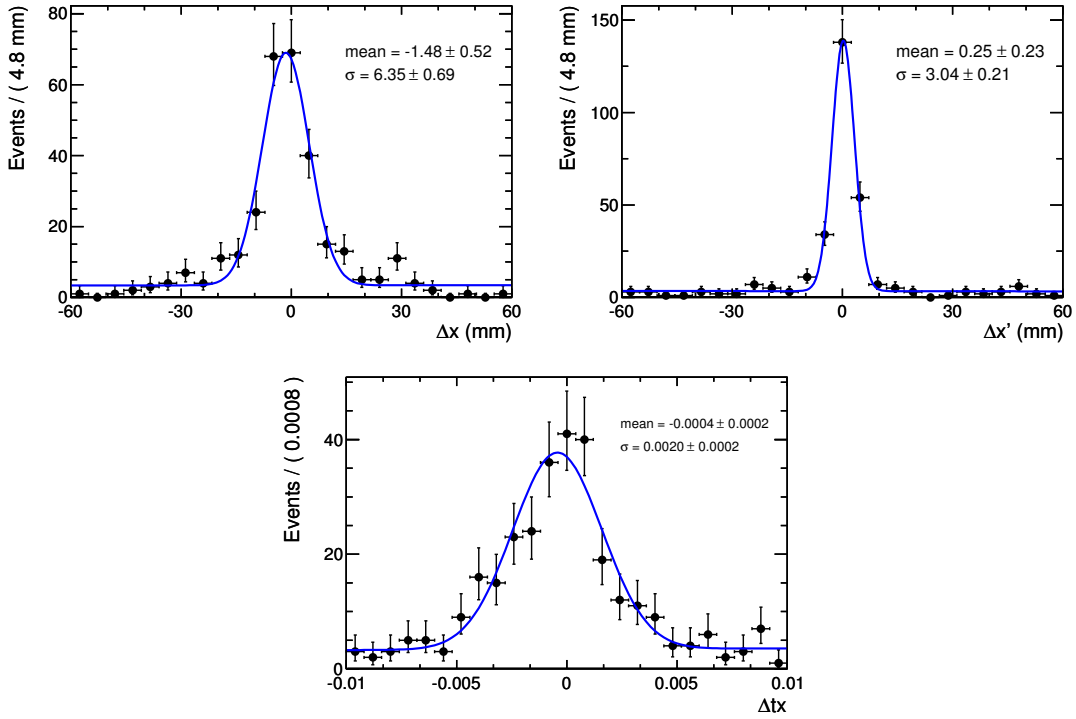

Figure 5.5: Track parameters distribution for long tracks in the inner region calorimeter area.

to the calorimeter cluster. For them the plane in which Δx and Δt_x are uncorrelated is the calorimeter plane, i.e. at ~ 5200 mm further downstream from the T–stations.

The $\Delta x'$ and Δt_x distributions are fitted with a single Gaussian distribution. For each calorimeter area, the distributions for all the algorithms have almost the same width of the $\Delta x'$ and Δt_x distribution. An additional loose cut on the curvature difference of a Velo can-

Table 5.2: Acceptance windows used to define "found" track sample.

Calorimeter Area	$\sigma(\Delta x')[mm]$	$\sigma(\Delta t_x)[10^{-3}]$	$\sigma(\Delta q/p)[MeV^{-1}]$
Inner	3.5	2.5	2.0
Middle	4.5	3.5	3.0
Outer	8.5	6.0	5.0

didate and a reconstructed track, $\Delta q/p$ distribution, were performed to avoid, especially for downstream tracks, that a candidate without consistent TT hits but with $\Delta x'$ and Δt_x inside the acceptance windows was considered as signal ("found candidate"). The final window sizes that define a track to be "found" are given by the widths listed in Tab. 5.2, multiplied by an optimised number.

The number of sigmas for $\Delta x'$ and Δt_x variables to produce an acceptance window were decided by analysing the stability of the efficiency results. For all the samples the plateau was achieved above 7σ of $\Delta x'$ and Δt_x distribution, as shown in Fig. 5.6 for 2009 data and simulation samples.

For long tracks two techniques are available to evaluate the tracking efficiency, where the "class II" definition does not apply any acceptance window. A 10σ acceptance window is found to minimise the difference between these two results in the 2009 simulation sample. This 10σ window is applied in the definition of found tracks for both data and MC and it is used for all track types[3].

5.4 Validation study

The validity of the Δy fit is investigated by comparing the results obtained analysing MC09 data with the results that come from the analysis of the same sample using MC–truth information. The extrapolation of the track state from the Velo to the Calorimeter is done using the "true" momentum of the particle associated to the Velo segment. Candidates are selected with only one Calorimeter cluster compatible within 100 mm in x and y as obtained from the extrapolation. This procedure gives a clean sample of Velo-Calo candidates (called "MC–truth" sample) on which the track finding procedure is tried. Subsequently, the tracking efficiency is determined on this sample in exactly the same way as described in the previous section. The comparison between MC and MC–truth was carried out both with and without an occupancy criterium, corresponding to the number of Velo tracks per event smaller than 15 in the event. At low occupancy the presence of less background makes, in principle, the fit more reliable. The results show a negligible dependence on the occupancy.

[3]Notice that a non–perfect window size will affect the results in two different ways: if the window is too small some signal could be lost artificially reducing the tracking efficiency results, while if it is too big more background will enter making the "found" fit less precise.

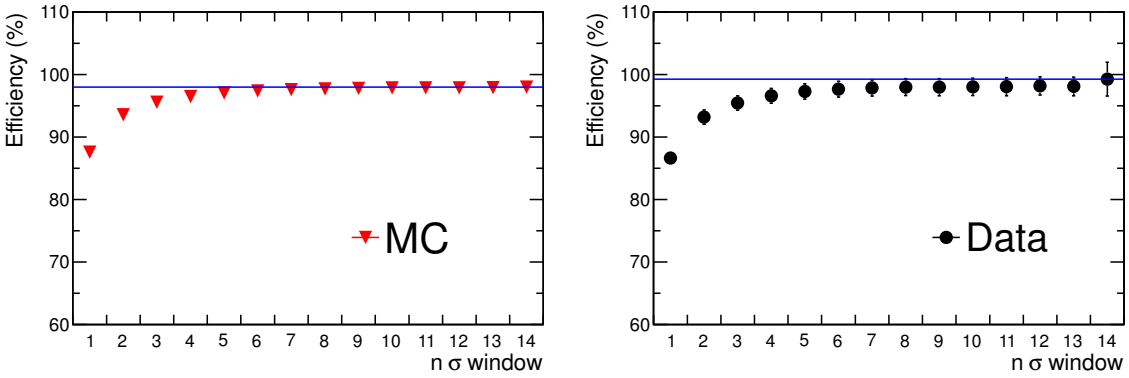

(a) MC09

(b) 2009 data

Figure 5.6: Stability of tracking efficiency estimation for different acceptance windows for Long tracks using the "class I" found candidates. The blue line is the value obtained with the "class II" found candidates.

The Δy distribution for "all" and "found" tracks without background were obtained for this sample. The comparison was performed in several bins of momentum, transverse momentum and pseudo–rapidity as well as for the integrated sample with no kinematical requirements. An example of these distributions in comparison with the ones obtained in the analysis without MC–truth information are shown in Fig. 5.7.

The probability density function (pdf) used to fit the signal shape, as described in Sec. 5.2, was a double Gaussian. As shown in Fig. 5.7, in the MC–truth sample the same shape describes both the "found" and "all" signal. In all the fits presented here the parameters obtained from the "found" distributions are fixed in the "all" distribution fit. This choice is motivated by the fact that the track candidates in the "found" and "all" samples are practically the same track candidates, thanks to a high track finding efficiency, close to 1.

The agreement between the two samples is shown in Figs. 5.8 (5.9) and Tabs. 5.3 (5.4) with (without) a requirement on the number of velo tracks respectively. Consistent results are obtained with and without an occupancy cut. Note that the method can find efficiency values higher than 100% since they are obtained by subtracting two independently fitted distributions on the "found" and "all" samples. A difference smaller or around 2% is found in all bins, with the exception of the first bin in momentum and transverse momentum. In this bins the signal and background shapes are different compared to all other bins. A small bias is observed since on average the MC result is somewhat higher than the MC–truth one. This suggests that a residual background is accounted as signal when the MC–truth information is not used. This is taken into account by assigning a systematic uncertainity. Above a transverse momentum of 5000 MeV/c and a momentum of 50000 MeV/c the track sample is too small to allow for a sensible comparison. The differences between MC and MC-truth sample results from Tab. 5.3 are used as a systematic uncertainty in each bin for both 2009 and 2010 samples.

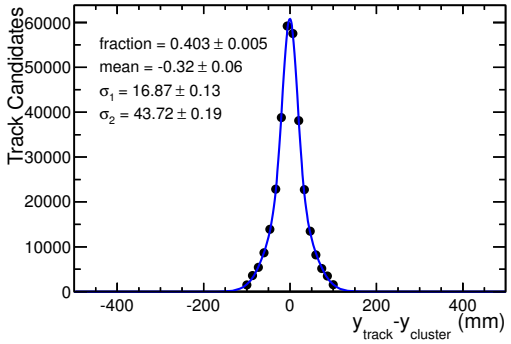

(a) "found" distribution using MC-truth information

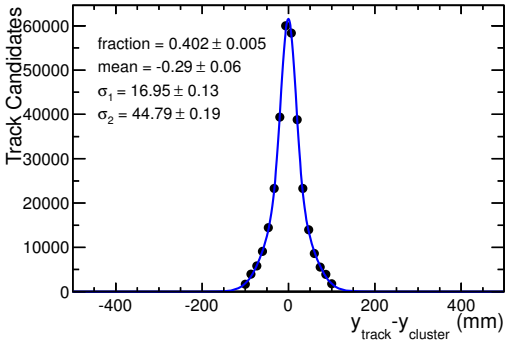

(b) "all" distribution using MC-truth information

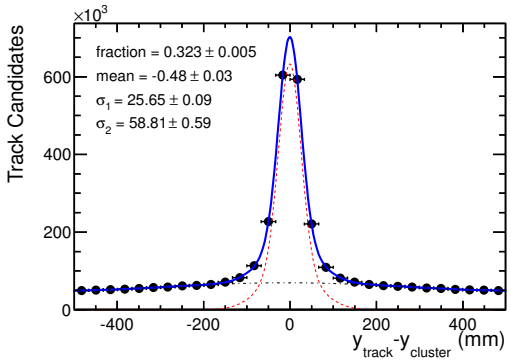

(c) "found" distribution without using MC-truth information

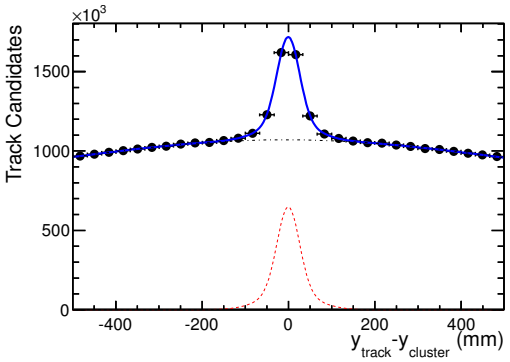

(d) "all" distribution without using MC-truth information

Figure 5.7: Comparison of the Δy distribution at the calorimeter using (top) or without using (bottom) the MC–truth information for the integrated sample. The left plots are related to "found" distribution, while the right plots are related to "all" distribution. The distributions are fitted with a double gaussian with a common mean and two separate sigmas. In the case where no MC–truth information is used, the background is fitted with a 4^{th} degree polynomial. Notice that the Gaussian parameters in the two top plots are almost identical.

Table 5.3: MC to MC-truth comparison with occupancy cut (number of Velo tracks smaller than 15)

		MC (%)	MC-truth (%)	Difference (%)
p (MeV/c)	$0-3000$	100.7 ± 1.1	97.6	3.0
	$3000-5000$	99.4 ± 0.7	98.3	1.1
	$5000-7000$	97.6 ± 0.6	97.8	-0.2
	$7000-10000$	97.2 ± 0.9	96.9	0.3
	$10000-50000$	100.0 ± 1.0	98.2	1.8
p_T (MeV/c)	$0-200$	102.8 ± 1.2	98.1	4.7
	$200-300$	99.8 ± 0.7	98.7	1.1
	$300-500$	97.2 ± 0.5	96.7	0.5
	$500-700$	98.6 ± 0.8	98.4	0.2
	$700-1000$	99.6 ± 1.1	98.4	1.1
	$1000-5000$	99.9 ± 2.1	98.2	1.7
η	$2-3$	98.5 ± 0.8	97.8	0.7
	$3-3.5$	99.1 ± 0.6	98.1	1.1
	$3.5-4.5$	98.8 ± 0.5	97.7	1.1
Integrated		98.8 ± 0.3	97.4	1.5

Table 5.4: MC to MC-truth comparison (no occupancy criterion applied)

		MC (%)	MC-truth (%)	Difference (%)
p (MeV/c)	$0-3000$	99.3 ± 0.8	97.0	2.3
	$3000-5000$	99.5 ± 0.5	98.1	1.4
	$5000-7000$	98.2 ± 0.5	98.1	0.1
	$7000-10000$	97.6 ± 0.7	97.6	0.0
	$10000-50000$	98.9 ± 1.0	98.6	0.3
p_T (MeV/c)	$0-200$	102.6 ± 0.9	98.3	4.3
	$200-300$	99.5 ± 0.6	98.8	0.7
	$300-500$	97.3 ± 0.4	97.1	0.2
	$500-700$	98.3 ± 0.6	98.1	0.2
	$700-1000$	99.4 ± 0.8	98.3	1.2
	$1000-5000$	98.7 ± 1.3	98.3	0.4
η	$2-3$	98.5 ± 0.5	97.2	1.3
	$3-3.5$	98.3 ± 0.4	98.4	-0.1
	$3.5-4.5$	99.1 ± 0.4	98.1	1.0
Integrated		98.7 ± 0.3	97.4	1.3

Table 5.5: Efficiency 2009. The first error is statistical while the second is systematic.

Track Type	Data	MC	Data/MC
Long	$98.7 \pm 1.2 \pm 1.5$	$98.7 \pm 0.3 \pm 1.5$	$1.00 \pm 0.01 \pm 0.02$
Downstream	$89.5 \pm 1.2 \pm 1.5$	$90.9 \pm 0.2 \pm 1.5$	$0.98 \pm 0.01 \pm 0.02$
Match	$91.3 \pm 1.1 \pm 1.5$	$94.1 \pm 0.2 \pm 1.5$	$0.97 \pm 0.01 \pm 0.02$
Forward	$94.3 \pm 1.1 \pm 1.5$	$97.1 \pm 0.2 \pm 1.5$	$0.97 \pm 0.01 \pm 0.02$
TSeg	$92.5 \pm 1.3 \pm 1.5$	$94.0 \pm 0.3 \pm 1.5$	$0.98 \pm 0.01 \pm 0.02$

Table 5.6: Efficiency 2010. The first error is statistical while the second is systematic.

Track Type	Data	MC	Data/MC
Long	$97.8 \pm 1.0 \pm 1.5$	$97.3 \pm 0.2 \pm 1.5$	$1.01 \pm 0.01 \pm 0.02$
Downstream	$90.3 \pm 1.1 \pm 1.5$	$92.3 \pm 0.2 \pm 1.5$	$0.98 \pm 0.01 \pm 0.02$
Match	$90.8 \pm 0.9 \pm 1.5$	$93.0 \pm 0.2 \pm 1.5$	$0.98 \pm 0.01 \pm 0.02$
Forward	$93.1 \pm 1.0 \pm 1.5$	$93.9 \pm 0.2 \pm 1.5$	$0.99 \pm 0.01 \pm 0.02$
TSeg	$93.2 \pm 1.1 \pm 1.5$	$94.1 \pm 0.2 \pm 1.5$	$0.99 \pm 0.01 \pm 0.02$

5.5 Results

The main goal of this study is to evaluate the agreement between efficiency results obtained on data and on simulation. The tracking efficiency can be evaluated as a function of kinematic variables like the momentum p, the transverse momentum p_T, or the pseudo-rapidity η. The results in bins of these variables as well as the integrated value over all these variables is given for 2009 and 2010 data and simulation (MC) for all type of tracks in Tabs. 5.7, 5.8 and Figs. 5.10, 5.11 and 5.12. A good agreement between data and simulation is found for all type of tracks for both run periods with typically an estimated error of around 3%, with the exception of the first bin in momentum and transverse momentum where the signal and background shapes are different compared to all other bins and a bigger systematic uncertainty was assigned.

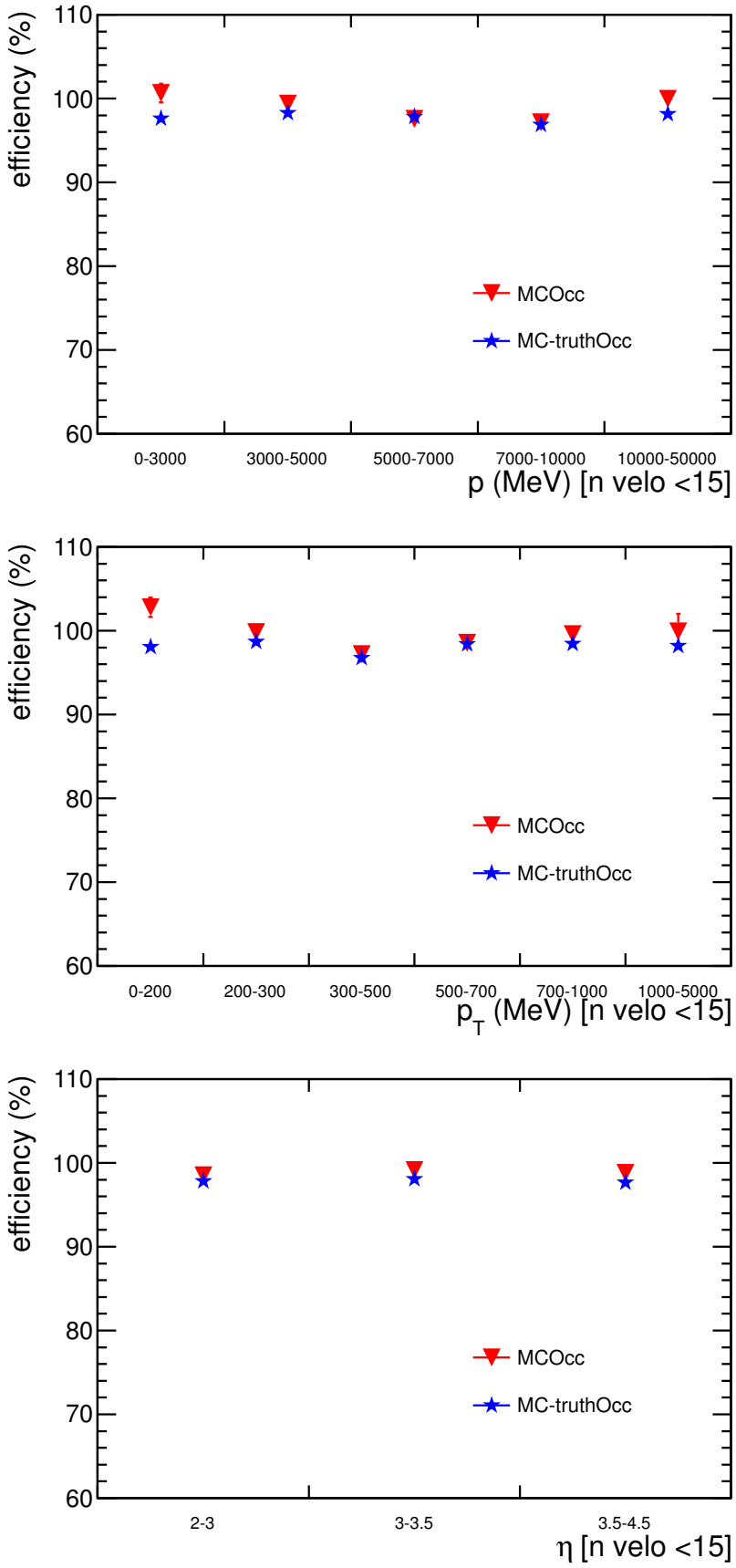

Figure 5.8: Comparison of efficiency results obtained with MC09 using (blue star) and without using (red triangle) MC–truth information. Events are preselected with an occupancy requirement of the number of Velo tracks smaller than 15.

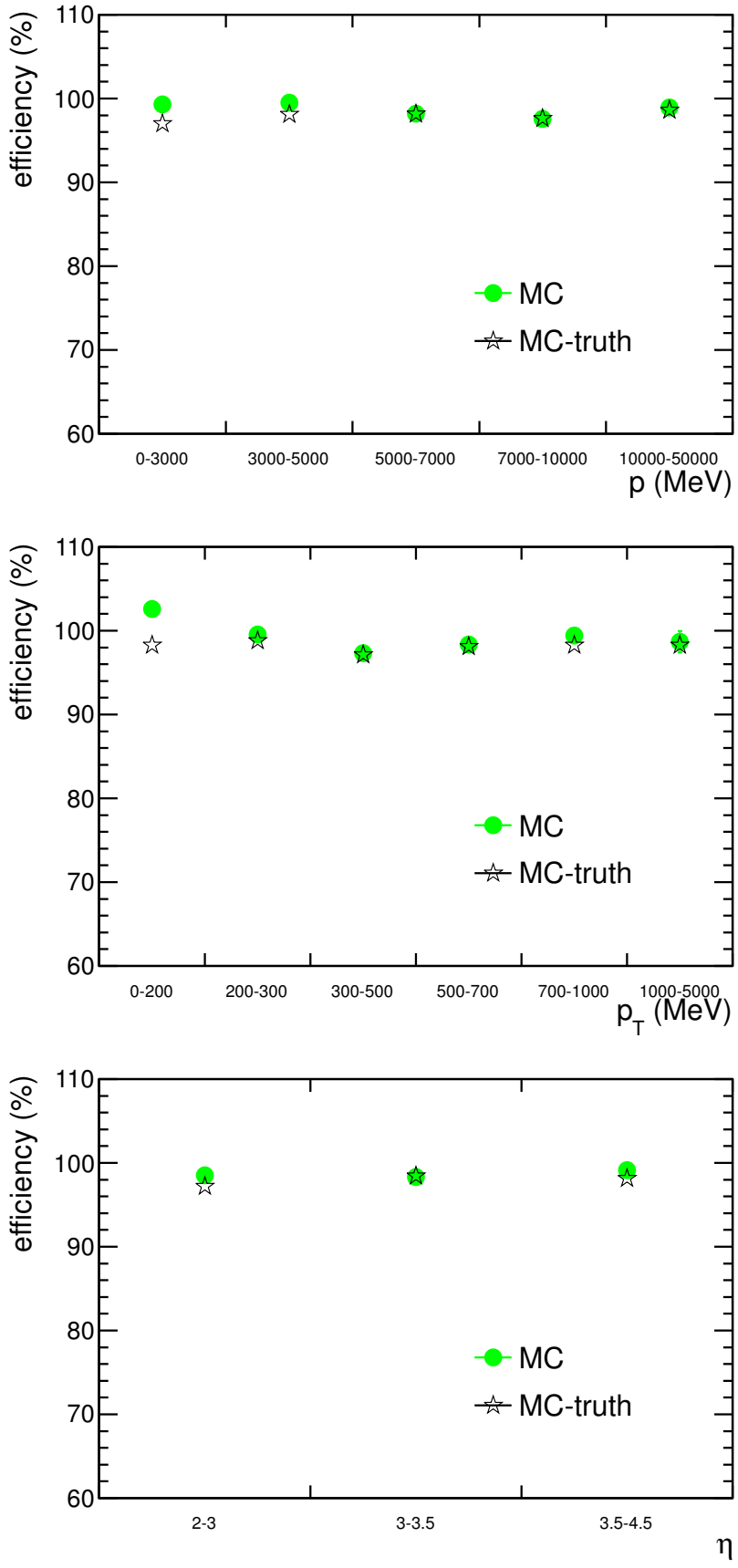

Figure 5.9: Comparison of efficiency results obtained with MC09 using (green circle) and without using (open star) MC–truth information. No occupancy preselection was applied.

Table 5.7: Summary of tracking efficiency results for 2009 sample with Long tracks. The first error is statistical while the second is systematic.

		Data (%)	MC (%)	Data/MC
p (MeV/c)	$0-3000$	$99.0 \pm 4.9 \pm 3.0$	$99.3 \pm 0.8 \pm 3.0$	$1.00 \pm 0.05 \pm 0.04$
	$3000-5000$	$99.5 \pm 2.4 \pm 1.1$	$99.5 \pm 0.5 \pm 1.1$	$1.00 \pm 0.02 \pm 0.02$
	$5000-7000$	$99.2 \pm 2.5 \pm 0.2$	$98.2 \pm 0.5 \pm 0.2$	$1.01 \pm 0.03 \pm 0.00$
	$7000-10000$	$97.4 \pm 3.4 \pm 0.3$	$97.6 \pm 0.7 \pm 0.3$	$1.00 \pm 0.04 \pm 0.00$
	$10000-50000$	$98.2 \pm 2.5 \pm 1.8$	$98.9 \pm 1.0 \pm 1.8$	$0.99 \pm 0.03 \pm 0.03$
p_T (MeV/c)	$0-200$	$102.4 \pm 4.2 \pm 4.7$	$102.6 \pm 0.9 \pm 4.7$	$1.00 \pm 0.04 \pm 0.06$
	$200-300$	$98.9 \pm 2.9 \pm 1.1$	$99.5 \pm 0.6 \pm 1.1$	$0.99 \pm 0.03 \pm 0.02$
	$300-500$	$99.2 \pm 2.4 \pm 0.5$	$97.3 \pm 0.4 \pm 0.5$	$1.02 \pm 0.02 \pm 0.01$
	$500-700$	$99.2 \pm 2.5 \pm 0.2$	$98.3 \pm 0.6 \pm 0.2$	$1.01 \pm 0.03 \pm 0.00$
	$700-1000$	$94.8 \pm 2.7 \pm 1.1$	$99.4 \pm 0.8 \pm 1.1$	$0.95 \pm 0.03 \pm 0.02$
	$1000-5000$	$99.3 \pm 3.4 \pm 1.7$	$98.7 \pm 1.3 \pm 1.7$	$1.01 \pm 0.04 \pm 0.02$
η	$2-3$	$97.1 \pm 2.8 \pm 0.7$	$98.5 \pm 0.5 \pm 0.7$	$0.99 \pm 0.03 \pm 0.01$
	$3-3.5$	$98.2 \pm 1.8 \pm 1.1$	$98.3 \pm 0.4 \pm 1.1$	$1.00 \pm 0.02 \pm 0.02$
	$3.5-4.5$	$99.7 \pm 1.8 \pm 1.1$	$99.1 \pm 0.4 \pm 1.1$	$1.01 \pm 0.02 \pm 0.02$
Integrated		$98.7 \pm 1.2 \pm 1.5$	$98.7 \pm 0.3 \pm 1.5$	$1.00 \pm 0.01 \pm 0.02$

Table 5.8: Summary of tracking efficiency results for 2010 sample with Long tracks. The first error is statistical while the second is systematic.

		Data (%)	MC (%)	Data/MC
p (MeV/c)	$0-3000$	$100.5 \pm 4.3 \pm 3.0$	$95.3 \pm 0.9 \pm 3.0$	$1.05 \pm 0.04 \pm 0.04$
	$3000-5000$	$100.2 \pm 2.3 \pm 1.1$	$98.6 \pm 0.4 \pm 1.1$	$1.02 \pm 0.02 \pm 0.02$
	$5000-7000$	$99.3 \pm 1.3 \pm 0.2$	$99.0 \pm 0.5 \pm 0.2$	$1.00 \pm 0.01 \pm 0.00$
	$7000-10000$	$98.8 \pm 1.5 \pm 0.3$	$97.3 \pm 0.7 \pm 0.3$	$1.02 \pm 0.02 \pm 0.00$
	$10000-50000$	$94.2 \pm 2.4 \pm 1.8$	$96.2 \pm 0.8 \pm 1.8$	$0.98 \pm 0.03 \pm 0.03$
p_T (MeV/c)	$0-200$	$107.3 \pm 3.5 \pm 4.7$	$101.8 \pm 0.8 \pm 4.7$	$1.05 \pm 0.03 \pm 0.06$
	$200-300$	$100.1 \pm 1.9 \pm 1.1$	$98.5 \pm 0.6 \pm 1.1$	$1.02 \pm 0.02 \pm 0.02$
	$300-500$	$97.8 \pm 1.7 \pm 0.5$	$96.8 \pm 0.4 \pm 0.5$	$1.01 \pm 0.02 \pm 0.01$
	$500-700$	$94.1 \pm 2.2 \pm 0.2$	$96.3 \pm 0.5 \pm 0.2$	$0.98 \pm 0.02 \pm 0.00$
	$700-1000$	$93.0 \pm 3.3 \pm 1.1$	$96.3 \pm 0.6 \pm 1.1$	$0.97 \pm 0.04 \pm 0.02$
	$1000-5000$	$87.0 \pm 9.0 \pm 1.7$	$96.4 \pm 0.8 \pm 1.7$	$0.90 \pm 0.10 \pm 0.03$
η	$2-3$	$96.0 \pm 3.5 \pm 0.7$	$97.4 \pm 0.5 \pm 0.7$	$0.99 \pm 0.04 \pm 0.01$
	$3-3.5$	$97.3 \pm 2.1 \pm 1.1$	$97.5 \pm 0.4 \pm 1.1$	$1.00 \pm 0.02 \pm 0.02$
	$3.5-4.5$	$98.2 \pm 1.3 \pm 1.1$	$97.1 \pm 0.4 \pm 1.1$	$1.01 \pm 0.01 \pm 0.02$
Integrated		$97.8 \pm 1.0 \pm 1.5$	$97.3 \pm 0.2 \pm 1.5$	$1.01 \pm 0.01 \pm 0.02$

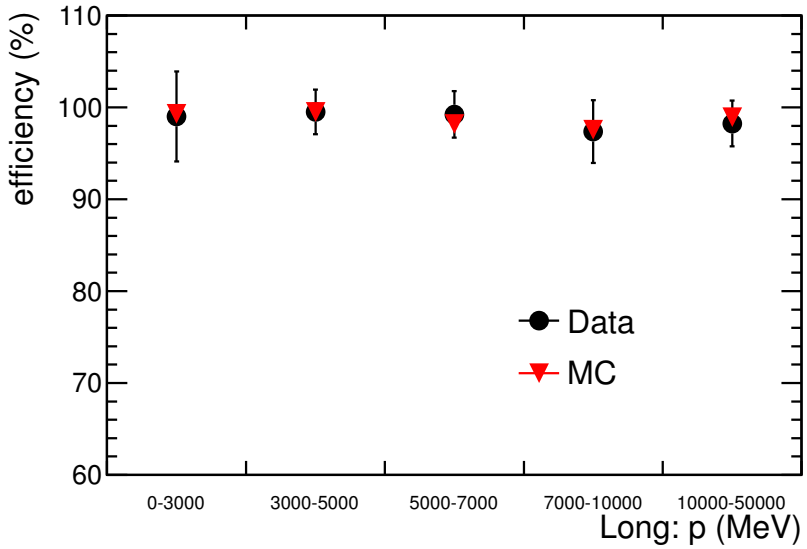

(a) 2009 samples

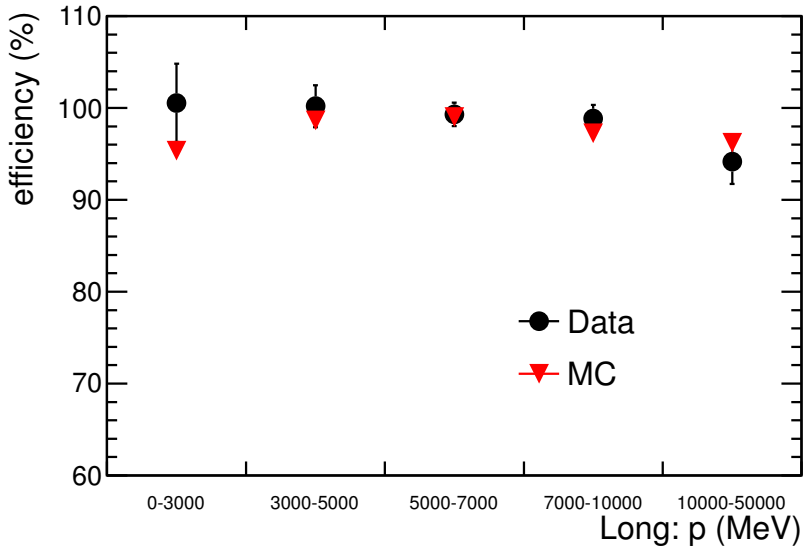

(b) 2010 samples

Figure 5.10: Tracking efficiency for Long tracks as a function of momentum.

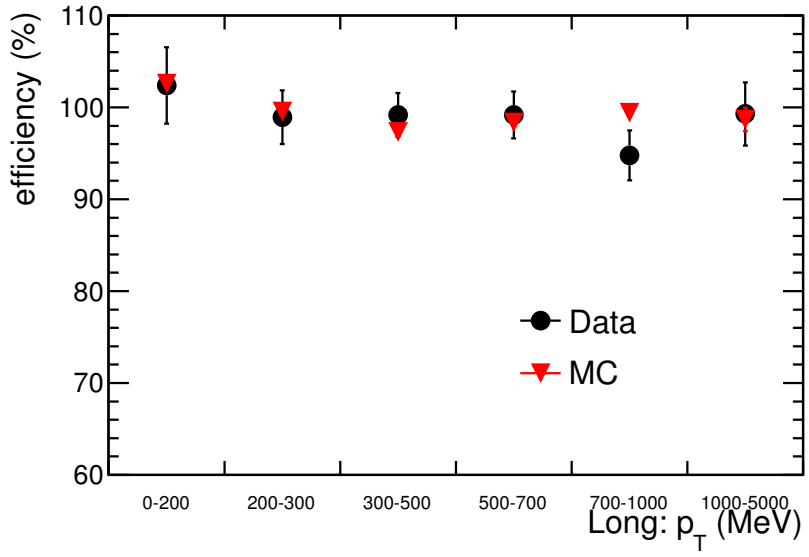

(a) 2009 samples

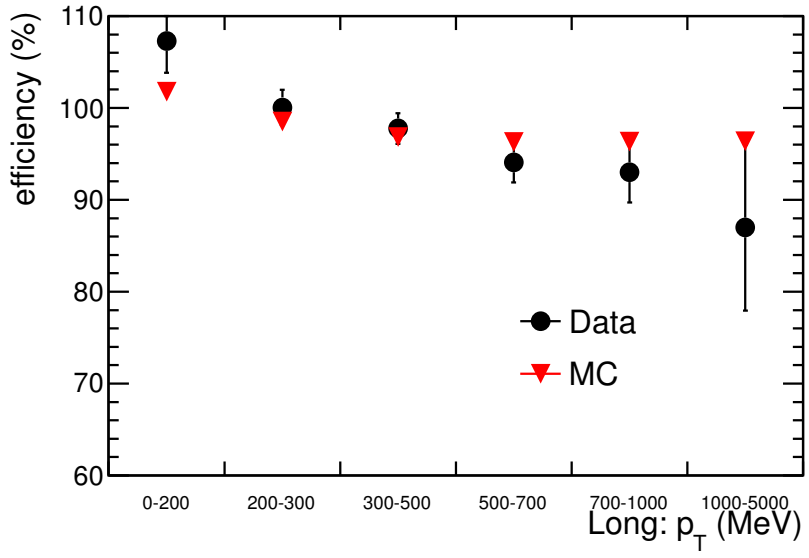

(b) 2010 samples

Figure 5.11: Tracking efficiency for Long tracks as a function of transverse momentum.

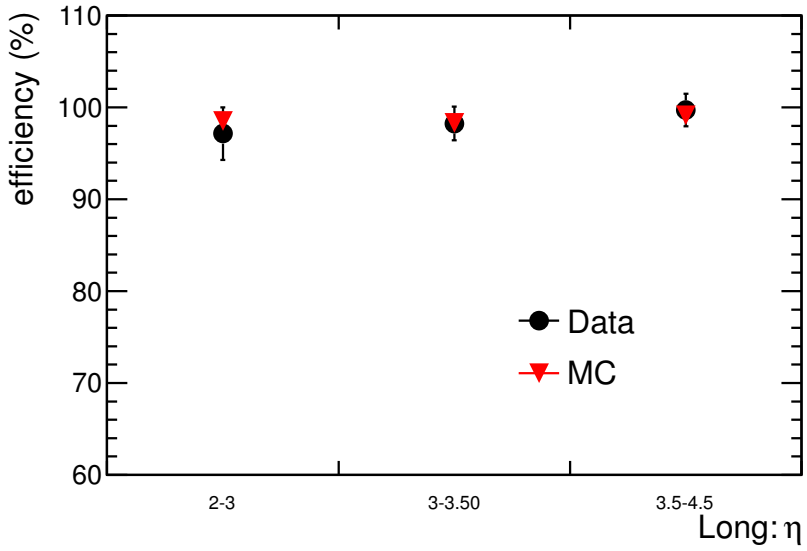

(a) 2009 samples

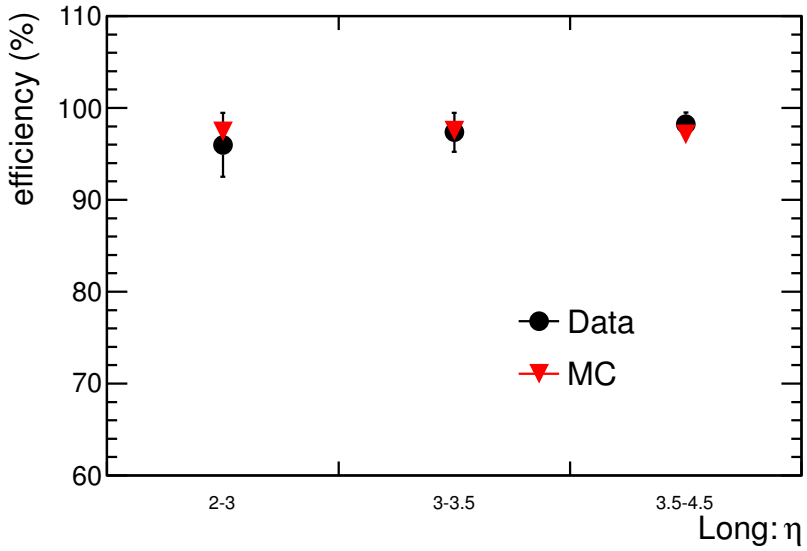

(b) 2010 samples

Figure 5.12: Tracking efficiency for Long tracks as a function of pseudo-rapidity.

5.6 Discussion

Traditionally, the tracking efficiency is calculated from MC simulations comparing the number of reconstructed tracks to the number of traversing MC particles using MC–truth information[24, 68]. The purpose of the analysis in this thesis is to evaluate whether a correction factor is needed to obtain the reconstruction efficiency in data. For this purpose only the ratio of the results between data and MC has an importance, as most of the uncertainties cancel out. To do this a new, data–driven, method is developed that allows to calculate the tracking efficiency in the T–Stations by comparing "found" tracks with Velo–Calo combination. The results presented in this chapter shows that the data and MC of the integrated sample agree to $1.00 \pm 0.01 \pm 0.02$ for 2009 data and to $1.01 \pm 0.01 \pm 0.02$ for 2010 data where the second error is a systematic effect on the ratio due to the method used.

These results are obtained with a new technique that is not dependent on any selection, and it is shown to be reliable between 300 and 5000 MeV/c for transverse momentum, or 3000 and 50000 MeV/c for momentum. A discrepancy smaller or around 2% is found in all bins, with the exception of the first bin in momentum and transverse momentum. In this bins the signal and background shapes are different compared to all other bins.

The Velo-Calo match method proposed in this chapter is applicable only for tracks in the calorimeter acceptance[4]. Moreover only the T-system tracking efficiency is considered: the Velo-Calo match method relies on the Vertex Locator information such that Velo tracking efficiency is not evaluated.

Although the method is developed to verify the relative efficiency between data and MC, the absolute efficiency values obtained here can be compared to the MC–truth based number from [24, 68]. A general agreement for high p and p_T values is observed, while the method developed here gives higher reconstruction efficiency for particles with low p and p_T. The difference could be due to the fact that in the data–driven method the presence of a calorimeter cluster is required.

In previous studies a dependence of the reconstruction efficiency on the multiplicity, i.e. the number of tracks in the event, was found[5] [53, 24]. In 2009 data and MC samples a maximum of 81 Velo tracks per event is found and in 2010 data and MC samples a maximum of 1109 is found. A study of the dependence of the results on the number of Velo tracks is carried out showing a good stability of the results within the uncertainty, as shown in Figs. 5.13 for 2009 (a) and 2010 (b) data respectively. This conclusion is confirmed by the MC–truth validation study where a good agreement was found both in case of a low occupancy and without any occupancy selection, see Sec. 5.4.

[4] A mechanical hole of 525.2 mm × 525.2 mm is left in the centre of the calorimeter and filled with shielding material [30]. All the tracks in this region are excluded with the Velo-Calo match method.

[5] Notice that a key difference is that in the presented method the tracking efficiency evaluation is based on the track parameters and not directly on the hits.

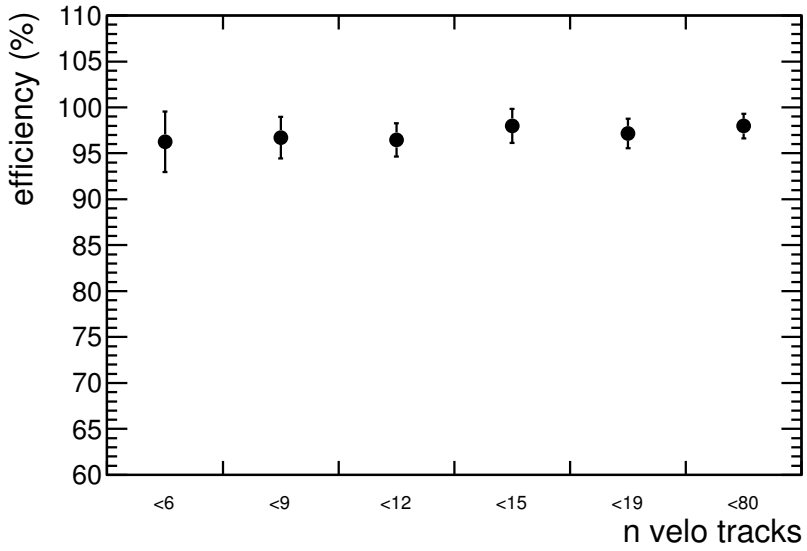

(a) 2009 data sample

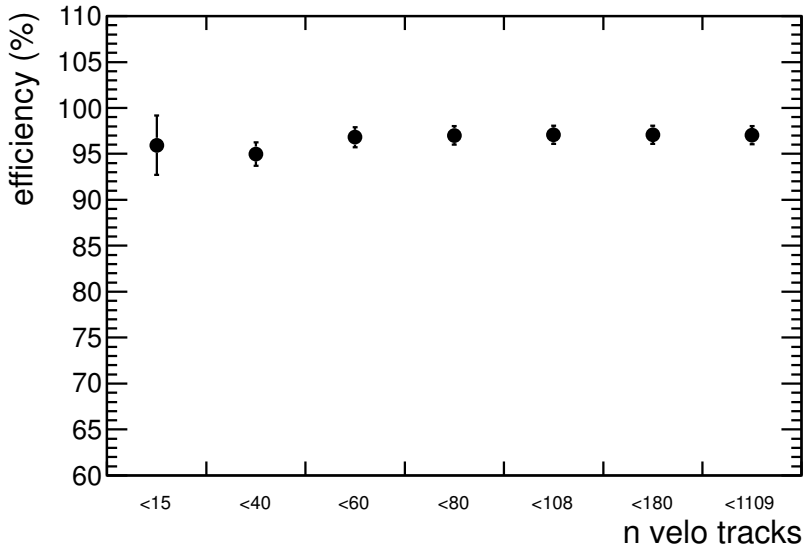

(b) 2010 data sample

Figure 5.13: Tracking Efficiency in bins of occupancy.

Sixth Chapter

The measurement of the fragmentation fraction ratio f_s/f_d

I hear and I forget. I see and I remember. I do and I understand.
Confucius

6.1 Introduction

This chapter is devoted to the measurement of the f_s/f_d branching fraction ratio through purely hadronic decays. The measurement of the branching ratio of the rare decay $B_s^0 \to \mu^\pm\mu^\mp$ is the prime example where knowledge on f_s/f_d is crucial to reach high sensitivity in the search for New Physics [70], as will be presented in the next chapter. This ratio can be determined by measuring the relative abundance of a B_s^0 decay with respect to a B^0 decay, provided that the ratio of branching ratios is known, as discussed in chapter 1.

The relative abundance of the three tree decay modes $B^0 \to D^-K^+$, $B^0 \to D^-\pi^+$ and $B_s^0 \to D_s^-\pi^+$ presented in this chapter are obtained analysing 35 pb^{-1} of data collected with the LHCb detector in the 2010 running period. From these, the relative branching ratio of $B^0 \to D^-K^+$ with respect to $B^0 \to D^-\pi^+$ is determined, resulting in the current world best measurement[1], and two new measurements of the fragmentation fraction f_s/f_d.

For the first f_s/f_d measurement, the two decay channels $B^0 \to D^-K^+$ and $B_s^0 \to D_s^-\pi^+$ are dominated by contributions from colour–allowed tree–diagram amplitudes and the ratio of branching ratios is therefore theoretically well understood in the factorisation framework. For the second f_s/f_d measurement, the ratio $BR(B_s^0 \to D_s^-\pi^+)/BR(B^0 \to D^-\pi^+)$ suffers from additional theoretical uncertainties due to contributions from the W–exchange diagram, see chapter 1. The ratio $BR(B_s^0 \to D_s^-\pi^+)/BR(B^0 \to D^-K^+)$ is therefore theoretically cleaner, but suffers from a larger statistical uncertainty due to the smaller branching fraction of $B^0 \to D^-K^+$.

[1] The previous best measurement was from the Belle experiment [1]

6.2 Event selection

The three decay modes, $B^0 \to D^-(K^+\pi^-\pi^-)\pi^+$, $B^0 \to D^-(K^+\pi^-\pi^-)K^+$ and $B_s^0 \to D_s^-(K^+K^-\pi^-)\pi^+$, are almost topologically identical and therefore can be selected using identical event selection, thus minimising efficiency differences between the modes[2].

The lifetime of the $D_s^\pm$ and $D^\pm$ are about 0.5 ps and 1.0 ps, respectively. This difference implies that any cut on the D flight distance or on the distance of closest approach of the D daughter particles to the primary vertex (also referred to as impact parameter, IP) will result in a different efficiency for the B^0 and B_s^0 decay modes. Therefore, no such criterion is imposed in the trigger or selection of these events.

The reconstruction plus acceptance efficiencies are computed on large samples of fully simulated $B^0 \to D^-\pi^+$, $B^0 \to D^-K^+$, $B_s^0 \to D_s^-\pi^+$ and $B_s^0 \to D_s^\pm K^\mp$ events and amount to $22.80 \pm 0.07\%$, $22.16 \pm 0.07\%$, $21.85 \pm 0.03\%$ and $21.40 \pm 0.07\%$, respectively. The $B_s^0 \to D_s^\pm K^\mp$ events are only included in the study of the efficiency, using simulated events, and are not further considered in the analysis of the 2010 data. The analysis of $B_s^0 \to D_s^\pm K^\mp$ events with the 2011 data will be presented in chapter 8.

Small differences in the reconstruction efficiency for final states with different numbers of pions and kaons are expected since the kaon lifetime is smaller than the pion lifetime, implying more kaon tracks lost due to decay in flight. Hence the efficiency depends on momentum, and the difference is more pronounced at low momentum.

The differences observed in MC samples are then used to correct the ratio of observed event yields. Three configurations are relevant for this analysis:

- **$BR(B^0 \to D^-K^+)$ measurement using $B^0 \to D^-\pi^+$ vs $B^0 \to D^-K^+$**: the main efficiency difference between these two decay channels is due to the pion or kaon, the "bachelor particle", that has to be matched with the D–meson to reconstruct the B–meson. The momentum spectrum of the bachelor particles in the B^0 and corresponding B_s^0 pairings is very similar, and therefore the two efficiency ratios $\epsilon(B^0 \to D^-\pi^+)/\epsilon(B^0 \to D^-K^+)$ and $\epsilon(B_s^0 \to D_s^-\pi^+)/\epsilon(B_s^0 \to D_s^\pm K^\mp)$ are averaged, giving a final correction factor of $\epsilon_1 = 1.025 \pm 0.003$;

- **f_s/f_d measurement using $B^0 \to D^-K^+$ vs $B_s^0 \to D_s^-\pi^+$**: the main difference between the two decay channels is the bachelor particle. From the ratio of efficiencies a correction factor of $\epsilon_2 = 1.014 \pm 0.004$ is obtained;

- **f_s/f_d measurement using $B^0 \to D^-\pi^+$ vs $B_s^0 \to D_s^-\pi^+$**: the main difference between the two decay channels is the total number of pions and kaons in the final state. Here the average from $\epsilon(B^0 \to D^-\pi^+)/\epsilon(B_s^0 \to D_s^-\pi^+)$ and $\epsilon(B^0 \to D^-K^+)/\epsilon(B_s^0 \to D_s^\pm K^\mp)$ is used to evaluate the correction factor of $\epsilon_3 = 1.039 \pm 0.003$ is obtained.

[2]The charge conjugate modes are implied throughout.

Trigger

There are three distinct layers of the trigger to consider: the L0, HLT1, and HLT2. In all three layers of the trigger, events are distinguished as being Triggered On Signal (TOS) or Triggered Independently of Signal (TIS), see Sec. 2.5 for more details. Since TIS events did not require the signal to be selected, their trigger efficiency is by definition identical for all decay modes; all such events are used in the fit. By contrast TOS triggered events may potentially have a different signal efficiency for the different modes and therefore only those TOS events corresponding to triggers which were designed to have the same efficiency across the different modes being fitted for are used, i.e. L0global TIS or L0Hadron TOS.

Events are selected at L0 with a hadron with high $E_T > 3.6$ GeV in the calorimeter. Subsequently, events are selected according to the HLT trigger decision where first a track with high transverse momentum (p_T) and with a good χ^2 per degree of freedom (χ^2/ndof) is selected, well displaced from the primary interaction point. This is followed by a topological trigger selecting a 2, 3, or 4–track secondary vertex with a high sum of the p_T of the tracks, and significant displacement from the primary interaction. Instead, for the first 3 pb^{-1}, a two–track displaced vertex trigger was used at the first HLT stage.

In principle, the TIS-TOS classification of triggers allows a data-driven way of extracting trigger efficiencies, but in practice this is impossible as there are not enough TIS events in the data taken in 2010. Hence all efficiencies are estimated using simulated events. The L0 efficiencies are found to be very similar for all four decay modes under analysis, but the decay channels with a kaon bachelor track tend to have significantly higher efficiencies than those where the bachelor particle is a pion. It seems like the bachelor particle contributes most to the overall L0 efficiency, and that kaons have a higher efficiency than pions at L0. This results in a 2% effect, assigned as a systematic uncertainty in the final calculations. A precise understanding of this effect is impossible because of the limited sample of simulated events available. On the other hand the HLT1 and HLT2 efficiencies show a significant difference between the B_s^0 and B^0 modes, although they are equal within each B–flavour separately.

When taking all trigger paths into account, an overall relative correction of 0.95 ± 0.020 is applied for B^0 modes with respect to B_s^0 modes. The two B^0 modes have equal trigger efficiencies, as expected, and no correction factor is applied for the relative B^0 yields.

Stripping

After the trigger stage, a loose selection, named "stripping", is performed to reduce the number of events for offline analysis. The same stripping line is used for all decay channels under study to avoid any differences.

The stripping selection is based on requirements for final state tracks and for B and D vertices. The range of invariant masses for D and B mesons is chosen wide enough to cover both B_s^0 and B^0 as well as D^- and D_s^- decay modes.

The full list of selection criteria applied at the stripping stage is given in Tab. 6.1. In addition, only events with a total number of long tracks not exceeding 180 are accepted. For the events that satisfy this requirement, $D_{(s)}$ candidates are built from any triplet of charged

Table 6.1: The stripping selection cuts for the $B^0_{(s)} \to D^-_{(s)} h^+$ channels. The "Inv. mass" cuts refer to mass windows opened around the nominal D or B mass. Notice that IPχ^2 stands for the impact parameter χ^2 , DIRA for the cosine of angle between momentum of particle and direction of flight from PV to decay vertex, and DOCA for distance of closest approach.

Cut Type	Parameter	Value
Global Event Cut	Number of long tracks in the event	≤ 180
D selection	χ^2/ndf for daughter tracks	< 5
	p_T for daughter tracks	> 250 MeV/c
	p for daughter tracks	> 2000 MeV/c
	IPχ^2 for daughter tracks (all)	> 4
	IPχ^2 for daughter tracks (highest)	> 40
	Inv. mass for D daughter combination	± 110 MeV/c^2
	Inv. mass for D after vertex fit	± 100 MeV/c^2
	D vertex fit χ^2/ndf	< 12
	p_T for D	> 1500 MeV/c
	D DIRA	> 0.9
	DOCA between D daughter tracks	< 1.5 mm
Bachelor selection	bachelor p_T	> 500 MeV/c
	bachelor p_T	> 500 MeV/c
	bachelor p	> 5000 MeV/c
	bachelor IPχ^2	> 16
Bselection	B vertex fit χ^2/ndf	< 12
	B IPχ^2	< 25
	B proper time	> 0.2 ps
	B DIRA	> 0.9998
	Inv. mass for B daughter combination	± 500 MeV/c^2

tracks (for all the mass hypothesis combinations) and then the $D_{(s)}$ candidate is combined with the bachelor track to form the neutral $B_{(s)}$ candidate. Notice that no particle identification requirements are applied at the stripping stage.

The efficiency of the stripping selection is evaluated on simulated events for the different decay modes with respect to reconstructable events passing the TOS trigger chain. The efficiencies for $B^0 \to D^-\pi^+$ and $B^0 \to D^-K^+$ decays are found to be $75.6 \pm 0.8\%$ and $76.6 \pm 0.8\%$, while those for $B^0_s \to D^-_s\pi^+$ and $B^0_s \to D^\pm_s K^\mp$ are found to be $75.5 \pm 0.3\%$ and $75.6 \pm 0.8\%$. As expected from the choice of variables, the efficiencies are in agreement for all the four channels and no correction factor is therefore assigned in the final calculation of the relative yields.

Multivariate analysis selection

The power of a selection to distinguish signal from background can be optimised by combining the information provided by each of the variables used in the event selection, instead of applying independent cuts on each variable [71]. The technique to take full advantage of the correlations between the discriminating variables is generally referred to as a Multivariate Analysis (MVA). The TMVA software package [72] is used to study the various multivariate methods available, in particular the "Fisher Discriminant" and "Boosted Decision Tree" (BDT).

The linear discriminant (Fisher Discriminant [72]) analysis produces a linear combination of the input variables such that signal and background are separated as much as possible, and events of the same class (signal or background) are grouped. For better performance, a gaussianisation[3] of the input variables is performed before building the Fisher discriminant. In the text and the figures this technique is referred to as "Fisher Gauss".

Secondly, a decision tree is tried, which is a binary tree structured classifier [72, 73]. Successive decision nodes are used to categorise the events out of the sample as either signal or background. Each node uses only a single discriminating variable to decide whether the event is signal–like ("goes right") or background–like ("goes left"). This forms a tree–like structure with "baskets" at the end (leave nodes), such that an event is classified as either signal or background according to whether the basket where it ends up has been classified as signal or background during the training. The training of a decision tree is the process to define the "cut criteria" for each node. The training starts with the root node. Here the full training event sample is taken and the variable and corresponding cut value is selected to have the best separation between signal and background at this stage. Using this cut criterion, the sample is then divided into two sub–samples, a signal–like (right) and a background–like (left) sample. Two new nodes are then created for each of the two sub–samples and they are constructed using the same mechanism as described for the root node. The division is stopped once a certain node has reached either a minimum number of events, or a minimum or maximum signal purity. These leave nodes are then called "signal" or "background" according to whether they contain more signal or background events from the training samples.

The boosting of a decision tree extends this concept from one tree to several trees, forming a so–called forest. The idea behind the boosting is, that signal events from the training sample that end up in a background node (and vice versa) are given a larger weight than events that are in the correct leave node. This results in a reweighted training event sample, with which then a new decision tree can be developed. The boosting can be applied several times (typically 100–500 times) and one ends up with a set of decision trees, the forest. Several boosting methods are available [72] and here the "gradient" boost method is used, as this method is the least sensitive to over–training[4]. In the text and the figures this technique

[3] The term "gaussianisation" is used to refer to the transformation applied to the variables to transform their distribution into a gaussian shape. More details how this procedure is performed can be found in [72].

[4] Over–training occurs when too many model parameters of an algorithm are adjusted to too few data points, and leads to a seeming increase in the classification performance over the objectively achievable one.

will be referred to as "BDTG".

MVA methods are based on machine learning techniques: a training sample is used to build the multivariate variable and subsequently an independent sample is used to evaluate the performance. In all cases the final selection is applied by cutting on the single variable created in the optimisation procedure, typically known as the "response" of the MVA.

The MVA analysis is trained on separate signal and background samples. The signal is described by a simulated event sample of $B^0 \to D^-\pi^+$ decays, representing all $B^0_{(s)} \to D^-_{(s)}h$ decay channels, whereas the background is taken from the sidebands in real data. The performance of the multivariate analysis methods, and the optimal cut value of the multivariate selection variable, are based on a training sample corresponding to a luminosity of 2 pb^{-1}.

Fig. 6.1 shows the distribution for the variables used in the multivariate analysis for signal and background.

The selection is optimised to reject the combinatorial background only, since partially reconstructed backgrounds have a kinematics similar to the signal. The agreement between simulated events and real data of the $B^0 \to D^-\pi^+$ sample after the selection is shown in Fig. 6.2. Note that a worse agreement between data and simulation would lead to a sub–optimal cut in the selection, but it would not bias the final result.

The MVA selection performances are evaluated by computing the signal significance in the usual way, $S/\sqrt{S+B}$. Although the optimisation uses $B^0 \to D^-\pi^+$ decay events, it is optimised for the Cabibbo–suppressed modes and the figure of merit is the significance:

$$\text{Sig}_{DK} = \frac{S_{D\pi}/20}{\sqrt{S_{D\pi}/20 + B}} \tag{6.1}$$

The factor 1/20 has been chosen as a compromise to optimise for both $B^0 \to D^-K^+$ and $B^0_s \to D^-_s K^+$. The former decay is suppressed by a factor $\lambda^2/(1-\lambda^2) = (V_{us}/V_{ud})^2$, while the latter has a further reduction due to the f_s/f_d factor.

The BDTG variable is peaked at -1 for background and at +1 for signal. Such a response is inconvenient for the use in subsequent analysis steps, and therefore the BDTG variable is transformed by an inverse sigmoid function, $f(x) = 1/(1+e^{-x})$. Subsequently, the results of both the BDTG and the Fisher Gauss procedures are transformed to the range $[0,1]$ to facilitate direct comparison.

In Fig. 6.3 (a), the performance of the three different event selections, based on BDTG, Fisher Gauss and rectangular cuts (for the latest see next section), are compared. The significance of two MVA methods are compared as a function of the different cut value on the output variable. The Receiver Operating Characteristic (ROC) curve is shown in Fig. 6.3 (b). This curve is obtained by evaluating the number of signal and background events from the fit in the signal region for different cut values on the MVA response.

Both MVA methods offer an improvement of the signal significance with respect to the rectangular cut selection. The Fisher Gauss method performs 15% better, and the BDTG method 25% better, as compared to the event selection based on rectangular cuts.

For the optimum point of the BDTG selection, corresponding to a cut on the response value of 0.65, the selection efficiencies for $B^0 \to D^-\pi^+$ and $B^0 \to D^-K^+$ decays with respect

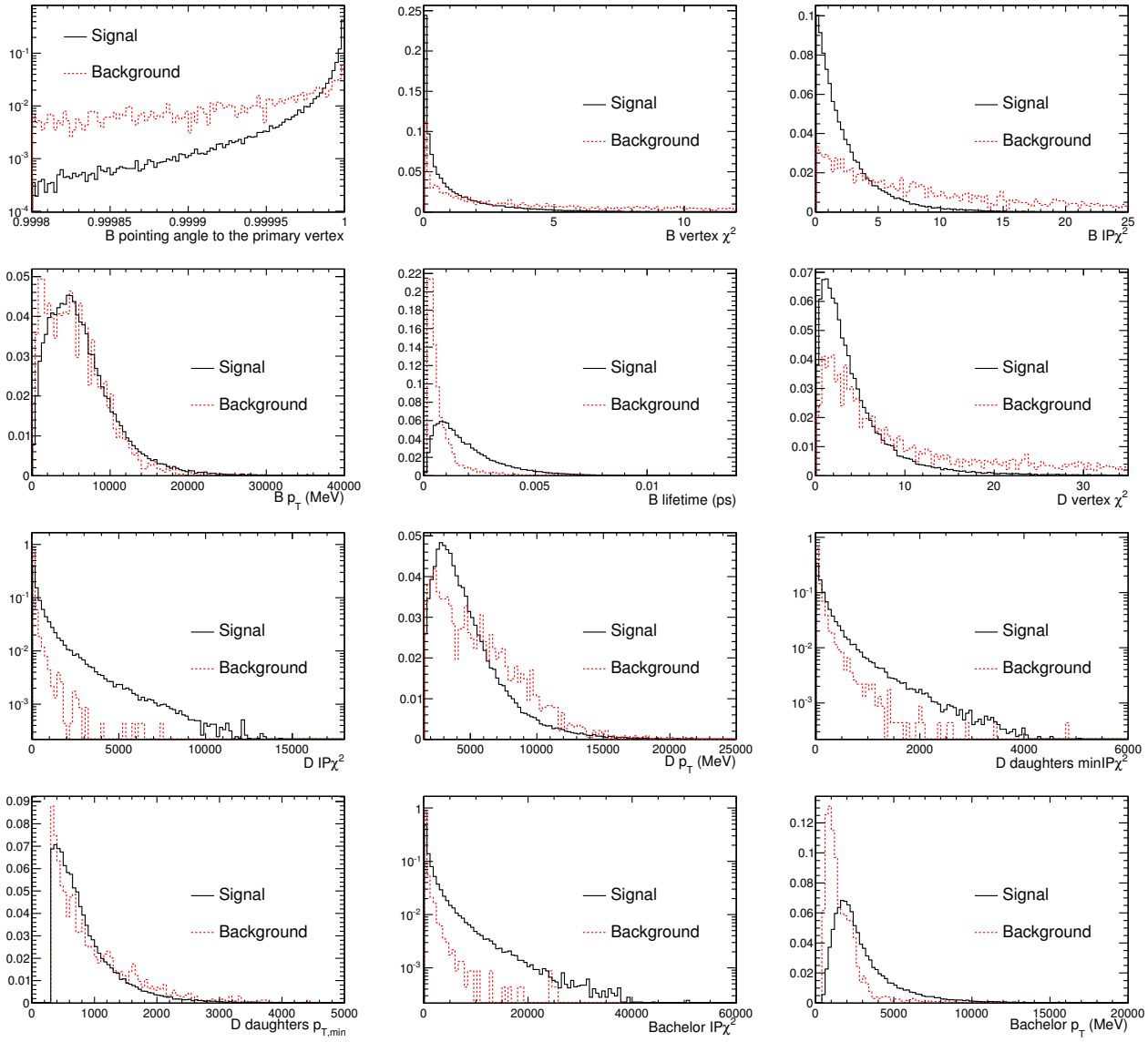

Figure 6.1: MVA input variables. Signal is $B^0 \to D^-\pi^+$ simulation, whereas background refers to the data in the mass sidebands. The number of both signal and background events is normalized to unity.

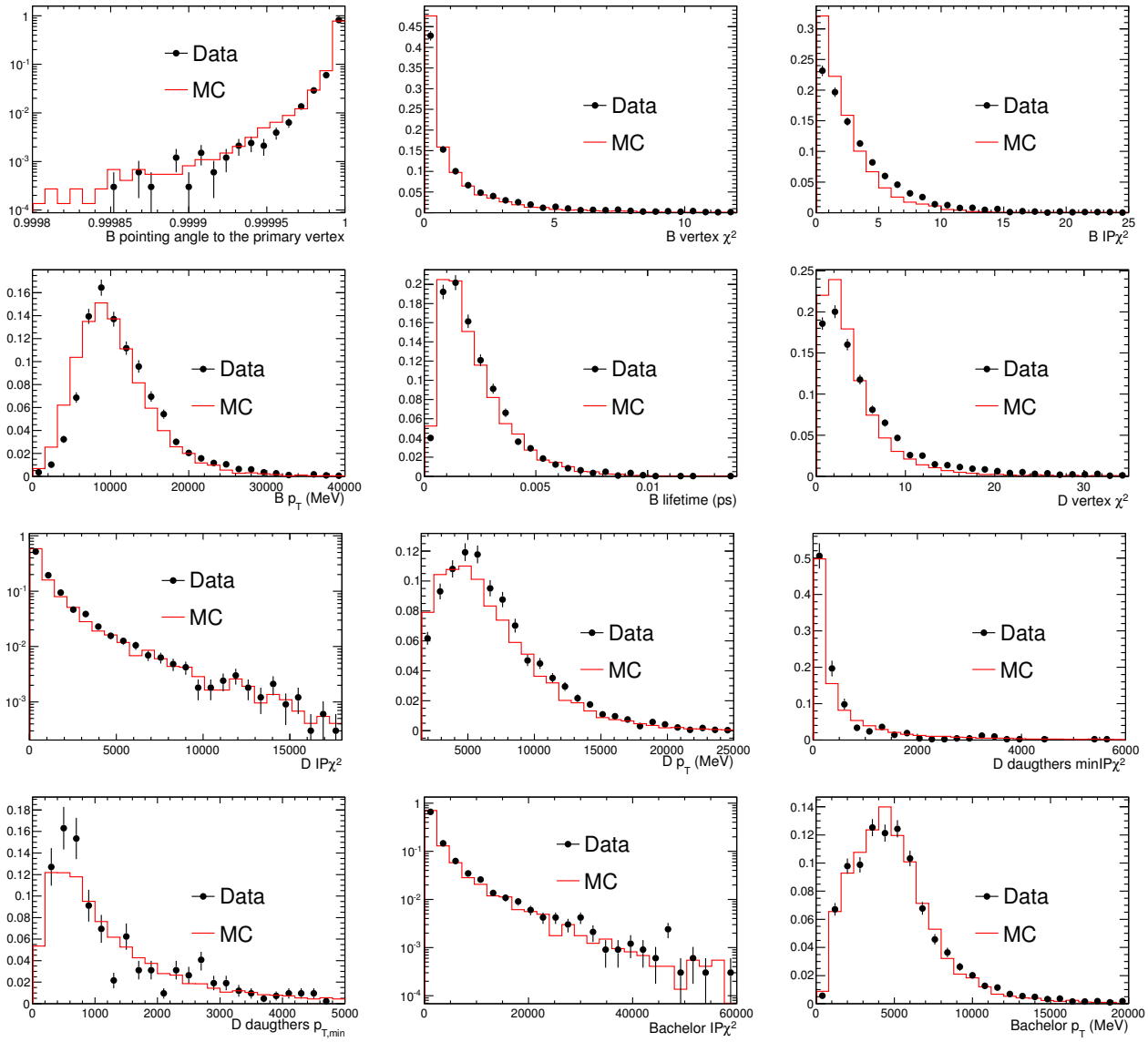

Figure 6.2: Data–simulation ($B^0 \to D^-\pi^+$ sample) comparison for most relevant variables. Data and simulation events events are selected applying the BDTG response and the trigger requirements and a mass window of 5200–5360 MeV/c^2. The cuts applied affected the MC–shapes, so no comparison with the MC–signal distribution in Fig. 6.1 is possible.

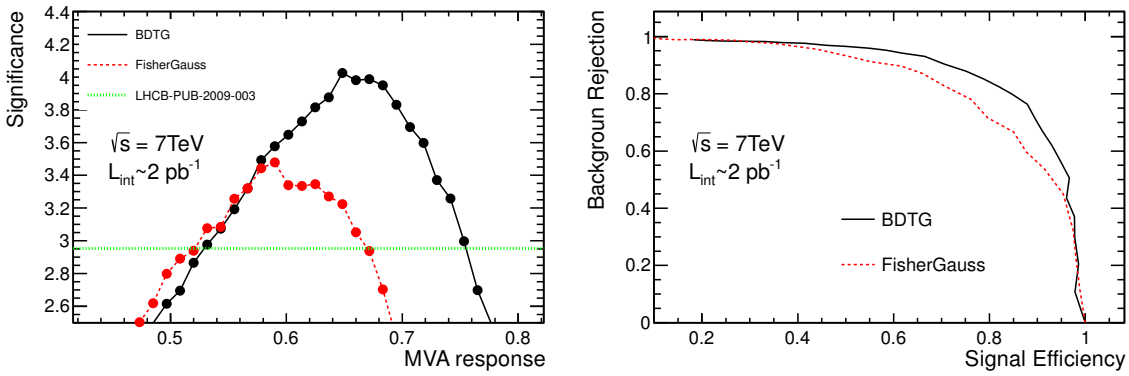

(a) (b)

Figure 6.3: Comparison of the BDTG, Fisher Gauss, and rectangular cut selections (from [74]) for the suppressed mode signal significance (a). Background rejection versus signal efficiency (also know as "ROC curve") for the two MVA methods (b).

to reconstructable events passing the TOS[5] trigger selection and the stripping selection are found to be $75.5 \pm 0.8\%$ and $76.3 \pm 0.8\%$. The efficiencies for $B_s^0 \to D_s^- \pi^+$ and $B_s^0 \to D_s^\pm K^\mp$ are found to be $75.2 \pm 0.4\%$ and $75.4 \pm 0.8\%$. As expected from the choice of discriminating variables, the efficiencies are in agreement for all channels and no correction factor is therefore assigned for this selection step in the final yield ratio evaluation.

Rectangular cut selection

As a cross check to the MVA selection also straight–forward rectangular cuts are applied to verify the stability of the final ratio of event yields. Rectangular cut selections for the modes in question have been studied extensively in [74, 75, 76, 77]. Only geometrical and kinematical, and no particle identification cuts are applied.

Since this selection was optimised using an early version of the LHCb simulation software it is probably suboptimal, but it is well suited as a cross–check of the multivariate selections described in the previous subsection.

The list of cuts proposed in [74] is reproduced in Tab. 6.2. The only change with respect to the original MC optimisation is the mass window around the D, which is increased to account for the worse mass resolution in real data, and additionally it is extended in the lower mass sideband to account for the radiative tails of the $D^\pm$ and $D_s^\pm$ mesons.

As with the trigger and stripping, the offline selection potentially has a different efficiency for B_s^0 and B^0 modes because of the different lifetime of the $D_s^\pm$ and $D^\pm$ mesons, and this is verified using simulated events. The selection efficiencies for $B^0 \to D^- \pi^+$ and $B^0 \to D^- K^+$ decays with respect to reconstructable events are found to be $32.7 \pm 0.2\%$ and $32.2 \pm 0.2\%$, while for $B_s^0 \to D_s^- \pi^+$ and $B_s^0 \to D_s^\pm K^\mp$ they are found to be $32.0 \pm 0.1\%$ and

[5] TOS, Triggered On Signal, is defined in chapter 2 Sec. 2.5

Table 6.2: Rectangular cuts for the channels $B^0_{(s)} \to D^{\pm}_{(s)} h^{\mp}$, where $h = \pi, K$.

All particle momenta	$> 2000\,\text{MeV}/c$
All particle IPχ^2	> 9
D daughter p_T	$> 300\,\text{MeV}/c$
D p_T	$> 2000\,\text{MeV}/c$
D IPχ^2	> 9
D vertex χ^2/ndf	< 15
D flight distance χ^2	> 100
D mass	$(1870, 1969)^{+24}_{-40}$
bachelor p_T	$> 500\,\text{MeV}/c$
B vertex χ^2/ndf	< 10
B IPχ^2	< 16
B flight distance χ^2	> 144
B $\cos\theta$	> 0.9999

$32.1 \pm 0.2\%$, therefore no correction is needed. The decay $B^0_s \to D^{\pm}_s K^{\mp}$ has only been used to study the relative selection efficiencies from simulation and is not further discussed in this chapter.

6.3 Yield extraction

Particle Identification

The data sample after event selection is subdivided into three subsets, depending on the mass of the D candidate and on the particle identification (PID) information of the bachelor particle, to obtain three samples for the decays $B^0 \to D^-\pi^+$, $B^0 \to D^-K^+$ and $B^0_s \to D^-_s\pi^+$.

The RICH detectors provide the probability for a particle to be a pion or a kaon expressed in terms of "delta log–likelihood", $DLL(K-\pi)$, as described in Sec. 2.4. The resulting efficiency and misidentification probability curves for the cut $DLL(K-\pi) > 5$ are shown in Fig. 6.4 (a) as this is the cut used to select the bachelor kaon and to distinguish the D_s from the D meson. The performance for selecting pions with $DLL(K-\pi) < 0$ is also shown. The full list of $DLL(K-\pi)$ cuts applied to select each decay channel is shown in Tab. 6.3.

This cut–based approach to the PID is preferred over using a simultaneous fit to the mass and PID distributions with the full PID likelihoods for the bachelors. The main motivation for this choice is that the simultaneous fit requires detailed knowledge of the mixture of pions, kaons and ghosts in the combinatorial background. The different components of the combinatorial background may also have different momentum distributions, which will affect their PID likelihood distribution. If these issues are not accounted for, the simultaneous

Table 6.3: $DLL(K-\pi)$ cuts applied to select the relevant decay channel.

Particle involved	$B^0 \to D^-\pi^+$ $DLL(K-\pi)$	$B^0 \to D^-K^+$ $DLL(K-\pi)$	$B_s^0 \to D_s^-\pi^+$ $DLL(K-\pi)$
π^+ or K^+ bachelor	<0	>5	<0
K^+ from $D^-_{(s)}$	>0	>0	>0
π^- from $D^-_{(s)}$	<10	<10	<10
K^- from D_s^-	–	–	>5

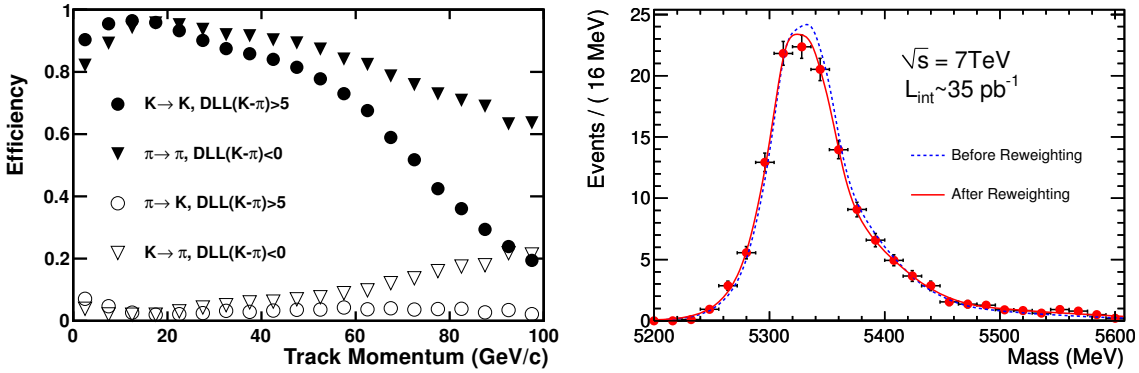

(a) (b)

Figure 6.4: Probability, as a function of momentum, to correctly identify (full symbols) a kaon or a pion when requiring DLL$(K-\pi)>5$ or DLL$(K-\pi)<0$, respectively. The corresponding probability to wrongly identify (open symbols) a pion as a kaon, or a kaon as a pion is also shown. The data are taken from a calibration sample of $D^* \to D(K\pi)\pi$ decays; the statistical uncertainties are smaller than the symbols (a). Invariant mass of $B^0 \to D^-\pi^+$ events with the bachelor misidentified as a $K^\mp$, for a PID cut of DLL$(K-\pi)>5$(b).

fit may become biased [78].

Signal under the correct mass hypothesis

The shape of the signal mass distribution is obtained from simulated events by convolution of the detector resolution and radiative effects of the B and D–meson decays. The radiated photons and resolution effects that are not reconstructed result in an asymmetric distortion of the mass distribution with a tail towards lower masses, described by a Crystal Ball (CB)

Table 6.4: The fitted values of parameters for the sum of two CB functions describing the signal shape of $B^0 \to D^-\pi^+$, $B^0 \to D^-K^+$ and $B_s^0 \to D_s^-\pi^+$. Both CB functions use the same mean value (m). The parameter Fract is the fraction of the first CB function.

	Parameter	$B^0 \to D^-\pi^+$	$B^0 \to D^-K^+$	$B_s^0 \to D_s^-\pi^+$
	m	5280.47 ± 0.06	5280.75 ± 0.06	5367.61 ± 0.04
	Fract	0.79 ± 0.02	0.73 ± 0.02	0.59 ± 0.02
Left CB	α_1	1.79 ± 0.02	1.82 ± 0.03	1.56 ± 0.01
	n_1	1.06 ± 0.02	1.09 ± 0.02	1.24 ± 0.01
	σ_1	14.22 ± 0.15	13.29 ± 0.16	12.99 ± 0.05
Right CB	α_2	-2.08 ± 0.04	-2.04 ± 0.04	-1.74 ± 0.07
	n_2	1.26 ± 0.08	1.48 ± 0.08	3.04 ± 0.37
	σ_2	26.46 ± 0.90	22.91 ± 0.80	18.95 ± 0.39

function:[6]

$$f(x,\alpha,n,m,\sigma) = N \cdot \begin{cases} e^{-\frac{(x-m)^2}{2\sigma^2}}, & \text{for } \frac{x-m}{\sigma} > \alpha \\ A \cdot \left(B - \frac{x-m}{\sigma}\right)^{-n}, & \text{for } \frac{x-m}{\sigma} \leq \alpha, \end{cases} \tag{6.2}$$

where $A = \left(\frac{n}{|\alpha|}\right)^n \cdot e^{-\frac{|\alpha|^2}{2}}$, $B = \frac{n}{\alpha} - |\alpha|$ and N is the normalisation factor. Here, x is the invariant mass, m is the mass mean value, σ is the mass resolution, α is the point where the shape changes from the Gaussian to the exponential tail, and n describes the size of the tail.

A second CB function with a tail oriented in the opposite direction describes non–Gaussian detector effects. Both CB functions use the same mean value. An example of these fit results is presented in Fig. 6.5 and the eight parameters are listed in Tab. 6.4 for the three decay modes.

Background

The various background contributions in the fit to the mass distributions are listed in Tab. 6.5. The contributions can be grouped into misidentified, combinatorial, and partially reconstructed backgrounds. A description of the main characteristics of each group is given in the next subsections.

Backgrounds from PID misidentification

The signal decays are also backgrounds to each other, in cases where one particle is misidentified. In such cases the mass shape of the misidentified events is distorted compared to the

[6]The Crystal Ball line shape is a Gaussian distribution with a power–law tail on the one side, [79, 80, 81].

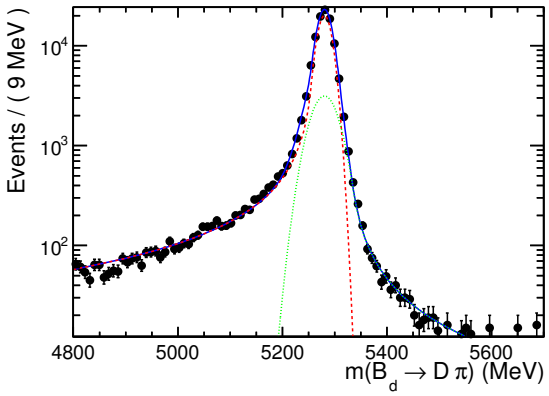

(a) $B^0 \to D^- \pi^+$

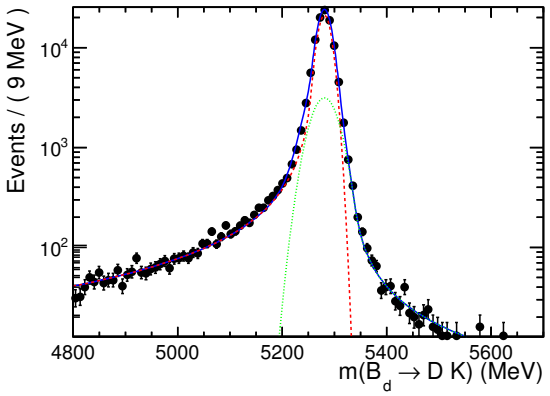

(b) $B^0 \to D^- K^+$

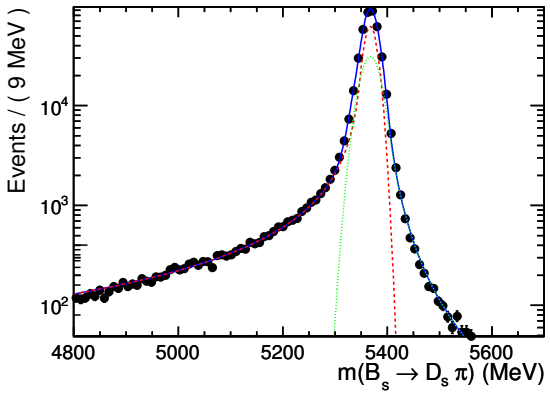

(c) $B_s^0 \to D_s^- \pi^+$

Figure 6.5: The invariant mass distributions obtained from the full Monte Carlo sample. The solid lines show the result of the fit to the sum of two CB functions. The contributions of individual CB functions are marked as dashed and dotted lines.

Table 6.5: The various background contributions in the fit to the mass distributions. For partially reconstructed backgrounds, a "missed" particle refers to a daughter particle in the background decay (for example $B^0 \to D^- \rho^+$ with $\rho^{\mp} \to \pi^{\mp}\pi^0$) which is not reconstructed when this decay is identified as one of the signal channels (for example $B^0 \to D^- \pi^+$).

Decay Mode	Backgrounds
$B^0 \to D^- \pi^+$	Combinatorial
	$B^0 \to D^{*-} \pi^+$, where the γ or π^0 from the D^* is missed
	$B^0 \to D^- \rho^+$, where the π^0 from the ρ is missed
$B^0 \to D^- K^+$	Combinatorial
	$B^0 \to D^- \pi^+$, where the π^+ is mis–identified as a K^+
	$B^0 \to D^{*-} K^+$, where the γ or π^0 from the D^* is missed
	$B^0 \to D^- \rho^+$, where the π^+ is mis–identified and the π^0 missed
$B_s^0 \to D_s^- \pi^+$	Combinatorial
	$B^0 \to D^- \pi^+$, where the π^+ is mis–identified
	$B_s^0 \to D_s^{*-} \pi^+$, where the γ or π^0 from the D_s^* is missed
	$B_s^0 \to D_s^- \rho^+$, where the π^0 from the ρ is missed
	$B_s^0 \to D_s^- (\pi\pi\pi)^+$, where two pions are missed
	$\Lambda_b^0 \to \Lambda_c^+ (pK^-\pi^+)\pi^-$ where the proton is misidentified as a kaon.

shape under the correct mass hypothesis due to two effects. Both the invariant mass distribution under the wrong mass hypothesis, and the misidentification probability depend on the momentum of the misidentified particle. Most prominently, this is the case for the Cabibbo–favoured $B^0 \to D^-\pi^+$ reconstructed as $B^0 \to D^-K^+$, where the bachelor pion is misidentified as well as for the $B^0 \to D^-\pi^+$ reconstructed as $B^0_s \to D^-_s\pi^+$, where one of the pions coming from the D is misidentified. The procedure to extract the shape and the number of misidentified $B^0 \to D^-\pi^+$ events under the $B^0 \to D^-K^+$ mass peak is described below. The same procedure is applied for the misidentified background in the $B^0_s \to D^-_s\pi^+$ fit.

- A clean sample of $B^0 \to D^-\pi^+$ events is obtained by requiring the bachelor particle to be a pion, $DLL(K-\pi)<0$.
- The mass distribution of this $B^0 \to D^-\pi^+$ sample is constructed, by assuming the kaon mass hypothesis for the bachelor particle.
- The efficiency of the DLL selection criterion is momentum dependent, and thus the momentum distribution of the pure $B^0 \to D^-\pi^+$ sample is corrected from the distortion due to the efficiency of the DLL cut applied in the previous step, see Fig. 6.4 (a).
- The $B^0 \to D^-K^+$ signal is selected by requiring the bachelor particle to be a kaon, $DLL(K-\pi)>5$. The performance of this cut, evaluated as a function of momentum using D^* decays, is also illustrated in Fig. 6.4 (a).
- This DLL selection criterion is again momentum dependent, and the resulting mass shape of the misidentified $B^0 \to D^-\pi^+$ events is reweighted according to the efficiency of the DLL cut applied in the previous step. The mass distribution before and after reweighting is shown in Fig. 6.4 (b).
- Finally, a PDF is constructed from this reweighted mass shape, which is used to describe the misidentified $B^0 \to D^-\pi^+$ background under the $B^0 \to D^-K^+$ signal.

Combinatorial background

The combinatorial background consists of events with random pion and kaon particles, forming a fake $D^\pm$ or $D^\pm_s$ decay. In addition, part of the combinatorial background originates from real, prompt, $D^\pm$ or $D^\pm_s$ mesons that combine with a random π or K into a fake B or B^0_s. The combinatorial background is modelled with a typical exponential shape, except in the case of $B^0 \to D^-K^+$ where the combinatorial background is a flat distribution, see Sec. 6.4.

Partially reconstructed background

Partially reconstructed backgrounds consist of all B decays with a missing final state particles, e.g. $B^0 \to D^{*-}\pi^+$. The full list of partially reconstructed backgrounds for each decay considered is shown in Tab. 6.5. These backgrounds are modelled with a non–parametric shape ("RooKeysPDF" [82]) obtained from simulated events, as shown in Figs. 6.6–6.9.

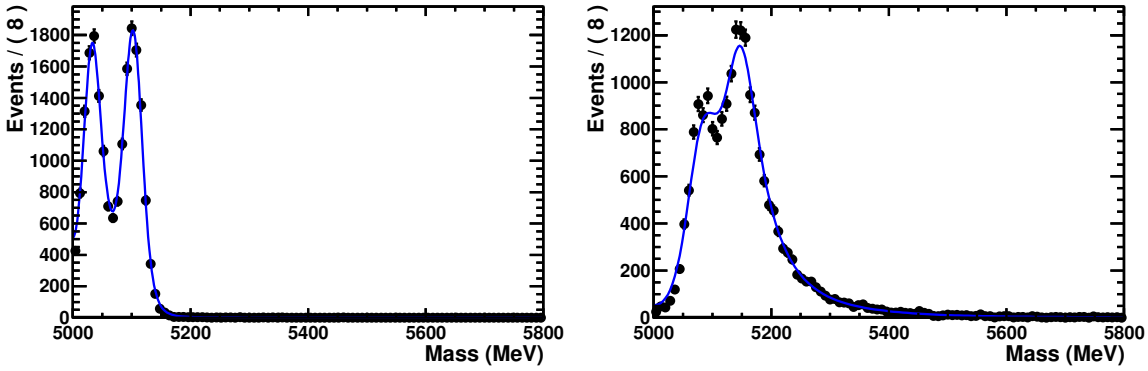

(a) (b)

Figure 6.6: $B^0 \to D^{*-}\pi^+$, $D^{*-} \to D^-\pi^0$ reconstructed B^0 mass shape (under the $\pi^\pm$ mass hypothesis (a), under the $K^\pm$ mass hypothesis (b) for the bachelor particle). The blue solid curve is the RooKeysPDF used to model them.

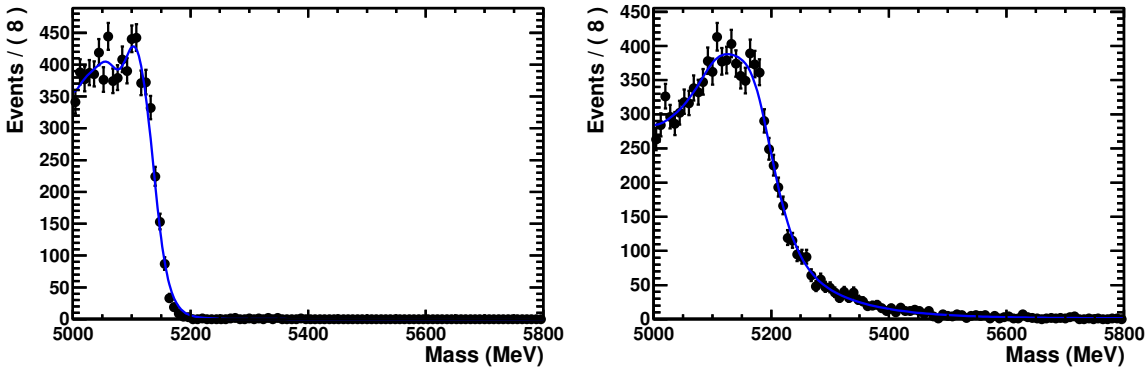

(a) (b)

Figure 6.7: $B^0 \to D^-\rho^+$, $\rho^+ \to \pi^+\pi^0$ reconstructed B^0 mass shape (under the $\pi^\pm$ mass hypothesis (a), under the $K^\pm$ mass hypothesis (b) for the bachelor particle). The blue solid curve is the RooKeysPDF used to model them.

6.4 Fit

In the fit of the three decay channels considered, the signal mass distribution is described with a double Crystal Ball function, as described in Sec. 6.3 with the values of some parameters, whenever possible, determined from data, while the others are fixed from the fit on the simulation signal samples[7]. The shapes of the partially reconstructed backgrounds are fully determined from simulated events. The reweighting procedure described in Sec. 6.3 is used to properly model the shape of each background with a misidentified pion. Details on the

[7] In particular for all the decays the α and n parameters are taken from the simulation fit result.

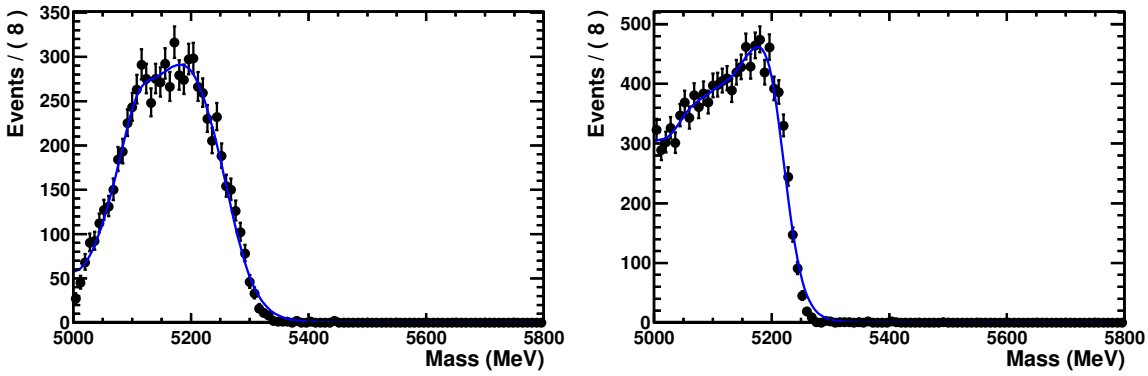

(a) (b)

Figure 6.8: $B_s^0 \to D_s^{*-}\pi^+$ (a), $B_s^0 \to D_s^-\rho^+$ (b) reconstructed B_s^0 mass shape under the $\pi^\pm$ mass hypothesis. The blue solid curve is the RooKeysPDF used to model them.

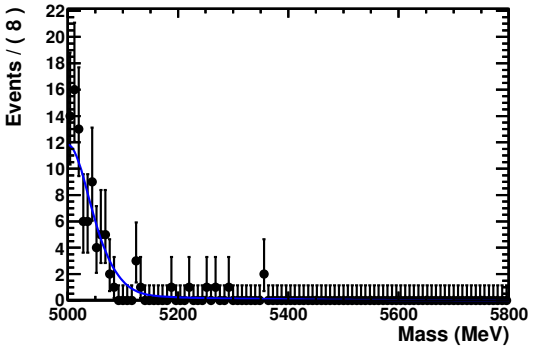

Figure 6.9: $B_s^0 \to D_s^-\pi^+\pi^+\pi^-$reconstructed B_s^0 mass shape under the $\pi^\pm$ mass hypothesis where two pions are not considered. The blue solid curve is the RooKeysPDF used to model them.

fit procedure for each signal decay is given in the next subsections, while the impact of the constraints used in the fit are discussed in the evaluation of the systematic uncertainties in Sec. 6.5.

$B^0 \to D^-K^+$

The backgrounds for the $B^0 \to D^-K^+$ channel arise from both pion misidentification and partially reconstructed backgrounds with a kaon as bachelor particle. Especially events from misidentified $B^0 \to D^-\pi^+$ decay are a sizable background due to the large branching ratio compared to the $B^0 \to D^-K^+$ decay channel. The mass shape for misidentified $B^0 \to D^-\pi^+$ events is derived with the procedure explained in Sec. 6.3. The same procedure was used for the partially reconstructed backgrounds that involved a misidentified bachelor

pion. Both the $B_s^0 \to D_s^- \pi^+$ and the $\Lambda_b \to \Lambda_c^- \pi^+$ backgrounds are negligible once the relevant PID cuts are applied. The combinatorial background is described with a flat distribution.

There are several free parameters in the fit, including the event yields of the different types of candidates: combinatorial, partially reconstructed background, reflections from misidentified backgrounds and signal events. The free parameters for the signal are the mean, m, and the relative fraction, Fract, of the two Crystal Ball functions.

The width, σ, of the Crystal Ball functions is fixed according to what is found in the fit of the $B^0 \to D^- \pi^+$ data. Since the widths from the fit on simulated events for $B^0 \to D^- \pi^+$ and $B^0 \to D^- K^+$ are different, see Tab. 6.4, a scaling factor is extracted from the simulation and it is applied in data to properly accommodate for the difference between the two channels. The results of the fit are summarised in Tab. 6.6 and shown in Fig. 6.10.

$B^0 \to D^- \pi^+$

The reflection from the $B^0 \to D^- K^+$ decay channel is negligible, and therefore ignored in the fit, because this decay is Cabibbo suppressed and most remaining events are rejected by the applied PID cut. The combinatorial background is described with an exponential function which accounts for both the prompt charm and the background from fake D–combinations. The fit for the $B^0 \to D^- \pi^+$ has the same free parameters of the $B^0 \to D^- K^+$ and in addition the width of the signal mass peak is left free. The results of the fit are summarised in Tab. 6.7 and shown in Fig. 6.11.

$B_s^0 \to D_s^- \pi^+$

The combinatorial background is described with an exponential function and the partially reconstructed background, as well as the $\Lambda_b \to \Lambda_c \pi$ background, are described with templates extracted from full simulations. The shape of the misidentified $B^0 \to D^- \pi^+$ background is extracted from data with the technique described in Sec. 6.3. Since the shape is similar to the signal, it is not possible to extract the yield from the fit. For the optimal cut of the BDTG, about 45 $B^0 \to D^- \pi^+$ background events, reconstructed as $B_s^0 \to D_s^- \pi^+$, are expected, see Sec. 6.4. This background will peak exactly under the signal, and therefore a Gaussian constraint is applied for the yield of this background. The mean of this Gaussian is 45 and the sigma is conservatively assumed to be 20 events. The two partially reconstructed background components for the $B_s^0 \to D_s^- \pi^+$ signal sample are $B_s^0 \to D_s^- \rho^+$ and $B_s^0 \to D_s^{*-} \pi^+$. Due to the large correlations between the $B_s^0 \to D_s^- \rho^+$ and $B_s^0 \to D_s^{*-} \pi^+$ contributions, it is not possible to fit both the components separately. A Gaussian constraint is used for the fraction of these two backgrounds. The relative yield is assumed to be the same as in the B^0 case, using $BR(B^0 \to D^- \rho^+)/BR(B^0 \to D^{*-} \pi^+) = BR(B_s^0 \to D_s^- \rho^+)/BR(B_s^0 \to D_s^{*-} \pi^+)$, while the uncertainty from $SU(3)$–breaking is conservatively assumed to be to 20%. The widths of the two CB functions for the signal are obtained from the measured widths from the $B^0 \to D^- \pi^+$ fit and scaled to the appropriate value for $B_s^0 \to D_s^- \pi^+$ decays, using simulation.

The results of the fit are summarised in Tab. 6.8 and shown in Fig. 6.12

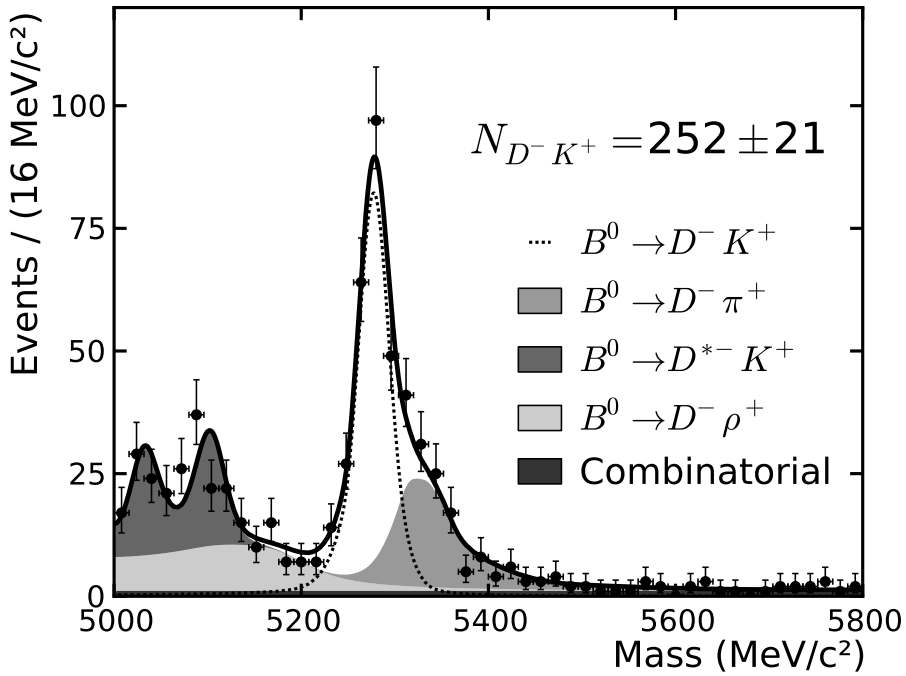

Figure 6.10: $B^0 \to D^- K^+$ fit on data for the optimal value of the BDTG variable.

Table 6.6: Fitted values of the parameters for $B^0 \to D^- K^+$ signal. The N_i parameters are the yield of the signal and the different backgrounds. The parameter Fract is the fraction of the two CB distributions used to parametrised the signal. The m parameter is the common mean of the two CB functions.

Parameter	Fitted value	Uncertainty
$N_{B^0 \to D^- K^+}$	252	21
Fract	0.38	0.17
m (MeV/c^2)	5277.5	1.8
N_{Comb}	58	14
$N_{D\pi}$	131	19
$N_{D\rho}$	125	24
N_{D^*K}	123	19

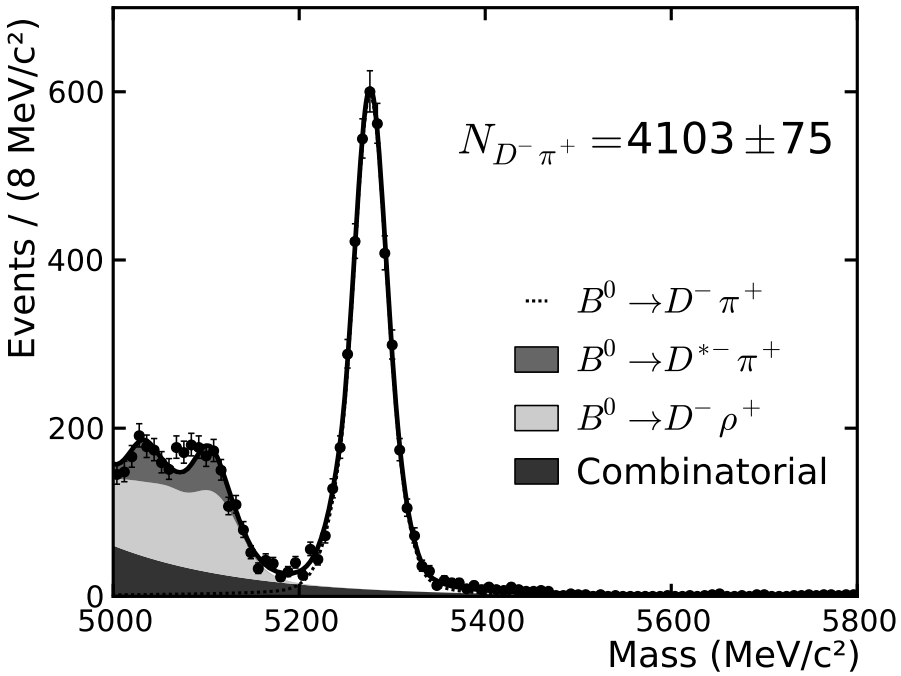

Figure 6.11: $B^0 \to D^-\pi^+$ fit on data for the optimal value of the BDTG variable.

Table 6.7: Fitted values of parameters for $B^0 \to D^-\pi^+$ signal. The N_i parameters are the yield of the signal and the different backgrounds. The parameter Fract is the fraction of the two CB distributions used to parametrised the signal. The m parameter is the common mean of the two CB functions. The two sigmas are denominated σ_1 and σ_2. The value a_1 is the exponent of the combinatorial background shape.

Parameter	Fitted value	Uncertainty
$N_{B^0\to D^-\pi^+}$	4103	75
Fract	0.58	0.06
m (MeV/c^2)	5276.3	0.4
σ_1 (MeV/c^2)	15.1	1.0
σ_2 (MeV/c^2)	27.1	1.2
N_{Comb}	1037	148
a_1	-7.2×10^{-3}	0.5×10^{-3}
$N_{D\rho}$	1631	198
$N_{D^*\pi}$	535	137

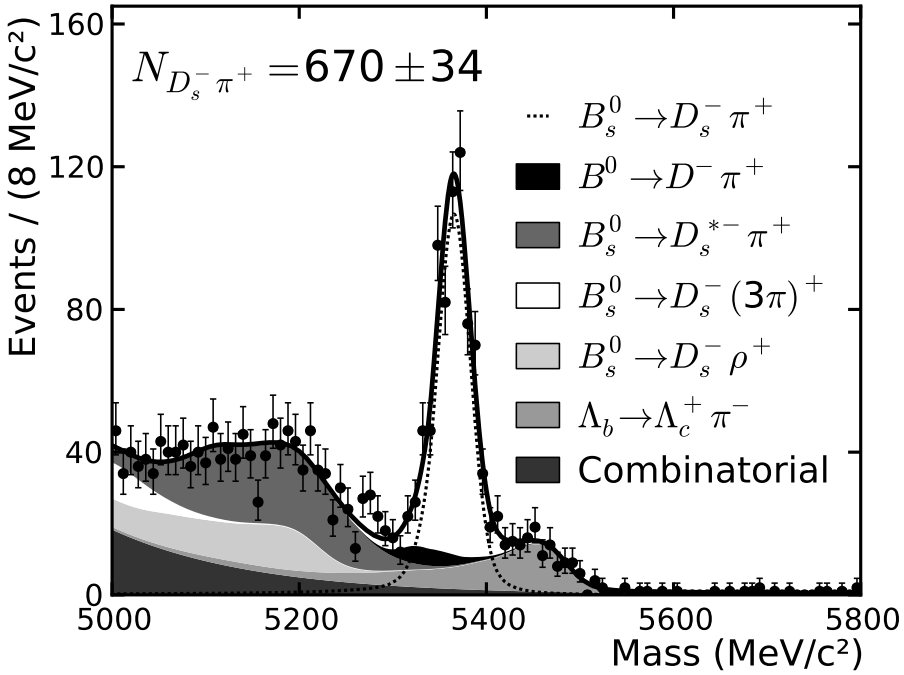

Figure 6.12: $B_s^0 \to D_s^-\pi^+$ fit on data for the optimal value of the BDTG variable.

Table 6.8: Fitted values of parameters for $B_s^0 \to D_s^-\pi^+$ signal. The N_i parameters are the yield of the signal and the different backgrounds. The parameter Fract is the fraction of the two CB distributions used to parametrise the signal. The parameter $\text{Fract}_{\text{Part}}$ is the fraction of the $B_s^0 \to D_s^-\rho^+$ and $B_s^0 \to D_s^{*-}\pi^+$. The m parameter is the common mean of the two CB functions. The value a_1 is the exponent of the combinatorial background shape.

Parameter	Fitted value	Uncertainty
$N_{B_s^0 \to D_s^-\pi^+}$	670	34
Fract	0.50	0.14
m (MeV/c^2)	5365.3	1.0
N_{Comb}	345	240
a_1	-6.6 × 10^{-3}	1.6 × 10^{-3}
$N_{D\pi}$	48	18
N_{Λ_b}	287	36
$N_{B_s^0 \to D_s 3\pi}$	79	79
N_{Part}	668	121
$\text{Fract}_{\text{Part}}$	0.34	0.06

Fit validation

Several cross checks are performed to validate the fit model:

- The stability of the fitted results with respect to the BDTG cut value is established. The ratio of $B^0 \to D^-\pi^+$ and $B^0 \to D^-K^+$, as well as the ratio $B^0 \to D^-\pi^+$ and $B_s^0 \to D_s^-\pi^+$, is constant as a function of the BDTG cut value, with a maximum discrepancy of 3% in both cases, for a sample with about 27% less events. The results are summarised in Tab. 6.9.

- The stability of the efficiency–corrected ratio between $B^0 \to D^-\pi^+$ and $B_s^0 \to D_s^-\pi^+$ is also probed using the rectangular cut selection, see Sec. 6.2. The efficiency–corrected ratio is found to be 5.54 ± 0.35, which is in agreement with the efficiency–corrected ratio of 5.64 ± 0.33 that is found using the BDTG selection. Since the rectangular cut based selection is suboptimal, too much combinatorial background is present in the sample of $B^0 \to D^-K^+$ to perform a sensible cross check.

- The expected number of $B^0 \to D^-\pi^+$ events misidentified as $B^0 \to D^-K^+$, 145 ± 5, is extracted from the average misidentification rate determined in the PID calibration sample. This number is compared with the yield obtained from the fit, 131 ± 19, and an excellent agreement is found. Although the yield of misidentified $B^0 \to D^-\pi^+$ under the $B_s^0 \to D_s^-\pi^+$ was loosely constrained to expectation (45 ± 20), the fitted yield of 48 ± 18 events did not show a tension in the fit, indicating that the average misidentification rate is understood.

- One thousand toy experiments[8] were generated and fitted to justify the fit procedure. The results of the pull for the three decay channels are given in Figs. 6.13 and they show that the fit is free from any bias and that the uncertainties are evaluated correctly.

6.5 Determination of corrected relative events yields

The fit results presented in Sec. 6.4 lead to measurements of the ratios of event yields listed in Sec. 6.1. The raw fitted yields must be corrected for known efficiency differences between the modes being considered, and a systematic uncertainty must be assigned.

Correction factors

The efficiency correction factors applied to the measurements of relative event yields are listed in Tab. 6.10 and in Tab. 6.11 for the ratio used to extract the $B^0 \to D^-K^+$ branching ratio and to measure f_s/f_d, respectively. Note that there are two separate correction factors,

[8]The notation "toy experiment" is used to indicate that the generated pseudo–experiments were produced in a simplified, but fully controlled environment. The background sources were generated according to MC shapes, and the relative amount was gaussian distributed around the value found in data.

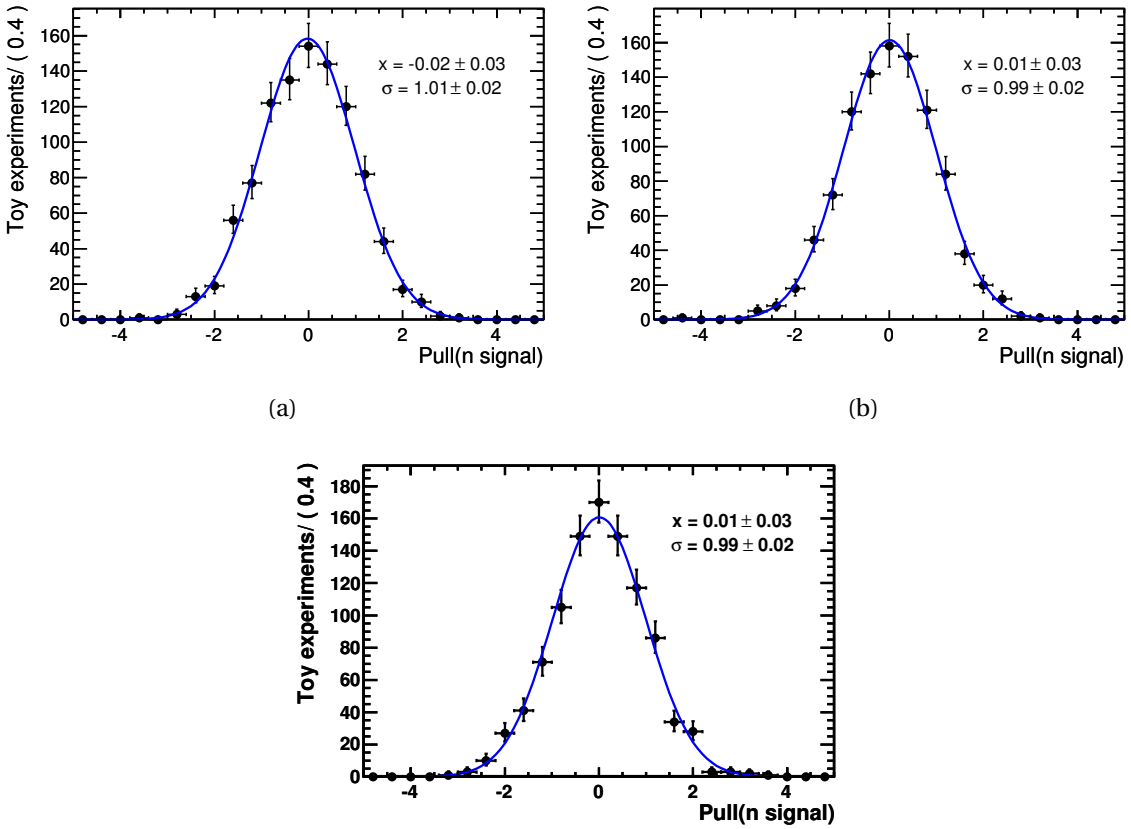

Figure 6.13: Pull distribution for the number of signal events in the case of $B^0 \to D^-\pi^+$ (a), $B^0 \to D^-K^+$ (b) and $B_s^0 \to D_s^-\pi^+$ (c).

corresponding to the extraction of f_s/f_d from the ratio of $N(B^0 \to D^-K^+)/N(B_s^0 \to D_s^-\pi^+)$ and $N(B^0 \to D^-\pi^+)/N(B_s^0 \to D_s^-\pi^+)$. In those cases where efficiencies for the B^0 and B_s^0 decays, as measured on simulated events, are equal within the uncertainty, and where there is no physical reason to suspect a different efficiency, no correction factor is applied.

Systematic uncertainties

The systematic uncertainties for the relative branching ratio of $B^0 \to D^-K^+$ and $B^0 \to D^-\pi^+$ are evaluated. The uncertainty on the PID-related part of the correction factors is calculated as follows. The errors on the individual K and π efficiencies, after reweighting of the D^* calibration sample, have been determined by the RICH group for the momentum spectra that are relevant for this analysis. The errors are found to be 1.5% for K and 0.5% for π. The ratio of PID efficiencies, following all of the PID cuts that are applied to obtain the $B^0 \to D^-\pi^+$ and $B^0 \to D^-K^+$ samples, are then re-calculated assuming that the individual efficiencies are incorrect by the amounts given above. Both positive and negative

Table 6.9: Fit stability for different BDTG cut values. Ratio$_1$ is the ratio between $B^0 \to D^-\pi^+$ and $B^0 \to D^-K^+$ decays, while ratio$_2$ is the ratio between $B^0 \to D^-\pi^+$ and $B_s^0 \to D_s^-\pi^+$. In bold characters are the results for the optimal cutting value of the BDTG.

BDTG value	ratio$_1$	ratio$_2$
0.6	15.8 ± 1.1	6.1 ± 0.3
0.65	$\mathbf{16.2 \pm 1.4}$	$\mathbf{6.1 \pm 0.3}$
0.7	15.7 ± 1.4	5.9 ± 0.2

Table 6.10: Correction factors for the relative branching ratio measurement.

Source	$\epsilon(D\pi)/\epsilon(DK)$
Bachelor reconstruction efficiency ratio	1.025 ± 0.003
PID cuts	1.183 ± 0.006
$P < 100$GeV/c efficiency for $B^0 \to D^-K^+$	1.007 ± 0.002
Trigger	1.00 ± 0.02
Overall correction	1.221 ± 0.021

Table 6.11: Correction factors for the f_s/f_d measurements.

Source	$\epsilon(DK)/\epsilon(D_s\pi)$	$\epsilon(D\pi)/\epsilon(D_s\pi)$
$K^\mp/\pi^\mp$reco.	1.014 ± 0.004	1.039 ± 0.003
PID cuts	0.959 ± 0.006	1.135 ± 0.005
$P < 100$ GeV/c cut	0.993 ± 0.001	N/A
Trigger eff. corr.	0.95 ± 0.020	0.95 ± 0.020
Overall correction	0.917 ± 0.020	1.120 ± 0.025

shifts in the efficiencies are considered. The largest shift in the ratio of PID efficiencies for $B^0 \to D^-\pi^+$ and $B^0 \to D^-K^+$ that is observed is around 2.5%. This is taken as systematic on the ratio of PID efficiency for the branching ratio measurement.

Systematic uncertainties due to approximations in the fit models, such as fixing the widths of the CB, assuming the background shape in the $B^0 \to D^-K^+$ fit, and not including the $B_s^0 \to D_s^-\pi^+$ and $\Lambda_b \to \Lambda_c^-\pi^+$ misidentified background contributions, were evaluated. A large numbers of toy Monte Carlo studies was performed, where data samples were generated with different parameter values, while keeping the same fit model as used for data [83].

For the $B^0 \to D^-\pi^+$ fit, the generated combinatorial background was changed from an exponential function to a linear distribution, while for the $B^0 \to D^-K^+$ fit — where this background is modelled using a uniform distribution — the shape was replaced by an exponential distribution, with a slope ranging between 0 and the value from the $B^0 \to D^-\pi^+$ fit. Uncertainties of 1.0% and 0.5% were found for the $B^0 \to D^-\pi^+$ and $B^0 \to D^-K^+$ yields respectively.

The dependence on the width of the CB, which is fixed in the $B^0 \to D^-K^+$ fit, is studied varying this parameter over a wide range. An uncertainty of 1.5% on the yield is found. An uncertainty is obtained of 1.5% and 0.5% for the respective $B^0 \to D^-\pi^+$ and $B^0 \to D^-K^+$ fits. The fit model uncertainty of both fits is rounded to 2.0% for further calculation, because of the small influence on the final uncertainty and for computational simplicity. Hence the total fit model uncertainty is 2.8%. The source of systematic uncertainties are listed in Tab. 6.12.

In addition to the systematic uncertainties considered in the relative branching ratio measurement above, other systematic uncertainties are considered for the f_s/f_d measurement. The most prominent uncertainty originates from the knowledge of the branching ratio of the $D_s^\pm$ into $KK\pi$ and of the branching ratio of $D^\pm$ into $K\pi\pi$.

The systematic uncertainties from the fit model in $B_s^0 \to D_s^-\pi^+$ decay are evaluated using toy Monte Carlo studies as described for the $B^0 \to D^-K^+$ decays leading to a total uncertainty of 2.8%. The systematic uncertainty on the ratio of PID efficiencies is calculated in the same way as described for the branching ratio measurement, leading to 2.5% of uncertainty for the measurement using the $B^0 \to D^-\pi^+$ and $B_s^0 \to D_s^-\pi^+$ decay modes, and to 1.0% in the measurement using the $B^0 \to D^-K^+$ and $B_s^0 \to D_s^-\pi^+$ decay modes[9].

6.6 Results

Relative Branching Ratio of $B^0 \to D^-K^+$ and $B^0 \to D^-\pi^+$

The correction factors listed in Sec. 6.5 are applied to the ratio of raw event yields computed from the fit results of Sec. 6.4, yielding:

$$\frac{BR\left(B^0 \to D^-K^+\right)}{BR\left(B^0 \to D^-\pi^+\right)} = 0.0750 \pm 0.0066 \pm 0.0035, \tag{6.3}$$

[9] The f_s/f_d measurement using $B^0 \to D^-K^+$ and $B_s^0 \to D_s^-\pi^+$ is more robust against PID uncertainties, since the final states have the same number of kaons and pions.

Table 6.12: Experimental systematic uncertainties for the branching ratio measurement BR($B^0 \to D^- K^+$) and the two f_s/f_dmeasurements.

Source	BR($B^0 \to D^- K^+$)	f_s/f_d
PID calibration	2.5%	1.0%/2.5%
Fit model	2.8%	2.8%
Trigger simulation	2.0%	2.0%
Correction factors	1.7%	2.2%
BR($B^0 \to D^- \pi^+$)	4.9%	
BR($D^+ \to K^- \pi^+ \pi^+$)		2.2%
BR($D_s^+ \to K^- K^+ \pi^+$)		4.9%
$\tau_{B_s^0}/\tau_{B^0}$		1.5%
Total	6.7%	7.0%/7.4%

where the first error is statistical, and the second is systematic. Using the PDG world average result for the branching ratio measurement of $B^0 \to D^- \pi^+$, $(2.68 \pm 0.13) \times 10^{-3}$, this results in a value of

$$BR\left(B^0 \to D^- K^+\right) = (2.01 \pm 0.18 \pm 0.14) \times 10^{-4}, \tag{6.4}$$

where the first error is statistical, and the second (including the 4.9% uncertainty on $BR(B^0 \to D^- \pi^+)$) is systematic. This value is in good agreement with the value measured by the Belle collaboration, $BR\left(B^0 \to D^- K^+\right) = (2.04 \pm 0.50 \pm 0.27) \times 10^{-4}$ [84].

As discussed in chapter 1 colour–favoured tree decays can be used to test factorisation by comparing the branching ratio to the semi–leptonic decay rate. So far no test of factorisation using the $B^0 \to D^- K^+$ decay channel was possible due to the large statistical uncertainties, but with the large data sample collected in 2011 by the LHCb experiment a precise test will be feasible.

Measurement of f_s/f_d

The raw yields from Tabs. 6.6,6.7, and 6.8, as well as the correction factors in Tab. 6.11 are used to extract two values for f_s/f_d.

f_s/f_d measurement from the ratio of $B^0 \to D^- K^+$ and $B_s^0 \to D_s^- \pi^+$

The theoretically cleaner extraction is performed using the decays $B^0 \to D^- K^+$ and $B_s^0 \to D_s^- \pi^+$. In this case the relevant formula is given in Eq. 1.3 [4], reproduced here for the reader's convenience

$$\frac{f_s}{f_d} = 0.0743 \times \frac{\tau_{B^0}}{\tau_{B_s^0}} \times \left[\frac{1}{\mathcal{N}_a \mathcal{N}_F} \frac{\epsilon_{DK}}{\epsilon_{D_s\pi}} \frac{N_{D_s\pi}}{N_{DK}} \right]. \tag{6.5}$$

The current world average for the B_s^0-to-B^0 lifetime ratio [3] is used

$$\frac{\tau_{B^0}}{\tau_{B_s^0}} = 1.028 \pm 0.016,$$

and the combined factor accounting for non–factorisable corrections and for the form factor ratio, is given by [4, 9]

$$\mathcal{N}_a \mathcal{N}_F = 1.24 \pm 0.084.$$

Using $BR(D^+ \to K^-\pi^+\pi^+) = (9.14 \pm 0.20)\%$ and $BR(D_s^+ \to K^-K^+\pi^+) = (5.50 \pm 0.27)\%$, the value of f_s/f_d is found to be

$$\frac{f_s}{f_d} = 0.250 \pm 0.024^{\text{stat}} \pm 0.017^{\text{syst}} \pm 0.017^{\text{theor}}, \tag{6.6}$$

where the first error is the statistical uncertainty, the second the experimental systematic, and the third the theoretical uncertainty arising mainly from the uncertainty on the form factor ratio. To allow a straightforward incorporation of future improved knowledge on the form factor ratio, the result can also be expressed as:

$$\frac{f_s}{f_d} = (0.310 \pm 0.030^{\text{stat}} \pm 0.021^{\text{syst}}) \frac{1}{\mathcal{N}_a \mathcal{N}_F}, \tag{6.7}$$

keeping the theoretical uncertainty separate.

f_s/f_d measurement from the ratio of $B^0 \to D^-\pi^+$ and $B_s^0 \to D_s^-\pi^+$

Since the statistical uncertainty in the prior determination of f_s/f_d is dominated by the yield of the $B^0 \to D^-K^+$ mode, the extraction of f_s/f_d is complemented by the modes $B^0 \to D^-\pi^+$ and $B_s^0 \to D_s^-\pi^+$, where an additional uncertainty in the theoretical value for $BR(B^0 \to D^-\pi^+)$ arises due to the W–exchange diagram,

$$\mathcal{N}_E = 0.966 \pm 0.075.$$

In this case the relevant formula is given in Eq. 1.7 [5], reproduced here for the reader's convenience

$$\frac{f_s}{f_d} = 0.982 \times \frac{\tau_{B^0}}{\tau_{B_s^0}} \times \left[\frac{1}{\tilde{\mathcal{N}}_a \mathcal{N}_F \mathcal{N}_E} \frac{\epsilon_{D\pi}}{\epsilon_{D_s\pi}} \frac{N_{D_s\pi}}{N_{D\pi}} \right]. \tag{6.8}$$

The value of f_s/f_d is found to be

$$\frac{f_s}{f_d} = 0.256 \pm 0.014^{\text{stat}} \pm 0.019^{\text{syst}} \pm 0.026^{\text{theory}}, \tag{6.9}$$

where the first error is the statistical uncertainty, the second systematic, and the third the theoretical uncertainty now arising from the uncertainty on the form factors as well as the W–exchange correction. This result can also be written as:

$$\frac{f_s}{f_d} = (0.307 \pm 0.017^{\text{stat}} \pm 0.023^{\text{syst}}) \frac{1}{\mathcal{N}_a \mathcal{N}_F \mathcal{N}_E}. \tag{6.10}$$

Measurements combination

The two measurement of f_s/f_d are in good agreement with each other and can be combined into a single value, by taking all correlated uncertainties into account[10].

The following averaged value for f_s/f_d is obtained:

$$\frac{f_s}{f_d} = 0.253 \pm 0.017^{\text{stat}} \pm 0.018^{\text{syst}} \pm 0.020^{\text{theor}}, \tag{6.11}$$

where all contributions to the uncertainty were assumed to be Gaussian distributed.

The fragmentation fractions can in principle depend on the center–of–mass energy, as well as on p_T and pseudo–rapidity. However, a good agreement is found with the measurements performed at LEP and at Tevatron[3], showing that the fragmentation fractions are consistent with being universal.

The LHCb experiment has reported a measurement of the ratio $f_s/(f_u + f_d)$ using semi–leptonic decays of b–hadrons, identified by the detection of a muon and a charmed hadron [6], $f_s/(f_u + f_d) = 0.134 \pm 0.004^{+0.011}_{-0.010}$. The combination of this result with the two measurements in Eq. 6.6 and 6.9 is performed with the assumption of isospin symmetry ($f_u = f_d$) and with consideration of the asymmetric systematic uncertainties [6]. The combined result is:

$$\frac{f_s}{f_d} = 0.267^{+0.021}_{-0.020}. \tag{6.12}$$

[10]The correlation factors found were 49% for statistics, 92% for systematics and 66% for theoretical errors.

Seventh Chapter

Implication of the knowledge of f_s/f_d on the extraction of $BR(B_s^0 \to \mu^\pm\mu^\mp)$

Truth is what stands the test of experience.
Albert Einstein

7.1 Introduction

The LHC accelerator started its physics run at a center–of–mass energy of $\sqrt{s} = 7$ TeV in 2010, delivering $\sim 10^{10}$ $b\bar{b}$ pairs over the year. This unprecedented production rate of b quarks allows precise testing of the flavour sector of the Standard Model (SM). Precise measurements in the B^0 sector were already obtained at the B factories, [85, 86, 1], while the first measurements are recently obtained in the B_s^0 sector from the Tevatron collider and from B factories, running at the $\Upsilon(5S)$ resonance. One of the most promising channels for detecting signals of physics beyond the SM is the rare decay $B_s^0 \to \mu^\pm\mu^\mp$. This decay channel occurs in the SM via penguin and box topologies, as shown in Figs. 7.1.

This decay is rare since it is both a flavor changing neutral current (FCNC) process as well as helicity suppressed. In the SM the corresponding branching ratio is predicted to be $(3.2 \pm 0.2) \times 10^{-9}$ [87, 88], where the dominant error originates from the non–perturbative "bag–

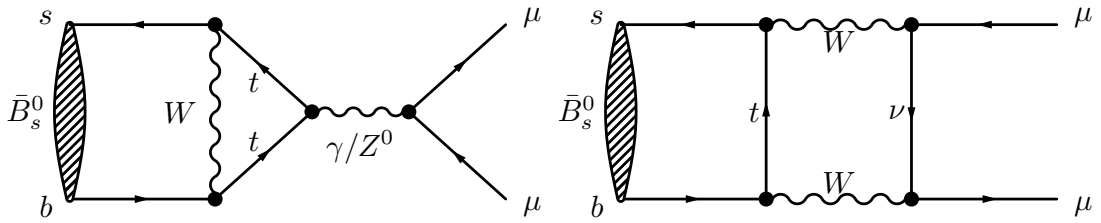

Figure 7.1: Examples of SM diagrams for $B_s^0 \to \mu^\pm\mu^\mp$ decay.

parameter" of the B_s^0 meson as determined from lattice QCD. New physics contributions can enhance this branching ratio as much as two orders of magnitude [89].

7.2 Branching fraction determination of $B_s^0 \to \mu^\pm\mu^\mp$

The branching ratio is given by the fraction of B_s^0 mesons decaying to two muons, corrected for the detection efficiency:

$$BR_{B_s^0\to\mu^\pm\mu^\mp} = \frac{N_{B_s^0\to\mu^\pm\mu^\mp}}{\epsilon \cdot N_{B_s^0}} \tag{7.1}$$

where $N_{B_s^0\to\mu^\pm\mu^\mp}$ is the number of observed events, ϵ is the total efficiency, and N_{B_s} is the number of B_s^0 mesons initially produced. The latter can be measured knowing the $b\bar{b}$ cross-section ($\sigma_{b\bar{b}}$), the absolute luminosity (L), and the probability of a b quark to hadronize in a B_s^0 (f_s) through the relation:

$$N_{B_s} = \sigma_{b\bar{b}} \cdot f_s \cdot L \tag{7.2}$$

The first two quantities are measured at LHCb: $\sigma_{b\bar{b}} = (75.3 \pm 5.4 \pm 13.0)\ \mu b$ [90] while the absolute luminosity is measured with an overall precision of 3.5% [91]. The fragmentation fraction f_s was measured by DELPHI at LEP as $0.19 \pm 0.06 \pm 0.08$ [92], by CDF as 0.160 ± 0.044 [93] and recently by Belle as 0.193 ± 0.29 [94]. This direct extraction of N_{B_s} would result in a large uncertainty in the branching ratio extraction measurement. Better precision can be achieved by measuring the $B_s^0 \to \mu^\pm\mu^\mp$ yield relative to a B–meson decay with a known branching fraction using the following relation:

$$BR_{B_s^0\to\mu^\pm\mu^\mp} = BR_{norm} \cdot \frac{N_{B_s^0\to\mu^\pm\mu^\mp} \cdot \epsilon_{norm}}{N_{norm} \cdot \epsilon_{B_s^0\to\mu^\pm\mu^\mp}} \cdot \frac{f_{norm}}{f_s} \tag{7.3}$$

In case the normalisation channel is a B_s^0–decay mode, the ratio of fragmentation fractions in Eq. 7.3 vanishes. Unfortunately, no absolute measurement with sufficient accuracy is present in literature. For instance, the branching ratio of the decay $B_s^0 \to J/\psi\phi$ is measured as $(3.4 \pm 0.9) \times 10^{-5}$ by the Belle collaboration where one of the largest uncertainties is due to the f_s estimation, $f_s = \frac{\sigma(e^+e^-\to\Upsilon(5S)\to B_s^{0(*)}\bar{B}_s^{0(*)}X)}{\sigma(e^+e^-\to\Upsilon(5S))}$ [94, 1]. In contrast, decays of the B^0 and B^+ mesons are known with a few percent uncertainty. For example $BR(B^+ \to J/\psi K^+)$ is measured to be $(6.01 \pm 0.21) \times 10^{-5}$, and $BR(B^0 \to K^\pm\pi^\mp)$ is $(1.94 \pm 0.06) \times 10^{-5}$ [1].

A precise normalisation with respect to B^0 and B^+ decays can be performed once the fragmentation fraction f_s/f_d is measured at LHCb. This parameter was measured at LEP and CDF and it was obtained from averages by the HFAG group [3] and reported in Tab. 7.1.

However, this parameter is in principle dependent on the centre-of-mass energy, and it can depend on transverse momentum and pseudo–rapidity since the fragmentation process behaviour cannot be reliable predicted being driven by strong dynamics in the non-perturbative regime. Therefore an extrapolation at LHCb of the ratio of fragmentation fractions introduces additional uncertainties. Since the uncertainty on this parameter is the main systematic uncertainty in the branching ratio determination, it will limit the physics

Table 7.1: Results present in literature for the measurement of f_s/f_d

	f_s/f_d
HFAG(CDF)	0.327 ± 0.039 [a]
HFAG(LEP)	0.256 ± 0.026
HFAG(all)	0.270 ± 0.034
LHCb(hadronic)	0.253 ± 0.032
LHCb(semi–leptonic)	$0.268^{+0.023}_{-0.021}$
LHCb(combination)	$0.267^{+0.021}_{-0.020}$

[a] Recently CDF discovered an error in the measurement and corrected this number to 0.269 ± 0.033 [95]

discovery potential in the $B_s^0 \to \mu^\pm\mu^\mp$decay. Here the LHCb measurement of the f_s/f_d, described in this thesis, will be applied to measure the $B_s^0 \to \mu^\pm\mu^\mp$ branching fraction.

7.3 Limit on $B_s^0 \to \mu^\pm\mu^\mp$branching fraction

LHCb recently published a limit on the $B_s^0 \to \mu^\pm\mu^\mp$ branching fraction based on 0.37 fb^{-1} [70], combining 2010 [96] and first half of 2011 [97] data samples. The analysis is optimised on simulated events obtaining an efficient selection around 98% in the most sensitive region for a background reduction of a factor four. The number of observed events is compared to the number of expected signal and background events in bins of two independent variables: the invariant mass and the output of a multivariate discriminant (BDT). The combination of variables entering in the BDT is optimised using simulated events. The probability for a signal or background event to have a given value of the BDT output is obtained using real data. The decay $B_{(s)}^0 \to h^+h'^-$ is topologically identical to $B_s^0 \to \mu^\pm\mu^\mp$ and selected $B_{(s)}^0 \to h^+h'^-$ candidates are used to calibrate the signal likelihood. Events from the mass sidebands of the $B_s^0 \to \mu^\pm\mu^\mp$ selection are used to evaluate the expected background. The invariant mass line shape used for the signal is a Crystal Ball function with parameters extracted from the $B_{(s)}^0 \to h^+h'^-$ control sample.

The number of expected events, for a given branching fraction hypothesis, is obtained by normalising to channels with a known branching fraction, namely $B^+ \to J/\psi K^+$, $B_s^0 \to J/\psi\phi$ and $B^0 \to K^+\pi^-$. These channels are selected using a similar method to the signal in order to minimise the relative systematic uncertainty. The two–dimensional space formed by the invariant mass and the BDT output is binned in six bins of mass and four bins in BDT. The distribution of the invariant mass in the four BDT bins is shown in Fig. 7.2.

In each bin the compatibility of the observed number of events with the number expected events for a given branching fraction hypothesis is computed using the CL_s method [98], which allows a given hypothesis to be excluded at a certain confidence level. This

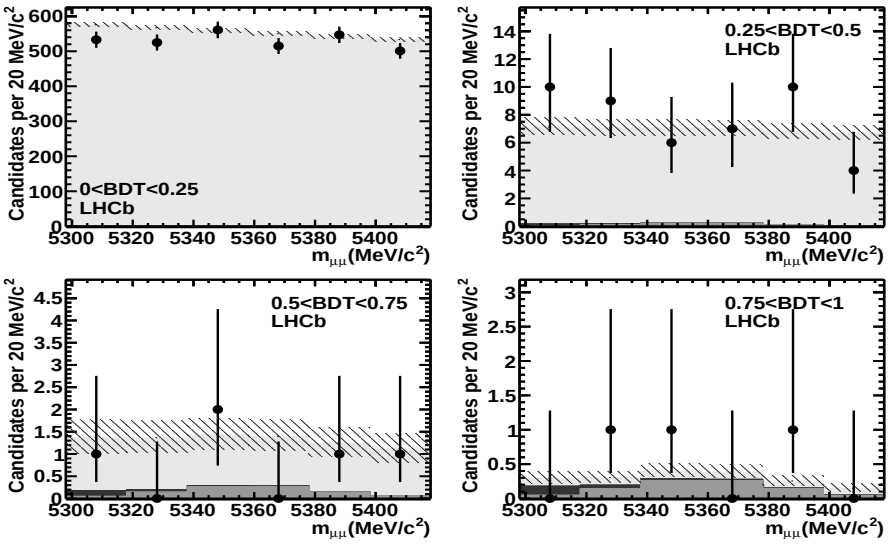

Figure 7.2: Distribution of selected di–muon events in the $B_s^0 \to \mu^\pm\mu^\mp$ mass window for the four BDT output bins. The black dots are data, the light grey histogram shows the contribution of the combinatorial background, the black filled histogram shows the contribution of the $B^0_{(s)} \to h^+h'^-$ background and the dark grey filled histogram the contribution of the $B_s^0 \to \mu^\pm\mu^\mp$ signal events according to SM rate. The hatched area depict the uncertainty on the sum of the expected contributions.

method provides three estimators: CL_{s+b}, a measure of the compatibility of the observed distribution with the signal and background hypotheses, CL_b, a measure of the compatibility with the background–only hypothesis and CL_s, a measure of the compatibility of the observed distribution with the signal and background hypotheses normalised to the background–only hypothesis.

The expected CL_s values are shown in Fig. 7.3. The number of observed events in the B_s^0 mass window are compatible with the expectations from the background–only hypothesis at 5% confidence level. The probability that the observed events are compatible with the sum of expected background events and signal events according to the SM rate is 33%. The 90% (95%) upper CL limits are 3.8 (4.4) times larger than the predicted SM branching fraction.

The best published limits are listed in Tab. 7.2. The world–best limit is obtained from the preliminary combination of the results from the LHCb and the CMS experiments as described in the next section.

7.4 Combination with CMS

A combination of the results of the search for the decay $B_s^0 \to \mu^\pm\mu^\mp$ is performed using about 0.37 fb^{-1} and 1.14 fb^{-1} collected by the LHCb and CMS experiments respectively, obtaining a limit of $BR < 1.08 \times 10^{-8}$ at 95% CL [102]. The background is dominated by combinatorial background. Other sources of background, such as the peaking background from $B \to hh'$

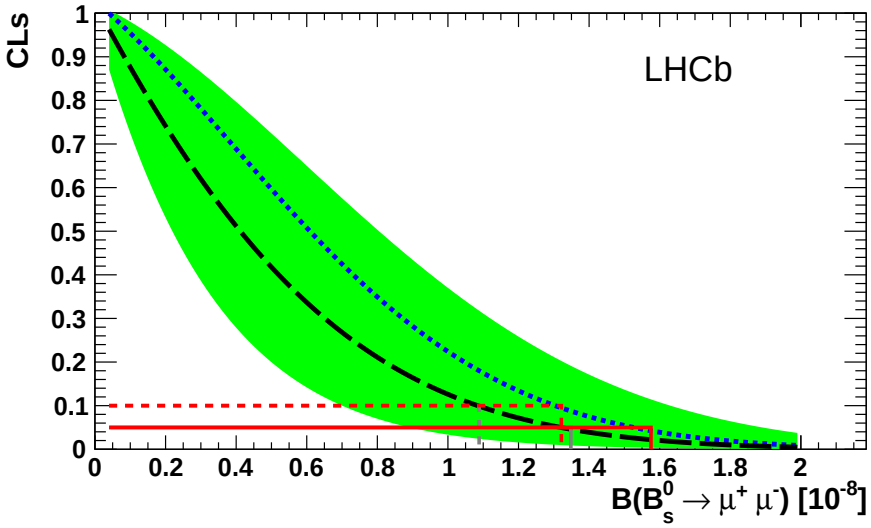

Figure 7.3: CL_s for $B_s^0 \to \mu^\pm\mu^\mp$ as a function of the assumed BR. Expected (observed) values are shown by dashed black (dotted blue) lines. The expected CL_s values have been computed assuming a signal yield corresponding to the SM branching fractions. The green (grey) shaded areas cover the region of $\pm 1\sigma$ of compatible observations. The measured upper limits at 90% and 95% CL are also shown.

Table 7.2: Upper limits for the branching fraction $\mathrm{BR}(B_s^0 \to \mu^\pm\mu^\mp)$.

Collaboration	95% CL ($B_s^0 \to \mu^\pm\mu^\mp$)	data sample (fb^{-1})
D0 [99]	$BR < 5.1 \times 10^{-8}$	6.1
CDF [100]	$BR < 4.0 \times 10^{-8}$	6.9
CMS [101]	$BR < 1.9 \times 10^{-8}$	1.4
LHCb [70]	$BR < 1.6 \times 10^{-8}$	0.37
Preliminary Results		
LHCb + CMS	$BR < 1.08 \times 10^{-8}$	(0.37 + 1.14)[102]

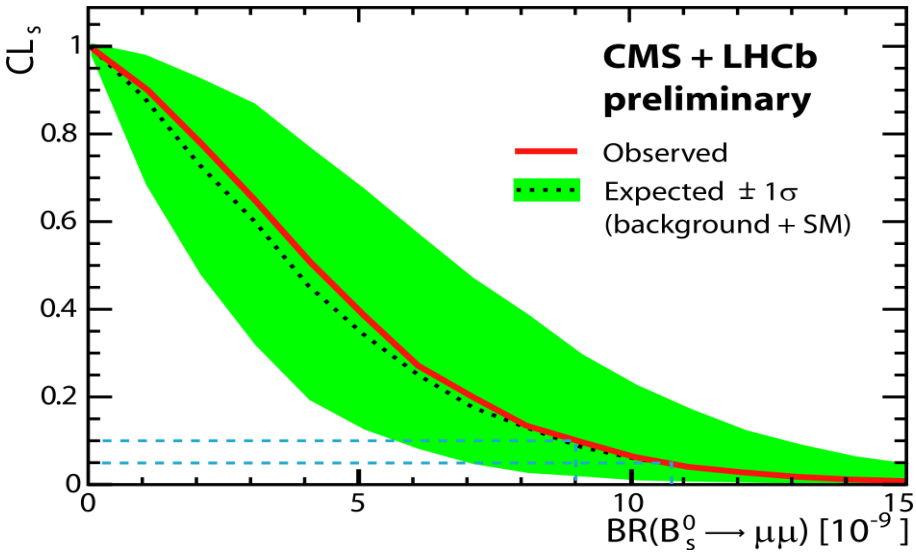

Figure 7.4: The value of CL_s as computed from the distribution of events observed by LHCb and CMS collaborations. The observed (solid curve) and expected (dotted curve) CL_s value for background plus the SM signal as a function of the true $BR(B_s^0 \to \mu^\pm\mu^\mp)$. The green dashed area contain the $\pm 1\sigma$ interval of possible results compatible with the expected value. The 90% and 95% CL observed limits are illustrated by the dashed lines.

decays (with hadrons misidentified as muons) are small, and therefore the combination is relatively straightforward.

In the combination procedure the measurement of $f_s/f_d = 0.267^{+0.021}_{-0.020}$ obtained by the LHCb collaboration is used to compute the expected number of signal events. It was assumed that this value is also valid in the CMS acceptance and no extra systematic uncertainty was assigned.

The value of CL_s, as computed from the distribution of events observed by LHCb and CMS collaborations, is shown in Fig. 7.4. The observed events in the B_s^0 mass window are compatible with the background expectations at 8% confidence level. The probability that the observed events are compatible with the sum of expected background events and signal events, assuming the SM branching ratio, is 57%. An enhancement of the branching ratio more than 3.4 times the Standard Model prediction is excluded at 95% CL, leaving still a large range for contributions from physics beyond the Standard Model.

7.5 Outlook

A direct measurement of the f_s/f_d parameter by the CMS collaboration is desirable. The measurement presented in this thesis is difficult at CMS since no low-p_T hadronic trigger is available at CMS and particle identification is less discriminative compared to the LHCb experiment. Given that the hadronic measurement of f_s/f_d in CMS is challenging, an alternative method would be to use the comparison of the measurement at LHCb and CMS of

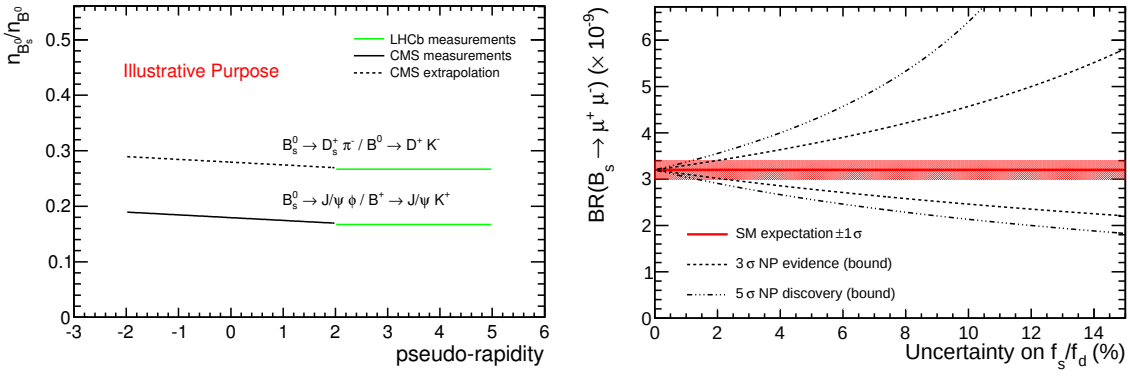

(a) (b)

Figure 7.5: (a): sketch to show the possibility to extrapolate the value of f_s/f_d to the pseudo–rapidity coverage at CMS, using $B^+ \to J/\psi K^+$ and $B_s^0 \to J/\psi\phi$ decay channels. The slope for the measurements related to the ratio of $B^+ \to J/\psi K^+$ and $B_s^0 \to J/\psi\phi$ decays as well as their offset for both CMS and LHCb are just illustrative. (b): limit of $B_s^0 \to \mu^\pm\mu^\mp$ discovery potential (3 and 5 σ) in the limit of infinite statistics and negligible systematic uncertainty as a function of the uncertainty on the f_s/f_d measurement. Currently the uncertainty is 8%.

the relative rates of $B^+ \to J/\psi K^+$ and $B_s^0 \to J/\psi\phi$ across $\eta \sim 2$. The hadronic measurement of f_s/f_d in LHCb can be used to calibrate the ratio of the $B^+ \to J/\psi K^+$ and $B_s^0 \to J/\psi\phi$ modes and extrapolate the f_s/f_d value to the phase–space relevant at CMS, see Fig. 7.5 (a).

The precision of the f_s/f_d measurement affects the discovery potential for the $B_s^0 \to \mu^\pm\mu^\mp$ decay. In the limit of infinite statistics and negligible systematic uncertainty, where only the uncertainty on f_s/f_d affects the result, it is only possible to claim an evidence or a discovery of new physics above a certain minimal value for the branching ratio. Assuming the simplest case of a gaussian distributed uncertainty for f_s/f_d[1] the range with sensitivity for NP contribution is given by:

$$BR_{limit} = \frac{BR_{SM}}{(1 \mp n \cdot \sigma)} \tag{7.4}$$

where n can be 3 for an evidence of new physics or 5 for a discovery, while σ is the relative uncertainty of f_s/f_d. Assuming an uncertainty of f_s/f_d of 8%, see chapter 6, and a SM branching ratio of $(3.2 \pm 0.2) \times 10^{-9}$ [87, 88] only branching fractions higher than 4.2×10^{-9} or lower than 2.6×10^{-9} can be distinguished from the SM–hypothesis for at 3σ confidence level, see Fig. 7.5 (b).

It is interesting to notice that at present the dominant sources of uncertainty in the f_s/f_d measurement are the theoretical uncertainty ($\sim 7\%$) and the uncertainty on the measurement of the branching fraction of the decay $D_s^+ \to K^-K^+\pi^+$ ($\sim 5\%$). Theoretical groups are performing new calculations to reduce the first uncertainty [12], while the CLEO collaboration might improve on the measurement of the decay $D_s^+ \to K^-K^+\pi^+$.

[1] For a more realistic case a numerical computation through pseudo-experiments can be performed.

Eighth Chapter

Measurement of the branching fraction of the decays $B_s^0 \to D_s^{\pm} K^{\mp}$ and $B_s^0 \to D_s^- \pi^+$

Science is built of facts the way a house is built of bricks; but an accumulation of facts is no more science than a pile of bricks is a house.
Henri Poincaré

In the first half of 2011 the LHCb experiment collected a data sample of 0.37 fb^{-1} proton-proton collisions at $\sqrt{s} = 7$ TeV. This data sample is used to measure the branching fraction of $B_s^0 \to D_s^- \pi^+$ and $B_s^0 \to D_s^{\pm} K^{\mp}$ decay modes with an analysis similar to the one presented in chapter 6. These measurements result in two branching fraction evaluations with a total uncertainty significantly smaller than the previous world average measurements, particularly interesting in the case of the $B_s^0 \to D_s^- \pi^+$ decay that is the most precise B_s^0 decay mode presently measured. The $B_s^0 \to D_s^{\pm} K^{\mp}$ branching fraction can be considered as the first ingredient towards the time dependent measurement of the angle γ that will be performed when more data will be available.

The text reproduced in the next pages is accepted for publication by the *Journal of High Energy Physics*

EUROPEAN ORGANIZATION FOR NUCLEAR RESEARCH (CERN)

CERN-PH-EP-2012-091
LHCb-PAPER-2011-022
5 April 2012

Measurements of the branching fractions of the decays $B_s^0 \to D_s^{\mp} K^{\pm}$ and $B_s^0 \to D_s^- \pi^+$

LHCb collaboration

Abstract

The decay mode $B_s^0 \to D_s^{\mp} K^{\pm}$ allows for one of the theoretically cleanest measurements of the CKM angle γ through the study of time-dependent *CP* violation. This paper reports a measurement of its branching fraction relative to the Cabibbo-favoured mode $B_s^0 \to D_s^- \pi^+$ based on a data sample corresponding to 0.37 fb^{-1} of proton-proton collisions at $\sqrt{s} = 7$ TeV collected in 2011 with the LHCb detector. In addition, the ratio of B meson production fractions f_s/f_d, determined from semileptonic decays, together with the known branching fraction of the control channel $B^0 \to D^- \pi^+$, is used to perform an absolute measurement of the branching fractions:

$$\mathcal{B}\left(B_s^0 \to D_s^- \pi^+\right) = (2.95 \pm 0.05 \pm 0.17^{+0.18}_{-0.22}) \times 10^{-3}\,,$$

$$\mathcal{B}\left(B_s^0 \to D_s^{\mp} K^{\pm}\right) = (1.90 \pm 0.12 \pm 0.13^{+0.12}_{-0.14}) \times 10^{-4}\,,$$

where the first uncertainty is statistical, the second the experimental systematic uncertainty, and the third the uncertainty due to f_s/f_d.

Submitted to JHEP

1 Introduction

Unlike the flavour-specific decay $B_s^0 \to D_s^- \pi^+$, the Cabibbo-suppressed decay $B_s^0 \to D_s^\mp K^\pm$ proceeds through two different tree-level amplitudes of similar strength: a $\bar{b} \to \bar{c}u\bar{s}$ transition leading to $B_s^0 \to D_s^- K^+$ and a $\bar{b} \to \bar{u}c\bar{s}$ transition leading to $B_s^0 \to D_s^+ K^-$. These two decay amplitudes can have a large *CP*-violating interference via $B_s^0 - \bar{B}_s^0$ mixing, allowing the determination of the CKM angle γ with negligible theoretical uncertainties through the measurement of tagged and untagged time-dependent decay rates to both the $D_s^- K^+$ and $D_s^+ K^-$ final states [1]. Although the $B_s^0 \to D_s^\mp K^\pm$ decay mode has been observed by the CDF [2] and Belle [3] collaborations, only the LHCb experiment has both the necessary decay time resolution and access to large enough signal yields to perform the time-dependent *CP* measurement. In this analysis, the $B_s^0 \to D_s^\mp K^\pm$ branching fraction is determined relative to $B_s^0 \to D_s^- \pi^+$, and the absolute $B_s^0 \to D_s^- \pi^+$ branching fraction is determined using the known branching fraction of $B^0 \to D^- \pi^+$ and the production fraction ratio between the strange and up/down B meson species, f_s/f_d [4]. The two measurements are then combined to obtain the absolute branching fraction of the decay $B_s^0 \to D_s^\mp K^\pm$. In addition to their intrinsic value, these measurements are necessary milestones on the road to γ as they imply a good understanding of the mass spectrum and consequently of the backgrounds. Charge conjugate modes are implied throughout. Our notation $B^0 \to D^- \pi^+$, which matches that of Ref. [5], encompasses both the Cabibbo-favoured $B^0 \to D^- \pi^+$ mode and the doubly-Cabibbo-suppressed $B^0 \to D^+ \pi^-$ mode.

The LHCb detector [6] is a single-arm forward spectrometer covering the pseudorapidity range $2 < \eta < 5$, designed for studing particles containing b or c quarks. In what follows "transverse" means transverse to the beamline. The detector includes a high-precision tracking system consisting of a silicon-strip vertex detector surrounding the pp interaction region, a large-area silicon-strip detector located upstream of a dipole magnet with a bending power of about 4 Tm, and three stations of silicon-strip detectors and straw drift tubes placed downstream. The combined tracking system has a momentum resolution $\Delta p/p$ that varies from 0.4% at 5 GeV/c to 0.6% at 100 GeV/c, an impact parameter resolution of 20 µm for tracks with high transverse momentum, and a decay time resolution of 50 fs. Impact parameter is defined as the transverse distance of closest approach between the track and a primary interaction. Charged hadrons are identified using two ring-imaging Cherenkov detectors. Photon, electron and hadron candidates are identified by a calorimeter system consisting of scintillating-pad and pre-shower detectors, an electromagnetic calorimeter, and a hadronic calorimeter. Muons are identified by a muon system composed of alternating layers of iron and multiwire proportional chambers.

The LHCb trigger consists of a hardware stage, based on information from the calorimeter and muon systems, followed by a software stage which applies a full event reconstruction. Two categories of events are recognised based on the hardware trigger decision. The first category are events triggered by tracks from candidate signal decays

which have an associated cluster in the hadronic calorimeter. The second category are events triggered independently of the particles associated with the candidate signal decay by either the muon or calorimeter triggers. This selection ensures that tracks from the candidate signal decay are not associated to muon segements or clusters in the electromagnetic calorimeter and suppresses backgrounds from semileptonic decays. Events which do not fall into either of these two categories are not used in the subsequent analysis. The second, software, trigger stage requires a two-, three- or four-track secondary vertex with a large value of the scalar sum of the transverse momenta ($p_{\rm T}$) of the tracks, and a significant displacement from the primary interaction. At least one of the tracks used to form this vertex is required to have $p_{\rm T} > 1.7$ GeV/c, an impact parameter $\chi^2 > 16$, and a track fit χ^2 per degree of freedom $\chi^2/{\rm ndf} < 2$. A multivariate algorithm is used for the identification of the secondary vertices [7]. Each input variable is binned to minimise the effect of systematic differences between the trigger behaviour on data and simulated events.

The samples of simulated events used in this analysis are based on the Pythia 6.4 generator [8], with a choice of parameters specifically configured for LHCb [9]. The EvtGen package [10] describes the decay of the B mesons, and the Geant4 package [11] simulates the detector response. QED radiative corrections are generated with the Photos package [12].

The analysis is based on a sample of pp collisions corresponding to an integrated luminosity of 0.37 fb^{-1}, collected at the LHC in 2011 at a centre-of-mass energy $\sqrt{s} = 7$ TeV. In what follows, signal significance will mean $S/\sqrt{S+B}$.

2 Topological selection

The decay modes $B_s^0 \to D_s^- \pi^+$ and $B_s^0 \to D_s^\mp K^\pm$ are topologically identical and are selected using identical geometric and kinematic criteria, thereby minimising efficiency corrections in the ratio of branching fractions. The decay mode $B^0 \to D^- \pi^+$ has a similar topology to the other two, differing only in the Dalitz plot structure of the D decay and the lifetime of the D meson. These differences are verified, using simulated events, to alter the selection efficiency at the level of a few percent, and are taken into account.

The B_s^0 (B^0) candidates are reconstructed from a D_s^- (D^-) candidate and an additional pion or kaon (the "bachelor" particle), with the D_s^- (D^-) meson decaying in the $K^+K^-\pi^-$ ($K^+\pi^-\pi^-$) mode. No requirements are applied on the K^+K^- or the $K^+\pi^-$ invariant masses. A mass constraint on the D meson, selected with a tight mass window of 1948-1990 MeV, is applied when computing the B meson mass.

All selection criteria will now be specified for the B_s^0 decays, and are implied to be identical for the B^0 decay unless explicitly stated otherwise. All final-state particles are required to satisfy a track fit $\chi^2/{\rm ndf} < 4$ and to have a high transverse momentum and a large impact parameter χ^2 with respect to all primary vertices in the event. In order to remove backgrounds which contain the same final-state particles as the signal decay, and therefore have the same mass lineshape, but do not proceed through the decay of a

charmed meson, the flight distance χ^2 of the D_s^- from the B_s^0 is required to be larger than 2. Only D_s^- and bachelor candidates forming a vertex with a $\chi^2/\mathrm{ndf} < 9$ are considered as B_s^0 candidates. The same vertex quality criterion is applied to the D_s^- candidates. The B_s^0 candidate is further required to point to the primary vertex imposing $\theta_{\mathrm{flight}} < 0.8$ degrees, where θ_{flight} is the angle between the candidate momentum vector and the line between the primary vertex and the B_s^0 vertex. The B_s^0 candidates are also required to have a χ^2 of their impact parameter with respect to the primary vertex less than 16.

Further suppression of combinatorial backgrounds is achieved using a gradient boosted decision tree technique [13] identical to the decision tree used in the previously published determination of f_s/f_d with the hadronic decays [14]. The optimal working point is evaluated directly from a sub-sample of $B_s^0 \to D_s^-\pi^+$ events, corresponding to 10% of the full dataset used, distributed evenly over the data taking period and selected using particle identification and trigger requirements. The chosen figure of merit is the significance of the $B_s^0 \to D_s^{\mp}K^{\pm}$ signal, scaled according to the Cabibbo suppression relative to the $B_s^0 \to D_s^-\pi^+$ signal, with respect to the combinatorial background. The significance exhibits a wide plateau around its maximum, and the optimal working point is chosen at the point in the plateau which maximizes the signal yield. Multiple candidates occur in about 2% of the events and in such cases a single candidate is selected at random.

3 Particle identification

Particle identification (PID) criteria serve two purposes in the selection of the three signal decays $B^0 \to D^-\pi^+$, $B_s^0 \to D_s^-\pi^+$ and $B_s^0 \to D_s^{\mp}K^{\pm}$. When applied to the decay products of the D_s^- or D^-, they suppress misidentified backgrounds which have the same bachelor particle as the signal mode under consideration, henceforth the "cross-feed" backgrounds. When applied to the bachelor particle (pion or kaon) they separate the Cabibbo-favoured from the Cabibbo-suppressed decay modes. All PID criteria are based on the differences in log-likelihood (DLL) between the kaon, proton, or pion hypotheses. Their efficiencies are obtained from calibration samples of $D^{*+} \to (D^0 \to K^-\pi^+)\pi^+$ and $\Lambda \to p\pi^-$ signals, which are themselves selected without any PID requirements. These samples are split according to the magnet polarity, binned in momentum and p_{T}, and then reweighted to have the same momentum and p_{T} distributions as the signal decays under study.

The selection of a pure $B^0 \to D^-\pi^+$ sample can be accomplished with minimal PID requirements since all cross-feed backgrounds are less abundant than the signal. The $\overline{\Lambda}_b^0 \to \overline{\Lambda}_c^-\pi^+$ background is suppressed by requiring that both pions produced in the D^- decay satisfy $\mathrm{DLL}_{\pi-p} > -10$, and the $B^0 \to D^-K^+$ background is suppressed by requiring that the bachelor pion satisfies $\mathrm{DLL}_{K-\pi} < 0$.

The selection of a pure $B_s^0 \to D_s^-\pi^+$ or $B_s^0 \to D_s^{\mp}K^{\pm}$ sample requires the suppression of the $B^0 \to D^-\pi^+$ and $\overline{\Lambda}_b^0 \to \overline{\Lambda}_c^-\pi^+$ backgrounds, whereas the combinatorial background contributes to a lesser extent. The D^- contamination in the D_s^- data sample is reduced by requiring that the kaon which has the same charge as the pion in $D_s^- \to K^+K^-\pi^-$ satisfies $\mathrm{DLL}_{K-\pi} > 5$. In addition, the other kaon is required to satisfy $\mathrm{DLL}_{K-\pi} > 0$.

Table 1: PID efficiency and misidentification probabilities, separated according to the up (U) and down (D) magnet polarities. The first two lines refer to the bachelor track selection, the third line is the D^- efficiency and the fourth the D_s^- efficiency. Probabilities are obtained from the efficiencies in the D^{*+} calibration sample, binned in momentum and $p_{\rm T}$. Only bachelor tracks with momentum below 100 GeV/c are considered. The uncertainties shown are the statistical uncertainties due to the finite number of signal events in the PID calibration samples.

	PID Cut	Efficiency (%)		Misidentification rate (%)	
		U	D	U	D
K	$\mathrm{DLL}_{K-\pi} > 5$	83.3 ± 0.2	83.5 ± 0.2	5.3 ± 0.1	4.5 ± 0.1
π	$\mathrm{DLL}_{K-\pi} < 0$	84.2 ± 0.2	85.8 ± 0.2	5.3 ± 0.1	5.4 ± 0.1
D^-		84.1 ± 0.2	85.7 ± 0.2	-	-
D_s^-		77.6 ± 0.2	78.4 ± 0.2	-	-

This helps to suppress combinatorial as well as doubly misidentified backgrounds. For the same reason the pion is required to have $\mathrm{DLL}_{K-\pi} < 5$. The contamination of $\overline{\Lambda}_b^0 \to \overline{\Lambda}_c^- \pi^+$, $\overline{\Lambda}_c^- \to \overline{p} K^+ \pi^-$ is reduced by applying a requirement of $\mathrm{DLL}_{K-p} > 0$ to the candidates that, when reconstructed under the $\overline{\Lambda}_c^- \to \overline{p} K^+ \pi^-$ mass hypothesis, lie within ± 21 MeV/c^2 of the $\overline{\Lambda}_c^-$ mass.

Because of its larger branching fraction, $B_s^0 \to D_s^- \pi^+$ is a significant background to $B_s^0 \to D_s^\mp K^\pm$. It is suppressed by demanding that the bachelor satisfies the criterion $\mathrm{DLL}_{K-\pi} > 5$. Conversely, a sample of $B_s^0 \to D_s^- \pi^+$, free of $B_s^0 \to D_s^\mp K^\pm$ contamination, is obtained by requiring that the bachelor satisfies $\mathrm{DLL}_{K-\pi} < 0$. The efficiency and misidentification probabilities for the PID criterion used to select the bachelor, D^-, and D_s^- candidates are summarised in Table 1.

4 Mass fits

The fits to the invariant mass distributions of the $B_s^0 \to D_s^- \pi^+$ and $B_s^0 \to D_s^\mp K^\pm$ candidates require knowledge of the signal and background shapes. The signal lineshape is taken from a fit to simulated signal events which had the full trigger, reconstruction, and selection chain applied to them. Various lineshape parameterisations have been examined. The best fit to the simulated event distributions is obtained with the sum of two Crystal Ball functions [15] with a common peak position and width, and opposite side power-law tails. Mass shifts in the signal peaks relative to world average values [5], arising from an imperfect detector alignment [16], are observed in the data. These are accounted for in all lineshapes which are taken from simulated events by applying a shift of the relevant size to the simulation. A constraint on the D_s^- meson mass is used to improve the B_s^0 mass resolution. Three kinds of backgrounds need to be considered: fully reconstructed (misidentified) backgrounds, partially reconstructed backgrounds with or

without misidentification (*e.g.* $B_s^0 \to D_s^{*-} K^+$ or $B_s^0 \to D_s^- \rho^+$), and combinatorial backgrounds.

The three most important fully reconstructed backgrounds are $B^0 \to D_s^- K^+$ and $B_s^0 \to D_s^- \pi^+$ for $B_s^0 \to D_s^\mp K^\pm$, and $B^0 \to D^- \pi^+$ for $B_s^0 \to D_s^- \pi^+$. The mass distribution of the $B^0 \to D^- \pi^+$ events does not suffer from fully reconstructed backgrounds. In the case of the $B^0 \to D_s^- K^+$ decay, which is fully reconstructed under its own mass hypothesis, the signal shape is fixed to be the same as for $B_s^0 \to D_s^\mp K^\pm$ and the peak position is fixed to that found for the signal in the $B^0 \to D^- \pi^+$ fit. The shapes of the misidentified backgrounds $B^0 \to D^- \pi^+$ and $B_s^0 \to D_s^- \pi^+$ are taken from data using a reweighting procedure. First, a clean signal sample of $B^0 \to D^- \pi^+$ and $B_s^0 \to D_s^- \pi^+$ decays is obtained by applying the PID selection for the bachelor track given in Sect. 3. The invariant mass of these decays under the wrong mass hypothesis ($B_s^0 \to D_s^- \pi^+$ or $B_s^0 \to D_s^\mp K^\pm$) depends on the momentum of the misidentified particle. This momentum distribution must therefore be reweighted by taking into account the momentum dependence of the misidentification rate. This dependence is obtained using a dedicated calibration sample of D^{*+} decays originating from primary interactions. The mass distributions under the wrong mass hypothesis are then reweighted using this momentum distribution to obtain the $B^0 \to D^- \pi^+$ and $B_s^0 \to D_s^- \pi^+$ mass shapes under the $B_s^0 \to D_s^- \pi^+$ and $B_s^0 \to D_s^\mp K^\pm$ mass hypotheses, respectively.

For partially reconstructed backgrounds, the probability density functions (PDFs) of the invariant mass distributions are taken from samples of simulated events generated in specific exclusive modes and are corrected for mass shifts, momentum spectra, and PID efficiencies in data. The use of simulated events is justified by the observed good agreement between data and simulation.

The combinatorial background in the $B_s^0 \to D_s^- \pi^+$ and $B^0 \to D^- \pi^+$ fits is modelled by an exponential function where the exponent is allowed to vary in the fit. The resulting shape and normalisation of the combinatorial backgrounds are in agreement within one standard deviation with the distribution of a wrong-sign control sample (where the D_s^- and the bachelor track have the same charges). The shape of the combinatorial background in the $B_s^0 \to D_s^\mp K^\pm$ fit cannot be left free because of the partially reconstructed backgrounds which dominate in the mass region below the signal peak. In this case, therefore, the combinatorial slope is fixed to be flat, as measured from the wrong sign events.

In the $B_s^0 \to D_s^\mp K^\pm$ fit, an additional complication arises due to backgrounds from $\overline{\Lambda}_b^0 \to D_s^- \overline{p}$ and $\overline{\Lambda}_b^0 \to D_s^{*-} \overline{p}$, which fall in the signal region when misreconstructed. To avoid a loss of $B_s^0 \to D_s^\mp K^\pm$ signal, no requirement is made on the DLL_{K-p} of the bachelor particle. Instead, the $\overline{\Lambda}_b^0 \to D_s^- \overline{p}$ mass shape is obtained from simulated $\overline{\Lambda}_b^0 \to D_s^- \overline{p}$ decays, which are reweighted in momentum using the efficiency of the $\mathrm{DLL}_{K-\pi} > 5$ requirement on protons. The $\overline{\Lambda}_b^0 \to D_s^{*-} \overline{p}$ mass shape is obtained by shifting the $\overline{\Lambda}_b^0 \to D_s^- \overline{p}$ mass shape downwards by 200 MeV/c^2. The branching fractions of $\overline{\Lambda}_b^0 \to D_s^- \overline{p}$ and $\overline{\Lambda}_b^0 \to D_s^{*-} \overline{p}$ are assumed to be equal, motivated by the fact that the decays $B^0 \to D^- D_s^+$ and $B^0 \to D^- D_s^{*+}$ (dominated by similar tree topologies) have almost equal branching fractions. Therefore the overall mass shape is formed by summing the $\overline{\Lambda}_b^0 \to D_s^- \overline{p}$ and

$\overline{\Lambda}_b^0 \to D_s^{*-}\overline{p}$ shapes with equal weight; this assumption is tested as part of the study of systematic uncertainties and is not found to contribute significantly to them.

The signal yields are obtained from unbinned extended maximum likelihood fits to the data. In order to achieve the highest sensitivity, the sample is separated according to the two magnet polarities, allowing for possible differences in PID performance and in running conditions. A simultaneous fit to the samples collected with the two magnet polarities is performed for each decay, with the peak position and width of each signal, as well as the combinatorial background shape, shared between the two. The fitted signal yields in each polarity are independent of each other.

The fit under the $B_s^0 \to D_s^-\pi^+$ hypothesis requires a description of the $B^0 \to D^-\pi^+$ background. A fit to the $B^0 \to D^-\pi^+$ spectrum is first performed to determine the yield of signal $B^0 \to D^-\pi^+$ events, shown in Fig. 1. The expected $B^0 \to D^-\pi^+$ contribution under the $B_s^0 \to D_s^-\pi^+$ hypothesis is subsequently constrained with a 10% uncertainty to account for uncertainties on the PID efficiencies. The fits to the $B_s^0 \to D_s^-\pi^+$ candidates are shown in Fig. 1 and the fit results for both decay modes are summarised in Table 2. The peak position of the signal shape is varied, as are the yields of the different partially reconstructed backgrounds (except $B^0 \to D^-\pi^+$) and the shape of the combinatorial background. The width of the signal is fixed to the values found in the $B^0 \to D^-\pi^+$ fit (17.2 MeV/c^2), scaled by the ratio of widths observed in simulated events between $B^0 \to D^-\pi^+$ and $B_s^0 \to D_s^-\pi^+$ decays (0.987). The accuracy of these fixed parameters is evaluated using ensembles of simulated experiments described in Sect. 5. The yield of $B^0 \to D_s^-\pi^+$ is fixed to be 2.9% of the $B_s^0 \to D_s^-\pi^+$ signal yield, based on the world average branching fraction of $B^0 \to D_s^-\pi^+$ of $(2.16 \pm 0.26) \times 10^{-5}$, the value of f_s/f_d given in [4], and the value of the branching fraction computed in this paper. The shape used to fit this component is the sum of two Crystal Ball functions obtained from the $B_s^0 \to D_s^-\pi^+$ sample with the peak position fixed to the value obtained with the fit of the $B^0 \to D^-\pi^+$ data sample and the width fixed to the width of the $B_s^0 \to D_s^-\pi^+$ peak.

The $\overline{\Lambda}_b^0 \to \overline{\Lambda}_c^-\pi^+$ background is negligible in this fit owing to the effectiveness of the veto procedure described earlier. Nevertheless, a $\overline{\Lambda}_b^0 \to \overline{\Lambda}_c^-\pi^+$ component, whose yield is allowed to vary, is included in the fit (with the mass shape obtained using the reweighting procedure on simulated events described previously) and results in a negligible contribution, as expected.

The fits for the $B_s^0 \to D_s^\mp K^\pm$ candidates are shown in Fig. 2 and the fit results are collected in Table 2. There are numerous reflections which contribute to the mass distribution. The most important reflection is $B_s^0 \to D_s^-\pi^+$, whose shape is taken from the earlier $B_s^0 \to D_s^-\pi^+$ signal fit, reweighted according to the efficiencies of the applied PID requirements. Furthermore, the yield of the $B^0 \to D^-K^+$ reflection is constrained to the values in Table 3. In addition, there is potential cross-feed from partially reconstructed modes with a misidentified pion such as $B_s^0 \to D_s^-\rho^+$, as well as several small contributions from partially reconstructed backgrounds with similar mass shapes. The yields of these modes, whose branching fractions are known or can be estimated (*e.g.* $B_s^0 \to D_s^-\rho^+$, $B_s^0 \to D_s^-K^{*+}$), are constrained to the values in Table 3, based on criteria such as relative branching fractions and reconstruction efficiencies and PID probabilities. An important

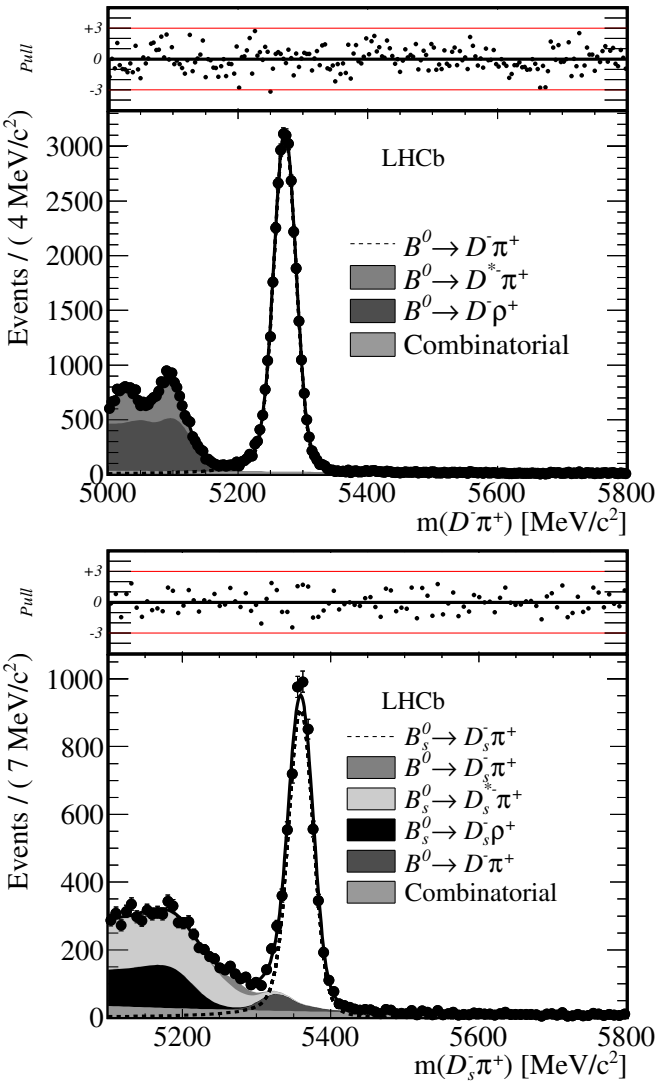

Figure 1: Mass distribution of the $B^0 \to D^-\pi^+$ candidates (top) and $B_s^0 \to D_s^-\pi^+$ candidates (bottom). The stacked background shapes follow the same top-to-bottom order in the legend and the plot. For illustration purposes the plot includes events from both magnet polarities, but they are fitted separately as described in the text.

cross-check is performed by comparing the fitted value of the yield of misidentified $B_s^0 \to D_s^-\pi^+$ events (318 ± 30) to the yield expected from PID efficiencies (370 ± 11) and an agreement is found.

Table 2: Results of the mass fits to the $B^0 \to D^-\pi^+$, $B_s^0 \to D_s^-\pi^+$, and $B_s^0 \to D_s^\mp K^\pm$ candidates separated according to the up (U) and down (D) magnet polarities. In the $B_s^0 \to D_s^\mp K^\pm$ case, the number quoted for $B_s^0 \to D_s^-\pi^+$ also includes a small number of $B^0 \to D^-\pi^+$ events which have the same mass shape (20 events from the expected misidentification). See Table 3 for the constrained values used in the $B_s^0 \to D_s^\mp K^\pm$ decay fit for the partially reconstructed backgrounds and the $B^0 \to D^-K^+$ decay channel.

Channel	$B^0 \to D^-\pi^+$		$B_s^0 \to D_s^-\pi^+$		$B_s^0 \to D_s^\mp K^\pm$	
	U	D	U	D	U	D
N_{Signal}	16304 ± 137	20150 ± 152	2677 ± 62	3369 ± 69	195 ± 18	209 ± 19
N_{Comb}	1922 ± 123	2049 ± 118	869 ± 63	839 ± 47	149 ± 25	255 ± 30
$N_{\text{Part-Reco}}$	10389 ± 407	12938 ± 441	2423 ± 65	3218 ± 69	-	-
$N_{B^0 \to D_s^- K^+}$	-	-	-	-	87 ± 17	100 ± 18
$N_{B_s^0 \to D_s^- \pi^+}$	-	-	-	-	154 ± 20	164 ± 22

Table 3: Gaussian constraints on the yields of partially reconstructed and misidentified backgrounds applied in the $B_s^0 \to D_s^\mp K^\pm$ fit, separated according to the up (U) and down (D) magnet polarities.

Background type	U	D
$B^0 \to D^-K^+$	16 ± 3	17 ± 3
$B_s^0 \to D_s^{*-}\pi^+$	63 ± 21	70 ± 23
$B_s^0 \to D_s^{*-}K^+$	72 ± 34	80 ± 27
$B_s^0 \to D_s^-\rho^+$	135 ± 45	150 ± 50
$B_s^0 \to D_s^-K^{*+}$	135 ± 45	150 ± 50
$B_s^0 \to D_s^{*-}\rho^+$	45 ± 15	50 ± 17
$B_s^0 \to D_s^{*-}K^{*+}$	45 ± 15	50 ± 17
$\overline{\Lambda}_b^0 \to D_s^-\overline{p} + \overline{\Lambda}_b^0 \to D_s^{*-}\overline{p}$	72 ± 34	80 ± 27

5 Systematic uncertainties

The major systematic uncertainities on the measurement of the relative branching fraction of $B_s^0 \to D_s^\mp K^\pm$ and $B_s^0 \to D_s^-\pi^+$ are related to the fit, PID calibration, and trigger and offline selection efficiency corrections. Systematic uncertainties related to the fit are evaluated by generating large sets of simulated experiments. During generation, certain parameters are varied. The samples are fitted with the nominal model. To give two examples, during generation the signal width is fixed to a value different from the width used in the nominal model, or the combinatorial background slope in the $B_s^0 \to D_s^\mp K^\pm$ fit is fixed to the combinatorial background slope found in the $B_s^0 \to D_s^-\pi^+$ fit. The deviations of the peak position of the pull distributions from zero are then included in the systematic uncertainty.

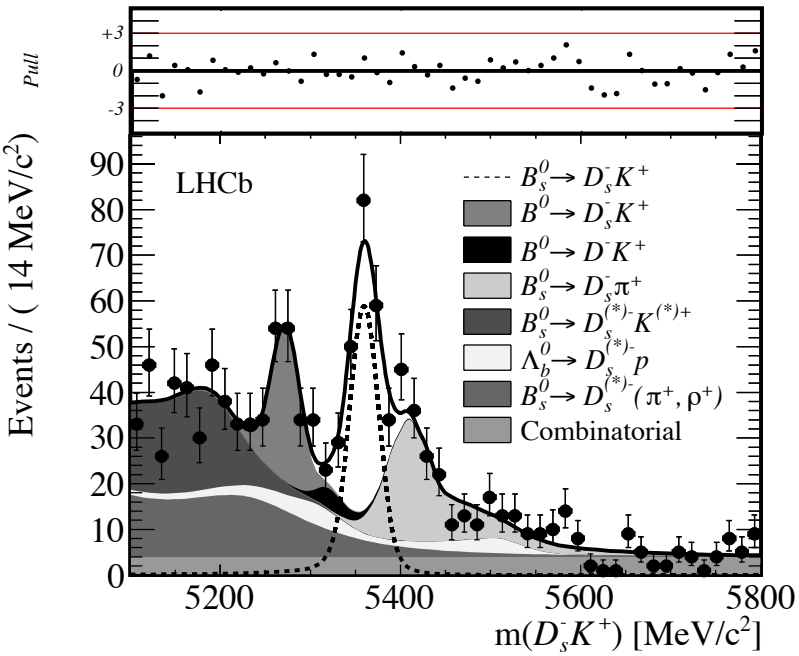

Figure 2: Mass distribution of the $B_s^0 \to D_s^{\mp} K^{\pm}$ candidates. The stacked background shapes follow the same top-to-bottom order in the legend and the plot. For illustration purposes the plot includes events from both magnet polarities, but they are fitted separately as described in the text.

Table 4: Relative systematic uncertainities on the branching fraction ratios.

Source	$\frac{B_s^0 \to D_s^{\mp} K^{\pm}}{B_s^0 \to D_s^- \pi^+}$ (%)	$\frac{B_s^0 \to D_s^- \pi^+}{B^0 \to D^- \pi^+}$ (%)	$\frac{B_s^0 \to D_s^{\mp} K^{\pm}}{B^0 \to D^- \pi^+}$ (%)
All non-PID selection	2.0	2.0	3.0
PID selection	1.8	1.3	2.2
Fit model	2.4	1.7	2.2
Efficiency ratio	1.5	1.6	1.6
Total	3.9	3.4	4.6

In the case of the $B_s^0 \to D_s^{\mp} K^{\pm}$ fit the presence of constraints for the partially reconstructed backgrounds must be considered. The generic extended likelihood function can

be written as

$$\mathcal{L} = \frac{e^{-N} N^{N_{\rm obs}}}{N_{\rm obs}!} \times \prod_j G(N^j; N_c^j, \sigma_{N_0^j}) \times \prod_{i=1}^{N_{\rm obs}} P(m_i; \vec{\lambda}) \,, \tag{1}$$

where the first factor is the extended Poissonian likelihood in which N is the total number of fitted events, given by the sum of the fitted component yields $N = \sum_k N_k$. The fitted data sample contains $N_{\rm obs}$ events. The second factor is the product of the j external constraints on the yields, $j < k$, where G stands for a Gaussian PDF, and $N_c \pm \sigma_{N_0}$ is the constraint value. The third factor is a product over all events in the sample, P is the total PDF of the fit, $P(m_i; \vec{\lambda}) = \sum_k N_k P_k(m_i; \vec{\lambda}_k)$, and $\vec{\lambda}$ is the vector of parameters that define the mass shape and are not fixed in the fit.

Each simulated dataset is generated by first varing the component yield N_k using a Poissonian PDF, then sampling the resulting number of events from P_k, and repeating the procedure for all components. In addition, constraint values N_c^j used when fitting the simulated dataset are generated by drawing from $G(N; N_0^j, \sigma_{N_0^j})$, where N_0^j is the true central value of the constraint, while in the nominal fit to the data $N_c^j = N_0^j$.

The sources of systematic uncertainty considered for the fit are signal widths, the slope of the combinatorial backgrounds, and constraints placed on specific backgrounds. The largest deviations are due to the signal widths and the fixed slope of the combinatorial background in the $B_s^0 \to D_s^\mp K^\pm$ fit.

The systematic uncertainty related to PID enters in two ways: firstly as an uncertainty on the overall efficiencies and misidentification probabilities, and secondly from the shape for the misidentified backgrounds which relies on correct reweighting of PID efficiency versus momentum. The absolute errors on the individual K and π efficiencies, after reweighting of the D^{*+} calibration sample, have been determined for the momentum spectra that are relevant for this analysis, and are found to be 0.5% for $\mathrm{DLL}_{K-\pi} < 0$ and 0.5% for $\mathrm{DLL}_{K-\pi} > 5$.

The observed signal yields are corrected by the difference observed in the (non-PID) selection efficiencies of different modes as measured from simulated events:

$$\begin{aligned} \epsilon^{\rm Sel}_{B_s^0 \to D_s^- \pi^+} / \epsilon^{\rm Sel}_{B^0 \to D^- \pi^+} &= 1.020 \pm 0.016 \,, \\ \epsilon^{\rm Sel}_{B_s^0 \to D_s^\mp K^\pm} / \epsilon^{\rm Sel}_{B_s^0 \to D_s^- \pi^+} &= 1.061 \pm 0.016 \,. \end{aligned}$$

A systematic uncertainty is assigned on the ratio to account for percent level differences between the data and the simulation. These are dominated by the simulation of the hardware trigger. All sources of systematic uncertainty are summarized in Table 4.

6 Determination of the branching fractions

The $B_s^0 \to D_s^\mp K^\pm$ branching fraction relative to $B_s^0 \to D_s^- \pi^+$ is obtained by correcting the raw signal yields for PID and selection efficiency differences

$$\frac{\mathcal{B}\left(B_s^0 \to D_s^{\mp} K^{\pm}\right)}{\mathcal{B}\left(B_s^0 \to D_s^- \pi^+\right)} = \frac{N_{B_s^0 \to D_s^{\mp} K^{\pm}}}{N_{B_s^0 \to D_s^- \pi^+}} \frac{\epsilon^{\rm PID}_{B_s^0 \to D_s^- \pi^+}}{\epsilon^{\rm PID}_{B_s^0 \to D_s^{\mp} K^{\pm}}} \frac{\epsilon^{\rm Sel}_{B_s^0 \to D_s^- \pi^+}}{\epsilon^{\rm Sel}_{B_s^0 \to D_s^{\mp} K^{\pm}}} \,, \tag{2}$$

where ϵ_X is the efficiency to reconstruct decay mode X and N_X is the number of observed events in this decay mode. The PID efficiencies are given in Table 1, and the ratio of the two selection efficiencies were given in the previous section.

The ratio of the branching fractions of $B_s^0 \to D_s^{\mp} K^{\pm}$ relative to $B_s^0 \to D_s^- \pi^+$ is determined separately for the down (0.0601 ± 0.0056) and up (0.0694 ± 0.0066) magnet polarities and the two results are in good agreement. The quoted errors are purely statistical. The combined result is

$$\frac{\mathcal{B}\left(B_s^0 \to D_s^{\mp} K^{\pm}\right)}{\mathcal{B}\left(B_s^0 \to D_s^- \pi^+\right)} = 0.0646 \pm 0.0043 \pm 0.0025 \,,$$

where the first uncertainty is statistical and the second is the total systematic uncertainty from Table 4.

The relative yields of $B_s^0 \to D_s^- \pi^+$ and $B^0 \to D^- \pi^+$ are used to extract the branching fraction of $B_s^0 \to D_s^- \pi^+$ from the following relation

$$\frac{\mathcal{B}(B_s^0 \to D_s^- \pi^+)}{\mathcal{B}\left(B^0 \to D^- \pi^+\right)} = \frac{\epsilon^{{\rm Sel}_{B^0 \to D^- \pi^+}}}{\epsilon^{{\rm Sel}_{B_s^0 \to D_s^- \pi^+}}} \frac{\epsilon^{{\rm PID}_{B^0 \to D^- \pi^+}}}{\epsilon^{{\rm PID}_{B_s^0 \to D_s^- \pi^+}}} \frac{N_{B_s^0 \to D_s^- \pi^+}}{\frac{f_s}{f_d} N_{B^0 \to D^- \pi^+}} \frac{\mathcal{B}\left(D^- \to K^+ \pi^- \pi^-\right)}{\mathcal{B}\left(D_s^- \to K^- K^+ \pi^-\right)} \,, \tag{3}$$

using the recent f_s/f_d measurement from semileptonic decays [4]

$$\frac{f_s}{f_d} = 0.268 \pm 0.008^{+0.022}_{-0.020} \,,$$

where the first uncertainty is statistical and the second systematic. Only the semileptonic result is used since the hadronic determination of f_s/f_d relies on theoretical assumptions about the ratio of the branching fractions of the $B_s^0 \to D_s^- \pi^+$ and $B^0 \to D^- \pi^+$ decays. In addition, the following world average values [5] for the B and D branching fractions are used

$$\begin{aligned}
\mathcal{B}(B^0 \to D^- \pi^+) &= (2.68 \pm 0.13) \times 10^{-3} \,, \\
\mathcal{B}(D^- \to K^+ \pi^- \pi^-) &= (9.13 \pm 0.19) \times 10^{-2} \,, \\
\mathcal{B}(D_s^- \to K^+ K^- \pi^-) &= (5.49 \pm 0.27) \times 10^{-2} \,,
\end{aligned}$$

leading to

$$\begin{aligned}
\mathcal{B}(B_s^0 \to D_s^- \pi^+) &= (2.95 \pm 0.05 \pm 0.17^{+0.18}_{-0.22}) \times 10^{-3} \,, \\
\mathcal{B}(B_s^0 \to D_s^{\mp} K^{\pm}) &= (1.90 \pm 0.12 \pm 0.13^{+0.12}_{-0.14}) \times 10^{-4} \,,
\end{aligned}$$

where the first uncertainty is statistical, the second is the experimental systematics (as listed in Table 4) plus the uncertainty arising from the $B^0 \to D^- \pi^+$ branching fraction, and the third is the uncertainty (statistical and systematic) from the semileptonic f_s/f_d measurement. Both measurements are significantly more precise than the existing world averages [5].

References

[1] R. Fleischer, *New strategies to obtain insights into CP violation through $B_s \to D_s^{\pm}K^{\mp}, D_s^{*\pm}K^{\mp}, ...$ and $B_d \to D^{\pm}\pi^{\mp}, D^{*\pm}\pi^{\mp}, ...$ decays*, Nucl. Phys. **B671** (2003) 459, arXiv:hep-ph/0304027.

[2] CDF collaboration, T. Aaltonen *et al.*, *First observation of $\bar{B}_s^0 \to D_s^{\pm}K^{\mp}$ and measurement of the ratio of branching fractions $B(\bar{B}_s^0 \to D_s^{\pm}K^{\mp})$ /$B(\bar{B}_s^0 \to D_s^{+}\pi^{-})$*, Phys. Rev. Lett. **103** (2009) 191802, arXiv:0809.0080.

[3] Belle collaboration, R. Louvot *et al.*, *Measurement of the decay $B_s^0 \to D_s^-\pi^+$ and evidence for $B_s^0 \to D_s^{\mp}K^{\pm}$ in e^+e^- annihilation at $\sqrt{s} \sim 10.87$ GeV*, Phys. Rev. Lett. **102** (2009) 021801, arXiv:0809.2526.

[4] LHCb collaboration, R. Aaij *et al.*, *Measurement of b hadron production fractions in 7 TeV pp collisions*, Phys. Rev. D **85** (2012) 032008, arXiv:1111.2357.

[5] Particle Data Group, K. Nakamura *et al.*, *Review of particle physics*, J. Phys. **G37** (2010) 075021.

[6] LHCb collaboration, A. A. Alves Jr. *et al.*, *The LHCb detector at the LHC*, JINST **3** (2008) S08005.

[7] V. V. Gligorov, C. Thomas, and M. Williams, *The HLT inclusive B triggers*, LHCb-PUB-2011-016.

[8] T. Sjöstrand, S. Mrenna, and P. Skands, *PYTHIA 6.4 Physics and manual*, JHEP **05** (2006) 026, arXiv:hep-ph/0603175.

[9] I. Belyaev *et al.*, *Handling of the generation of primary events in* Gauss*, the LHCb simulation framework*, Nuclear Science Symposium Conference Record (NSS/MIC) **IEEE** (2010) 1155.

[10] D. J. Lange, *The EvtGen particle decay simulation package*, Nucl. Instrum. Meth. **A462** (2001) 152.

[11] GEANT4 collaboration, S. Agostinelli *et al.*, *GEANT4: A simulation toolkit*, Nucl. Instrum. Meth. **A506** (2003) 250.

[12] P. Golonka and Z. Was, *PHOTOS Monte Carlo: A Precision tool for QED corrections in Z and W decays*, Eur. Phys. J. **C45** (2006) 97, arXiv:hep-ph/0506026.

[13] A. Hoecker *et al.*, *TMVA: Toolkit for multivariate data analysis*, PoS **ACAT** (2007) 040, arXiv:physics/0703039.

[14] LHCb collaboration, R. Aaij *et al.*, *Determination of f_s/f_d for 7 TeV pp collisions and measurement of the $B^0 \to D^-K^+$ branching fraction*, Phys. Rev. Lett. **107** (2011) 211801, arXiv:1106.4435.

[15] T. Skwarnicki, *A study of the radiative cascade transitions between the Upsilon-prime and Upsilon resonances*. PhD thesis, Institute of Nuclear Physics, Krakow, 1986, DESY-F31-86-02.

[16] LHCb collaboration, R. Aaij *et al.*, *Measurement of b-hadron masses*, Phys. Lett. **B708** (2012) 241, arXiv:1112.4896.

Summary
First measurement of the fragmentation fraction ratio f_s/f_d with tree level hadronic decays at 7 TeV pp collisions

The important thing is not to stop questioning.
Albert Einstein

A bit of history

Curiosity is an intrinsic characteristic of the human nature. One puzzle that philosophers and physicists have pondered for centuries is the question "what is matter?". The Greek philosopher Democritus proposed it is made of indivisible elements, that he called "atoms". Incredibly, this first intuition from 400 a.C. was closer to our present description than he might imagined. The long tale of physics brings us to particle physics where matter is depicted through theories describing the existence and interactions of particles using a mathematical language.

A scientific theory has to be able to describe the known observations but at the same time to predict new observables that can be measured with experiments. In the 70s a great revolution in particle physics happened: a theory, called Standard Model (SM), was developed. This theory accounts for three of the four fundamental interactions between elementary particles, missing to describe only the role of gravity. This theory was confirmed by a wealth of experimental results over the last decades. Despite its success, the SM is not considered to be the conclusive theory of elementary particles. The presence of a large number of parameters leaves the physicists unsatisfied. Moreover looking to the sky, it turnes out there is much more material than we would expect. Most of this matter is invisible: it cannot be detected by telescope, but it can be only inferred through gravitational effects like gravitational lensing or rotation curves. None of the known particles is a satisfactory candidate to build up

this “dark matter”. These examples show that our description of the world is incomplete and stimulate theoretical physicists to propose new theories to extend the SM. The experimental physicists are therefore encouraged to look for and study the properties of new particles predicted by these theories. The race for looking for “New Physics” started several years ago with the Tevatron accelerator and now it is the main goal of the experiments located at LHC.

How to search for new physics

There are two possible ways to search for new physics (NP): direct production of new particles, as e.g. in the ATLAS and CMS experiments, or looking for the indirect effects of these new particles on other observables. The advantage of the latter is that it is possible to see indirect effects at lower beam energies than that needed to produce them directly: if the masses of the new particles are greater than those which the LHC can produce, the indirect approach would be the only way to discover NP soon. Moreover, since the two techniques are complementary, by bringing together their results, new physics scenario can be confirmed or excluded in the near future.

Not all the particles are stable: after a certain time they can decay in a set of other particles (called “final state”). One of the interesting observables that can be looked at is the branching fraction. This quantity represents the fraction of particles which decay in a specific final state with respect to the total number of particles. We consider a decay to be “rare” if its final state can be reached only few times every billion of events. In these decays, new physics contributions would perceivably enhance the SM branching fraction expectation showing clearly the presence of new phenomena beyond this model. The fact that they happen so rarely sets up a technical challenge that brings us to build detectors with high performance and to put a constant effort to calibrate and monitor their behaviour.

B–meson decays

Quarks are elementary particles that clump together, (“confinement”), in the process called “hadronization” to form groups named “hadrons”. Anti–quarks differ from quarks only with their electric charge, which has opposite sign. If only a quark and an anti–quark ($q\bar{q}$) form an hadron we have a particle called “meson”.

There are several unstable particles, and the kind relevant for this thesis are the B–mesons. Two kinds of B–meson are considered: the B^0 (with a $d\bar{b}$ pair) the B_s^0 (with a $s\bar{b}$ pair). The first meson is lighter and was deeply studied in the past, obtaining precise measurements of its decay rate. Much less precise measurements are instead available in literature for the B_s^0–meson.

Detector monitoring

The decays considered in this thesis have a similar final state made of two kinds of charged mesons: pions ($\pi^{\pm}$) and kaons ($K^{\pm}$). For their identification and to limit the amount of background in the analysis we need to achieve an excellent particle identification[1] and mass resolution[2].

One of the main components of an experiment is the "tracking system": a set of sub–detectors used to identify where a particle passes, what is its charge, and to have information about its mass and velocity. The trajectory of the particle in these sub–detectors is called "track". In the LHCb experiment we define the "track type" by looking which tracking sub–detector was traversed. A high quality of the track reconstruction represents a key ingredient for an excellent mass resolution. Several methods have been developed in the LHCb experiment to determine the track finding efficiency for charged particles. We propose in this thesis a novel technique that is not affected by any selection requirements and that gives the agreement between data and simulation per type of track. This technique was determinant in the evaluation of the tracking efficiency uncertainty for the first data acquired at LHCb when the beam conditions were peculiar. We found a good agreement between data and simulation for all types of track for both 2009 and beginning of 2010 data taking periods with typically an estimated uncertainty of around 3%.

An important sub–detector of the tracking system in LHCb is the Outer Tracker (OT) which is a gas detector covering the external part of the tracking system. A detector has to withstand a large dose of irradiation due to the traversing particles during the "life time" of an experiment (typically 10 years). This large irradiation dose can decrease the performance of the detector, what is usually called "ageing". In a gas detector a typical sign of ageing is the reduction of the signal height. In 2005 a first evidence of an unexpected ageing, due to an insulating carbon deposit on the wires, in the OT modules was found. Several years of studies were devoted in understanding the characteristics and the origin of this ageing, as well as to device long term solutions to deal with this problem without rebuilding all the modules. We present in this thesis the evidence that the culprit of the ageing is the plastifier in the glue used to seal the modules, as well as several techniques to reduce the gain loss or even to restore the original gain. It is shown that the addition of oxygen (1.5%) in the gas–mixture reduces the gain loss of a factor of two, probably because of the formation of beneficial radicals (ozone) that neutralize the malicious deposits. Moreover, a technique, called HV–training, showed to be able to prevent and restore the original gain after an insulating layer was deposited on the wires. This technique is applicable also *in situ* on the final modules, if need. The ageing rate *in situ* is constantly monitored with several techniques, like for example periodic radioactive source scans during LHC shut–down periods. No sign of gain loss has been observed to date.

The monitor of the ageing rate is important, but it is not sufficient to guarantee high per-

[1] With particle identification we mean the process of using information left by a particle passing through a particle detector to identify the type of particle. In LHCb two Cherenkov detectors are used for this.

[2] With mass resolution we mean the ability to distinguish two peaks of slightly different mass in a mass spectrum.

formance of the detector. We need, in fact, to monitor also the stability and the quality of the readout signal. In this thesis we present a number of monitoring and data–quality analysis tasks that have been developed and that were continuously used to detect noisy or broken components. This allowed to have the number of working channel constantly higher than 98% during the whole data taking period between 2009 and 2011. The high performance maintained during these first years of data taking brought the LHCb experiment to already have a leading role in the field of B–physics.

Looking for precision

The $B_s^0 \to \mu^+\mu^-$ decay channel is one of the most promising rare decays for testing the SM since its branching fraction prediction is theoretically precise: the experimental measurement of a branching fraction significantly different from this prediction would be a clear sign of new physics. On the other hand, it is also a perfect way to test new possible models: a precise limit or even a measurement at the expected value from the SM, together with other results from direct searches for new physics, would rule out a set of possible theories. However, to be sensitive to a discrepancy between the predicted SM value of the branching fraction and the measured one, the final uncertainty has to be as small as possible. There are three main sources of uncertainty:

- **statistical**: this uncertainty is mainly related to the collected amount of data surviving the selection
- **systematic**: this uncertainty is mainly related to the assumptions needed during the analysis process
- **normalisation**: this uncertainty is related to the need at hadron colliders to normalise your decay channel of interest to another well known decay

The best precision for the $B_s^0 \to \mu^+\mu^-$ branching fraction measurement can be achieved by normalising this channel to a B^0 decay, for which a precise measured of the branching fraction is available in literature. However, this requires the measurement of the parameter f_s/f_d, that represents the probability ratio that a b–quark hadronizes with a d or an s–quark. This parameter was measured by the experiments at the LEP and Tevatron colliders but its value can *a priori* not be extrapolated to the LHC environment since it can in principle depend on the environmental conditions. This parameter was usually measured with semi–leptonic decays. These decays have a neutrino particle in the final state. The neutrinos are particularly difficult to detect since they interact only through the so called "weak force": from an experimental point of view, decays with a neutrino are challenging since one of the final state particles cannot be reconstructed. An alternative method, exploited in this thesis, is to measure f_s/f_d through the combined measurement of the hadronic decays $B^0 \to D^-K^+$, $B^0 \to D^-\pi^+$ and $B_s^0 \to D_s^-\pi^+$. These are very favourable from an experimental point of view for LHCb, robust with respect to new physics contributions and theoretically well understood.

We present in this thesis two measurements of f_s/f_d with 35 pb^{-1} of data. The first measurement is obtained looking at the relative amount of $B^0 \to D^- K^+$ and $B_s^0 \to D_s^- \pi^+$ while the second comes from the relative amount of $B^0 \to D^- \pi^+$ and $B_s^0 \to D_s^- \pi^+$. The former measurement is dominated by the statistical uncertainty, because of the amount of data available at the time of the analysis, while the latter is dominated by the theoretical uncertainty. The first measurement will be soon updated with 1.0 fb^{-1} of data acquired in 2011. The two measurements are in good agreement with each other and can be combined into a single value, by taking all correlated uncertainties into account. An averaged value of $f_s/f_d = 0.253 \pm 0.017^{\text{stat}} \pm 0.018^{\text{syst}} \pm 0.020^{\text{theor}}$ for f_s/f_d is obtained. Moreover, the LHCb experiment has reported a measurement of the ratio $f_s/(f_u + f_d)$ using semi–leptonic decays of b–hadrons, $f_s/(f_u + f_d) = 0.134 \pm 0.004^{+0.011}_{-0.010}$ [6]. The combination of these results with the two hadronic measurements resulted in the world best measurement $f_s/f_d = 0.267^{+0.021}_{-0.020}$.

The precision of the f_s/f_d measurement affects the NP discovery potential for the $B_s^0 \to \mu^+\mu^-$ decay. For large data samples and small experimental systematic uncertainty (i.e. in ideal conditions), the uncertainty in f_s/f_d becomes the key element for a discovery of new physics, determining the minimal value of the branching fraction (BR) for which one can claim evidence of new physics, as shown in Fig. 8.5. In particular, we show that these limits are $BR < 2.6 \times 10^{-9}$ or $BR > 4.2 \times 10^{-9}$ if we use the presented f_s/f_d uncertainty around 8% and the SM branching ratio of $(3.2 \pm 0.2) \times 10^{-9}$ in the ideal conditions. This range is already much tighter than what was accessible with the previous best world measurement of f_s/f_d at Tevatron that was affected by an uncertainty of 12%.

The f_s/f_d parameter is in principle dependent on the environmental characteristics, therefore a direct measurement of it by the CMS collaboration is desirable. The measurement presented in this thesis, as well as the semi–leptonic measurement are difficult at CMS since different detector design choices were made. We propose therefore an alternative method based on the extrapolation of the LHCb result using the measurement of other two B^0 and B_s^0 decays, this time with an accessible final state for the CMS experiment.

An other way to test the Standard Model

In the SM there are six quarks with masses ranging between ~ 2.5 MeV/c^2 for the "up" quark (u) to ~ 172.2 GeV/c^2 for the "top" quark (t). The probability of the transition from a quark q to a quark q' is proportional to $|V_{qq'}|^2$ where $V_{qq'}$ is the element of a matrix called Cabibbo-Kobayashi-Maskawa (CKM), see Fig. 8.6 (a).

The CKM matrix has a property known as "unitarity" due to the physical properties it represents. Mathematically, this defines a set of equations that the matrix elements must satisfy and that can be represented as a triangle in a complex plane, see Fig. 8.6 (b).

The properties of this triangle, the side lengths, total area and angles, can be evaluated experimentally by studying particular B-decays. The least precise direct measured parameter of the unitary triangle is the angle γ. One way to access this angle is studying the $B_s^0 \to D_s^\pm K^\mp$ decay channel. Before we can extract the angle γ it is necessary to show that we are able to precisely measure its branching fraction, that is up to now poorly known (uncer-

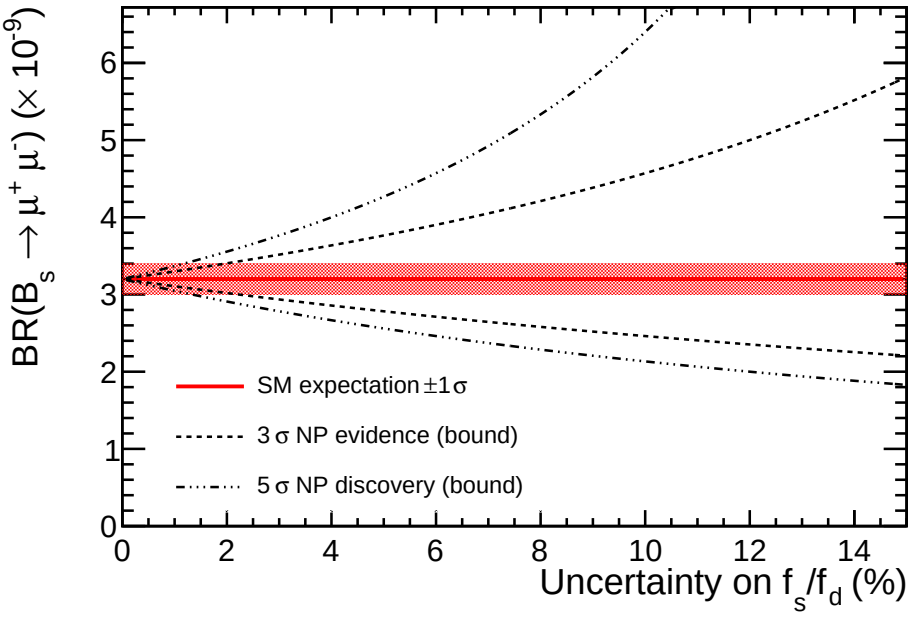

Figure 8.1: Limit of $B_s^0 \to \mu^\pm\mu^\mp$ discovery potential (3 and 5 σ) in the limit of infinite statistics and negligible systematic uncertainty as a function of the uncertainty on the f_s/f_d measurement. Currently the uncertainty is 8%.

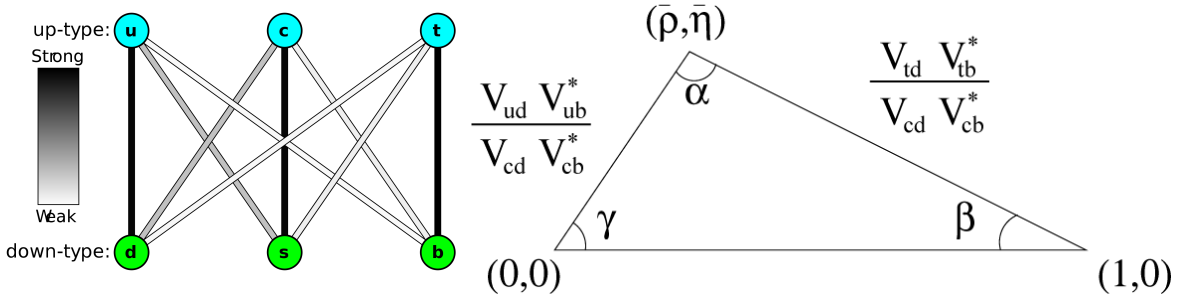

(a) (b)

Figure 8.2: (a): Representation of the six quarks in the SM and their relations. The "intensities" (grey scale) of the lines are determined by the elements of the CKM matrix. (b): unitarity triangle in the complex plane $(\bar{\rho},\bar{\eta})$ [103].

tainty of 23%). We present in this thesis the new world best measurement of the branching fraction of the $B_s^0 \to D_s^\pm K^\mp$ decay obtained from the analysis of a data sample of 0.37 fb^{-1}. The result obtained is $1.90 \pm 0.12^{stat} \pm 0.13^{syst}{}^{+0.12}_{-0.14}{}^{f_s/f_d}$ where the total uncertainty is now around 12%. At the same time, we presented the new world best branching fraction measurement of the $B_s^0 \to D_s^- \pi^+$ decay channel $2.95 \pm 0.05^{stat} \pm 0.17^{syst}{}^{+0.18}_{-0.22}{}^{f_s/f_d}$, with a total uncertainty around 10% and it represents the best known B_s^0 decay mode to date.

Outlook

The results presented in this thesis show that it is possible to monitor and guarantee high performance of an important sub–detector of the LHCb experiment in the first years of data taking. This is reflected, for example, in the possibility of a precise measurement of the f_s/f_d fragmentation fraction ratio: a key element in the determination of the branching fraction of the $B_s^0 \to \mu^+\mu^-$ decay used for the NP search. Moreover, with the data from 2011, the study of this value as a function of kinematic parameters is foreseen. This dependency study, together with the evaluation of the ratio of other decay channels easily measurable in CMS, would allow an extrapolation of f_s/f_d factor to the CMS acceptance.

In addition, the LHCb collaboration announced recently the new world best measurement of the limit on the $B_s^0 \to \mu^+\mu^-$ branching fraction using the f_s/f_d result presented in this thesis. The LHCb experiment obtained the probability that a B_s^0–meson decays into a pair of oppositely charged muons not larger than 4.5 times out of one billion decays [104]. The new result represents a milestone in the search for new physics beyond the Standard Model. This result can bring a slight wind of pessimism: everybody had been hoping to see the first signs of new physics revealed by a small excess in the branching ratio predicted by the Standard Model. On the other hand it is still possible to find a smaller branching ratio than the one predicted by the Standard Model. This would be another way to open the door for new physics, a fact that received little attention before but that is becoming possible now with the increase in precision. In any case thanks to this measurement, the LHCb experiment is already probing the region accessible to new models, ruling out a large area of the parameter space for different models predicting new physics.

Samenvatting
Eerste meting van de fragmentatiebreukverhouding f_s/f_d met laagste orde hadronische vervallen bij 7 TeV pp botsingen

Het belangrijkste in het leven, is om niet op te houden met het stellen van vragen.
Albert Einstein

Een beetje geschiedenis

Nieuwsgierigheid is een intrinsieke eigenschap van de mens. Een puzzel die filosofen en fysici honderden jaren bezighield is de vraag "Wat is materie?". De griekse filosoof Democritus stelde voor dat het gemaakt is uit ondeelbare elementen die hij "atomen" noemde. Ongelooflijk is deze eerste intuitie dichter bij onze hedendaagse beschrijving komt dan hij had kunnen voorstellen. Het lange verhaal van de natuurkunde brengt ons bij de elementaire-deeltjesfysica waar materie wordt verbeeld door theorieën die het bestaan en de interacties van deeltjes beschrijven door gebruik te maken van een wiskundige taal.

Een wetenschappelijke theorie moet de bekende observaties kunnen beschrijven maar tegelijkertijd ook nieuwe observabelen kunnen voorspellen die kunnen worden gemeten in experimenten. In de jaren 70 van de vorige eeuw was een grote revolutie gaande in de deeltjesfysica: Er werd een theorie ontwikkeld, genaamd het Standaard Model (SM). Deze theorie beschrijft drie van de vier fundamentele interacties tussen elementaire deeltjes, slechts gemankeerd in zijn beschrijving door de rol van de zwaartekracht. Deze theorie werd gedurende de voorgaande tientallen jaren door een weelde van experimentele resultaten bevestigd. Ondanks zijn succes wordt het SM niet gezien als de allesbeslissende

theorie van elementaire deeltjes. De aanwezigheid van een groot aantal parameters laat de fysici veel te wensen over. Bovendien, kijkend naar de hemel, blijkt dat er veel meer materiaal is dan we zouden verwachten. De meeste materie is onzichtbaar: Het kan niet met een telescoop worden gedetecteerd, maar slechts afgeleid worden uit gravitationele effecten zoals zwaartekrachtslenzen of rotatiecurves. Geen van de bekende deeltjes is een toereikende kandidaat om deze "donkere materie" uit op de bouwen. Deze voorbeelden laten zien dat onze beschrijving van de wereld incompleet is en stimuleren de theoretisch fysici om nieuwe theorieën voor te stellen om het SM uit te breiden. De experimentele fysici worden aangemoedigd om te zoeken naar nieuwe deeltjes en de eigenschappen te bestuderen die door de theorie worden voorspelt. De race om naar "Nieuwe Natuurkunde" te zoeken is een aantal jaren geleden gestart met de Tevatron versneller en het is nu het belangrijkste doel van de experimenten aan de LHC.

Hoe te zoeken naar nieuwe natuurkunde

Er zijn twee verschillende manieren om naar nieuwe natuurkunde te zoeken: Directe productie van nieuwe deeltjes, zoals in de ATLAS en CMS experimenten, of het zoeken naar de indirecte effecten van deze nieuwe deeltjes op andere grootheden. Het voordeel van het laatste is dat het mogelijk is om de indirecte effecten bij een lagere bundel energieën te zien dan welke nodig zijn voor directe productie: Als de massa's van de deeltjes groter zijn dan de LHC kan produceren, is de indirecte benadering de enige manier om nieuwe natuurkunde snel te ontdekken. Bovendien, omdat de twee technieken complementair zijn, kunnen ze bijeengevoegd worden, en scenarios waarin nieuwe natuurkunde een rol speelt kunnen worden bevestigd of uitgesloten worden in de nabije toekomst.

Niet alle deeltjes zijn stabiel: na verloop van tijd kunnen ze vervallen in een verzameling andere deeltjes (genaamd de "eindtoestand"). Een van de interessante observabelen waar naar gekeken kan worden, is de vertakkingsverhouding. Deze grootheid stelt het gedeelte voor van de van de deeltjes die naar een bepaalde eindtoestand vervallen tenopzichte van het totale aantal deeltjes.

We kunnen een verval als "zeldzaam" beschouwen als de eindtoestand bereikt kan worden in slechts enkele van miljarden vervalsgebeurtenissen. In deze vervallen zullen de bijdragen van nieuwe fysica waarneembaar de SM vertakkingsverhouding vergroten, en zodoende duidelijk de aanwezigheid van nieuwe effecten buiten dit model tonen. Het feit dat het zo zelden gebeurt, brengt een technische uitdaging met zich mee om detectoren te bouwen met een grote efficientie en stelt een continue inspanning om ze te calibreren en hun gedrag in de gaten te houden.

B–meson vervallen

Quarks zijn elementaire deeltjes die samenklonteren, ("confinement"), in een proces genaamd "hadronisatie" om groepen te vormen genaamd "hadronen". Anti–quarks verschillen van de quarks alleen in hun elektrische lading, die een tegengesteld teken heeft.

Als alleen een quark en een anti-quark ($q\bar{q}$) een hadron vormen, hebben we een deeltje genaamd "meson".

Er zijn verscheidene instabiele deeltjes, en het relevante soort voor dit proefschrift zijn de B-mesonen. Twee soorten B-mesonen worden in beschouwing genomen: B^0 (met een $d\bar{b}$ paar) en B_s^0 (met een $s\bar{b}$ paar). Het eerste meson is lichter en werd uitgebreid onderzocht in het verleden, waarbij precieze metingen van het vervalstempo zijn verkregen. Tegengesteld zijn er veel minder precieze metingen beschikbaar in de literatuur voor het B_s^0–meson.

Detectorbewaking

De vervallen die in dit proefschrift in ogenschouw zijn genomen, hebben een vergelijkbare eindtoestand gemaakt uit twee soorten geladen mesonen: pionen ($\pi^{\pm}$) en kaonen ($K^{\pm}$). Om deze deeltjes te identificeren en om de hoeveelheid achtergrond in de analyse te beperken, moeten we een uitmuntende deeltjesidentificatie[3] en een massaresolutie[4] bewerkstelligen.

Een van de voornaamste componenten van een experiment is het "tracking" systeem: een verzameling subdetectoren die worden gebruikt om de sporen te identificeren waar een deeltje is langs gegaan, wat zijn lading is, en om informatie te verkrijgen over zijn massa en snelheid. De baan van een deeltje door de subdetectoren heet een "spoor". In het LHCb experiment wordt een spoortype bepaald aan de hand van welke subdetector gepasseerd wordt. Een hoge kwaliteit van de spoorreconstructie vormt een sleutelingrediënt voor een uitmuntende massaresolutie. Verschillende methoden zijn ontwikkeld binnen het LHCb experiment om de efficientie van spoorreconstructie voor geladen deeltjes te bepalen. Wij presenteren in dit proefschrift een nieuwe techniek die niet beïnvloed wordt door selectievoorwaarden en die een overeenstemming biedt tussen de gegevens en de simulatie per spoortype. Deze techniek is gebruikt in de evaluatie van de onzekerheid van de spoorefficientie in de eerstverkregen meetgegevens bij LHCb toen de bundelcondities vreemd waren. We vonden een goede overeenstemming tussen de meetgegevens en simulatie voor alle spoortypes voor de meetperioden van zowel 2009 alsook het begin van 2010, met een geschatte onzekerheid van ongeveer 3%.

Een belangrijke sub-detector van het "tracking" systeem in LHCb is de Outer Tracker (OT), dit is een gasdetector die het buitenste gedeelte van het spoorreconstructiesysteem beslaat. De detector moet een grote dosis straling weerstaan door de grote flux deeltjes die door de detector gaan tijdens de levensduur van het experiment (normaal 10 jaar). Deze grote stralingsdosis kan de prestatie van de detector verlagen, dit wordt 'ageing' of veroudering genoemd. Een teken van veroudering in een gasdetector is de verlaging van de signaalhoogte. In 2005 werd het eerste bewijs voor detectorveroudering in de OT gevonden, veroorzaakt door een laagje koolstofafzetting op de draden. Enkele jaren van onderzoek werden gewijd om de eigenschappen en oorzaak van deze veroudering te begrijpen, alsook

[3] Met deeltjesidentificatie wordt bedoeld het proces om de informatie achtergelaten door een deeltje in een detector te gebruiken om het type deeltje te identificeren. In LHCb worden hiervoor twee Cherekov detectoren gebruikt.

[4] Met massaresolutie wordt bedoeld het vermogen om twee pieken met een klein verschil in massa te onderscheiden in een massa spectrum.

om lange-termijn oplossingen te vinden zonder alle modules opnieuw te hoeven bouwen. We presenteren in dit proefschrift het bewijs dat de schuldige factor van de veroudering de weekmaker in de lijm is die gebruikt werd om de modules te sluiten, en ook beschrijven we enkele technieken om het verlies in versterking (gain) te verminderen of om de originele versterking te herstellen. We laten zien dat de toevoeging van zuurstof (1.5%) in het gasmengsel het verlies in versterking met een factor twee vermindert, waarschijnlijk door het ontstaan van heilzame radicalen (ozon) die de schadelijke afzettingen neutraliseren. Bovendien liet een techniek genaamd HV training zien dat een bescherming mogelijk is en om de originele versterkingsfactor te herstellen nadat er een isolerende laag was afgezet op de draden. Indien nodig kan deze techniek ook *in situ* worden gebruikt op de modules. De verouderingssnelheid *in situ* wordt continu gecontroleerd met verschillende technieken, zoals bijvoorbeeld periodieke radioactieve scans gedurende een periode dat de LHC niet in gebruik is. Geen verlies in de versterkingsfactor is tot op heden gemeten.

Het bewaken van het verouderingstempo is belangrijk, maar het is niet voldoende om een grote detectorprestatie te garanderen. We moeten ook de stabiliteit en de kwaliteit van het uitgangssignaal bewaken. In dit proefschrift presenteren we een aantal taken voor de bewaking en kwaliteitsanalyses die ontwikkeld werden en die gebruikt werden om gebroken componenten of componenten met ruis op te sporen. Dit stelde ons in de gelegenheid om het aantal werkende kanalen hoger te houden dan 98% gedurende de gehele periode waarin gegevens werden genomen tussen 2009 en 2011. De grote presaties die gehaald zijn gedurende deze eerste meetjaren hebben het LHCb experiment nu al een leidende rol gegeven binnen de B-fysica.

Speuren naar precisie

Het $B_s^0 \to \mu^+\mu^-$ vervalskanaal is een van de meest veelbelovende zeldzame vervallen voor het testen van het SM omdat de voorspelde vertakkingsverhouding theoretisch nauwkeurig is: De experimentele meting van een vertakkingsverhouding die voldoende afwijkt van deze voorspelling zou een duidelijk signaal zijn van nieuwe natuurkunde. Aan de andere kant is het ook een perfecte manier om nieuwe modellen te testen: Een nauwkeurige limiet of zelfs een meting bij dezelfde verwachte waarde van het SM zou, in combinatie met andere resultaten van directe zoektochten, een verzameling mogelijke theorieën uitsluiten. Echter, om gevoelig te zijn voor een verschil tussen de verwachte SM waarde en de gemeten vertakkingsverhouding moet de uiteindelijke onzekerheid zo klein mogelijk zijn. Er zijn drie bronnen voor deze onzekerheid:

- **statistisch**: deze onzekerheid is voornamelijk gerelateerd aan de hoeveelheid verzamelde gegevens die de selectie overleven
- **systematisch**: deze onzekerheid is voornamelijk gerelateerd aan de aannames die nodig zijn gedurende de analyse
- **normalisatie**: deze onzekerheid is gerelateerd aan de eis bij hadronversnellers om het interessante vervalskanaal te normaliseren tegen een ander bekend vervalskanaal.

De beste nauwkeurigheid voor de meting voor de vertakkingsverhouding van $B_s^0 \to \mu^+\mu^-$ kan worden bereikt om dit kanaal te normaliseren met een B^0 vervalskanaal waarvoor een nauwkeurig gemeten waarde van de vertakkingsverhouding bestaat in de literatuur. Echter, dit vereist de meting van de parameter f_s/f_d, die representeert de waarschijnlijkheidsverhouding dat een b-quark hadroniseert met een d- of een s-quark. Deze parameter is gemeten bij de experimenten aan de LEP en Tevatron versnellers maar de waarde kan *a priori* niet worden geëxtrapoleerd naar de LHC omgeving omdat hij in principe kan afhangen van de omgevingsomstandigheden. Deze parameter werd meestal gemeten met semi-leptonische vervallen. Deze vervallen hebben een neutrino in de eindtoestand. De neutrino's zijn in het bijzonder moeilijk te meten omdat ze alleen wisselwerken via de "zwakke kernkracht": vanuit een experimenteel gezichtspunt zijn de vervallen met een neutrino een uitdaging omdat een van de deeltjes in de eindtoestand niet gereconstrueerd kan worden. Een alternatieve methode, gebruikt in dit proefschrift, is om f_d/f_s te meten door de gecombineerde meting van de hadronische vervallen $B^0 \to D^-K^+$, $B^0 \to D^-\pi^+$ en $B_s^0 \to D_s^-\pi^+$. Deze zijn erg gunstig voor LHCb vanuit een experimenteel gezichtspunt, robuust met betrekking tot bijdragen van nieuwe natuurkunde en theoretisch goed begrepen.

We presenteren in dit proefschrift twee metingen van f_s/f_d met 35 pb^{-1} aan gegevens. De eerste meting is verkregen door te kijken naar de relatieve hoeveelheid $B^0 \to D^-K^+$ en $B_s^0 \to D_s^-\pi^+$ terwijl de tweede komt van de relatieve hoeveelheid $B^0 \to D^-\pi^+$ and $B_s^0 \to D_s^-\pi^+$. De eerste meting wordt gedomineerd door de statistische onzekerheid, door de hoeveelheid gegevens die beschikbaar waren ten tijde van de analyse, terwijl de tweede meting wordt gedomineerd door de theoretische onzekerheid. De eerste meting zal spoedig worden vernieuwd met 1.0 fb^{-1} aan gegevens verkregen in 2011. De twee metingen zijn in goede overeenstemming met elkaar en kunnen worden gecombineerd tot een enkele waarde door alle gecorreleerde onzekerheden in rekening te brengen. Een gemiddelde waarde voor f_s/f_d is verkregen van $f_s/f_d = 0.253 \pm 0.017^{\text{stat}} \pm 0.018^{\text{syst}} \pm 0.020^{\text{theor}}$. Bovendien heeft het LHCb experiment een waarde gegeven voor de verhouding $f_s/(f_u+f_d)$ gebruikmakend van de semi-leptonische vervallen van b-hadronen, $f_s/(f_u+f_d) = 0.134 \pm 0.004^{+0.011}_{-0.010}$ [6]. De combinatie van deze resultaten samen met de twee hadronische vervallen heeft geresulteerd in 's werelds beste meting $f_s/f_d = 0.267^{+0.021}_{-0.020}$.

De nauwkeurigheid van de f_s/f_d -meting beïnvloedt de ontdekkingsmogelijkheid van NP voor het $B_s^0 \to \mu^+\mu^-$ verval. Voor grote gegevensmonsters en kleine experimentele systematische onzekerheid wordt de onzekerheid het belangrijkste element voor de ontdekking van nieuwe natuurkunde, en bepaalt deze de minimale waarde van de vertakkingsverhouding (BR) waarvoor het bewijs voor nieuwe natuurkunde mag worden beweerd, zoals is beschreven in Fig. 8.5. In het bijzonder laten we zien dat de limieten $BR < 2.6 \times 10^{-9}$ of $BR > 4.2 \times 10^{-9}$ zijn als we de gepresenteerde onzekerheid op f_s/f_d van 8% gebruiken en ook de SM vertakkingsverhouding van $(3.2 \pm 0.2) \times 10^{-9}$ in het ideale geval. Dit bereik is al vele malen kleiner dan wat beschikbaar was met de vorige beste meting van f_s/f_d bij de Tevatron met een onzekerheid van 12%.

De parameter f_s/f_d is in principe afhankelijk van de omgevingsfactoren, en daarom is een directe meting hiervan door de CMS collaboratie wenselijk. De meting gepresenteerd in dit proefschrift zowel als de semi-leptonische meting zijn moeilijk om bij het CMS ex-

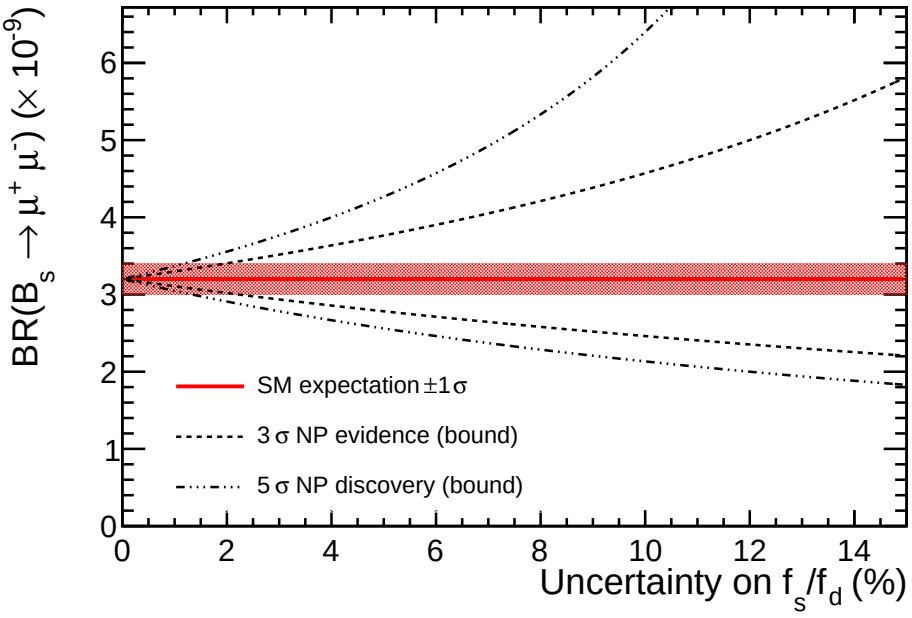

Figure 8.3: Limiet van de $B_s^0 \to \mu^\pm\mu^\mp$ ontdekkingsmogelijkheid (3 en 5 standaarddeviaties in de limiet van oneindige statistiek en verwaarloosbare systematische fouten als een functie van de onzekerheid op de f_s/f_d meting. Op dit moment is de onzekerheid 8%.

periment te doen omdat andere detectorkeuzes zijn gemaakt. We stellen hiervoor een andere methode voor gebaseerd op de extrapolatie van het LHCb resultaat waarbij we gebruikmaken van de meting van twee andere vervallen, B^0 and B_s^0, met een eindtoestand die wel toegankelijk is voor het CMS experiment.

Een andere manier om het Standaard Model te testen

Binnen het SM zijn er zes quarks met massa's tussen ~ 2.5 MeV/c^2 voor het 'up' quark (u) tot ~ 172.2 GeV/c^2 voor het 'top' quark (t). De waarschijnlijkheid van de overgang tussen een quark q naar een quark q' is proportioneel met $|V_{qq'}|^2$ waar $V_{qq'}$ een element is van de matrix genaamd Cabibbo-Kobayashi-Maskawa (CKM), zie Fig. 8.6 (a).

De CKM matrix heeft een eigenschap genaamd "unitariteit" door de fysische eigenschappen die ze representeert. Wiskundig definiëert dit een verzameling vergelijkingen die de matrixelementen moeten voldoen en die verbeeld kunnen worden als een driehoek in het complexe vlak, zie Fig. 8.6 (b).

De eigenschappen van deze driehoek, de lengtes van de zijden, totale oppervlak en hoeken, kunnen experimenteel worden bepaald door bijzondere B-vervallen te bestuderen. De minst precies gemeten parameter van de unitariteitsdriehoek is de hoek γ. Een manier om toegang tot deze hoek te krijgen, is om het vervalskanaal $B_s^0 \to D_s^\pm K^\mp$ te bestuderen. Alvorens we de hoek γ kunnen verkrijgen is het noodzakelijk om te laten zien

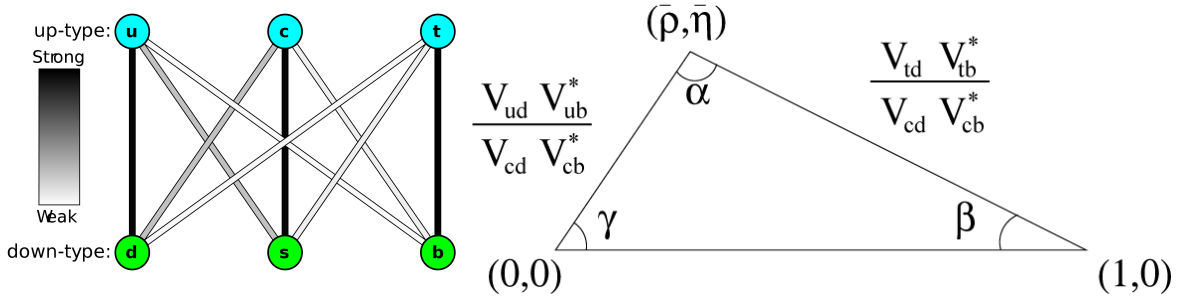

(a) (b)

Figure 8.4: (a): Representatie van de zes quarks in het SM en hun relaties. De intensiteiten (kleur/grijs waarden) van de lijnen worden bepaald door de CKM matrix. (b): Unitariteits driehoek in het complexe vlak $(\bar{\rho},\bar{\eta})$ [103].

dat we de vertakkingsverhouding precies kunnen meten, die tot nog toe slecht bekend is (onzekerheid van 23%). We presenteren in dit proefschrift 's werelds beste nieuwe meting van de vertakkingsverhouding van het $B_s^0 \to D_s^{\pm} K^{\mp}$ verval verkregen uit de analyse van een gegevensmonster met een grootte van 0.37 fb^{-1}. Het verkregen resultaat is $1.90 \pm 0.12^{stat} \pm 0.13^{syst}{}^{+0.12}_{-0.14}{}^{f_s/f_d}$ waarbij de totale onzekerheid nu rond de 12% is. Tegelijkertijd presenteren we 's werelds beste vertakkingsverhoudingsmeting van het $B_s^0 \to D_s^- \pi^+$ verval $2.95 \pm 0.05^{stat} \pm 0.17^{syst}{}^{+0.18}_{-0.22}{}^{f_s/f_d}$, met een totale onzekerheid van rond de 10% en dit is het best bekende B_s^0 vervalskanaal tot op heden.

Vooruitblik

De resultaten zoals gepresenteerd in dit proefschrift laten zien dat het mogelijk is om een belangrijke sub-detector van het LCHb experiment te bewaken en de en een hoog prestatievermogen te garanderen in de eerste jaren van het nemen van data. Dit wordt duidelijk gemaakt, bijvoorbeeld, in de mogelijkheid van een precieze meting van de fragmentatiebreukverhouding f_s/f_d, een belangrijk element in de bepaling van de vertakkingsverhouding van het $B_s^0 \to \mu^+\mu^-$ verval dat gebruikt is voor de zoektocht naar nieuwe natuurkunde. Bovendien, met de gegevens uit 2011, is de studie van deze waarde als functie van de kinematische parameters voorzien. Deze afhankelijkheidsstudie in combinatie met de evaluatie van de verhouding van andere vervalskanalen die makkelijk te bepalen zijn binnen CMS, staat toe om een extrapolatie te doen van de f_s/f_d factor in de CMS acceptantie.

De LHCb collaboratie heeft bovendien een nieuwe wereld-beste meting aangekondigd van de limiet op de $B_s^0 \to \mu^+\mu^-$ vertakkingsverhouding door gebruik te maken van het f_s/f_d resultaat gepresenteerd in dit proefschrift. Het LHCb experiment verkreeg de waarschijnlijkheid dat een B_s^0-meson in een paar tegengesteld geladen muonen vervalt, niet groter is dan 4.5 uit een miljard vervallen [104]. Het nieuwe resultaat vertegenwoordigt een mijlpaal in de zoektocht naar nieuwe natuurkunde voorbij het standaard model. Dit resultaat kan

hierover een beetje pessimisme afroepen: Iedereen had gehoopt om de eerste tekenen van nieuwe natuurkunde te zien door de onthulling van een klein overschot in de vertakkingsverhouding voorspeld door het standaard model. Aan de andere kant is het nog steeds mogelijk om een kleinere vertakkingsverhouding te vinden dan voorspeld door het standaard model. Dit zou een andere manier zijn om een deur te openen naar nieuwe natuurkunde, iets wat minder aandacht kreeg voorheen maar nu een mogelijkheid wordt met de beschikbare verhoogde nauwkeurigheid. In elk geval, dankzij deze meting onderzoekt het LHCb experiment reeds het mogelijke gebied toegankelijk voor nieuwe modellen, en sluit het een groot deel van de faseruimte uit voor andere modellen die nieuwe natuurkunde voorspellen.

Riassunto
Prima misura del rapporto delle probabilità di frammentazione f_s/f_d attraverso decadimenti adronici a piu' basso ordine in collisioni pp a 7 TeV

L'importante è *non smettere mai di interrogarsi.*
Albert Einstein

Un po' di storia

La curiosità è una caratteristica intrinseca della natura umana. Uno dei misteri che ha affascinato per secoli sia filosofi che fisici è la domanda "di che cosa è fatta la materia?". Il filosofo greco Democrito propose che la materia fosse costituita da elementi indivisibili che chiamo per questo "atomi". Incredibilmente, questa sua intuizione risalente al 400 a.C. è molto più simile alla presente descrizione della natura di quanto si possa immaginare. La lunga avventura della fisica ci ha portato a svilupparle una branca, chiamata fisica delle particelle, che si occupa di descrivere la materia. In questo contesto la materia è descritta attraverso teorie che prevedono l'esistenza e l'interazioni di particelle utilizzando un linguaggio matematico.

Una teoria scientifica deve essere in grado di descrivere quanto già noto e allo stesso tempo di predire nuove osservabili che possano essere misurate tramite esperimenti. Negli anni 70 avvene una delle più importanti rivoluzioni della fisica con la formulazione di una teoria, chiamata Modello Standard (SM). Questa teoria tiene conto di tre delle quattro interazioni fondamentali tra particelle elementari: solo il ruolo della gravità non trova il suo spazio. Questa teoria è stata confermata da una vasta serie di esperimenti negli ultimi decenni. Nonostante il suo successo, lo SM non viene considerato la teoria finale per descrivere

la materia. La presenza di un gran numero di parametri lascia i fisici profondamente insoddisfatti. Inoltre, volgendo lo sguardo al cielo, si è scoperto che c'è molta più materia di quanta ce ne si aspetterebbe. Buona parte di questa materia è invisibile: non può cioè essere rivelata da un telescopio, ma può essere solamente dedotta da effetti gravitazionali, come "l'effetto lente gravitazionale", o le curve di rotazione. Nessuna delle particelle al momento note sono delle candidate soddisfacenti per formare questa "materia oscura". Questi esempi mostrano come la nostra attuale descrizione della natura sia ancora incompleta e stimolano perciò i fisici teorici a proporre nuove teorie per estendere lo SM. I fisici sperimentali, dal canto loro, sono perciò incoraggiati a guardare e studiare le proprietà delle nuove particelle predette da queste nuove teorie.

La corsa per la ricerca di "nuova fisica" (NP) è cominciata diversi anni fa con gli esperimenti all'acceleratore di particelle Tevatron negli Stati Uniti ed ora è l'obbiettivo principale degli esperimenti all'acceleratore LHC a Ginevra.

Come cercare nuova fisica

Ci sono due modi possibili per cercare NP: la produzione diretta di nuove particelle come viene fatto dagli esperimenti di ATLAS e CMS, oppure cercando effetti indiretti di queste particelle sulle osservabili che possono essere misurate. Il vantaggio di quest'ultima tecnica è che è possibile osservare questi effetti ad energie molto più basse di quelle necessarie per produrre le nuove particelle direttamente. Se le masse delle nuove particelle dovessero essere molto più elevate di quelle accessibili da LHC, il metodo indiretto sarebbe l'unico modo per scoprire NP nel breve futuro. Inoltre, dal momento che le due tecniche sono complementari tra loro, sarà possibile a breve confermare o escludere nuovi scenari combinando i loro rispettivi risultati.

Non tutte le particelle sono stabili: dopo un certo periodo di tempo possono decadere in una serie di altre particelle (chiamate "stato finale"). Una delle osservabili considerate è il "rapporto di decadimento" (BR). Questa quantità rappresenta la frazione di particelle che decadono in uno specifico stato finale rispetto al numero totale di particelle. Vengono considerati "rari" i decadimenti in cui lo stato finale può essere raggiunto solo poche volte ogni miliardo di eventi. In questi decadimenti, contributi di nuova fisica possono essere sensibilmente aumentare il valore atteso per il rapporto di decadimento mostrando così chiaramente la presenza di fenomeni oltre questo modello. Il fatto che questi decadimenti avvengano così raramente, dall'atra parte, implica una serie di sfide tecniche che ci obbligano a costruire rivelatori con prestazioni molto elevate e a mettere uno sforzo costante nel calibrarli e nel controllare il loro stato di funzionamento.

Decadimenti del mesone B

I quark sono particelle elementari che si raggruppano ("confinamento"), con un processo chiamato "adronizzazione" per formare gruppi (ossia nuove particelle questa volta non più elementari) chiamati "adroni". Gli anti–quark differiscono dai quark solamente per la

loro carica elettrica che ha segno opposto. Se un adrone è costituito unicamente da un quark e un anti–quark ($q\bar{q}$) siamo in presenza di una particella chiamata "mesone".

Ci sono diverse particelle instabili, e quelle rilevanti per questa tesi sono chiamate mesoni B. I mesoni B considerati sono il B^0 (con una coppia $d\bar{b}$) e il B_s^0 (con una coppia $s\bar{b}$). Il primo mesone è più leggero ed è stato ampiamente studiato in passato, ottenendo precise misurazioni della frequenza di decadimento. In compenso, non sono disponibili in letteratura precise misurazioni relative al mesone B_s^0.

Prestazioni del detector nel tempo

Questi canali sono caratterizzati da uno stato finale molto simile costituito da mesoni carichi: i pioni ($\pi^{\pm}$) e i kaoni ($K^{\pm}$). Per identificarli e per limitare un eccessivo contributo di fondo, sono essenziali un'ottima capacità di identificazione delle particelle (cioè di distinguere una particella da un'altra) e un'eccellente risoluzione in massa (necessaria per distinguere due picchi con masse leggermente diverse).

Una delle componenti fondamentali di un esperimento è il "sistema di tracciamento": una serie di sotto–rivelatori usati per identificare dove è passata una particella, quale era la sua carica e per avere delle informazioni relative alla sua massa e velocità. La traiettoria delle particelle in questi sotto-rivelatori è chiamata "traccia". In LHCb definiamo il "tipo di traccia" guardando quale sotto–rivelatore è stato attraversato. Un ruolo chiave nell'ottenere un'eccellente risoluzione in massa è legata alla qualità delle tracce ricostruite. Diversi studi sono stati svolti all'interno dell'esperimento per determinare l'efficienza di tracciamento per le particelle cariche e un nuovo metodo è stato proposto in questa tesi per essere completamente idipendenti da qualsiasi selezione e ottenere una valutazione della bontà dell'accordo tra dati e simulazione per diversi algoritmi di ricostruzione di traccia. Questo si è rivelato particolarmente decisivo soprattutto con i primissimi dati che sono stati ottenuti in condizioni molto particolari. Con questo studio abbiamo trovato un ottimo accordo tra dati e simulazione per tutti i tipi di traccia sia per i dati acquisiti nel 2009 che per quelli acquisiti all'inizio del 2010, con una incertezza di circa 3%.

Un importante sotto–rivelatore del sistema di tracciamento in LHCb è l'Outer Tracker, "tracciatore esterno", (OT). Esso consiste in un rivelatore a gas che copre la parte più esterna del sistema di tracciamento. In generale un rivelatore deve essere in grado di sopportare una grande dose di radiazione dovuta alle particelle che lo attraversano durante il "tempo di vita" di un esperimento (tipicamente 10 anni). Questa grande quantità di radiazione può ridurre le prestazioni di un rivelatore: quello che solitamente viene chiamato "invecchiamento". Nei rivelatori a gas un tipico segno di invecchiamento è la riduzione dell'altezza del segnale in uscita. Nel 2005 l'allarme di un possibile invecchiamento dopo soli 1-2 anni di presa dati, dovuto alla presenza di depositi di carbonio sul filo, ha reso necessario investigare sia le cause del problema sia le sue possibili soluzioni, che non necessitassero, però, la ricostruzione dell'intero rivelatore. Oltre ad aver scoperto, come presentato in questa tesi, che la causa era l'additivo impiegato dal produttore per aumentare la malleabilità della colla impiegata per sigillare i moduli, diverse tecniche sono state indivi-

duate per prevenire e recuperare il guadagno iniziale. In particolare l'aggiunta di ossigeno (1.5 %) nella miscela di gas utilizzata ha permesso di dimezzare il ritmo di invecchiamento grazie probabilmente alla produzione di radicali benefici (ozono) che contrastano il deposito di carbonio sui fili. Mentre una tecnica, chiamata "HV-training", ha mostrato buoni risultati nel prevenire e soprattutto nel recuperare l'originale guadagno dopo che si era formato un deposito isolate. Questa tecnica può essere utilizzata, se necessario, anche *in situ* sui moduli finali. Il ritmo di invecchiamento è costantemente controllato con diverse tecniche tra cui periodiche scansioni dei moduli con una sorgente durante i periodi in cui non c'è fascio circolante nell'acceleratore (shutdown). Da questi studi nessuna evidenza di invecchiamento è stata riscontrata a tutt'oggi.

Il controllo costante del ritmo di invecchiamento di un rivelatore è sicuramente importante, ma non è l'unico aspetto da considerare per garantire elevate prestazioni. È infatti essenziale anche il controllo costante dell'elettronica, in particolare della stabilità e qualità del suo segnale in uscita. In questa tesi presentiamo diverse procedure sviluppate per compiere questi controlli. Queste procedure hanno permesso una tempestiva sostituzione delle componenti meno efficienti o eccessivamente rumorose, garantendo più dell'89% di canali funzionanti durante tutto il periodo di presa dati compreso tra il 2009 e il 2011. Questo, unito all'assenza di segni di invecchiamento, ha permesso di ottenere eccellenti prestazioni durante i primi due anni di presa dati di LHCb e di far sì che LHCb stia già ricoprendo un ruolo chiave nel campo della "fisica del B".

Alla ricerca della precisione

Il canale di decadimento $B_s^0 \to \mu^+\mu^-$ è uno dei decadimenti più promettenti, tra quelli rari, per testare il Modello Standard, dal momento che il suo rapporto di decadimento è teoricamente preciso: una misura sperimentale del suo rapporto di decadimento molto diversa sarebbe un chiaro segno di nuova fisica. D'altra parte è anche un canale interessante per testare nuovi possibili modelli: un limite preciso sul possibile valore del suo rapporto di decadimento o addirittura una misura al valore previsto dalla teoria permetterebbero di scartare diverse nuove possibili teorie. In compenso, per essere sensibili a differenze tra il valore predetto dallo SM e quello misurato, l'incertezza finale sulla misura sperimentale deve essere la più piccola possibile. Ci sono tre sorgenti principali di incertezza:

- **statistica**: questa incertezza è principalmente connessa con il quantitativo di dati raccolti e che sono sopravvissuti alla selezione necessaria per ridurre il livello di rumore
- **sistematica**: questa incertezza è principalmente connessa alle assunzioni fatte durante il processo di analisi
- **normalizzazione**: questa incertezza è principalmente connessa con il bisogno agli "hadron colliders"[5] di fare misure relative ad un canale di decadimento ben noto.

[5]Acceleratori in cui le particelle che vengono fatte collidere non sono elementari, come ad esempio gli elettroni, ma sono degli adroni, come ad esempio i protoni

La miglior precisione accessibile a LHCb per la misura del BR del decadimento $B_s^0 \to \mu^+\mu^-$ è ottenuta normalizzando questo canale con un decadimento del mesone B^0, per il quale misure molto precise del suo BR sono presenti in letteratura. D'altra parte questo richiede la misura di un altro parametro, chiamato f_s/f_d, che rappresenta il rapporto di probabilità che un quark b adronizzi con un quark d o con un quark s. Questo parametro è stato misurato dagli esperimenti a LEP e al Tevatron, ma il suo valore non può *a priori* essere estrapolato a LHC dal momento che in linea di principio può dipendere dalle condizioni in cui operano i vari esperimenti. Questo parametro è solitamente misurato tramite decadimenti semi–leptonici. Questi decadimenti hanno un neutrino, particella di carica elettrica neutra e di massa quasi nulla, nello stato finale. I neutrini sono particolarmente difficili da rilevare in quanto interagiscono solo tramite la "forza debole": da un punto di vista sperimentale i decadimenti con un neutrino rappresentano una grande sfida in quanto una delle particelle dello stato finale non può essere ricostruita. Un metodo alternativo, affrontato in questa tesi, è di misurare f_s/f_d tramite la misura combinata di tre decadimenti adronici: $B^0 \to D^-K^+$, $B^0 \to D^-\pi^+$ and $B_s^0 \to D_s^-\pi^+$. Questi decadimenti sono vantaggiosi da un punto di vista sperimentale per LHCb, non sono affetti da possibili contributi di nuova fisica e sono teoricamente ben compresi.

Presentiamo in questa tesi due misure del rapporto f_s/f_d con 35 pb^{-1} di dati. La prima misura è stata ottenuta calcolando il quantitativo relativo di $B^0 \to D^-K^+$ e $B_s^0 \to D_s^-\pi^+$ mentre il secondo proviene dal quantitativo relativo di $B^0 \to D^-\pi^+$ e $B_s^0 \to D_s^-\pi^+$. La prima misura è dominata dall'incertezza statistica dovuta al limitato quantitativo di dati a disposizione al tempo dell'analisi, mentre la seconda misura è dominata dall'incertezza teorica. La prima misura sarà presto aggiornata con il risultato ottenuto con 1.0 fb^{-1} di dati raccolti nel 2011. Le due misure ottenute sono in accordo tra loro e possono essere combinate in un unico valore. È stato trovato, tenendo conto di tutte le correlazioni nelle incertezze, un valore medio di $f_s/f_d = 0.253 \pm 0.017^{\text{stat}} \pm 0.018^{\text{syst}} \pm 0.020^{\text{theor}}$. Inoltre, LHCb ha pubblicato una misura del rapporto $f_s/(f_u+f_d)$ dall'analisi di decadimenti semi–leptonici di adroni b, $f_s/(f_u+f_d) = 0.134 \pm 0.004^{+0.011}_{-0.010}$ [6]. La combinazione dei risultati presentati in questa tesi con questo valore ha condotto alla miglior misura al mondo di questo parametro con un valore di: $f_s/f_d = 0.267^{+0.021}_{-0.020}$.

La precisione sulla misura di questo parametro ha degli effetti diretti sulle potenzialità di scoperta di nuova fisica tramite il canale $B_s^0 \to \mu^+\mu^-$. Infatti, per grandi quantitativi di dati e piccole incertezze sperimentali (cioè in condizioni ideali), l'incertezza su f_s/f_d diventa l'elemento chiave per la scoperta di nuova fisica, determinando il valore minimo del rapporto di decadimento per il quale si può affermare un'evidenza di nuova fisica, come mostrato in Fig. 8.5. In particolare, i limiti trovati sono $BR < 2.6 \times 10^{-9}$ o $BR > 4.2 \times 10^{-9}$ se consideriamo un'incertezza intorno all'8%, come presentata in questa tesi, e il rapporto di decadimento previsto dallo SM di $(3.2 \pm 0.2) \times 10^{-9}$ nelle condizioni ideali. Questo intervallo è già molto più stretto di quanto fosse accessibile con la miglior misura al mondo di f_s/f_d ottenuta al Tevatron, che era affetta da un'incertezza intorno al 12%.

Il parametro f_s/f_d è potenzialmente dipendente dalle condizioni in cui operano i vari esperimenti, perciò sarebbe necessaria una sua misura diretta da parte, ad esempio, di CMS. D'altra parte la misura presentata in questa tesi, così come la misura attraverso i canali semi–

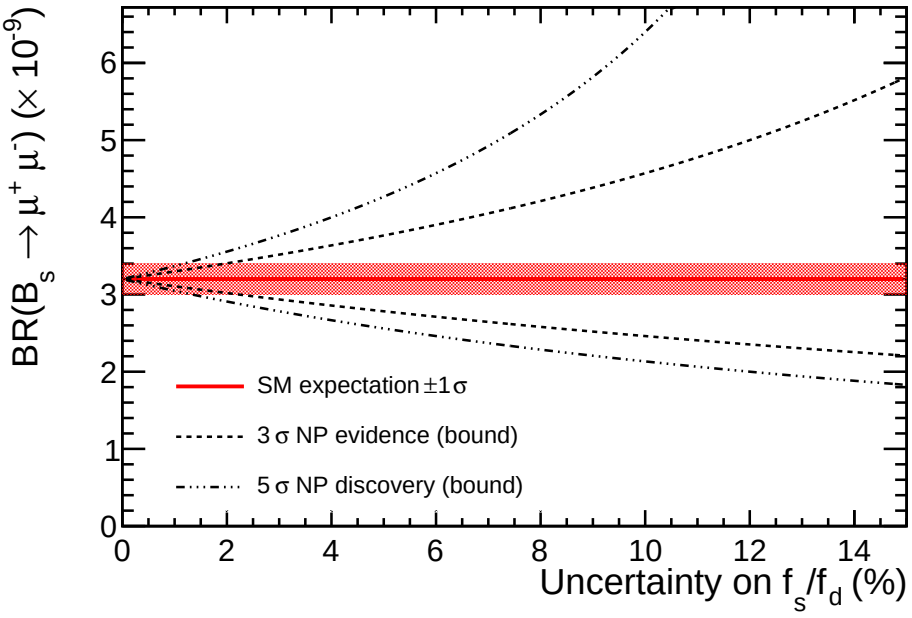

Figure 8.5: Limite delle potenzialità di scoperta di nuova fisica tramite il canale $B_s^0 \to \mu^\pm\mu^\mp$ (a 3 e 5 σ), nel limite di infinita statistica e trascurabili incertezze sperimentali, in funzione dell'incertezza di cui è affetta la misura del rapporto f_s/f_d. Al momento l'incertezza su questo rapporto è dell'8%.

leptonici, risultano molto difficili a CMS visto le differenti scelte fatte nel progettare il rivelatore. In questa tesi proponiamo perciò un metodo alternativo basato sull'estrapolazione del risultato di LHCb usando la misura di altri due decadimenti dei mesoni B^0 and B_s^0, questa volta però con uno stato finale che sia facilmente ricostruibile anche a CMS.

Un altro modo per testare il Modello Standard

Nello SM ci sono sei tipi di quark con masse che variano tra ~ 2.5 MeV/c^2 per il quark "up" (u) fino a ~ 172.2 GeV/c^2 per il quark "top" (t). La probabilità della transizione tra un quark q e un quark q' è proporzionale a $|V_{qq'}|^2$ dove $V_{qq'}$ è l'elemento della matrice chiamata Cabibbo-Kobayashi-Maskawa (CKM), si veda Fig. 8.6 (a).

La matrice CKM ha una proprietà nota come "unitarietà" dovuta alla proprietà fisiche che rappresenta. Matematicamente, questa definisce una serie di equazioni che gli elementi della matrice devono soddisfare e che possono essere rappresentati tramite un triangolo nel piano complesso, si veda Fig. 8.6 (b).

Le proprietà di questo triangolo, lunghezza dei lati, area totale, valore degli angoli, può essere misurata sperimentalmente studiando particolari decadimenti del mesone B. Il parametro la cui misura diretta risulta la meno precisa è l'angolo γ. Un modo per accedere alla misura di quest'angolo è lo studio del decadimento $B_s^0 \to D_s^\pm K^\mp$. Prima di poter estrarre

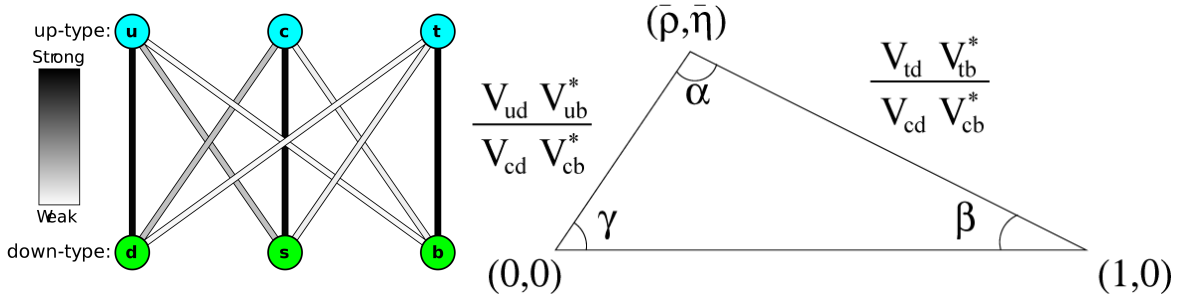

(a) (b)

Figure 8.6: (a): Rappresentazione dei sei quark nello SM e delle loro relazioni. L'intensità(scala di grigi) delle linee èdeterminata dagli elementi della matrice CKM. (b): triangolo di unitarietà nel piano complesso $(\bar{\rho},\bar{\eta})$ [103].

l'angolo γ è però necessario mostrare che si è in grado di misurare precisamente il suo rapporto di decadimento, che al momento è conosciuto con una grande imprecisione (con un'incertezza di circa il 23%). Presentiamo in questa tesi la nuova miglior misura al mondo del rapporto di decadimento del canale $B_s^0 \to D_s^{\pm} K^{\mp}$ ottenuto dall'analisi di 0.37 fb^{-1} di dati. Il risultato ottenuto è $1.90 \pm 0.12^{stat} \pm 0.13^{syst}{}^{+0.12}_{-0.14}{}^{f_s/f_d}$ dove l'incertezza totale è ora intorno al 12%. Allo stesso tempo, presentiamo la miglior misura al mondo del rapporto di decadimento del canale $B_s^0 \to D_s^- \pi^+$, pari a $2.95 \pm 0.05^{stat} \pm 0.17^{syst}{}^{+0.18}_{-0.22}{}^{f_s/f_d}$, con un'incertezza totale intorno al 10% e che rappresenta il più noto decadimento del mesone B_s^0 al momento disponibile.

Uno sguardo al futuro

Gli studi presentati in questa tesi perciò, oltre ad aver mostrato e reso possibile il controllo costante della qualità di un importante sotto–rivelatore di LHCb nei primi anni di presa dati, hanno anche permesso, con la misura di f_s/f_d, di ottenere uno degli ingredienti più importanti per la ricerca di nuova fisica in canali come $B_s^0 \to \mu^+\mu^-$ così come di misurare qualsiasi decadimento di B_s^0 tramite il confronto con il decadimento di un canale noto di B^0. Questi studi hanno inoltre aperto la strada per i successivi studi a piu' alta statistica dell'andamento di questo parametro in funzione di variabili cinematiche come p, p_T, η, che insieme allo studio di canali facilmente misurabili in altri esperimenti come CMS permetteranno di estrapolare f_s/f_d nell'accettanza di altri esperimenti, permettendo una misura piu' corretta di tutti i decadimenti del mesone B_s^0.

In aggiunta, la collaborazione di LHCb ha recentemente annunciato la miglior misura al mondo del limite del rapporto di decadimento del canale $B_s^0 \to \mu^+\mu^-$ utilizzando il valore di f_s/f_d presentato in questa tesi. LHCb ha ottenuto una probabilità che un mesone B_s^0 decada in una coppia di muoni con carica opposta non più grande di 4.5 volte su un miliardo di decadimenti [104]. Il nuovo risultato rappresenta una pietra miliare nella ricerca di

nuova fisica oltre il Modello Standard. Questo risultato può portare un certo vento di pessimismo: gran parte della comunità scientifica sperava di vedere un primo segno di nuova fisica in un piccolo eccesso nel valore misurato del rapporto di decadimento per questo decadimento rispetto a quanto predetto dal Modello Standard. D'altra parte, però, è ancora possibile trovare un rapporto di decadimento più piccolo di quanto predetto dal Modello Standard. Questo sarebbe un altro modo per aprire una porta su della nuova fisica: una strada che se fino ad ora ha ricevuto poca attenzione, oggi, grazie alle nuove precisioni raggiungibili, può rivelarsi molto interessante. In ogni caso, grazie a questa misura, LHCb ha già ristretto le regioni di esistenza dei parametri su cui sono basati i nuovi modelli mietendo così già molte vittime tra questi modelli di nuova fisica.

Bibliography

[1] Particle Data Group, K. Nakamura *et al.*, *Review of particle physics*, J. Phys. **G37** (2010) 075021.

[2] BABAR Collaboration, B. Aubert *et al.*, *Measurement of the Branching Fraction of* $\Upsilon(4S) \to B^0\bar{B}^0$, Phys. Rev. Lett. **95** (2005) 042001.

[3] Heavy Flavor Averaging Group, D. Asner *et al.*, *Averages of b-hadron, c-hadron, and* τ*-lepton properties*, arXiv:1010.1589, online update at *http://www.slac.stanford.edu/xorg/hfag*.

[4] R. Fleischer, N. Serra, N. Tuning, *New Strategy for* B_s *Branching Ratio Measurements and the Search for New Physics in* $B_s^0 \to \mu^+\mu^-$, Phys. Rev. D **82** (2010) 034038, arXiv:1004.3982.

[5] R. Fleischer, N. Serra, N. Tuning, *Tests of factorization and* SU(3) *relations in B decays into heavy-light final states*, Phys. Rev. D **83** (2011) 014017, arXiv:1012.2784.

[6] LHCb Collaboration, R. Aaij *et al.*, *Measurement of b hadron production fractions in 7 TeV pp collisions*, Phys. Rev. D **85** (2012) 032008, arXiv:1111.2357.

[7] G. Buchalla, M. Neubert, C. T. Sachrajda, M. Beneke, *QCD factorization for exclusive non-leptonic B-meson decays: general arguments and the case of heavy light final states*, Nucl. Phys. B **591** (2000), no. 1-2 313, arXiv:hep-ph/0006124.

[8] C. W. Bauer, D. Pirjol, I. W. Stewart, *Proof of Factorization for* $B \to D\pi$, Phys. Rev. Lett. **87** (2001) 201806, arXiv:hep-ph/0107002.

[9] P. Blasi, P. Colangelo, G. Nardulli, N. Paver, *Phenomenology of* B_s *Decays*, Phys. Rev. Lett. D **49** (1994) 238, arXiv:hep-ph/9307290.

[10] J. D. Bjorken, *Topics in B-Pysics*, Nucl. Phys. Proc. Suppl. **11** (1989) .

[11] I. Caprini, L. Lellouch, M. Neubert, *Dispersive Bounds on the Shape of* $B \to D^{(*)} l\nu$ *Form Factors*, Nucl. Phys. B **530** (1998) 153, arXiv:hep-ph/9712417.

[12] J. A. Bailey *et al.*, *$B_s \to D_s/B \to D$ Semileptonic Form-Factor Ratios and Their Application to BR($B_s^0 \to \mu^+\mu^-$)*, arXiv:1202.6346.

[13] P. Bryant, L. Evans, *LHC Machine*, JINST **3** (2008), no. 08 S08001.

[14] LHCb Collaboration, A. A. Alves Jr. *et al.*, *The LHCb Detector at the LHC*, JINST **3** (2008), no. 08 S08005.

[15] ATLAS Collaboration, G. Aad *et al.*, *The ATLAS Experiment at the CERN Large Hadron Collider*, JINST **3** (2008), no. 08 S08003.

[16] CMS Collaboration, S. Chatrchyan *et al.*, *The CMS experiment at the CERN LHC*, JINST **3** (2008), no. 08 S08004.

[17] ALICE Collaboration, K. Aamodt *et al.*, *The ALICE experiment at the CERN LHC*, JINST **3** (2008), no. 08 S08002.

[18] T. Sjöstrand, S. Mrenna, and P. Skands, *PYTHIA 6.4 Physics and manual*, JHEP **05** (2006) 026, arXiv:0603175.

[19] LHCb collaboration, R. Aaij *et al.*, *Measurement of b-hadron masses*, Phys. Lett. B **708** (2012) 241, arXiv:1112.4896.

[20] B. P. Marius, *Performance of the LHCb Vertex Locator*, LHCb-PROC-2011-087, Dec, 2011.

[21] O. Callot, *LHCb: From the detector to the first physics results*, LHCb-PROC-2011-060, Oct, 2011.

[22] LHCb Collaboration, R. Aaij *et al.*, *Measurement of the $B_s^0 - \bar{B}_s^0$ oscillation frequency Δm_s in $B_s^0 \to D_s^-(3)\pi$ decays*, Physics Letters B **709** (2012), no. 3 177 , arXiv:1112.4311.

[23] S. Borghi, *Performance of the Tracking System at the LHCb Experiment*, LHCb-PROC-2010-064, Dec, 2010.

[24] LHCb Collaboration, R. Antunes-Nobrega *et al.*, *LHCb reoptimized detector design and performance*, Technical Design Report LHCb (2003), CERN-LHCC/2003-030.

[25] M. Adinolfi *et al.*, *Performance of the LHCb RICH photo-detectors and readout in a system test using charged particles from a 25 ns-structured beam*, Nucl. Instrum. Meth. **603** (2009), no. 3 287.

[26] A. Braem *et al.*, *The Pad HPD as photodetector of the LHCb RICH detectors*, LHCb-2000-063, 2001.

[27] A. Powell, *Reconstruction and PID performance of the LHCb RICH detectors*, Nucl. Instr. Meth. **639** (2011), no. 1 260.

[28] A. Powell, *Particle identification at LHCb*, PoS **ICHEP2010** (2010) 020.

[29] LHCb Collaboration, R. Aaij *et al.*, *Determination of f_s/f_d for 7 TeV pp collisions and measurement of the branching ratio of the decay $B^0 \to D^- K^+$*, Phys. Rev. Lett. **107** (2011) 211801, arXiv:1106.4435.

[30] LHCb Collaboration, S. Amato *et al.*, *LHCb calorimeters*, Technical Design Report LHCb 2 (2000), CERN-LHCC/2000-036.

[31] B. Sciascia, *Private comunication*, Feb, 2012.

[32] V. Gligorov, *A single track HLT1 trigger*, LHCb-PUB-2011-003, Jan, 2011.

[33] M. Williams *et al.*, *The HLT2 Topological Lines*, LHCb-PUB-2011-002, Jan, 2011.

[34] J. Albrecht *et al.*, *Commissioning and Performance of the LHCb HLT1 muon trigger*, LHCb-PUB-2011-006, Feb, 2011.

[35] B. Bevensee *et al.*, *Progress report on the development of a bipolar asic for the atlas transition radiation detector*, Tech. Rep. ATL-INDET-94-080. ATL-I-PN-80, CERN, Geneva, Sep, 1994.

[36] B. Bevensee *et al.*, *A amplifier shaper discriminator with baseline restoration for the atlas transition radiation tracker*, IEEE Transactions on Nuclear Science **43** (1996).

[37] N. Dressnandt *et al.*, *Radiation hardness: design approach and measurements of the ASDBLR ASIC for the ATLAS TRT*, in *Nuclear Science Symposium Conference Record, 2002 IEEE*, vol. 1, pp. 151–155, Nov, 2002.

[38] E. Simioni, *New physics from rare beauty*, 2010. CERN-THESIS-2010-031, PhD Thesis.

[39] G. Cervelli, A. Marchioro, and P. Moreira, *A 0.13-mu-m CMOS serializer for data and trigger optical links in particle physics experiments*, IEEE Trans. Nucl. Sci. **51** (2004) 836.

[40] U. Uwer, D. Wiedner, A. Pellegrino, *Address scheme for the Outer Tracker FE electronics*, LHCb-2003-041, May, 2003.

[41] R. Brun and F. Rademakers, *ROOT: An object oriented data analysis framework*, Nucl. Instrum. Meth. **A389** (1997) 81.

[42] L. Hommels, T. Bauer, A. Berkien, A. Pellegrino, T. Sluijk, *Noise Studies with the LHCb Outer Tracker ASDBLR Board*, LHCb-2004-117, Dec, 2004.

[43] E. L. Visser, *Preventing, monitoring and curing the ageing in the lhcb outer tracker*, 2010. CERN-THESIS-2010-094, Master thesis.

[44] M. R. Blom, *Ageing of the LHCb outer tracker*, 2009. CERN-THESIS-2009-089, Master thesis.

[45] M. P. Titov, *Radiation damage and long term aging in gas detectors*, ICFA Instrum. Bull. **26** (2004) 002, arXiv:physics/0403055.

[46] J. Va'vra, *Review of wire chamber aging*, Nucl. Instrum. Meth. **A252** (1986) 547.

[47] J. A. Kadyk, *Wire chamber aging*, Nucl. Instrum. Meth. A **300** (1991) 436.

[48] LHCb Collaboration, P. R. Barbosa-Marinho *et al.*, *LHCb Outer Tracker*, Technical Design Report LHCb 6 (2001), CERN-LHCC/2001-024.

[49] F. Guarino, S. Ilie, A. Romaniouk, S. Soutchkov, and F. Tartarelli, *Outgassing studies of materials for the TRT construction*, ATL-INDET-99-011, Aug, 1999.

[50] M. Capeans, *Aging and materials: Lessons for detectors and gas systems*, Nucl. Instrum. Meth. A **515** (2003) 73.

[51] T. Akesson *et al.*, *Aging effects in the ATLAS transition radiation tracker and gas filtration studies*, IEEE Nucl. Sci. Symp. Conf. **2** (2005) 1185.

[52] I. Mous, *Aging in the LHCb Outer Tracker*, 2007. CERN-THESIS-2008-005, Master thesis.

[53] LHCb Collaboration, R. Aaij *et al.*, *Letter of Intent for the LHCb Upgrade*, CERN-LHCC-2011-001, Mar, 2011.

[54] T. Haas, *Alterungsstudien und Studium der Betriebseigenschaften des Outer Trackers des LHCb Detektors*, 2007. PhD Thesis.

[55] M. Capéans-Garrido, *Recent aging studies for the ATLAS transition radiation tracker*, IEEE Trans. Nucl. Sci. **51** (2004) 960.

[56] ATLAS TRT Collaboration, T. Akesson *et al.*, *Operation of the ATLAS Transition Radiation Tracker under very high irradiation at the CERN LHC*, Nucl. Instrum. Meth. **522** (2004), no. 1-2 25.

[57] S. Bachmann *et al.*, *Ageing in the LHCb outer tracker: Phenomenon, culprit and effect of oxygen*, Nucl. Instrum. Meth. **A617** (2010) 202.

[58] M. Blom, I. Mous, N. Tuning, *Effects of Adding Oxygen to the Outer Tracker Gas Mixture*, LHCb-2008-064, Nov, 2008.

[59] C. Faerber, *Alterungsstudien am Outer Tracker des LHCb Experiments*, 2007. Master thesis.

[60] N. Tuning *et al.*, *HV Training as a Cure for the Ageing in the Outer Tracker*, LHCb-PUB-2010-010, Mar, 2010.

[61] R. Openshaw, R. Henderson, W. Faszer, and M. Salomon, *Etching of anode wire deposits with CF-4 / isobutane (80:20) avalanches*, Nucl. Instrum. Meth. **A307** (1991) 298.

[62] J. Va'vra, *Wire ageing with the TEA photocathode*, Nucl. Instrum. Meth. **A387** (1997) 183.

[63] G. Van Apeldoorn *et al.*, *Outer Tracker Module Production at NIKHEF - Quality Assurance*, LHCb-2004-078, Oct, 2004.

[64] V. Suvorov, G. van Apeldoorn, I. Gouz, T. Sluijk, *Avalanche and streamer production in Ar/CO_2 mixtures*, LHCb-2005-038, Jul, 2005.

[65] C. Faerber, *Private comunication*, (Presentation at the LHCb OT meeting on 26 Aug 2009).

[66] N. Tuning *et al.*, *Ageing in the LHCb Outer Tracker: Aromatic hydrocarbons and wire cleaning*, Nucl. Instrum. Meth. **A656** (2011) 45.

[67] D. van Eijk *et al.*, *Radiation tolerance of the LHCb Outer Tracker*, Submitted to Nucl. Instrum. Meth. (2012).

[68] E. Bos, *Reconstruction of charged particles in the LHCb experiment*, 2010. CERN-THESIS-2010-049, PhD Thesis.

[69] LHCb Collaboration, R. Aaij *et al.*, *Prompt production in pp collisions at $\sqrt{s} = 0.9$ TeV*, Phys. Lett. B **693** (2010), no. 2 69, arXiv:1008.3105.

[70] LHCb Collaboration, R. Aaij *et al.*, *Search for the rare decays $B_s^0 \to \mu^+\mu^-$ and $B^0 \to \mu^+\mu^-$*, Phys. Lett. B **708** (2012) 55 , arXiv:1112.1600.

[71] S. Easo, *Selection of $B_s^0 \to D_s^- K^+$ and $B_s^0 \to D_s^- \pi^+$ decay modes in LHCb using Multivariate Methods Corrections for the Hadronic Final State*, LHCb-PUB-2010-009, 2010.

[72] A. Hoecker *et al.*, *TMVA: Toolkit for multivariate data analysis*, PoS **ACAT** (2007) 040, arXiv:0703039.

[73] I. H. Witten, E. Frank, *Data Mining, practical machine learning tools and techniques*, Morgan Kaufmann-Elsevier (2005).

[74] V. Gligorov, *Reconstruction of the decay modes $B^0_d \to D^\pm_d \pi^\mp$, $B^0_s \to D^-_s \pi^+$, and $B^0_s \to D^\pm_s K^\mp$ at LHCb*, LHCb-PUB-2009-003, May, 2009.

[75] A. Golutvin, R. Hierck, J. van Hunen, M. Prokudin, R. White, *$B^0_s \to D^\mp_s K^\pm$ and $B^0_s \to D^-_s \pi^+$ event selection*, CERN-LHCb-2003-127, 2003.

[76] J. Borel, L. Nicolas, O. Schneider, J. Van Hunen, *The $B^0_s \to D^-_s \pi^+$ and $B^0_s \to D^\mp_s K^\pm$ selections*, CERN-LHCb-2007-017, 2007.

[77] V. Gligorov, *Reconstruction of the Channel $B^0_d \to D^+ \pi^-$ and Background Classification at LHCb.*, CERN-LHCb-2007-044, 2007.

[78] G. Punzi, *Comments on Likelihood fits with variable resolution*, arXiv:physics/0401045. Phystat 2003. SLAC, 2003.

[79] J. Gaiser, *Charmonium spectroscopy from radiative decays of the $J\psi$ and ψ', Ph.D. thesis, Appendix F*, SLAC-R-255, 1982.

[80] T. Skwarnicki, *A study of the radiative cascade transitions between the Υ and Υ' resonances*. PhD thesis, 1986, DESY F31-86-02 (Appendix E).

[81] W. Verkerke, D. Kirkby, *The RooFit toolkit for data modeling*, arXiv:physics/0306116v1, 2003.

[82] K. S. Cranmer, *Kernel estimation in high-energy physics*, Comput. Phys. Commun. **136** (2001) 198, arXiv:hep-ex/0011057.

[83] P. David, *Bepaling van de verhouding van deb-quark fragmentatiefracties f_s/f_d voor 7 TeV proton-protonbotsingen en een meting van de relatieve vervalbreedte van het verval $B^0 \to D^- K^+$*, 2011. CERN-THESIS-2011-076, Master thesis.

[84] Belle Collaboration, Belle Collaboration, *Observation of Cabibbo suppressed $B \to D^{-(*)} K^-$ decays at Belle*, Phys. Rev. Lett. **87** (2001) 111801, arXiv:hep-ex/0104051.

[85] N. Gagliardi, *Recent CKM Element Results from BaBar and Belle*, Nucl. Phys. B - Proceedings Supplements **210-211** (2011), no. 0 71.

[86] H. Neal, *Recent Results on CP-Violation at the BaBar and Belle B-Factories*, Int. J. Mod. Phys. A **26** (2011) 480.

[87] A. J. Buras, G. Isidori, and P. Paradisi, *EDMs versus CPV in $B_{s,d}$ mixing in two Higgs doublet models with MFV*, Phys. Lett. **B694** (2011) 402, arXiv:1007.5291.

[88] A. J. Buras, *Minimal flavour violation and beyond: Towards a flavour code for short distance dynamics*, Acta Phys. Polon. **B41** (2010) 2487, arXiv:1012.1447.

[89] A. Buras, *Flavour Theory: 2009*, PoS (2009) 024, arXiv:0910.1032.

[90] LHCb Collaboration, R. Aaij *et al.*, *Measurement of $\sigma(pp \to b\bar{b}X)$ at $\sqrt{s}$=7 TeV in the forward region*, Phys. Lett. B **694** (2010) 209, arXiv:1009.2731.

[91] LHCb Collaboration, R. Aaij *et al.*, *Absolute luminosity measurements with the LHCb detector at the LHC*, JINST **7** (2012), no. 01 P01010, arXiv:1110.2866.

[92] DELPHI Collaboration, P. Abreu *et al.*, *Production rate and decay lifetime measurements of B_s^0 mesons at LEP using D_s and ϕ mesons*, Z. Phys. C **61** (1993) 407.

[93] CDF Collaboration, T. Affolder *et al.*, *Measurement of b quark fragmentation fractions in $p\bar{p}$ collisions at $\sqrt{s}$ = 1.8 TeV*, Phys. Rev. Lett. **84** (2000) 1663, arXiv:hep-ex/9909011.

[94] R. Louvot, *Υ(5S) Results at Belle*, arXiv:0905.4345.

[95] J. Lewis, *CP violation and suppressed B_s^0 decays at CDF. Proceedings XXV Rencontres de Physique de La Vallee d'Aoste*, Submitted to Nuov. Cim. (2011).

[96] LHCb Collaboration, R. Aaij *et al.*, *Search for the rare decays $B_s^0 \to \mu^+\mu^-$ and $B^0 \to \mu^+\mu^-$*, Phys. Lett. B **699** (2011), no. 5 330, arXiv:1103.2465.

[97] LHCb Collaboration, R. Aaij *et al.*, *The Search for the rare decays $B^0_{(s)} \to \mu^+\mu^-$ with 300 pb^{-1} at LHCb*, LHCb-CONF-2011-034, Jul, 2011.

[98] A. Read, *Presentation of search results: the* CL_s *technique*, J. Phys. **G28** (2002) 2693.

[99] D0 Collaboration, V. M. Abazov *et al.*, *Search for the rare decay $B_s^0 \to \mu^+\mu^-$*, Phys. Lett. B **693** (2010) 539, arXiv:1006.3469.

[100] CDF Collaboration, T. Aaltonen *et al.*, *Search for $B_s^0 \to \mu^+\mu^-$ and $B^0 \to \mu^+\mu^-$ decays with CDF–II*, Phys. Rev. Lett. **107** (2011) 239903, arXiv:1107.2304.

[101] CMS Collaboration, S. Chatrchyan *et al.*, *Search for $B_s^0 \to \mu^+\mu^-$ and $B^0 \to \mu^+\mu^-$ decays in pp collisions at $\sqrt{s} = 7$ TeV*, Phys. Rev. Lett. **107** (2011) 191802.

[102] LHCb Collaboration and CMS Collaboration, *Search for the rare decay $B_s^0 \to \mu^+\mu^-$ at the LHC with the CMS and LHCb experiments*, CMS-PAS-BPH-11-019, LHCb-CONF-2011-047, Aug, 2011.

[103] A. J. Bevan, *The Physics of Heavy Flavours at SuperB*, J. Phys. G **39** (2012) 023001, arXiv:1110.3901.

[104] LHCb collaboration, R. Aaij *et al.*, *Strong constraints on the rare decays $B_s \to \mu^+\mu^-$ and $B^0 \to \mu^+\mu^-$*, arXiv:1203.4493.

Acknowledgements

Amicus certus in re incerta
cernitur
Ennio

Before thanking the important people that helped and taught me a lot in these years, I need few lines to thank an important person that taught me a lot about life and that is not here anymore: addio Zione, tu sei stato molto di più di un semplice zio e rimarrai sempre nel mio cuore, grazie di tutto!

Four years ago I left, with some tears, the Milano-Bicocca group to come to Nikhef. I was at the same time sad and happy, scared and curious. Here at Nikhef I found fantastic people, and these years have passed in a glimpse and now I am ready to cry again this time because I am leaving you. First of all I would like to thank Marcel Merk for the time he spent with me, teaching a lot of physics and showing me how a good supervisor has to be. I think you are one of the few cases of a supervisor who was not hated during the reviewing process of the thesis, and I have to admit that this period in which I had to interact a lot with you was absolutely incredible, and I was always surprised and amazed how you could detect always the most important or critical thing of all the discussions without having been involved in them before. My thesis would not be like this without your help. A special thanks must be reserved for Niels Tuning: I have bothered you so much in these years, and you were always nice and patient with me. It was great to work with you and I appreciated so much your constant enthusiasm. You were always present when I needed you and your help, and the time with you was always great. With your example I learnt how to deal with comments and criticisms without taking them personally but as a good occasion to improve myself and my work. This is a fantastic gift for life. An other incredible person of this time at Nikhef is for sure Antonio: I do not think my English capabilities are enough to explain how incredible were working with you. You showed me that is possible to combine professionalism and fun. The months I worked with you were the funniest I ever had at work, but it was also one of the most productive period in which I learnt so much about how to work and about physics in general.

My PhD would not be the same without one of the most clever and important friend I have: Nico!!! Saying simply “thanks” is clearly not enough. In these years we stayed together more time than with our families, we were colleagues and we are good friends, all I know about analysis is thanks to you and doing analysis with you was fantastic. You helped me in growing and you followed me day by day. You are my hero in the world of Physics, and I am happy to have had the opportunity to meet you and to work with you. I am looking forward to do it again in Zurich!

Life is not life without a family and I am so lucky to have a fantastic family with me. First of all my husband: always present and ready to help me. You are the best husband, father, lover, friend and man I could imagine and I manage to arrive at the end of this adventure also because you are with me. You are also the origin of the best “things” I did in my life, and I would say also in my PhD: Justine and Camille. Thanks babies because you are the sun of my life. JuJu, with your nice voice, you brilliant eyes and your smile, you are able to convert any terrible day in a fantastic adventure. It is nice to have a good reason to leave work and you teach me everyday that there is a life outside CERN that has to be lived. You, together with Nikhef in general, managed to show me that you can be productive also taking sometimes to enjoy life and this is the best present I have received. For Camille I have a special thank: you were all the time with me typing this thesis, feeling the stress, and motivating me with your kicks. Thanks a lot for your help! Outside this close relatives there are a lot of other fantastic people that, even if being faraway are always with us. Un saluto spaciale va alla mia mamma e al mio papà che sono assolutamente i migliori genitori che si possano immaginare. Sempre pronti ad aiutare e a mettere i loro bisogni al secodo posto. Senza di voi non sarebbe stato così facile il primo anno con Justine e senza i vostri insegnamenti sicuramente non sarei qui oggi a scrivere questi ringraziamenti. Mi avete dato la passione per la cultura e la libertà di fare sempre le mie scelte responsabilizzandomi dai primi giorni della mia vita. Questo mi ha forgiato, ha reso la vostra vita molto più difficile, ma ve ne sarò sempre grata. Un grande saluto va anche a mio fratello che ancora una volta avrà una mia tesi da leggere e non lo farà. Così come a lui anche alla sua famiglia, ai piccoli Enrico, Giulia, Riccardo e alla mia cognatina Giuditta va un saluto speciale, perchè anche se siamo sempre ai capi opposti del mondo siete sempre vicini a noi nei nostri pensieri. La lista della famiglia e’ ancora molto lunga e non posso certo dimenticare i miei zii: la Zietta, cosi’ come lo zio Gigi, la zia Carla, la zia Maria, che ancora mi pensa con il camice bianco, ma anche Alessandra e la nonna Bianca. E’ sempre un piacere rivedervi ogni volta che torniamo in Italia. Nella lunga lista di parenti rientra anche la magnifica famiglia di Sam che è ormai anche la mia famiglia. Con i miei cari suoceri, Michael, Monica, Ivo, Sara, Rachele, Emanuele, Raffaele, Gioele, Noemi, Marco, Martino, Stefano, Sophie. Voi non potete immaginare quanto siate nella nostra vita quotidiana grazie a Justine che non fa altro che parlare di voi e dello zio Gggabriel. Questo mi porta quindi a ringraziare una persona ben più che speciale: lo zio Gggabriel. You are the first friend I had at Nikhef and all the time spent with you was special. You are a good

physicist, but especially you are a nice person and thanks to you I felt less alone during my period in Amsterdam. It was very nice to have you two weeks with us in our house, and I have to admit you never left us since Justine is everyday (not an exaggeration) talking about you and asking where are you and what are you doing. I think you have to come back again. I cannot even imagine how to thank you for all the things you are doing for me as paranimf. You took care of all the boring part of the thesis bureaucracy and you were always present in chat when I needed to talk with somebody. You are sharing your difficult duty of being my paranimf with an other special person: Cristian. You are always enthusiastic and ready to let me talk about things, especially physics, for hours. It is always a pleasure when you come to our place and also if we are living so far away I am happy to meet you and that our friendship is growing nicely in these years.

Special thanks are also reserved for all the friends we have around us: Carol, Nicola (and the little Mario) who "fed us" so many times. Every time we can stay with you we have a lot of fun and we can understand once more how special you are. It was a pleasure also to become friend and soon neighbour of Maike, Jacopo, Dalia and the "littlest one" Giuseppe. It is nice being all friends and see how parties transformed from late beer party in early afternoon party with cakes and fruit juices.

At Nikhef I found a lot of nice friends, Alexander, Chiara, Daan, Eduard, Faab, Hella, Jan, Jeroen, Kristof, Manuel, Rob, Roel, Serena, Siim, Suvayu, Veerle, Victor, ... it was nice to work, eat and have beers with all of you. A special thank is reserved for the friends who shared the office in the last period, Maurizio, Rose and Pieter. It was especially a pleasure to work with you, Rose, and try to learn how to become a post-doc. I hope I was not a total disaster in helping you, anyway for me it was a nice experience and I hope we still collaborate as well as stay friends in the future. I am also happy to have met Maurizio who is sitting in front of me ready for taking an ice–cream or discuss about something, from normal–life problems to physics issue. If Francesco is wondering if I forgot him... I'm not! I just want to put you together with Domenico and say thanks for the parties, and write in the stone that you gave the "salame/salsiccia" to Justine. She is still happy and remembering you as the uncles who did this.

Here at CERN there is also the possibility to work with a lot of people not from your group. So special thanks are reserved for friends like Vava and Laurence who shared with me the experience of several analyses. Thanks a lot especially to Vava for the time you spent to explain me things about the trigger, or for the nice experience of being contact authors together. A special thanks goes also to Yasmin who was always nice and ready to talk when needed. It was nice being in Lake Louise together. Here at CERN there are also special friends such as Thierry and Ken. I do not need to say how important you were the first time I came to CERN, and I am so happy to still have the occasion to chat with you. You are really nice person, and I will be always proud of the score I did with you, Thierry, during the football match in my weeding party.

In the period I was at Nikhef I met a lot of nice people, and I would like to remember especially all the technicians who taught me a lot with their experience, and to Jan Visser: with you around there is always a bit of Italy also in the the Netherlands. Thanks for all the pasta you gave me every times I traveled to Nikhef, and it was cool to cook for the first, and probably the last time in my life, the “cannoli alla siciliana”. They were really good, and we had a lot of fun in cooking them. You are a nice friend and I hope I will still manage to stay in contact with you in the coming years.

A space in this acknowledgements goes for sure to the people living around me in Thoiry. There are our friends, Saverio and Anna with their nice daughters Filomena and Maria-Martina, our friends and neighbours Eric and Jacqueline, Erwan and Guri with the little/huge Eric and Hugo, and Mr. Bobbink, as well as the lady who sold me so many tea and fruit-juices during these years at the cafeteria on the last floor of my building at CERN giving me all the time nice occasions to improve my French. At the same time I would like to remember all the colleagues of Sam that are also nice friends for me and special uncles and aunts for Justine.

In Italy we left lots of friends. Although it is now difficult to see each other again, it is always nice to know that you are there and that sooner or later we can meet again for a pizza or a “cioccolata calda” and summarize our lives. Quindi un saluto speciale a tutti voi, Maurizio e Ombretta con i quali il tempo sembra non passare mai e ogni volta è come se ci si fosse visti fino al giorno prima, Giancarlo e la sua nuova famiglia, Bred, Cristian, Elena, Chicco, ... così come un saluto speciale va a Gabriele e Laura. Non è facile mantenere i contatti, ma il ricordo dell’anno passato insieme a casa di “Frap” non potrà mai essere cancellato. In fine, uno spazio speciale per le prime persone che mi hanno accompagnato nel mondo della fisica Tito e Davide. È stato bello lavorare con voi e siete sempre stati degli amici speciali. Ci sarà sempre un posto per dormire e una cena pronta per voi ogni volta che vorrete passare dal CERN.

Before finishing I cannot forget three of the most important people in the early years of my experience with physics. First I would like to thank Piergiorgio Giudici who showed me what does it mean making an experiment and producing a scientific result. If I did not give up with physics during the difficult years of high-school is only thanks to you, and this is the basis of all the happiness I have now in doing the job I always dreamt about, in a cool place surrounded by a lot of smart and international people. Then I cannot forget Giovanni Tonzig that, with his pre-university course, let me meet Sam and let me increase my love for physics during the hard time of the high-school. Last but not least, Clara Matteuzzi who introduced me to CERN, followed me in the last years of university with the bachelor and master theses, and who proposed me to go to Nikhef. You are a fantastic supervisor and group leader as well as a great person. It is always a pleasure to pass by your office, and I will never forget all the things you did and you taught to me in these years.

At the end of this long story I would like also to thanks my reading committee Bob, Els, Robert, Tjeerd and Tim: they dedicated their time to read my thesis and helped me in im-

proving the quality of final text. I appreciate a lot your effort.

Therefore, thank you to all the people, also the one I could have forgot, that contribute to achieve such a beautiful life and arrive to the end of this thesis.